Multiscale assessment of food lipid structures Tatiana Nikolaeva 2019

MULTISCALE ASSESSMENT OF FOOD LIPID STRUCTURES

Tatiana Nikolaeva

You are cordially invited to attend the public defense of my PhD thesis

MULTISCALE ASSESSMENT OF FOOD LIPID STRUCTURES

On Monday
the 7th of October 2019
at 16:00 in the Aula of
Wageningen University
Generaal Foulkesweg 1,
Wageningen

TATIANA NIKOLAEVA
tatiana.nikolaeva@wur.nl

PARANYMPHS:
Mattia Fontana
mattia.fontana@wur.nl

Koen J.A. Martens
koen.martens@wur.nl

Invitation

MULTISCALE ASSESSMENT OF FOOD LIPID STRUCTURES

Tatiana Nikolaeva

Thesis committee

Promotor
Prof. Dr J.P.M. van Duynhoven
Special Professor of Magnetic Resonance in relation to Food
Wageningen University & Research

Co-promotor
Dr H. Van As
Associate professor, Laboratory of Biophysics
Wageningen University & Research

Other members
Prof. Dr E van der Linden, Wageningen University & Research
Prof. Dr G. Guthausen, Karlsruhe Institute of Technology, Germany
Dr. C. Rondeau-Mouro, IRSTEA, Rennes, France
Prof. Dr E. Flöter, Technical University, Berlin, Germany

This research was conducted under the auspices of the Graduate School VLAG (Advanced studies in Food Technology, Agrobiotechnology, Nutrition and Health Sciences).

MULTISCALE ASSESSMENT OF FOOD LIPID STRUCTURES

Tatiana Nikolaeva

Thesis

submitted in fulfilment of the requirements for the degree of doctor

at Wageningen University

by the authority of the Rector Magnificus,

Prof. Dr A.P.J. Mol,

in the presence of the

Thesis Committee appointed by the Academic Board

to be defended in public

on Monday 7 October 2019

at 4 p.m. in the Aula.

Tatiana Nikolaeva

Multiscale assessment of food lipid structures,
206 pages.

PhD thesis, Wageningen University, Wageningen, the Netherlands (2019)
With references, with summary in English

ISBN: 978-94-6395-115-9

DOI: https://doi.org/10.18174/499301

CONTENT

CHAPTER 1

General Introduction

1.1. Lipid multiscale structures in food

Plant lipids are a major component of our diet and critically define flavour, texture, and nutritional value of food products. Oleaginous plants store lipids in their nuts, beans and seeds (Figure 1.1). Their cells contain food-relevant lipid molecules, like triacylglycerols (TAGs) and phospholipids (PLs), in so-called oil bodies (Nikiforidis, Matsakidou, & Kiosseoglou, 2014; Tzen, Cao, Laurent, Ratnayake, & Huang, 1993). In these storage organelles lipids exist in liquid and liquid-crystalline (LC) phases, the latter as interfacial layers. In order to use plant lipids in food ingredients and products, they must undergo several structural and compositional conversions in the "farm-to-fork" chain. These processing routes have schematically been depicted for several fat-continuous food products in Figure 1.1. Industrial processing involving shear, temperature and pressure can significantly modulate the self-assembly of lipids (Leser, Sagalowicz, Michel, & Watzke, 2006; Farnaz Maleky, 2015). Lipids can organise themselves in a wide range of hierarchical crystalline and LC structures, which can span multiple scales from nano-, via meso- to macro (Kulkarni, 2012; Leser et al., 2006; Michalski et al., 2013). The organisation of both multiscale crystalline and LC lipid systems is governed by interplay of molecular and colloidal interactions. These underlie the physical properties of lipid systems when they undergo melting, crystallisation, and flow.

Figure 1.1. Schematic example of lipid structures as they occur changes throughout the farm-to-fork supply chain of fat-continuous foods.

For most lipid-based food products multiscale architectures underlie critical functionalities such as shelf life stability, water holding capacity, texture and mouth feel (Marangoni et al., 2011; Ramel, Co, Acevedo, & Marangoni, 2016). Understanding of these multiscale organisations is therefore a prerequisite for designing lipid-based food products with desired functionalities. The food industry well appreciates that establishing structure-function relationships is a key step in the development of novel sustainable food formulations and processing technologies. The aim of this thesis is to develop and apply novel methodologies to characterize and quantify multiscale structures of food lipids under dynamic processing conditions. This thesis will focus on investigation of structure-function relationships of both crystalline and liquid crystalline (LC) multiscale structures composed of TAGs and phospholipids, respectively.

1.1.1. Multiscale TAG crystalline structures

Triacylglycerols (TAGs) (Figure 1.2) represent the majority of lipid molecules present in edible fats and oils. The backbone of a TAG molecule is a glycerol molecule to which three fatty acids (FFAs) are esterified. These long hydrocarbon chains can adopt different configurations depending on the saturation and the presence of trans-or cis-bonds (Marangoni, 2004) which determine the melting point of TAGs. In foods TAGs are often used as blends of crystalline fat and liquid oil. In such blends crystalline structures form a continuous colloidal network comprising the liquid oil phase (Figure 1.2). These networks define texture of a wide variety of fat-continuous food products such as chocolate, margarine, spread and shortenings (Marangoni et al., 2011). Over the last decades the market for fat-continuous food products has changed dramatically due to changing lifestyles of consumers and their growing concerns with respect to a healthy diet (Marangoni et al., 2019; Sato & Ueno, 2011). Industrial innovations therefore aim at manufacturing fat-based products with both nutritional benefits and superior textural properties (spreadability, mouthfeel). This has prompted renewed interest in structural investigation of TAG crystalline structures so that they can be used effectively as ingredients in food products. In order to manipulate the visual and textural properties of food products one needs to know dimensions of crystals and their space-filling network. For maintaining texture and visual appearance during shelf-life one also needs to understand how the liquid phase migrates through this TAG crystal network (Green & Rousseau, 2015; Rousseau, 2013; Rousseau, Foresti, Hill, Marangoni, & Forestière, 1996). Fat crystal networks have also gained interest as a stabilising structures in

colloidal dispersions (water-in-oil (W/O) and oil-in-water (O/W) emulsions) which can present a route for effective manufacturing of emulsified food products (Rousseau, 2000; Sato & Ueno, 2011).

Current insights in the hierarchical multiscale architecture of fats are schematically summarized in Figure 1.2 (Farnaz Maleky, 2015; Marangoni et al., 2011). The formation of fat crystal network starts with the self-assembly of the TAG molecules into crystalline lamellar mesostructures. These lamellae stack epitaxially to form a crystalline domain, known as a crystalline nanoplatelet (CNP) (Acevedo & Marangoni, 2014). The CNPs can aggregate to larger microstructures that are plate-like, needle-like or spherulitic. Many factors affect the formation and the properties of fat crystal networks (Marangoni et al., 2011). The structural properties of TAG CNPs are influenced by the molecular properties of TAGs and their composition. Traditionally, formation of fat crystal networks via industrial processing routes involves melting and cooling steps. It is well known that changes in the shear rate and temperature during these steps lead to changes in the multiscale crystal network structures in fat-based systems (Farnaz Maleky & Mazzanti, 2018). They determine an intricate interplay between formation of fat crystals and their aggregation into larger structures. The strong coupling of the crystallisation and aggregation is adding significant complexity to the industrial manufacturing of fat-based food products.

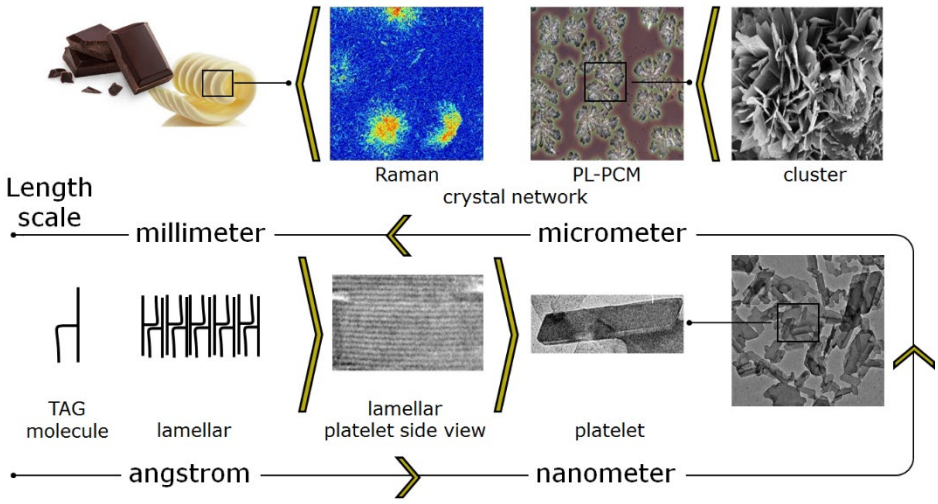

Figure 1.2. Structural levels present in a triacylglycerol (TAG) crystal network. Adapted from (Marangoni et al., 2019) with permission from Springer.

1.1.2. Multiscale phospholipid liquid-crystalline structures

Liquid-crystalline (LC) self-assembled structures typically are formed when polar lipids are mixed with water (Leser et al., 2006; Sagalowicz et al., 2016). These are highly organized structures possessing long range order. Their multiscale structures cover the nano- to micro scales (Figure 1.3). Most relevant for food applications are phospholipids (PLs) and glycolipids (Heertje, Roijers, & Hendrickx, 1998; Leser et al., 2006). They are also commonly referred to as surface active lipids, amphiphiles or low molecular weight surfactants due to the fact that they consist of both a hydrophilic and a lipophilic parts (Leser et al., 2006). When mixed with water they are able to create various LC mesophases, typically illustrated in a hypothetical lipid/water binary phase diagram as a function of water concentration (Heertje et al., 1998; Kulkarni, 2012; Leser et al., 2006; Michalski et al., 2013; Sagalowicz et al., 2016). Figure 1.3 shows basic phospholipid LC mesophase structures which can occur in food products. Phospholipids monolayers play an important role as stabilizers of interfaces in foams and emulsions (Leser et al., 2006; Michalski et al., 2013; Sagalowicz et al., 2016). Recently, micelles formed by PLs and other polar lipids have been proposed as Self-Assembling Structures (SASs) to deliver lipophilic food/pharma ingredients (Porter, Trevaskis, & N Charman, 2007; Sagalowicz et al., 2016; Salentinig, Phan, Hawley, & Boyd, 2015).

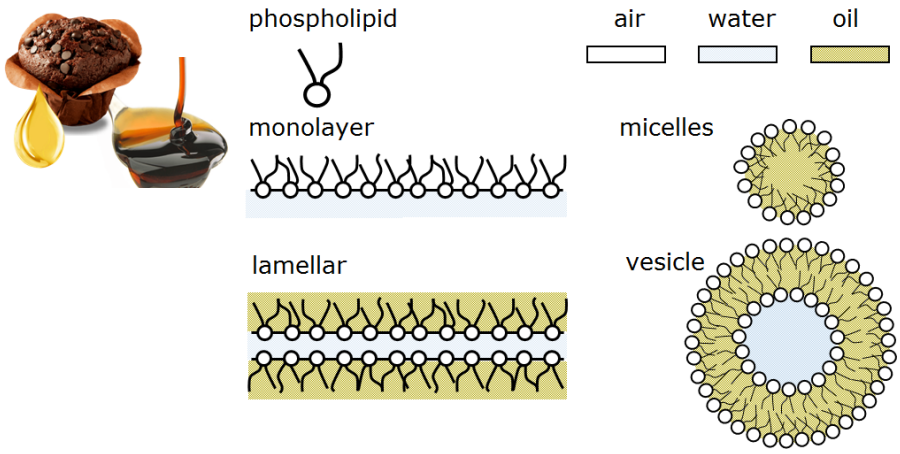

Figure 1.3. Phospholipid liquid-crystalline structures as they can occur in food products.

1.2. Assessment of multiscale lipid structures

The heterogeneous composition and structure of lipid-based foods put them among the most challenging systems to be studied at different length scales. Microscopy, rheology, NMR and X-ray or neutron scattering methods can be used to unveil the crystalline and liquid crystalline lamellar lipid structures from nano- to microscales (Nagle & Tristram-Nagle, 2000; Ramel et al., 2016; Voda, Den Adel, van Malssen, & van Duynhoven, 2017). Rheology can provide bulk information of flow behaviour of crystalline and LC systems under dynamic conditions but cannot deliver structural information in a direct manner. Microscopic techniques can provide a direct visualisation of the crystalline and LC structures. Single TAG crystalline nanoplatelets were observed for the first time using cryogenic transmission electron microscopy (cryo-TEM) (Acevedo & Marangoni, 2010). Scanning and transmission electron microscopy (SEM and TEM) are the only techniques that can provide images of single fat nanoplatelets with dimensions of 5-1000 nm (Acevedo & Marangoni, 2014). Raman imaging was employed to study the microstructure of TAG crystalline networks in terms of fat cluster sizes and fractal dimensions (Martens et al., 2018; van Dalen et al., 2017). PLM and SEM are also used to characterise phase of LC structures (Sein, Hitchman, & Dayton, 2019). However, most of the microscopic techniques require time consuming, invasive and tedious sample preparations and are not capable of spanning different length scales and quantification of structures. Quantification of structural features can be performed by image analysis methods but requires careful imaging procedures and a high level of expertise. Moreover, the available arsenal of microscopic techniques lacks the ability to assess dynamic events in a quantitative manner.

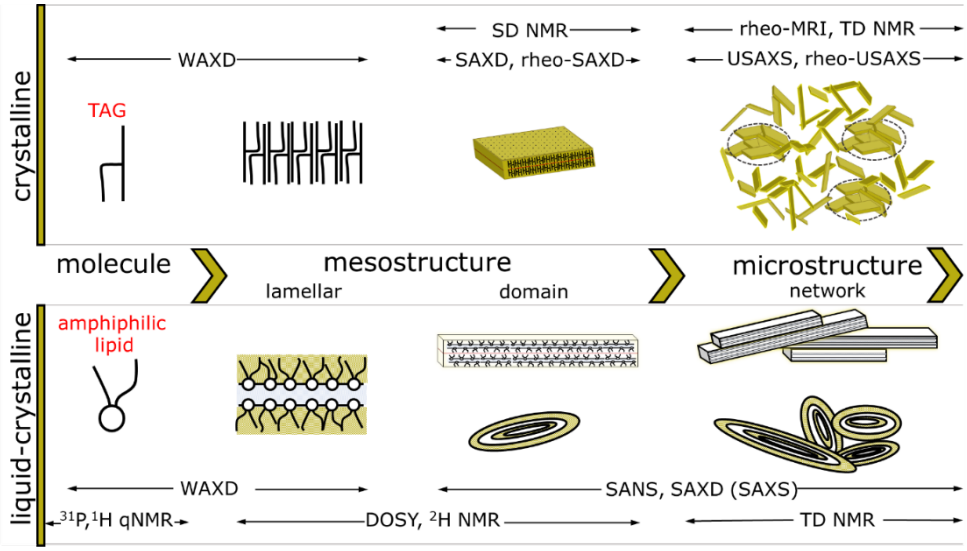

Figure 1.4. Hierarchical multiscale structure representation of the crystalline and liquid crystalline lipid systems.

X-ray and neutron scattering (SAS) and NMR techniques do not suffer from these limitations. These techniques can span multiple length scales in a non-invasive manner and can be used in combination with rheological measurements. In the next sections SAS and NMR techniques are discussed with respect to their use in this thesis for multiscale assessment of characterisation of crystalline and LC structures (Figure 1.4).

1.2.1. Diffraction and scattering techniques in assessment of multiscale lipid structures

1.2.1.1. X-ray diffraction and scattering in assessment of TAG multiscale structures

X-ray scattering and diffraction techniques are commonly used in investigations of the TAG crystalline structures to obtain quantitative information on molecular packing, polymorphism, phase transitions, crystallite thickness and organization in fractal networks (Acevedo & Marangoni, 2014; Peyronel, Quinn, Marangoni, & Pink, 2014; Sato, Bayés-García, Calvet, Cuevas-Diarte, & Ueno, 2013). Atomic and molecular characteristics of TAG

crystals have been extensively studied by wide and small angle X-ray diffraction (WAXD and SAXD) (Marangoni et al., 2011).

Bragg diffraction happens due to interference of X-rays with electron clouds of atoms organized in periodic structures (Giannini et al., 2016). Bragg diffraction peaks that occur at wide angles (WAXD) provide information on length scales in the q-region from 1 to 5 $Å^{-1}$ (Peyronel, Ilavsky, Pink, & Marangoni, 2014) and can be used to recognize TAG crystal polymorphism (Figure 1.4). Diffraction at small angles (SAXD) gives structural information in the q-region from 0.05 to 1 $Å^{-1}$ which corresponds to the longitudinal order of the TAG layers and thus allows for estimating periodical spacings within crystal nanoplatelets (Figure 1.4).With the use of SAXD, also the average and distribution of the thicknesses of these nanoplatelets can be determined based on diffraction peak shape analysis (den Adel, van Malssen, van Duynhoven, Mykhaylyk, & Voda, 2018). The accessible length scale of SAXD is defined by the instrumental capability to measure diffraction at small angles. In the case of a synchrotron radiation source, this can be as large as 200 nm.

In order to assess size and shape of fat crystallites X-ray scattering should be used. Small angle X-ray scattering (SAXS) is a technique where the elastic scattering of X-rays by electron clouds of atoms in any structures is recorded providing information on size and shape of nano-size particles and their distribution over space. The most useful for assessment of fat crystal networks (Peyronel, Pink, & Marangoni, 2014) is ultra-small angle X-ray scattering (USAXS) which covers the q-range from $5x10^{-5}$ $Å^{-1}$ to 10^{-1} $Å^{-1}$. USAXS is able to obtain information about the morphology of CNPs at nanoscale and their aggregates up to micronscale (Figure 1.4) (Peyronel, Pink, & Marangoni, 2014; Peyronel, Quinn, et al., 2014; Pink, Peyronel, Quinn, Singh, & Marangoni, 2015). USAXS provides also fractal dimensions of the fat crystal networks, which contain information about spatial distribution of the fat crystalline structures and possible mechanisms of the network formation.

X-ray scattering and diffraction measurements can be performed at different temperature and shear conditions (Farnaz Maleky & Mazzanti, 2018; Fatemeh Maleky & Marangoni, 2008; Mazzanti, Marangoni, & Idziak, 2009). Detailed rheo-X-ray studies have been carried out on fat crystallization under shear in a concentric cylinder (CC) geometry where the beam was oriented tangentially. In this configuration polymorphic transformations changes in the number of crystal nuclei can be quantified. Two-dimensional X-ray diffraction (2D XRD)

under shear provides information about shear-induced alignment of the fat crystals. Effects of shear on microscales of fat crystal networks can be studied by means of rheo-USAXS to obtain insights about aggregation of the crystalline nanoplatelets.

1.2.1.2. Small angle X-ray and neutron scattering in assessment of phospholipid liquid-crystalline multiscale structures

Structural characterisation of the liquid crystalline structures (Figure 1.3), similar to the crystalline structures, can be assessed by WAXD and SAXD. However, SANS is also widely used as a complementary technique (Figure 1.4). The main advantage of SANS is the opportunity to distinguish intensities of two isotopes of the same element due to differences in scattering lengths (Gilbert, 2019; Lopez-Rubio & Gilbert, 2009). The created contrast allows to emphasise or to suppress specific elements of multi-component structures. In the case LC structures components may be contrast-matched using mixtures of heavy and light water for which the scattering length density for H_2O is negative and for D_2O is positive. Contrast variation may also be achieved by a specific labelling of individual functional groups by deuteration. This is an advantage of neutron scattering compared to X-ray scattering, whose scattering amplitude depends on the number of electrons in the atomic shell and thus does not distinguish between different isotopes of the same element (Belička, Devínsky, & Balgavý, 2014).

Both, SAXS (SAXD) and SANS are commonly used to investigate phospholipid LC lipid structures (Belička et al., 2014; Feng et al., 2004; Kučerka et al., 2008; Kučerka, Pencer, Sachs, Nagle, & Katsaras, 2007; Kučerka, Tristram-Nagle, & Nagle, 2006; Martiel, Handschin, Fong, Sagalowicz, & Mezzenga, 2015; Nagle & Tristram-Nagle, 2000; Nieh, Glinka, Krueger, Prosser, & Katsaras, 2001). These techniques are valuable in, both, structural characterization and quantification. They are able to assign curved or planar PL LC structures and then to monitor their ternary phase behaviour under different external factors (Kučerka, Nieh, & Katsaras, 2010; Kučerka et al., 2007; Lei, Ma, Kodali, Liang, & Ted Davis, 2003; Montalvo, Pons, Zhang, Díaz, & Valiente, 2013). Advances in experiments have stimulated the development of more complex models for LC structures. However, the focus of most of these studies lies on model and single type PL systems neglecting multicomponent PL systems with high structural heterogeneities which are used to be in lipid-based food materials.

1.2.2. NMR assessment of multiscale lipid structures

1.2.2.1. NMR assessment of TAG multiscale structures

The NMR capabilities for assessment of TAG crystal networks structures is presented in Figure 1.4. Solid fat content (SFC) as determined by time domain (TD) NMR is widely used to quantify the amount of crystalline structures in relation to liquid part of the sample (Thurmond, Otten, Brown, & Beyer, 1994). The non-invasive and almost real-time nature of SFC measurements allows for monitoring of lipid crystallisation and further crystal growth under shear and variable temperature conditions (Marangoni et al., 2011; Marangoni & Wesdorp, 2013). The crystalline mesostructure, from a few tens up to a few hundred nanometers, can be explored by ^{1}H spin-diffusion NMR (Voda et al., 2017). In application to the fat crystal systems this technique can provide the thickness of the crystalline domains (Figure 1.4).

Rheo-MRI can be used to follow structure formation and breakdown (Figure 1.3) in a non-invasive manner and provide spatially resolved characteristics of flow behaviour. Flow visualization by rheo-MRI provides information about complex non-Newtonian materials (Bonn et al., 2008) including a direct view on shear banding (Coussot, Raynaud, Bertrand, & Moucheront, 2002b; Møller et al., 2008; Raynaud et al., 2002), wall slip and migration (Colbourne et al., 2018; Mitchell et al., 2017), that cannot be accessed by standard (bulk) rheology. Such local flow heterogeneities cannot be inferred directly from standard rheology experiments. Rheo-MRI therefore significantly facilitates the interpretation of the complex rheology (Callaghan, 1999) of colloidal dispersions (Li, Seymour, Powell, & McCarthy, 1994; Seymour, Maneval, McCarthy, McCarthy, & Powell, 1993) and emulsions (Britton & Callaghan, 2000).

1.2.2.2. NMR assessment of liquid-crystalline phospholipid multiscale structures

The NMR techniques that can be deployed for assessment of multiscale lamellar liquid crystalline (LC) are schematically shown in Figure 1.4. Detailed information on lipid (or PL) structural and dynamical properties can be obtained from ^{31}P and ^{2}H NMR spectroscopic techniques (Thurmond et al., 1994; J. P. M. van Duynhoven et al., 2005). Among different NMR-techniques, ^{31}P and ^{2}H NMR have been widely used to get information about the average molecular conformations, supramolecular organization, and orientational properties

of phospholipid LC mesophases. In ^{31}P NMR spectra chemical shift anisotropy is a prominent feature which can be used to identify micellar, lamellar, hexagonal and other LC phases (Figure 1.3). ^{2}H NMR spectroscopy provides a particularly convenient and conclusive means for the determination of order and mobility in LC mesophases via the line shape of D_2O comprised within the phospholipid bilayers. Time domain (TD) NMR relaxometry and diffusometry have been used to characterise rotational and translational motility of PLs in LC phases. These techniques were able to monitor domain formation through characterisation of lipid lateral diffusion in PL bilayers which is affected by lipid packing and acyl chain ordering (Filippov, Orädd, & Lindblom, 2004; Lindblom & Orädd, 2009; Orädd & Lindblom, 2005; Orädd, Westerman, & Lindblom, 2005). However, applications of this methodological approach were limited to model PL LC systems. Although TD NMR techniques have shown to be powerful for assessment of structural changes in food systems during processing (Bosmans & Delcour, 2016; Mariette, 2009; J. van Duynhoven, Voda, Witek, & Van As, 2010) they have not been used so far to the best of our knowledge to investigate and quantify mobile properties of PLs in multicomponent LC food structures.

1.3. Demonstrator systems

1.3.1. TAG crystalline structures: MFC networks

Conventional processing routes for fat-continuous food products mostly rely on melt-cooling processing routes where crystallisation and network formation are strongly coupled. Dispersing micronized fat crystal (MFC) nanoplatelets in oil (Münüklü & Jansens, 2007) has been proposed as a route to decouple crystallisation and network formation. However, no detailed investigation on the multiscale structural organization and the mechanisms of MFC network formation has appeared yet. Obtaining such insights will open up the opportunity to design flexible processing routes for stable continuous fat products with superior sensorial properties.

1.3.2. Liquid-crystalline structures: phospholipid gums

Oil degumming is an oil refining process which critically relies on formation of phospholipid LC structures (Lei et al., 2003) in order to remove them from crude oils. This is a critical step

in obtaining shelf-life stable and high-quality edible oils. Degumming implies removing phospholipids (PLs) by adding water to crude oils and transforming partially oil-soluble PLs into oil-insoluble lamellar LC structures, called gums. These oil-insoluble liquid crystals have higher density and can aggregate into bigger particles (Figure 1.4), which can be separated from crude oil by centrifugation. The described process is widely practiced and known as water degumming (WD). The separation efficiency of WD is however poor and strongly depends on the composition of the polar lipids in crude oils.

A novel more efficient alternative to WD process is enzymatic degumming (ED) (Dayton & Galhardo, 2014; Dijkstra, 2011). ED involves phospholipases dispersed in water. They specifically affect different types of PLs which occur in crude oils and convert them into polar and non-polar moieties (Dijkstra, 2011; Jiang, Chang, Wang, Jin, & Wang, 2014; Sein, 2018; Xie & Dunford, 2017; Ye et al., 2016). The non-polar enzymatic conversion products (monoglycerides (MG), diglycerides (DG) and free fatty acids (FFA)) are expected to dissolve in oil. The polar lipids in contact with water are expected to form LC structures which can be removed as a gum. In comparison to WD the ED is assumed to be more efficient than WD and to remove PLs from crude oils in a more environment-friendly manner with minor loss of vegetable oil. The insights in the multiscale structure of gums are limited. This can be attributed to the strong compositional heterogeneity of gums, which hampers the straightforward deployment of scattering and NMR techniques.

1.4. Outline of the thesis

The overall aim of this thesis is to develop, validate and apply methodological toolboxes for assessment of multiscale MFC networks and LC structures formed after degumming. Techniques which could provide quantitative structural information under dynamic conditions are in focus of this thesis. **Chapter 2** describes implementation and validation of rheo-microMRI in millimeter gap sized concentric cylinder (CC) geometries at high magnetic field and strong magnetic field gradients. At this setup experimental precautions need to be taken to allow for high quality measurements of flow characteristics in lipid-based systems. Particular attention will be paid to the validation of this technique for spatially resolved visualisation and quantification of heterogeneous and transient flow behaviour.

Chapter 3 presents a new design for a highly flexible rheo-cell which can be used by X-ray sources from both a high-end synchrotron facility as well as lab-based equipment. Critical details necessary for assessment of X-ray diffraction and scattering of complex lipid dispersions under shear and variable temperature are discussed.

In **Chapter 4** and **Chapter 5** the aforementioned methodologies are deployed to assess multiscale structure of MFC networks under static and dynamic conditions. **Chapter 4** describes the characterisation of MFC networks under static and dynamic conditions by a methodological toolbox including confocal Raman-imaging, rheological, SFC NMR, rheo-microMRI, X-ray diffraction and scattering techniques. The hypotheses generated in **Chapter 4** are further explored in **Chapter 5** where network formation of MFC networks under dynamic conditions is investigated. Confocal Raman-imaging, rheo-SAXD and rheo-microMRI techniques are deployed to unravel how formation of MFC networks depends on oil composition, shear and temperature.

Chapter 6 presents for the first time a multiscale investigation of gums formed under industrial relevant conditions. SAXS, SANS and NMR are deployed in a complementary manner to investigate of multiscale LC structures (gums) after water degumming and different types of enzymatic degumming in crude soybean oils. Structural quantification is performed by SANS and SAXS on mesoscale through estimation of thicknesses of the hydration water layers. These measurements are complemented with ^{1}H time-domain (TD) NMR T2 relaxometry measurements.

References

Acevedo, N. C., & Marangoni, A. G. (2010). Toward nanoscale engineering of triacylglycerol crystal networks. *Crystal Growth and Design*, *10*(8), 3334–3339. https://doi.org/10.1021/cg100469x

Acevedo, N. C., & Marangoni, A. G. (2014). Nanostructured Fat Crystal Systems. *Annual Review of Food Science and Technology*, *6*, 1–26. https://doi.org/10.1146/annurev-food-030713-092400

Belička, M., Devínsky, F., & Balgavý, P. (2014). Neutrons in studies of phospholipid bilayers and bilayer–drug interaction. I. Basic principles and neutron diffraction. *Acta Facultatis Pharmaceuticae Universitatis Comenianae*, *61*(2), 1–11. https://doi.org/10.2478/afpuc-2014-0010

Bosmans, G., & Delcour, J. (2016). TD NMR Relaxation Studies of Cereal Products. In G. A. Webb (Ed.), *Modern Magnetic Resonance* (pp. 1–18). Springer International Publishing. https://doi.org/10.1007/978-3-319-28275-6_13-1

Colbourne, A. A., Blythe, T. W., Barua, R., Lovett, S., Mitchell, J., Sederman, A. J., & Gladden, L. F. (2018). Validation of a low field Rheo-NMR instrument and application to shear-induced migration of suspended non-colloidal particles in Couette flow. *Journal of Magnetic Resonance*, *286*, 30–35. https://doi.org/10.1016/j.jmr.2017.11.010

Dayton, C. L. G., & Galhardo, F. (2014). Enzymatic Degumming. *Green Vegetable Oil Processing*, 107–145. https://doi.org/10.1016/B978-0-9888565-3-0.50009-1

den Adel, R., van Malssen, K., van Duynhoven, J., Mykhaylyk, O. O., & Voda, A. (2018). Fat crystallite thickness distribution based on SAXD peak shape analysis. *European Journal of Lipid Science and Technology*, *1800222*, 1–6. https://doi.org/10.1002/ejlt.201800222

Dijkstra, A. J. (2011). Enzymatic degumming. *Lipid Technology*, *23*(2), 36–38. https://doi.org/10.1002/lite.201100085

Feng, Y., Rainteau, D., Chachaty, C., Yu, Z. W., Wolf, C., & Quinn, P. J. (2004). Characterization of a Quasicrystalline Phase in Codispersions of Phosphatidylethanolamine and Glucocerebroside. *Biophysical Journal*, *86*(4), 2208–2217. https://doi.org/10.1016/S0006-3495(04)74279-4

Filippov, A., Orädd, G., & Lindblom, G. (2004). Lipid Lateral Diffusion in Ordered and Disordered Phases in Raft Mixtures. *Biophysical Journal*, *86*(2), 891–896. https://doi.org/10.1016/S0006-3495(04)74164-8

Giannini, C., Ladisa, M., Altamura, D., Siliqi, D., Sibillano, T., & De Caro, L. (2016). X-ray Diffraction: A Powerful Technique for the Multiple-Length-Scale Structural Analysis of Nanomaterials. *Crystals*, *6*(8), 87. https://doi.org/10.3390/cryst6080087

Gilbert, E. P. (2019). Small Angle X-Ray and Neutron Scattering in Food Colloids. *Current Opinion in Colloid & Interface Science*. https://doi.org/10.1016/j.cocis.2019.03.005

Green, N. L., & Rousseau, D. (2015). Oil diffusivity through fat crystal networks. *Soft Matter*, *11*, 5523–5530. https://doi.org/10.1039/c5sm01355k

Heertje, I., Roijers, E. C., & Hendrickx, H. A. C. M. (1998). Liquid Crystalline Phases in the Structuring of Food Products. *LWT - Food Science and Technology*, *31*(4), 387–

396. https://doi.org/https://doi.org/10.1006/fstl.1998.0369

Kučerka, N., Nagle, J. F., Sachs, J. N., Feller, S. E., Pencer, J., Jackson, A., & Katsaras, J. (2008). Lipid Bilayer Structure Determined by the Simultaneous Analysis of Neutron and X-Ray Scattering Data. *Biophysical Journal*, *95*(5), 2356–2367. https://doi.org/10.1529/biophysj.108.132662

Kučerka, N., Nieh, M.-P., & Katsaras, J. (2010). Small-angle scattering from homogeneous and heterogeneous lipid bilayers. In A. Iglic & H. T. Tien (Eds.), *Advances in Planar Lipid Bilayers and Liposomes* (Vol. 12, pp. 201–235). Elsevier Inc. Academic Press. https://doi.org/10.1016/S1554-4516(10)12008-0

Kučerka, N., Pencer, J., Sachs, J. N., Nagle, J. F., & Katsaras, J. (2007). Curvature effect on the structure of phospholipid bilayers. *Langmuir*, *23*(3), 1292–1299. https://doi.org/10.1021/la062455t

Kučerka, N., Tristram-Nagle, S., & Nagle, J. F. (2006). Structure of fully hydrated fluid phase lipid bilayers with monounsaturated chains. *Journal of Membrane Biology*, *208*(3), 193–202. https://doi.org/10.1007/s00232-005-7006-8

Kulkarni, C. V. (2012). Lipid crystallization: From self-assembly to hierarchical and biological ordering. *Nanoscale*, *4*(19), 5779–5791. https://doi.org/10.1039/c2nr31465g

Lei, L., Ma, Y., Kodali, D. R., Liang, J., & Ted Davis, H. (2003). Ternary phase diagram of soybean phosphatidylcholine-water-soybean oil and its application to the water degumming process. *JAOCS, Journal of the American Oil Chemists' Society*, *80*(4), 383–388. https://doi.org/10.1007/s11746-003-0708-y

Leser, M. E., Sagalowicz, L., Michel, M., & Watzke, H. J. (2006). Self-assembly of polar food lipids. *Advances in Colloid and Interface Science*, *123–126*(SPEC. ISS.), 125–136. https://doi.org/10.1016/j.cis.2006.07.003

Lindblom, G., & Orädd, G. (2009). Lipid lateral diffusion and membrane heterogeneity. *Biochimica et Biophysica Acta - Biomembranes*, *1788*(1), 234–244. https://doi.org/10.1016/j.bbamem.2008.08.016

Lopez-Rubio, A., & Gilbert, E. P. (2009). Neutron scattering: a natural tool for food science and technology research. *Trends in Food Science & Technology*, *20*(11–12), 576–586. https://doi.org/10.1016/j.tifs.2009.07.008

Maleky, Farnaz. (2015). Nanostructuring triacylglycerol crystalline networks under external shear fields: A review. *Current Opinion in Food Science*, *4*, 56–63. https://doi.org/10.1016/j.cofs.2015.05.005

Maleky, Farnaz, & Mazzanti, G. (2018). Lipid Crystal Networks Structured under Shear Flow. In K. Sato (Ed.), *Crystallization of Lipids: Fundamentals and Applications in Food, Cosmetics, and Pharmaceuticals* (First, pp. 211–239). John Wiley & Sons Ltd. https://doi.org/10.1002/9781118593882

Maleky, Fatemeh, & Marangoni, A. G. (2008). Process development for continuous crystallization of fat under laminar shear. *Journal of Food Engineering*, *89*(4), 399–407. https://doi.org/10.1016/j.jfoodeng.2008.05.019

Marangoni, A. G. (2004). *Fat Crystal Networks*. CRC Press. https://doi.org/10.1201/9781420030549

Marangoni, A. G., Acevedo, N., Maleky, F., Co, E., Peyronel, F., Mazzanti, G., … Pink, D.

(2011). Structure and functionality of edible fats. *Soft Matter*, *8*, 1275. https://doi.org/10.1039/c1sm06234d

Marangoni, A. G., van Duynhoven, J. P. M., Acevedo, N. C., Mensink, R., Nicholson, R. A., & Patel, A. R. (2019). Fat mimetics for the replacement of saturated and hydrogenated fat in food products. *Nature Food*, submitted.

Marangoni, A. G., & Wesdorp, L. (2013). *Structure and Properties of Fat Crystal*.

Mariette, F. (2009). Investigations of food colloids by NMR and MRI. *Current Opinion in Colloid & Interface Science*, *14*(3), 203–211. https://doi.org/10.106/j.cocis.2008.10.006

Martens, K. J. A., van Dalen, G., Heussen, P. C. M., Voda, M. A., Nikolaeva, T., & van Duynhoven, J. P. M. (2018). Quantitative Structural Analysis of Fat Crystal Networks by Means of Raman Confocal Imaging. *Journal of the American Oil Chemists' Society*. https://doi.org/10.1002/aocs.12035

Martiel, I., Handschin, S., Fong, W. K., Sagalowicz, L., & Mezzenga, R. (2015). Oil transfer converts phosphatidylcholine vesicles into nonlamellar lyotropic liquid crystalline particles. *Langmuir*, *31*(1), 96–104. https://doi.org/10.1021/la504115a

Mazzanti, G., Marangoni, A. G., & Idziak, S. H. J. (2009). Synchrotron study on crystallization kinetics of milk fat under shear flow. *Food Research International*, *42*(5–6), 682–694. https://doi.org/10.1016/j.foodres.2009.02.009

Michalski, M. C., Genot, C., Gayet, C., Lopez, C., Fine, F., Joffre, F., … Raynal-Ljutovac, K. (2013). Multiscale structures of lipids in foods as parameters affecting fatty acid bioavailability and lipid metabolism. *Progress in Lipid Research*, *52*(4), 354–373. https://doi.org/10.1016/j.plipres.2013.04.004

Mitchell, J., Sederman, A. J., Colbourne, A. A., Gladden, L. F., Blythe, T. W., Barua, R., & Lovett, S. (2017). Validation of a low field Rheo-NMR instrument and application to shear-induced migration of suspended non-colloidal particles in Couette flow. *Journal of Magnetic Resonance*, *286*, 30–35. https://doi.org/10.1016/j.jmr.2017.11.010

Montalvo, G., Pons, R., Zhang, G., Díaz, M., & Valiente, M. (2013). Structure and phase equilibria of the soybean lecithin/PEG 40 monostearate/water system. *Langmuir*, *29*(47), 14369–14379. https://doi.org/10.1021/la402764w

Münüklü, P., & Jansens, P. J. (2007). Particle formation of an edible fat (rapeseed 70) using the supercritical melt micronization (ScMM) process. *Journal of Supercritical Fluids*, *40*(3), 433–442. https://doi.org/10.1016/j.supflu.2006.07.015

Nagle, J. F., & Tristram-Nagle, S. (2000). Structure of lipid bilayers. *Biochimica et Biophysica Acta - Reviews on Biomembranes*, *1469*(3), 159–195. https://doi.org/10.1016/S0304-4157(00)00016-2

Nieh, M.-P., Glinka, C. J., Krueger, S., Prosser, R. S., & Katsaras, J. (2001). SANS Study of the Structural Phases of Magnetically Alignable Lanthanide-Doped Phospholipid Mixtures. *Langmuir*, *17*(9), 2629–2638. https://doi.org/10.1021/la001567w

Nikiforidis, C. V., Matsakidou, A., & Kiosseoglou, V. (2014). Composition, properties and potential food applications of natural emulsions and cream materials based on oil bodies. *RSC Advances*, *4*(48), 25067–25078. https://doi.org/10.1039/c4ra00903g

Orädd, G., & Lindblom, G. (2005). Pfg NMR studies of lateral diffusion in oriented lipid

bilayers. *Spectroscopy*, *19*(4), 191–198. https://doi.org/10.1155/2005/753418

Orädd, G., Westerman, P. W., & Lindblom, G. (2005). Lateral diffusion coefficients of separate lipid species in a ternary raft-forming bilayer: A Pfg-NMR multinuclear study. *Biophysical Journal*, *89*(1), 315–320. https://doi.org/10.1529/biophysj.105.061762

Peyronel, F., Ilavsky, J., Pink, D. A., & Marangoni, A. G. (2014). Quantification of the physical structure of fats in 20 minutes: Implications for formulation. *Lipid Technology*, *26*(10), 223–226. https://doi.org/10.1002/lite.201400051

Peyronel, F., Pink, D. A., & Marangoni, A. G. (2014). Triglyceride nanocrystal aggregation into polycrystalline colloidal networks: Ultra-small angle X-ray scattering, models and computer simulation. *Current Opinion in Colloid and Interface Science*, *19*(5), 459–470. https://doi.org/10.1016/j.cocis.2014.07.001

Peyronel, F., Quinn, B., Marangoni, A. G., & Pink, D. a. (2014). Ultra small angle x-ray scattering in complex mixtures of triacylglycerols. *Journal of Physics: Condensed Matter*, *26*(46), 464110. https://doi.org/10.1088/0953-8984/26/46/464110

Pink, D. A., Peyronel, F., Quinn, B., Singh, P., & Marangoni, A. G. (2015). Condensation versus diffusion. A spatial-scale-independent theory of aggregate structures in edible oils: applications to model systems and commercial shortenings studied via rheology and USAXS. *Journal of Physics D: Applied Physics*, *48*(38), 384003. https://doi.org/10.1088/0022-3727/48/38/384003

Porter, C., Trevaskis, N., & N Charman, W. (2007). Lipids and lipid-based formulations: Optimizing the oral delivery of lipophilic drugs. *Nature Reviews Drug Discovery*, *6*, 231–248. https://doi.org/10.1038/nrd2197

Ramel, P. R., Co, E. D., Acevedo, N. C., & Marangoni, A. G. (2016). Structure and functionality of nanostructured triacylglycerol crystal networks. *Progress in Lipid Research*, *64*, 231–242. https://doi.org/10.1016/j.plipres.2016.09.004

Rousseau, D. (2000). Fat crystals and emulsion stability - A review. *Food Research International*, *33*(1), 3–14. https://doi.org/10.1016/S0963-9969(00)00017-X

Rousseau, D. (2013). Trends in structuring edible emulsions with Pickering fat crystals. *Current Opinion in Colloid and Interface Science*, *18*(4), 283–291. https://doi.org/10.1016/j.cocis.2013.04.009

Rousseau, D., Foresti, K., Hill, A. R., Marangoni, A. G., & Forestière, K. (1996). Restructing butterfat through blending and chemical interesterification. 1. Melting behavior and triacylglycerol modifications. *Journal of the American Oil Chemists' Society*, *73*(8), 963–972. https://doi.org/10.1007/bf02523403

Sagalowicz, L., Moccand, C., Davidek, T., Ghanbari, R., Martiel, I., Negrini, R., … Michel, M. (2016). Lipid self-assembled structures for reactivity control in food. *Philosophical Transactions A*, *374*, 20150136. https://doi.org/10.1098/rsta.2015.0136

Salentinig, S., Phan, S., Hawley, A., & Boyd, B. (2015). Self-Assembly Structure Formation during the Digestion of Human Breast Milk. *Angewandte Chemie*, *54*(5), 1600–1603. https://doi.org/10.1002/ange.201408320

Sato, K., Bayés-García, L., Calvet, T., Cuevas-Diarte, M. À., & Ueno, S. (2013). External factors affecting polymorphic crystallization of lipids. *European Journal of Lipid Science and Technology*, *115*(11), 1224–1238. https://doi.org/10.1002/ejlt.201300049

Sato, K., & Ueno, S. (2011). Crystallization, transformation and microstructures of polymorphic fats in colloidal dispersion states. *Current Opinion in Colloid and Interface Science*, *16*(5), 384–390. https://doi.org/10.1016/j.cocis.2011.06.004

Sein, A., Hitchman, T., & Dayton, C. L. G. (2019). Enzymes in Vegetable Oil Degumming Processes. In A. Vogel & O. May (Eds.), *Industrial Enzyme Applications* (pp. 323–350). Wiley-VCH.

Thurmond, R. L., Otten, D., Brown, M. F., & Beyer, K. (1994). Structure and packing of phosphatidylcholines in lamellar and hexagonal liquid-crystalline mixtures with a nonionic detergent: A wide-line deuterium and phosphorus-31 NMR study. *Journal of Physical Chemistry*, *98*(3), 972–983. https://doi.org/10.1021/j100054a038

Tzen, J., Cao, Y., Laurent, P., Ratnayake, C., & Huang, A. (1993). Lipids, Proteins, and Structure of Seed Oil Bodies from Diverse Species. *Plant Physiology*, *101*(1), 267–276. https://doi.org/https://doi.org/10.1104/pp.101.1.267

van Dalen, G., van Velzen, E. J. J., Heussen, P. C. M., Sovago, M., van Malssen, K. F., & van Duynhoven, J. P. M. (2017). Raman hyperspectral imaging and analysis of fat spreads. *Journal of Raman Spectroscopy*, (February), 1075–1084. https://doi.org/10.1002/jrs.5171

van Duynhoven, J. P. M., Broekmann, I., Sein, A., Van Kempen, G. M. P., Goudappel, G. J. W., & Veeman, W. S. (2005). Microstructural investigation of monoglyceride-water coagel systems by NMR and CryoSEM. *Journal of Colloid and Interface Science*, *285*(2), 703–710. https://doi.org/10.1016/j.jcis.2004.12.008

van Duynhoven, J., Voda, A., Witek, M., & Van As, H. (2010). *Time-Domain NMR Applied to Food Products*. *Annual Reports on NMR Spectroscopy* (Vol. 69). https://doi.org/10.1016/S0066-4103(10)69003-5

Voda, A., Den Adel, R., van Malssen, K., & van Duynhoven, J. (2017). Quantitative Assessment of Triacylglycerol Crystallite Thickness by 1H Spin-Diffusion NMR. *Crystal Growth and Design*, *17*(4), 1484–1492. https://doi.org/10.1021/acs.cgd.6b00501

CHAPTER 2

High field microMRI velocimetric measurement of quantitative local flow curves

This chapter has been submitted as T. Nikolaeva, F. J. Vergeldt, R. Serial, J. A. Dijksman, P. Venema, A. Voda, J. van Duynhoven, H. Van As (2019). High field microMRI velocimetric measurement of quantitative local flow curves.

Abstract

Performing rheo-microMRI velocimetry at high magnetic field with strong pulsed field gradients has clear advantages in terms of (chemical) sensitivity and resolution in velocities, time and space. To benefit from these advantages some artefacts need to be minimized. Significant sources of such artefacts are chemical shift dispersion due to the high magnetic field, eddy currents caused by the pulsed magnetic field gradients, and possible mechanical instabilities in concentric cylinder (CC) rheo-cells. These in particular hamper quantitative assessment of spatially resolved velocity profiles needed to construct local flow curves (LFCs) in CC geometries with millimeter gap sizes. A major improvement was achieved by chemical shift selective suppression of signals that are spectroscopically different from the signal of interest. By also accounting for imper-fections in pulsed field gradients, LFCs were obtained that were virtually free of artefacts. The approach to obtain quantita-tive LFCs in millimeter gap CC rheo-MRI cells was validated for a Newtonian and a simple yield stress fluid, which both showed quantitative agreement between local and global flow curves. The acquisition of LFCs during heterogeneous and transient flow of a fat crystal dispersion demonstrated that local constitutive laws can be assessed by rheo-microMRI at high magnetic field in a non-invasive, quantitative and real-time manner.

2.1. Introduction

Many colloidal dispersions express their intriguing flow properties in a non-linear relationship between shear stress and rate. This non-Newtonian flow behaviour can be observed for various food products, body fluids and materials with designed functionalities. (Balmforth, Frigaard, & Ovarlez, 2014; Coussot, 2014; Macias-Rodriguez & Marangoni, 2017) The non-linear relationship between shear stress σ and rate $\dot{\gamma}$ can be summarized in so-called flow curves $\sigma(\dot{\gamma})$. (Macosko, 1996; Mezger, 1966) These are used to define constitutive laws for flowing materials and classification of non-Newtonian behaviour. (Coussot, Nguyen, Huynh, & Bonn, 2002; de Kort, Nikolaeva, & Dijksman, 2017; Dekker et al., 2018; Fall, Lemaître, & Ovarlez, 2017; Macosko, 1996; Mezger, 1966; Moller, Fall, Chikkadi, Derks, & Bonn, 2009) Well-known classes are shear-thickening or -thinning materials, for which viscosity, respectively, increases or decreases under shear. A peculiar case is presented by yield stress fluids, which behave as elastic solids, when the applied stress is small and as flowing fluids once a critical stress is exceeded. Macroscopic or global flow curves are typically measured by conventional rotational rheometers, (Callaghan, Rogers, & Vlassopoulos, 2008; Macosko, 1996; Mezger, 1966; Moller et al., 2009) which vary shear stress as a function of shear rate, or vice versa. A limitation of such global rheology-derived flow curves is that they cannot always completely probe the constitutive laws for materials, for example for materials with heterogeneous flow and/or transient behaviour. (Goyon, Colin, Ovarlez, Ajdari, & Bocquet, 2008; Masselon, Salmon, & Colin, 2008; Nikolaeva et al., 2018; Guillaume Ovarlez, Bertrand, & Rodts, 2006; Ragouilliaux, Herzhaft, Bertrand, & Coussot, 2006; Rodts et al., 2010)

This limitation can be overcome by rheo-MRI velocimetry which can assess spatially resolved velocities of complex fluids with microscopic resolution. (Britton & Callaghan, 2000; Callaghan, 2011; Colbourne et al., 2018; Galvosas, Brox, & Kuczera, 2019; Kuczera et al., 2015) In a label-free, real-time and non-invasive manner, rheo-MRI can thus uniquely visualize regions governed by different constitutive laws. When rheo-MRI is performed in a concentric cylinder (CC) or Couette geometry with a known spatial stress distribution $\sigma(r)$ over the gap between the cylinders, (Bird, 1987) the determination of the spatial distribution of the shear rates $\dot{\gamma}(r)$ opens up the possibility to deduce the constitutive law in the form of a so-called local flow curve (LFC) $\sigma(\dot{\gamma}(r))$. (Coussot, Tocquer, Lanos, & Ovarlez, 2009; G.

Ovarlez et al., 2008; Guillaume Ovarlez et al., 2006) A main advantage of obtaining LFCs based on rheo-MRI velocimetry is that they can be obtained in a non-invasive real-time manner, which allows monitoring of transient changes in non-Newtonian flow behaviour under shear. Furthermore, heterogeneous flow in the form of shear banding, (Divoux, Fardin, Manneville, & Lerouge, 2015; Møller, Rodts, Michels, & Bonn, 2008; G. Ovarlez, Rodts, Chateau, & Coussot, 2009) wall slip (Britton & Callaghan, 2000; Coussot et al., 2009) and shear-induced migration (Colbourne et al., 2018; Guillaume Ovarlez et al., 2006) can be recognized, which facilitates the identification of the underlying colloidal mechanisms.

Currently, rheo-MRI based LFCs are typically obtained using a CC geometry with centimeter sized gaps, mounted in wide-bore low-field magnets (0.5 T) which compromises sensitivity and temporal resolution. (Coussot et al., 2009; Fall et al., 2017; G. Ovarlez et al., 2008) Such systems are typically equipped with low magnetic field gradients (0.05 T/m) and therefore are limited in providing high spatial resolution as well as in capturing small amplitude velocities. In this respect, rheo-microMRI velocimetry at a high magnetic field strength B_0 (7 T) with strong magnetic field gradients (typically of the order of 1 T/m) can offer significant improvements in performance. (Callaghan, Grant, Harris, & Wiley, 2002; Galvosas et al., 2019) The use of a higher B_0 field enhances sensitivity, and temporal resolution. In addition, the strong gradients allow for the acquisition of profiles with high spatial resolution over millimeter sized gaps and in a large dynamic range in rotational velocities. These benefits, however, come at the expense of losing robustness towards experimental artefacts.

The goal of this work is to show how to recognize and overcome artefacts observed in rheo-microMRI velocity profiles collected at high B_0 field employing high amplitude gradients when applied to complex colloidal dispersions. Given the chemical complexity of such systems we can expect multiple signals in the NMR spectrum, which can lead to artefacts due to chemical shift dispersion at high B_0 fields. Several of these artefacts are well known and have been addressed in the MRI literature before, also during flow measurements. (Bley, Wieben, Francois, Brittain, & Reeder, 2010; Middione, Thompson, & Ennis, 2014; Tayler, Benning, Sederman, Holland, & Gladden, 2014) However, the chemical shift artefacts have not been discussed so far in relation to spatially resolved velocimetric measurements performed in a rheo-microMRI setup with millimeter gap sized CC cells and with strong

magnetic field gradients. In addition, we discuss the implications of using strong gradients during velocimetric measurements at low rotational velocities, as well as the effects of mechanical instabilities that become noticeable when highly resolved velocity profiles are acquired over a millimeter gap CC cell. The suppression of these artefacts is a prerequisite for obtaining quantitative LFCs. The validation of the LFCs obtained in the millimeter gap sized CC cell is shown for both a Newtonian and a non-Newtonian yield stress fluid. The real-time and non-invasive measurements of LFCs by rheo-microMRI for monitoring structure formation will be demonstrated for a micronized fat crystal dispersion which undergoes localized transient structural rearrangements under shear.

2.2. Materials and methods

2.2.1. Materials

A commercial olive oil was used as a sample to work on artefacts occurred during rheo-microMRI experiments. Silicone oil standards of different viscosities (500 and 5000 mPa s at 25 ^{o}C) (AMETEK Brookfield) were used as Newtonian fluids. A commercial hair gel was used, where Carbopol was the main ingredient responsible for its yield stress behaviour. Due to the virtual absence of thixotropy, the hair gel was considered as a simple yield stress fluid. Micronized fat crystal dispersions were used as a model for materials with transient yield stress properties. A powder of micronized fat crystals (MFCs) was dispersed in sunflower oil at a concentration of 10 w/w%, the full procedure can be found in (Nikolaeva et al., 2018). Fat crystal dispersions were obtained under combined intense mixing and vacuum at 20 °C during 2 hours at constant speed. The fat dispersions were immediately frozen after preparation, stored at -20 °C and warmed up to room temperature before rheo-microMRI and rheology measurements.

2.2.2. High field rheo-microMRI

Rheo-microMRI experiments were conducted on a Bruker Avance III spectrometer, in combination with a commercial rheo-NMR accessory. A vertical wide bore (89 mm) superconducting magnet with a magnetic field strength B_0 =7 T, was used, corresponding to a resonance frequency of 300 MHz for ^{1}H. Excitation and detection of the ^{1}H signal was

performed with a bird-cage rf coil of inner diameter 25 mm. In the standard micro imaging gradient system Mic2.5 (Bruker) gradients up to G_{max} = 0.987 T/m were available along all three axes. 1D velocity profiles were measured with a slice thickness of 1 or 2 mm in two dimensions by a pulsed gradient spin echo (PGSE) sequence implemented for that purpose (mic_SEFLOW in ParaVision version 5.1) with Gaussian rf pulses of duration p_{90}=1 ms, and p_{180} =0.59 ms. The velocity-encoding gradient pulses had a duration δ =1 ms and the observation time was Δ=20 ms or 13.1 ms. The frequency-encoding read gradient provided a FOV=25 mm over 512 pixels, such that the spatial resolution was Δx=48.8 μm. The time needed to obtain a single velocity profile within the gap was 3 min 12 s or 1 min 36 s for, respectively, a number of scans of NS = 64 or 32. The velocity profiles were recorded with an echo time TE=17.5 s (Δ=13.1 s) or 24.4 ms (Δ=20 ms) and a repetition time TR=1.5 s.

Flow experiments were performed with concentric cylinder CC (also called Couette) geometries made from PEEK (Figure 2.1). Both outer and inner cylinders had serrated walls with diamond grid of the depth 100 μm to prevent/counter a wall slip. The outer cylinder had a radius $r_{o,}$=11 mm suited to the rf insert used in the MicWB40 microMRI probehead. Three different inner cylinders of the same length, 58 mm, were used in order to perform experiments in CC cells with 1, 2.5 and 4 mm gap sizes. Rheo-microMRI velocity profiles, respectively, comprised 20, 51 and 81 pixels across the CC gap with (48.8 μm resolution). The stability of the ^{1}H NMR signal was monitored in order to assure that no significant temperature variation occurred during the performed experiments in the rheo-microMRI CC cells. Standard deviations of the velocity values were obtained by repeating the measurements and were less than 10%.

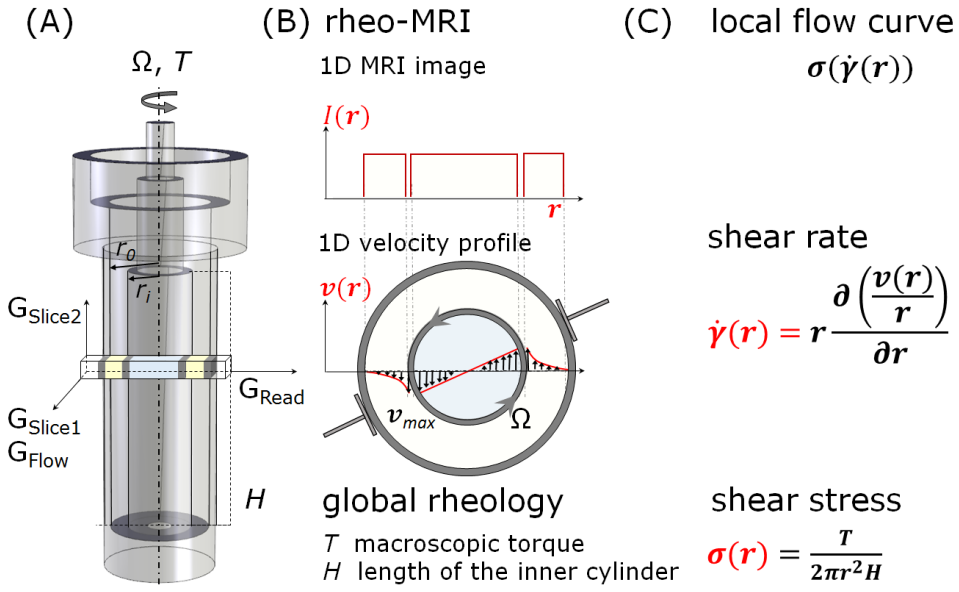

Figure 2.1. (A) Sketch of the rheo-microMRI concentric cylinder (CC) or Couette cell with a static outer cylinder of radius r_o, a rotating inner cylinder of radius r_i, and height H, rotating with velocity Ω. A column is selected by conventional slice selection with two orthogonal gradients G_{Slice1} and G_{Slice2}. G_{Flow} and G_{Read} indicate the directions of flow encoding and read gradients, respectively, which were used to obtain flow as a function of position r. **(B)** Rheo-microMRI provides a spatially resolved 1D intensity profile I(r) and velocity profile v(r) with 48.8µm resolution. The velocity profile v(r) is shown as a sketch overlaid on the CC top view, with maximum velocities (v_{max}) close to the rotating inner cylinder and zero velocities close to the static outer cylinder. The inner rotating cylinder is hollow and can be filled with a reference fluid (blue). Global rheology provides macroscopic torque values T as a function of time and rotational velocity Ω. **(C)** Equations used to calculate local shear rates $\dot{\gamma}(r)$ from rheo-microMRI velocimetric measurements and shear stresses $\sigma(r)$ from global rheology torque measurements, in order to construct a local flow curve (LFC) $\sigma(\dot{\gamma}(r))$.

2.2.3. Data processing

All calculations and corrections of rheo-microMRI velocity profiles, as well as the determination of local shear rates and stresses, were performed in Matlab-R2015b (MathWorks). A Savitzky-Golay (SG) FIR smoothing filter (available in Matlab) was used to obtain the first derivative of the velocity data, in order to calculate the shear rate variations as a function of position in the gap (Figure 2.1(C)). For all experiments, a first order polynomial fit was used with a window length set to 5 to 7 points, depending on the gap size. LFC data points corresponding to the firsts 2 - 4 pixels near the walls (98-195 μm) could not be provided, due to the use of the SG filter.An estimation of apparent yield stress σ_y values was done through a fit of the whole LFC or its parts with a power law function presenting the Herschel-Bulkley model. Some of the obtained LFCs could not be fitted by a single power law function over the whole gap due to banding and were therefore pragmatically fitted by two or three power law functions with different parameters, each describing the constitutive law for a band in the gap.

2.2.4. Rheology measurements

Rheological measurements were performed in parallel to rheo-microMRI experiments. They were conducted on a conventional Modular Compact Rheometer 301 (MCR301, Anton Paar). Global flow curves and macroscopic torque measurements were done in a home-built CC cell made from PEEK with exactly the same dimensions as the rheo-microMRI CC cell (Figure 2.1) with 1, 2.5 and 4 mm gap sizes. Before every measurement we verified the rheometer and the home-built CC cell performance with a standard motor adjustment and an air check as provided by the Rheoplus software The macroscopic torque T measurements were performed using the same conditions and protocols as for rheo-microMRI velocity measurements. The macroscopic torque T measurements were collected every 5 s in synchronization with the obtained velocity profiles.

2.3. Results and discussion

2.3.1. Chemical shift artefact during velocimetric measurements

Figure 2.2 shows the ^{1}H NMR spectrum (A), and intensity I(r) (B) and velocity v(r) (C) profiles of olive oil obtained for a 1mm gap rheo-microMRI CC cell at constant rotational velocity Ω=0.96 rpm. The intensity and velocity profiles clearly show a chemical shift (CS) artefact. Such artefacts are well-known to occur for systems where protons have different resonance frequencies due to their different chemical environment and have been discussed thoroughly in literature. (Bley et al., 2010; Middione et al., 2014) For the shown ^{1}H NMR spectrum we can indeed distinguish different proton signals with a maximal CS difference of 1200 Hz (4 ppm) (Figure 2.2 (A)). The observed CS artefact expressed in pixels depends on the chosen receiver bandwidth (BW) and matrix size. A displacement of 25 pixels due to CS differences is expected for BW=25 kHz and matrix size N=512. This is in line with the rheo-microMRI results presented in Figure 2.2 (B) and (C).

One way to reduce the CS artefact, clearly observed at a BW of 25 kHz, is to record intensity and velocity profiles at larger BW values (the full set of the rheo-MRI data as a function of the BW can be found in Figure S2.1). Figure 2.3 demonstrates how this improved rheo-microMRI intensity and velocity profiles recorded at 125kHz. Even though the broadening of the profiles decreased significantly and the deviation from the expected position became less, the CS artefact is still noticeable (about 5 pixels). Further increase of BW values up to 250kHz reduced the shift to 3 pixels (Figure S2.1).

The chemical shift artefact can also be minimized by suppressing unwanted proton signals. To do this, we added a CHESS (Bley et al., 2010; Haase & Frahm, 1985; Lakshmanan, Maru, Holland, Mantle, & Sederman, 2017) module before the flow encoding pulsed gradient spin echo (PGSE) sequence (Figure 2.4). Three CHESS pulses with frequency selective 90^{o} rf pulses for unwanted proton frequencies in combination with spoiler gradients effectively suppress signals from protons different from the on-resonance one that should remain. For olive oil we applied 90^{o} pulses with a bandwidth of 1000 Hz on resonance for protons at a chemical shift difference of -3.5 ppm (Figure 2 (A)) suppressing signals between -4.8 and -2.6 ppm. The resulting velocity and density profiles are shown in Figure 2.3. Significantly improved profiles were obtained even for a receiver BW of 25 kHz. However, a chemical

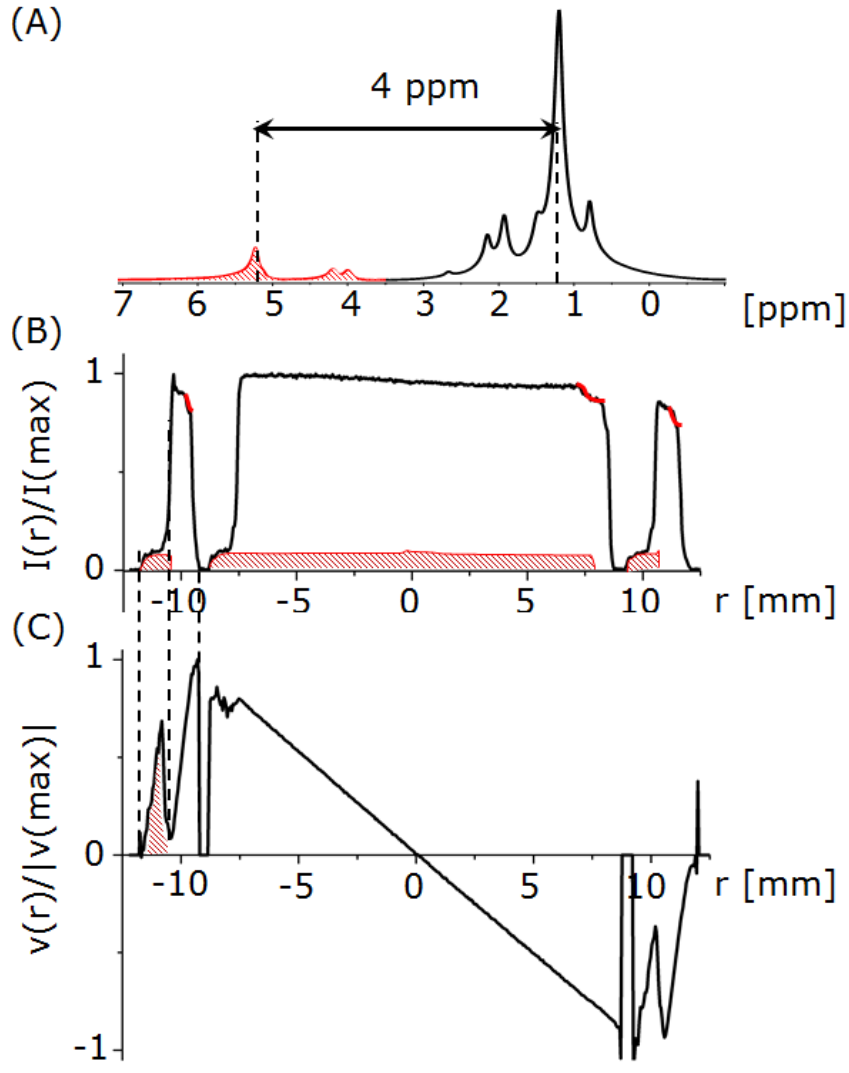

Figure 2.2. ^{1}H NMR spectrum and chemical shift artefacts observed during rheo-microMRI measurements of olive oil at a magnetic field strength B_0 of 7T. In the ^{1}H NMR spectrum **(A)** a maximal chemical shift difference of 4ppm is indicated. Normalized intensity I(r) **(B)** and velocity v(r) **(C)** profiles were obtained as a function of position r in a 1mm gap CC rheo-microMRI cell at a constant rotational velocity Ω=0.96rpm. The profiles were measured with a pulsed gradient spin echo (PGSE) sequence with Δ=15ms and a receiver BW of 25kHz.

shift displacement of 6 pixels was still observed in the acquired profiles, which were attributed to protons being 1 ppm off-resonance and therefore not suppressed. Hence, we deployed the CHESS suppression pulses in combination with an increased BW (Figure S2.1). The resulting well-defined rectangular intensity and straight velocity profiles (Figure 2.3, red line) showed that the broadening due to CS dispersion now hardly affected the rheo-microMRI measurements any more.

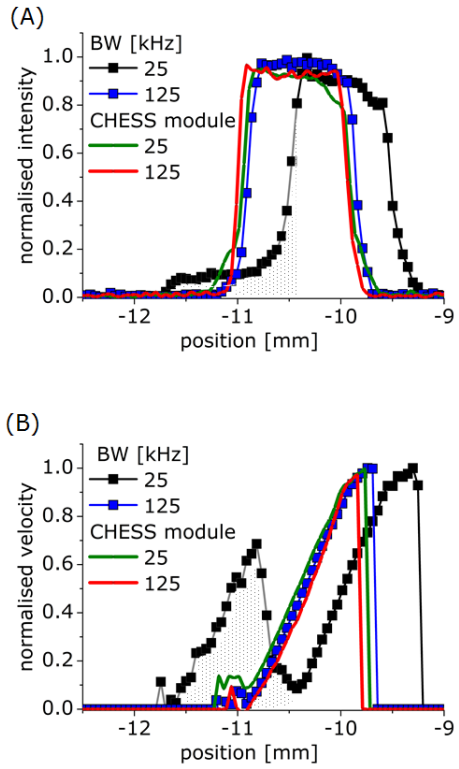

Figure 2.3. Normalized intensity **(A)** and velocity **(B)** profiles of olive oil obtained at B_0 =7T as function of BW when using a pulsed gradient spin echo (PGSE) sequence (squares) and one modified with a CHESS selection module (lines). All profiles were obtained at a rotational velocity Ω=0.96rpm in a 1 mm gap CC rheo-microMRI cell.

We note that in previous work we used a different strategy by combining the PGSE with a chemical shift suppression module consisting of a series of frequency selective 90^0 pulses with a time separation of $5*T_2$ between them (Figure S2.1) (Serial, Nikolaeva, Vergeldt, van Duynhoven, & Van As, 2019). In hindsight we found no clear advantage to the simpler CHESS suppression approach. The complications of employing CS selective pulses for recording velocity profiles have been discussed in previous work (G. Ovarlez et al., 2008), here we have experimentally demonstrated that a conventional CHESS module provides an effective alternative for reducing chemical shift artefacts.

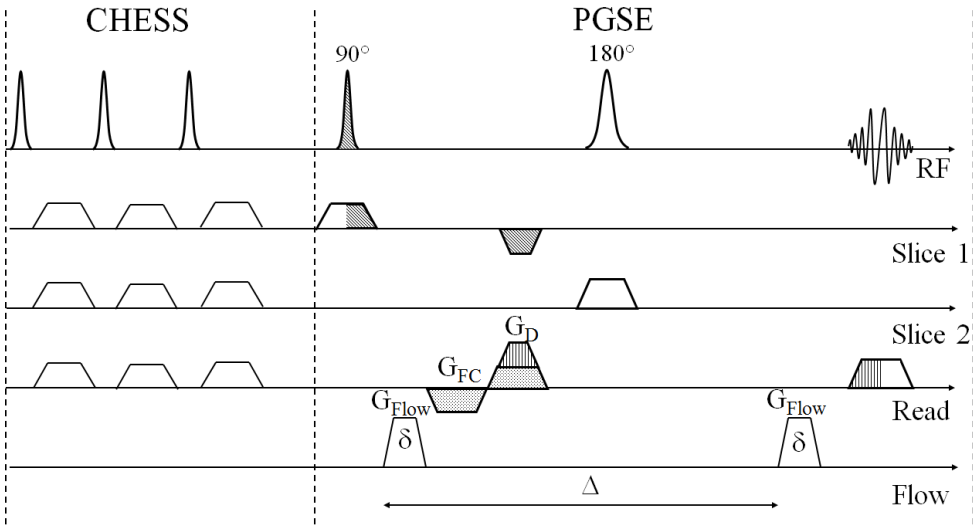

Figure 2.4. Modified pulsed gradient spin echo (PGSE) sequence with CHESS pulses to suppress proton signals with different chemical shifts. G_{Flow}, G_D and G_{FC} respectively denote flow encoding, read dephasing and flow compensating gradients. The pattern filled areas indicate equal values of the gradient integrals. In the actual sequence there are also flow compensation gradients for both slice encoding directions, but those are not shown for the sake of simplicity.

2.3.2. Artefacts occurring during velocimetric measurements at low rotational velocities

Velocimetric measurements at low rotational velocities Ω, as implemented on our commercial rheo-microMRI setup, required us to work at the edge of possible experimental settings for observation time Δ, flow encoding G_{Flow} and flow compensated G_{FC} gradients (Figure 2.4). These conditions resulted in velocity profiles with artefacts that were enhanced at short flow encoding time (small Δ) and large gradient values, which were intrinsic to the pulse sequence. We distinguished artefacts related to gradient imperfections and to mechanical instabilities of the used rheo-microMRI setup.

The gradient related artefacts appeared in non-centered and non-symmetric velocity profiles with negative velocities on one side and unrealistically high velocities on another side (Figure 2.5). The shift of the velocity data is likely to be caused by phase shift related to technical imperfections of the gradient systems such as eddy currents (Middione et al., 2014; Peeters, Bos, & Bakker, 2005). One route to minimize influence of these artefacts is to record the velocities at reduced G_{Flow} gradient strength. For our commercial rheo-microMRI setup and its related sequences to measure flow, however, the implementation of G_{FC} gradients along the read direction (Figure 2.4) forced us to use short observation time (Δ) leading to strong G_{Flow} gradients to record low velocities (Callaghan, 2011). Once the G_{FC} gradients were disabled, by modifying the pulse sequence, longer Δ could be used, which resulted in a reduction in G_{Flow} and an increase in sensitivity of the velocimetric measurements at low rotational velocities Ω.

Another workaround was the correction of the (phase-shifted) non-centered velocity profile in post-processing. This approach is based on the expected velocity profile for the rotating inner cylinder of the rheo-MRI CC cell, which is supposed to be centered and linear as a function of position r (Figure 2.5). First, a theoretical velocity profile was calculated based on the actual applied velocities and was centered, considering the symmetry of the CC cell. Next, the measured velocities of the inner cylinder were analyzed by a linear fit. The fitted and theoretical velocity profiles for the rotating inner cylinder were extrapolated over the whole dimension of the rheo-cell (FOV 25 mm). The difference between them was used to

correct the initially measured velocity profile, including velocities within the gaps. The correction resulted in well-centered and symmetric velocity profiles (Figure 2.5).

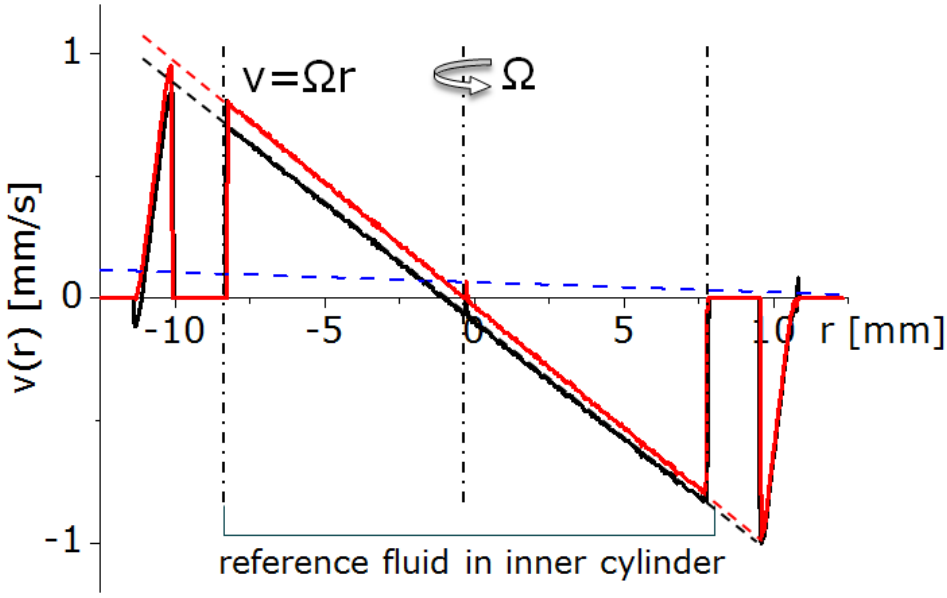

Figure 2.5. Outline of the procedure to correct non-centered and non-symmetric velocity profiles obtained at low shear rates with strong flow encoding (G_{Flow}) and flow compensating (G_{FC}) gradients. The measured velocity profile (black solid line) was obtained for olive oil in the 1 mm rheo-microMRI CC cell with a rotational velocity Ω=0.96rpm, Δ=15.7ms; G_{ENC}=0.429T/m, and BW=125kHz. The velocity profile of the inner rotating cylinder was fitted by a linear function and extrapolated to all positions in the rheo-cell (black dotted line). A theoretical flow profile was plotted based on velocities calculated from the known imposed shear rate and positions within the inner rotating cylinder and was extrapolated to all positions in the rheo-microMRI cell (FOV 25mm) (red dotted line). The dashed blue line shows the difference between the black and red dotted lines, and is used to correct the measured flow profile, resulting in the corrected flow profile (red solid line).

The above-mentioned remedies also alleviated the impact of mechanical instabilities due to wobbling of the rotating inner cylinder of the CC cell (Figure 2.6 (A)). Reducing the gradient strengths of G_{Flow} by increasing the observation time Δ effectively reduced the impact of wobbling on the velocity profile (Figure 2.6 (B). This approach turned out to be more effective in suppressing the wobbling artefact and less time-consuming than using a trigger to record velocity profiles in sync with the rotation of the inner cylinder (Figure 2.6(C)).

Recently, the effects of curved streamlines in relation to slice thicknesses as they occur in millimeter sized gaps of CC cells on the accuracy of the velocity profiles have been discussed (Colbourne et al., 2018; Kuczera & Galvosas, 2015) and the chosen slice thickness of 1-2 mm was in line with the recommendations that were made. Therefore, in our current work we can assume that the impact of curved stream lines was minor.

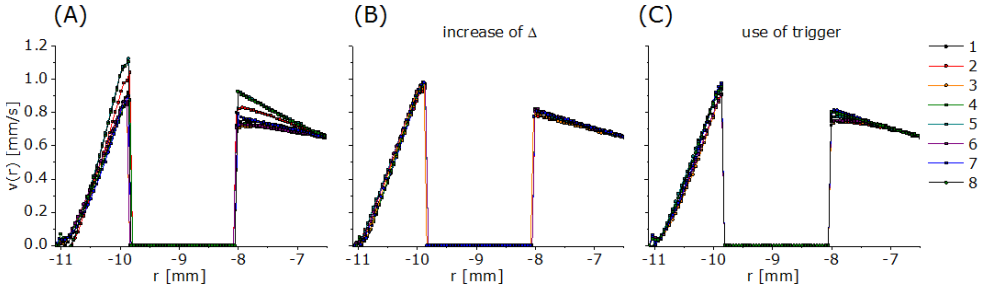

Figure 2.6. Velocity profiles of olive oil measured 8 times repeatedly in a 1 mm gap rheo-microMRI CC cell with rotational velocity Ω=0.96rpm (Δ=8.06 ms, BW=100kHz, NS=4). Only part of the overall velocity profile is shown, including the gap, inner wall and part of the reference fluid. **(A)** Instability of velocity profiles due to wobbling of the rotating inner cylinder in the CC rheo-cell. The wobbling artefacts affected, both, the reference fluid inside the bob and the fluid within the gap. They were symmetric with respect to the rotating center and appeared periodically (Figure S2.2, supplementary material). **(B)** Velocity profiles recorded under similar conditions but using and increased observation time Δ=15.47ms and **(C)** using a trigger to synchronize the imaging sequence with the rotation of the inner cylinder (Δ=8.061ms).

2.3.3. Local flow curves: validation for wide gap CC (Couette) geometry

The previously described approaches to obtain artefact free rheo-MRI velocity profiles for fluids in CC cells at high magnetic field strength opened up the possibility to obtain LFCs in a quantitative manner (Coussot et al., 2009). First, shear rate profiles $\dot{\gamma}(r)$ were deduced from rheo-MRI velocity profiles according to the equation $\dot{\gamma}(r)=r\,\partial(v(r)/r)/\partial r$ (Figure 2.1 (C)). Macroscopic torque T values were obtained with an identical CC cell mounted in a conventional rotational rheometer and allowed for the calculation of shear stress as a function of position using $\sigma(r) = T/2\pi Hr^2$ (Figure 2.1 (C)), where H is the fluid height in the gap and r is the position within the gap (Bird, 1987; de Kort et al., 2017). We used different gap sizes to vary the shear stress field which is a function of the gap size and position as in $\sigma(r) = \sigma_i r_i^2/r^2$ (σ_i is the stress exerted by the rotating inner cylinder and r_i the radius of the inner cylinder). By using rheo-microMRI CC cells with gap sizes of 1, 2.5 and 4 mm shear stress variations of 17%, 40% and 60% could be applied.

This approach was validated by a comparison of LFCs with global flow curves for silicone oil and a commercial Carbopol dispersion (hair gel) as examples of a Newtonian and a yield stress fluid, respectively. These model fluids were selected since their flow behaviour is neither heterogeneous nor time-dependent. That made them well-suited to validate the approach to obtain quantitative LFCs, since these should be identical to the global flow curves obtained by a conventional rotational rheometer.

Figure 2.7 (A) shows global flow curves for silicone oil, displaying the expected linear behaviour for a Newtonian fluid. The LFCs measured for silicone oil in CC cells all overlap with the global flow curves for the applied gap sizes (1, 2.5 and 4 mm) and the applied rotational velocities Ω between 1-32rpm. This demonstrates that LFCs can be obtained in a quantitative manner for relevant gap sizes and shear rate conditions. This agreement was also observed for the hair gel (Figure 2.7 (B)) where the applied rotational velocities Ω were varied between 1-150 rpm. For this Carbopol dispersion the global flow curve can be well fitted with a single power law function and be described with the Herschel-Bulkley behaviour, as expected for a simple yield stress fluid (M. Dinkgreve, Fazilati, Denn, & Bonn, 2018; Maureen Dinkgreve, Denn, & Bonn, 2017; Moller et al., 2009).

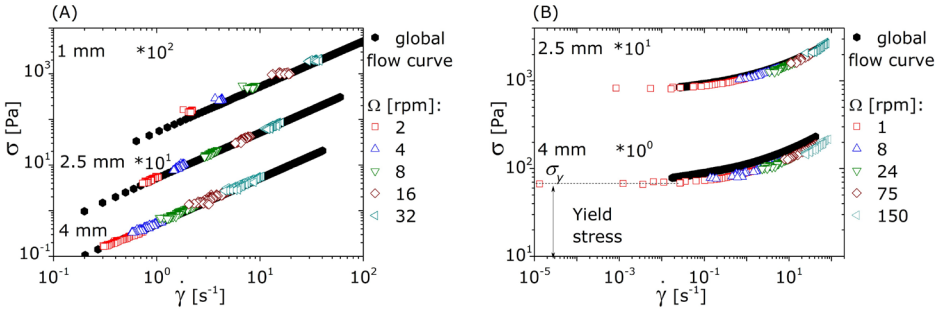

Figure 2.7. Local and global flow curves obtained for silicon oil **(A)** and hair gel **(B)**, respectively, representing a Newtonian and yield stress fluids. The local flow curve (LFC) $\sigma(\dot{\gamma}(r))$ were obtained with applied rotational velocities Ω displayed in the legend. To aid the visualization, the local and global flow curves obtained in CC cells with different gap sizes (1, 2.5 and 4mm) are presented with an offset (multiplication factors are indicated in the plot).

2.3.4. Local flow curves: a local view on transient structure formation and degradation

The potential of real-time assessment of LFCs by rheo-microMRI was demonstrated for a dispersion of micronized fat crystals (MFCs) in sunflower oil, which is known to form a network under low shear (Nikolaeva et al., 2018, 2019) (Figure 2.8). The MFC dispersion was measured in a 2.5mm gap size rheo-MRI CC cell at a rotational velocity Ω=0.96rpm for 13 hours. The velocity profiles, recorded every 5 minutes, showed a continuous development of heterogeneous flow behaviour within the gap during whole experiment (Figure S2.3, supplementary material). In parallel, the same dispersion was placed into an identical CC cell mounted in a commercial rheometer to measure T values over the same time frame, imposed at constant rotational velocity Ω. The evolution of torque T demonstrated three stages: an increase during the first 3 hours; a fast decrease within the next 4 hours and a subsequent slow decrease (Figure S2.4, supplementary material). This pattern could be interpreted as initial formation of the MFC network followed by subsequent disruption (Nikolaeva et al., 2018, 2019). The corresponding time-dependent LFCs are shown in Figure 2.8 (A) and they point to the development of a yield stress fluid. The LFCs could not be fitted with a single

Herschel-Bulkley model over the whole range of shear rates for most of the time points, which indicates that the MFC dispersion at different positions in the CC gap was governed by different constitutive laws. The LFCs, however, could be described by a two (or even three) component Herschel-Bulkley model, correlated to different bands in the CC gap (Figure S2.5, supplementary material). To find an interpretation for the multicomponent LFCs, the different regions were then fitted with a power law function being in line with the Herschel-Bulkley model. In this way local yield stress values σ_y over the gap were estimated. The results are presented as a function of time in the two-dimensional map in Figure 2.8 (B). Initially, for all positions over the gap an overall increase in apparent yield stress σ_y could be observed, indicating formation of a MFC network. The map also showed that this increase in yield stress was heterogeneous over the gap. For two positions at different distances from the rotating inner cylinder r_i (light and dark blue columns indicate these positions in Figure 2.8 (B)) we have plotted the local time-dependences of σ_y (Figure 2.8(C) and 2.8(D)). One can observe that for the position close to the inner rotating cylinder the apparent yield stress σ_y was always overcome by a larger local shear stress σ (Figure 2.8(C)). Further away from the rotating cylinder the apparent yield stress σ_y became too high to be overcome by the local stress after 5 - 6 hours (Figure 2.8 (D)). Hence, this region became stagnant after 6 hours (hatched area in Figure 2.8 (B)). In Figures 2.8 (C) and (D) we have also presented the local effective viscosity $\mu_{eff}(r) = \sigma(r)/\dot{\gamma}(r)$. In the region near the rotating inner wall we observed an increase in μ_{eff}, followed by a decrease. This was similar to our previous results obtained in a 1mm gap with a much more homogeneous stress distribution where it was concluded that the rapid increase of apparent σ_y corresponded to the formation of a weak-link MFC network(Nikolaeva et al., 2018), followed by a decrease corresponding to its disruption due to recrystallisation and aggregation of the MFCs (Nikolaeva et al., 2019). In the wider CC gap a static band appeared in time in the region near the outer wall (Figure 2.8 (D)), where the MFC network can continue to grow in strength. These results illustrate the potential of rheo-microMRI for assessment of time-dependent and spatially heterogeneous constitutive laws.

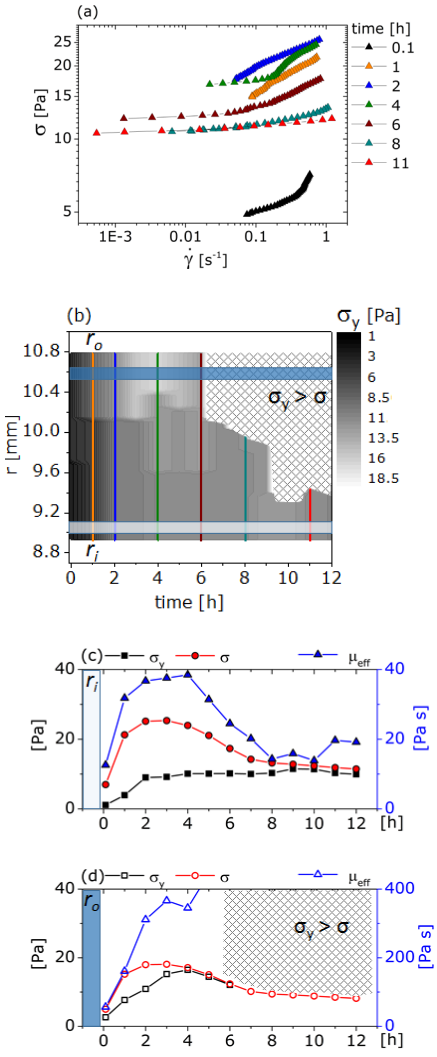

Figure 2.8. (A) Evolution of local flow curve (LFC) $\sigma(\dot{\gamma}(r))$ reflecting network formation of micronized fat crystals in sunflower oil under shear stress at a rotational velocity Ω=0.96rpm in a rheo-microMRI CC cell with a 2.5mm gap size. **(B)** 2D map of the yield stress σ_y, resulting from a power low fit, as a function of position within the gap and time. The hatched area indicates regions with no flow. Colored lines indicate how regions in **(B)** corresponded to LFCs in **(A)**. For two positions indicated with light and dark blue columns within the local yield and shear stresses and effective viscosity μ_{eff} were plotted as a function of time **(C)** and **(D)**.

We note that in our approach we did not measure the macroscopic torque T in situ in a CC cell mounted in a MRI probehead. Current designs for in situ torque measurement in a CC cell in superconducting magnet are compromised by the long shaft and consequent mechanical instabilities (Brox, Douglass, Galvosas, & Brown, 2016) which limits the operational range of Ω and T. Our approach employing two parallel measurements delivered reproducible results for a wide range of rotational velocities (Ω =0.1-150rpm) and torques (T=0.01–100mNm) and can be implemented in a straightforward manner in laboratories equipped with a standard wide bore high field NMR spectrometer, equipped with a microMRI probehead and a commercial rotational rheometer using the same rheo cell.

2.4. Conclusions

Chemical shift artefacts in rheo-microMRI at high B_0 field can be minimized by introducing CHESS pulses to suppress unwanted proton signals. By also accounting for eddy currents generated by pulsed field gradients, velocity profiles can be obtained that are virtually free of artefacts. This allows for construction of LFCs which quantitatively match global flow curves for a Newtonian and a simple yield stress fluid. The approach allows for assessment of the transient local constitutive laws for a micronized fat crystal dispersion that undergo structural rearrangements in a CC cell under shear.

Acknowledgements

John Philippi and the technical workshop of Wageningen University are thanked for designing and manufacturing the CC cells. Daan de Kort is acknowledged for his input on the design and fruitful discussion of the first rheological and rheo-MRI experiments. Julia Krug is acknowledged for input on the design of the MRI experiments. This work is part of the SSCANFOODS (project number 13386) research program, which is financed by The Netherlands Organisation for Scientific Research (NWO).

References

Balmforth, N. J., Frigaard, I. A., & Ovarlez, G. (2014). Yielding to Stress: Recent Developments in Viscoplastic Fluid Mechanics. *Annual Review of Fluid Mechanics*, *46*(1), 121–146. https://doi.org/10.1146/annurev-fluid-010313-141424

Bird, R. B. (1987). *Dynamics of polymeric liquids. Vol. 2, Vol. 2,*. New York; Chichester: Wiley.

Bley, T. A., Wieben, O., Francois, C. J., Brittain, J. H., & Reeder, S. B. (2010). Fat and water magnetic resonance imaging. *Journal of Magnetic Resonance Imaging*, *31*(1), 4–18. https://doi.org/10.1002/jmri.21895

Britton, M. M., & Callaghan, P. T. (2000). NMR velocimetry study of the temperature dependent rheology of butter, semisoft butter and margarine. *J. Texture Stud.*, *31*(3), 245–255. https://doi.org/10.1111/j.1745-4603.2000.tb00288.x

Brox, T. I., Douglass, B., Galvosas, P., & Brown, J. R. (2016). Observations of the influence of Taylor-Couette geometry on the onset of shear-banding in surfactant wormlike micelles. *Journal of Rheology*, *60*(5), 973–982. https://doi.org/10.1122/1.4961478

Callaghan, P. T. (2011). *Translational Dynamics and Magnetic Resonance: Principles of Pulsed Gradient Spin Echo NMR*. Oxford: Oxford University Press. https://doi.org/10.1093/acprof:oso/9780199556984.001.0001

Callaghan, P. T., Grant, D. M., Harris, R. K., & Wiley, J. (2002). Rheo-NMR : A New Window on the Rheology of Complex Fluids Rheo-NMR : A New Window on the Rheology of Complex Fluids. *Advances*, *9*, 737–750. https://doi.org/10.1002/9780470034590.emrstm0470

Callaghan, P. T., Rogers, S. A., & Vlassopoulos, D. (2008). Aging, yielding, and shear banding in soft colloidal glasses. *Physical Review Letters*, *100*, 128304. https://doi.org/10.1103/PhysRevLett.100.128304

Colbourne, A. A., Blythe, T. W., Barua, R., Lovett, S., Mitchell, J., Sederman, A. J., & Gladden, L. F. (2018). Validation of a low field Rheo-NMR instrument and application to shear-induced migration of suspended non-colloidal particles in Couette flow. *Journal of Magnetic Resonance*, *286*, 30–35. https://doi.org/10.1016/j.jmr.2017.11.010

Coussot, P. (2014). Yield stress fluid flows: A review of experimental data. *J. Non-Newtonian Fluid Mech.*, *211*, 31–49.

Coussot, P., Nguyen, Q. D., Huynh, H. T., & Bonn, D. (2002). Viscosity bifurcation in thixotropic, yielding fluids. *Journal of Rheology*, *46*(3), 573. https://doi.org/10.1122/1.1459447

Coussot, P., Tocquer, L., Lanos, C., & Ovarlez, G. (2009). Macroscopic vs. local rheology of yield stress fluids. *Journal of Non-Newtonian Fluid Mechanics*, *158*(1–3), 85–90. https://doi.org/10.1016/j.jnnfm.2008.08.003

de Kort, D. W., Nikolaeva, T., & Dijksman, J. A. (2017). Rheo-NMR: Applications to Food. In G. A. Webb (Ed.), *Modern Magnetic Resonance.* (pp. 1–21). Springer, Cham. https://doi.org/10.1007/978-3-319-28275-6_19-1

Dekker, R. I., Dinkgreve, M., Cagny, H. de, Koeze, D. J., Tighe, B. P., & Bonn, D. (2018). Scaling of flow curves: Comparison between experiments and simulations. *Journal of Non-Newtonian Fluid Mechanics*, *261*, 33–37. https://doi.org/10.1016/j.jnnfm.2018.08.006

Dinkgreve, M., Fazilati, M., Denn, M. M., & Bonn, D. (2018). Carbopol: From a simple to a thixotropic yield stress fluid. *Journal of Rheology*, *62*(3), 773–780. https://doi.org/10.1122/1.5016034

Dinkgreve, Maureen, Denn, M. M., & Bonn, D. (2017). "Everything flows?": elastic effects on startup flows of yield-stress fluids. *Rheologica Acta*, *56*(3), 189–194. https://doi.org/10.1007/s00397-017-0998-z

Divoux, T., Fardin, M. A., Manneville, S., & Lerouge, S. (2015). Shear Banding of Complex Fluids. *Annual Review of Fluid Mechanics*, *48*(1), 150724171740009. https://doi.org/10.1146/annurev-fluid-122414-034416

Fall, A., Lemaître, A., & Ovarlez, G. (2017). Discontinuous Shear Thickening in Cornstarch Suspensions. *EPJ Web of Conferences*, *140*, 1–4. https://doi.org/10.1051/epjconf/201714009001

Galvosas, P., Brox, T., & Kuczera, S. (2019). Rheo-NMR in food science - recent opportunities. *Magnetic Resonance in Chemistry*. https://doi.org/10.1002/mrc.4861

Goyon, J., Colin, A., Ovarlez, G., Ajdari, A., & Bocquet, L. (2008). Spatial cooperativity in soft glassy flows. *Nature*, *454*, 84. Retrieved from https://doi.org/10.1038/nature07026

Haase, A., & Frahm, J. (1985). Multiple chemical-shift-selective NMR imaging using stimulated echoes. *Journal of Magnetic Resonance (1969)*, *64*(1), 94–102. https://doi.org/10.1016/0022-2364(85)90034-4

Kuczera, S., & Galvosas, P. (2015). Advances and artefact suppression in RARE-velocimetry for flow with curved streamlines. *Journal of Magnetic Resonance*, *259*, 135–145. https://doi.org/10.1016/j.jmr.2015.07.015

Kuczera, S., Perge, C., Fardin, M. A., Brox, T. I., Williams, M. A. K., Manneville, S., & Galvosas, P. (2015). Anomalous shear banding revisited with Rheo-NMR and Rheo-USV. *Rheologica Acta*, *54*(7), 619–636. https://doi.org/10.1007/s00397-015-0854-y

Lakshmanan, S., Maru, W. A., Holland, D. J., Mantle, M. D., & Sederman, A. J. (2017). Measurement of an oil – water fl ow using magnetic resonance imaging. *Flow Measurement and Instrumentation*, *53*, 161–171. https://doi.org/10.1016/j.flowmeasinst.2016.04.001

Macias-Rodriguez, B. A., & Marangoni, A. A. (2017). Linear and nonlinear rheological behavior of fat crystal networks. *Critical Reviews in Food Science and Nutrition*, 1–18. https://doi.org/10.1080/10408398.2017.1325835

Macosko, C. W. (1996). *Rheology: Principles, Measurements and Applications*. *Powder Technology* (Vol. 86).

Masselon, C., Salmon, J.-B., & Colin, A. (2008). Nonlocal Effects in Flows of Wormlike Micellar Solutions. *Physical Review Letters*, *100*, 38301. https://doi.org/10.1103/PhysRevLett.100.038301

Mezger, T. G. (1966). *In Reply: BEHAVIOUR THERAPY. The British Journal of Psychiatry* (Vol. 112). https://doi.org/10.1192/bjp.112.483.211-a

Middione, M. J., Thompson, R. B., & Ennis, D. B. (2014). Velocity encoding with the slice select refocusing gradient for faster imaging and reduced chemical shift-induced phase errors. *Magnetic Resonance in Medicine*, *71*(6), 2014–2023. https://doi.org/10.1002/mrm.24861

Møller, P. C. F., Rodts, S., Michels, M. A. J., & Bonn, D. (2008). Shear banding and yield stress in soft glassy materials. *Physical Review E - Statistical, Nonlinear, and Soft Matter Physics*, *77*, 041507. https://doi.org/10.1103/PhysRevE.77.041507

Moller, P., Fall, A., Chikkadi, V., Derks, D., & Bonn, D. (2009). An attempt to categorize yield stress fluid behaviour. *Philosophical Transactions. Series A, Mathematical, Physical, and Engineering Sciences*, *367*(1909), 5139–5155. https://doi.org/10.1098/rsta.2009.0194

Nikolaeva, T., Adel, R. den, Velichko, E., Bouwman, W. G., Hermida-Merino, D., Van As, H., … van Duynhoven, J. (2018). Networks of micronized fat crystals grown under static conditions. *Food & Function*, *9*, 2102–2111. https://doi.org/10.1039/C8FO00148K

Nikolaeva, T., den Adel, R., van der Sman, R., Martens, K. J. A., Voda, A., Van As, H., & van Duynhoven, J. (2019). Manipulation of Recrystallization and Network Formation of Oil-Dispersed Micronized Fat Crystals. *Langmuir*, *35*(6), 2221–2229. https://doi.org/10.1021/acs.langmuir.8b03349

Ovarlez, G., Rodts, S., Chateau, X., & Coussot, P. (2009). Phenomenology and physical origin of shear localization and shear banding in complex fluids. *Rheologica Acta*, *48*(8), 831–844. https://doi.org/10.1007/s00397-008-0344-6

Ovarlez, G., Rodts, S., Ragouilliaux, A., Coussot, P., Goyon, J., & Colin, A. (2008). Wide-gap Couette flows of dense emulsions: Local concentration measurements, and comparison between macroscopic and local constitutive law measurements through magnetic resonance imaging. *Physical Review E - Statistical, Nonlinear, and Soft Matter Physics*, *78*, 036307. https://doi.org/10.1103/PhysRevE.78.036307

Ovarlez, Guillaume, Bertrand, F., & Rodts, S. (2006). Local determination of the constitutive law of a dense suspension of non-colloidal particles through MRI. *Journal of Rheology*, *50*(3), 1–32. https://doi.org/10.1122/1.2188528

Peeters, J. M., Bos, C., & Bakker, C. J. G. (2005). Analysis and correction of gradient nonlinearity and B0 inhomogeneity related scaling errors in two-dimensional phase contrast flow measurements. *Magnetic Resonance in Medicine*, *53*(1), 126–133. https://doi.org/10.1002/mrm.20309

Ragouilliaux, A., Herzhaft, B., Bertrand, F., & Coussot, P. (2006). Flow instability and shear localization in a drilling mud. *Rheologica Acta*, *46*, 261–271. https://doi.org/10.1007/s00397-006-0114-2

Serial, M. R., Nikolaeva, T., Vergeldt, F. J., van Duynhoven, J., & Van As, H. (2019). Selective oil-phase rheo-MRI velocity profiles to monitor heterogeneous flow behavior of oil/water food emulsions. *Magnetic Resonance in Chemistry*, 1–5. https://doi.org/10.1002/mrc.4811

Tayler, A. B., Benning, M., Sederman, A. J., Holland, D. J., & Gladden, L. F. (2014). Ultrafast magnetic-resonance-imaging velocimetry of liquid-liquid systems : Overcoming chemical-shift artifacts using compressed sensing, *89*(6), 1–9. https://doi.org/10.1103/PhysRevE.89.063009

Supplementary material

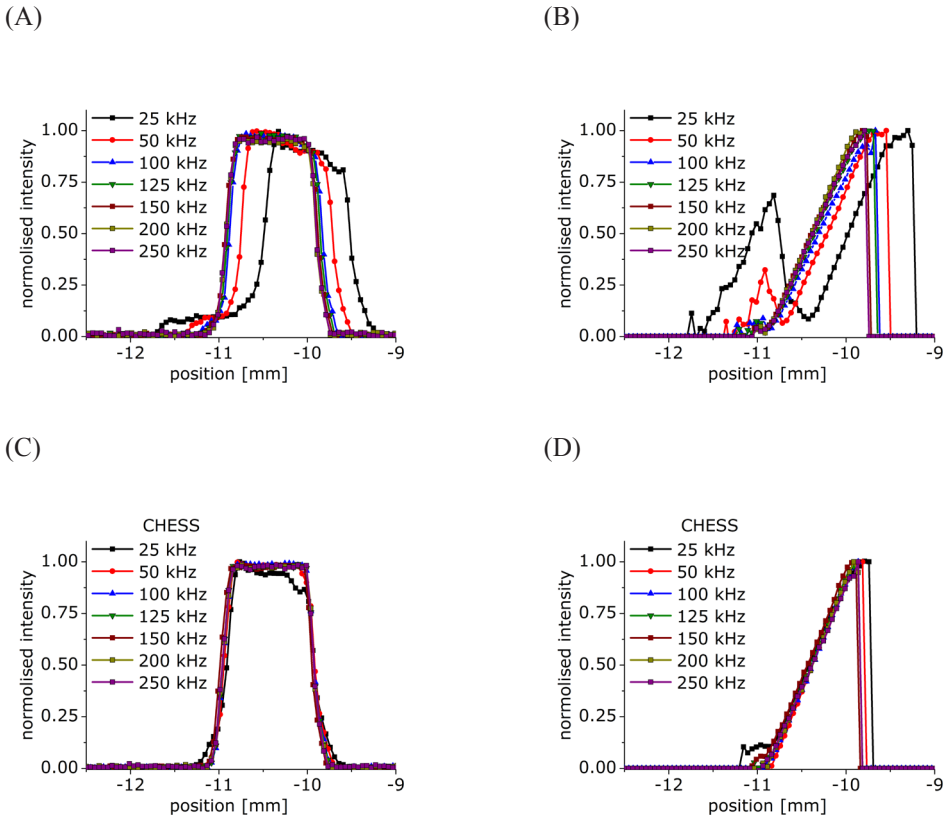

Figure S2.1. Normalized intensity and velocity profiles of olive oil obtained at B_0 =7T as function of BW when using a pulsed gradient spin echo (PGSE) sequence (**(A)** and **(B)**) and one modified with a CHESS selection module (**(C)** and **(D)**). All profiles were obtained at a rotational velocity Ω=0.96rpm in a 1 mm gap CC rheo-microMRI cell.

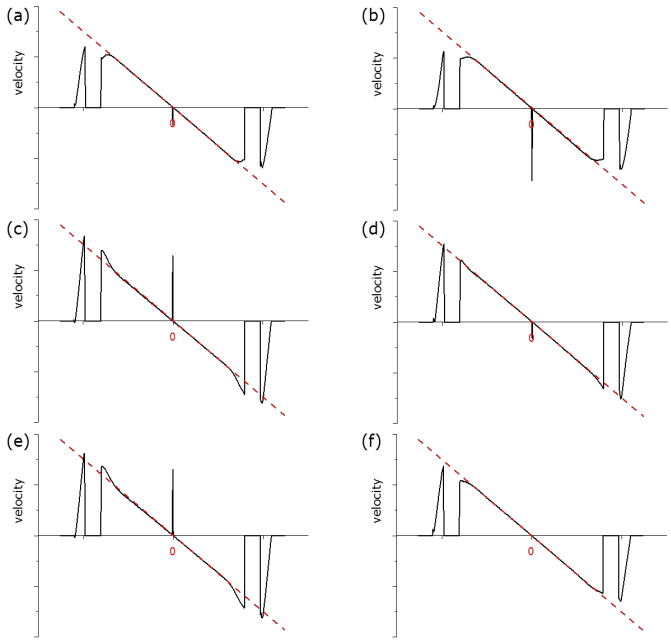

Figure S2.2. Velocity profiles of olive oil in 1 mm gap Geometry recorded at the observation time Δ= 8.061 ms, BW=100kHz and at shear rate $\dot{\gamma}$ =0.87s^{-1} (0.72 rpm) with NS = 4 one after each other (A) – (F).

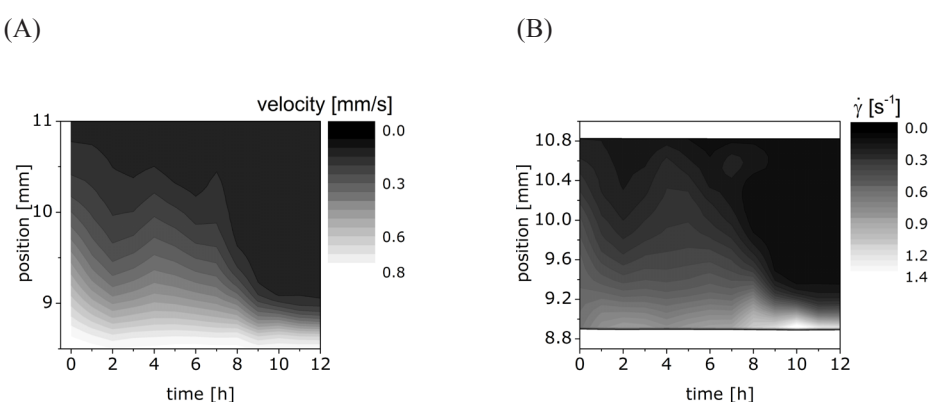

Figure S2.3. 2D map of the velocities (A) and shear rates (B) as a function of position within the gap and time. The black area indicates regions with no flow.

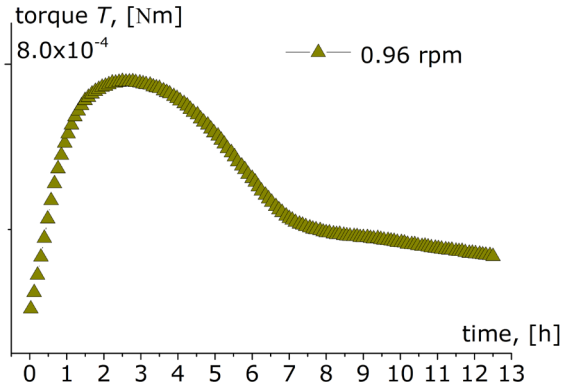

Figure S2.4. Torque T values as a function of time obtained by using a conventional Modular Compact Rheometer 301 (MCR301, Anton Paar) in parallel to the rheo-microMRI measurements.

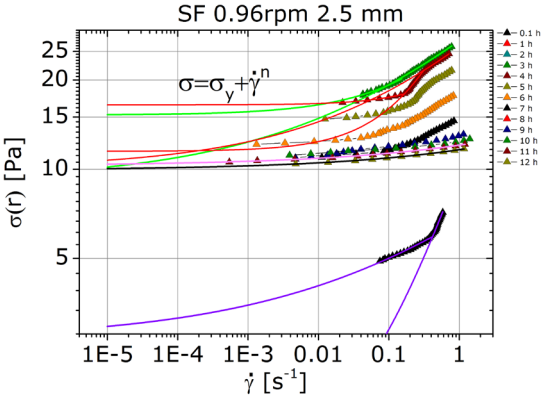

Figure S2.5. Fitting of the local flow curves (LFCs) by a power law function mimicking the Herschel-Bulkley model. The LFCs that could not be fitted by a single power law function over the whole gap due to banding, were therefore pragmatically fitted by two or three power law functions with different parameters, each describing the constitutive law for a band in the gap.

CHAPTER 3

A versatile shear cell for investigation of structure of food materials under shear

This chapter has been published as E. Velichko, B. Tian[1], T. Nikolaeva[1], J. Koning, J. van Duynhoven, W. G. Bouwman (2019). A versatile shear cell for investigation of structure of food materials under shear. Colloids and Surfaces A: Physicochemical and Engineering Aspects, 566, 21-28. https://doi.org/10.1016/j.colsurfa.2018.12.046

[1] These authors contributed equally to this work.

Abstract

A versatile cell for X-ray and neutron scattering experiments on samples under shear has been designed. To our knowledge, it is the first shear cell which can be used for both SAXS and SANS in respectively synchrotron or reactor beamlines. The cell is mainly intended for scattering experiments in so-called “1–2 plane geometry”, but can also be modified into cone–plate and plate–plate rheological geometries, giving access to the 1–3 scattering plane. The latter two geometries, however, can only be used with neutron scattering. The final cell design is compact, which allows it to be used even with lab-based X-ray sources. A special thermostatic shell allows for the temperature control of the samples under investigation in the range from 5 up to 100 °C. Several X-ray and neutron scattering experiments performed with the cell have helped in better understanding of the structuring under shear of food materials, such as: cellulose suspensions, fat crystal networks and milk proteins.

3.1. Introduction

A major challenge for food science is to reconcile the societal drive towards sustainable food production with the consumers demand for natural, stable and superior tasting foods (Van Der Goot et al., 2016). Conventional routes for food manufacturing have been optimized over decades and have reached their limits. The required radical redesign of food formulation and processing routes requires deepened insights in relationships between product structure and functionality (Augustin et al., 2016). When processing raw materials to final consumer food products, their structures undergo changes at multiple length scales (Mezzenga, Schurtenberger, Burbidge, & Michel, 2005; Ubbink, 2012). A prerequisite for rational redesign of food processing routes is to have insights in how these hierarchical multiscale structures evolve under dynamic condition (Ubbink, 2012).

Small-angle scattering (SAS) of X-rays (SAXS) and neutrons (SANS) is widely utilized to study structures of food colloids (Doutch & Gilbert, 2013; López-Rubio, Flanagan, Shrestha, Gidley, & Gilbert, 2008; Nieuwland, Bouwman, Bennink, Silletti, & Jongh, 2015; Nikolaeva et al., 2018; Peyronel, Quinn, Marangoni, & Pink, 2014; Ramel, Peyronel, & Marangoni, 2016a). A number of works has also been done on application of these techniques on materials under shear or flow conditions (Eberle & Porcar, 2012; Vermant & J Solomon, 2005). Both methods, SAXS and SANS (Lopez-Rubio & Gilbert, 2009) are capable of investigations on nano- and mesoscale size range, moreover, by utilizing a spin-echo principle for SANS encoding (SESANS (Rekveldt et al., 2005)), the range can be extended up to 20 μm. However, these methods have certain advantages and disadvantages related to the employed type of radiation. X-rays interact with electron clouds of atoms, which leads to linear dependency of scattering power on the atomic number of the element. Neutrons interact with atom nuclei, which causes different scattering power for different isotopes of the same chemical element. This effect is widely employed in experiments with contrast variation. Moreover, due to the weak interaction of neutrons with matter, rather bulky samples can be studied with neutron scattering. Since X-rays are easy to generate, a multitude of laboratory-scale plug-and-play SAXS instruments came to the market in recent years. Compact neutron sources are still under development and SANS experiments still require large-facilities like nuclear reactors, or spallation sources. Synchrotrons, large-facilities generating X-ray are also open for SAXS experiments. One of the great advantages of synchrotrons is their high

flux of X-rays, which is 6–7 orders of magnitude higher than average flux of neutrons at neutron large-facilities. Such a high flux allows for a very high time resolution, as well as high spatial resolution of the experiment, as X-ray beam at synchrotron can easily be focused to 100 μm, or, with special optics, even to a few nm. However, such high flux might be a considerable disadvantage in studies of soft matter, as samples can easily get radiation damage or even destroyed within a fraction of a second. Taking into account compatibility of X-rays and neutrons, we decided to make our shear-cell suitable for both kind of radiation, so that we could perform (SE)SANS and SAXS experiments on complex fluids under the same conditions. In the following the cells, suitable for either SANS or SAXS on the samples under shear, will be called shear-SAS cells.

Table 3.1 gives an overview of the shear-SAS cells described in the literature. As can be seen, the most popular cell geometry is Taylor–Couette, which allows for radial and tangential passage of the beam along the cell (for more details of various cell geometries as well as scattering planes see the review (Eberle & Porcar, 2012)). Depending on the direction of the beam relative to the shear cell, three different scattering geometries are possible. Figure 3.1 shows three possible scattering geometries based on the Taylor–Couette cell. AntonPaar was the first company able to combine a rheometer with a suitable Taylor–Couette cell with small-angle scattering of X-rays (Panine, Gradzielski, & Narayanan, 2003), a few years later simultaneous SANS and torque measurements were performed with a rheometer of Rheowis-Fluid (Labplus, Jona, Switzerland) (Stellbrink, Lonetti, Rother, Willner, & Richter, 2008). Another way of evolution of shear-SAS cells was a development of so-called "1–2 plane shear cell" (Gurnon et al., 2014; W Liberatore, Nettesheim, Wagner, & Porcar, 2006). As such a cell allows spatial resolution along the shear-gradient direction across the gap, it is very attractive for investigation of materials showing shear-banding (Helgeson, D. Reichert, Hu, & Wagner, 2009; Helgeson, Porcar, López-Barrón, & Wagner, 2010; Helgeson, Vasquez, Wagner, Cook, & Hu, 2009; M. Weigandt, Porcar, & Pozzo, 2011; W Liberatore et al., 2006). However, this geometry does not allow for a simultaneous torque measurement, as the cell is placed horizontally, while all of the existing rheometers are vertical. For our design we decided to omit possibility for a simultaneous torque measurement and chose for horizontal cell geometry.

Table 3.1. Shear-SAS cells described in the literature.

Source	Simultaneous torque measurement	Type of radiation	Cell geometry	Scattering plane(s)
(Lindner & Oberthür, 1984)	−	Neutrons	Taylor–Couette	1–3
(Straty, 1989)	−	Neutrons	Taylor–Couette	1–3
(Cummins, Staples, Millen, & Penfold, 1990)	−	neutrons	Taylor–Couette	1–3
(C. Straty, J. M. Hanley, & J. Glinka, 1991)	−	Neutrons	Taylor–Couette	1–3
(Okamoto, Saijo, & Hashimoto, 1994)	−	X-rays	Plate–plate	1–2
(Baker et al., 1994)	−	Neutrons	Poiseuille	1–2
(Noirez & Lapp, 1997)	−	Neutrons	Plate–plate	1–2
(Dux et al., 1998)	−	Neutrons	Plate–plate	1–3
(Molino, Berret, Porte, Diat, & Lindner, 1998)	−	X-rays	Taylor–Couette	1–3, 2–3
(E. Caputo & R. Burghardt, 2001)	−	X-rays	Cone–plate	1–2
(Porcar, Hamilton, D. Butler, & Warr, 2002)	−	Neutrons	Taylor–Couette	1–2
(Panine et al., 2003)	+	X-rays	Taylor–Couette	1–3, 2–3
(Gurnon et al., 2014; W Liberatore et al., 2006)	−	Neutrons	Taylor–Couette	1–2
(Stellbrink et al., 2008)	+	Neutrons	Taylor–Couette	1–3, 2–3
(Struth et al., 2011)	+	X-rays	Plate–plate	1–3
(Porcar, Pozzo, Langenbucher, Moyer, & D Butler, 2011)	+	Neutrons	Taylor–Couette	1–3, 2–3
(Pfleiderer et al., 2014)	+	X-rays	Sliding plate	1–2
(J. Richards, Wagner, & D. Butler, 2017)	+	Neutrons	Taylor–Couette	1–3, 2–3

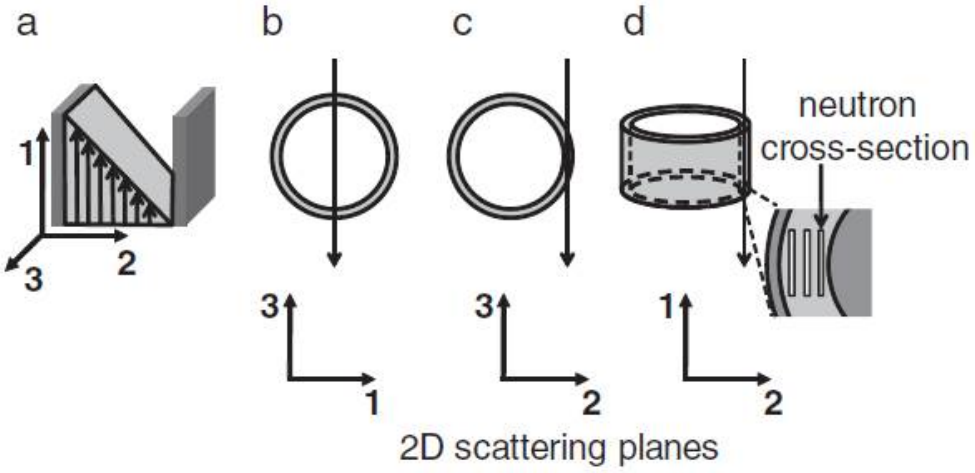

Figure 3.1. The common Taylor–Couette flow cell geometries with accessible scattering planes. **(A)** Rectilinear coordinate frame where the 1-, 2-, and 3-directions are defined as the velocity (V), velocity gradient (ΔV), and vorticity (ω) directions, respectively. **(B)**, **(C)**, and **(D)** are the radial, tangential, and 1–2 plane flow cell geometries that allow for scattering along the 1–3, 2–3, and 1–2 planes, respectively. In the latter, an incident beam cross-section smaller than the fluid gap allows for spatial resolution along the gap. The figure is adopted from (Eberle & Porcar, 2012).

In this article we present detailed design of the versatile shear-cell suitable for SAXS, SANS and SESANS measurements. Three examples of shear-SAS cell application for studies of food colloids are presented in the experimental section. Although in our research we focused mostly on application of the shear-SAS cell for investigation of food colloidal dispersions, the applications can be extended to the much broader field of soft matter.

3.2. Apparatus

Figure 3.2 shows a schematic drawing of the developed shear-SAS cell and Figure S3.1 (supplementary material) shows an image of the cell mounted at the SAXS DUBBLE (BM-26) beamline at ESRF (Borsboom et al., 1998; Bras et al., 2003). As can be seen from Figure

S3.1 (supplementary material), the cell with its drive and motor is rather compact (it can fit in a box of 25 × 25 × 25 cm^3), which makes it easy in transportation, it even has been transported as hand luggage on an airplane. The compactness made it possible to mount it on various beamlines and even laboratory X-ray sources. The cell consists of an inner rotating disk (rotor) and an outer stable container (stator), leaving a gap which is filled up with the material under investigation. Rotor and stator are both made of aluminum.

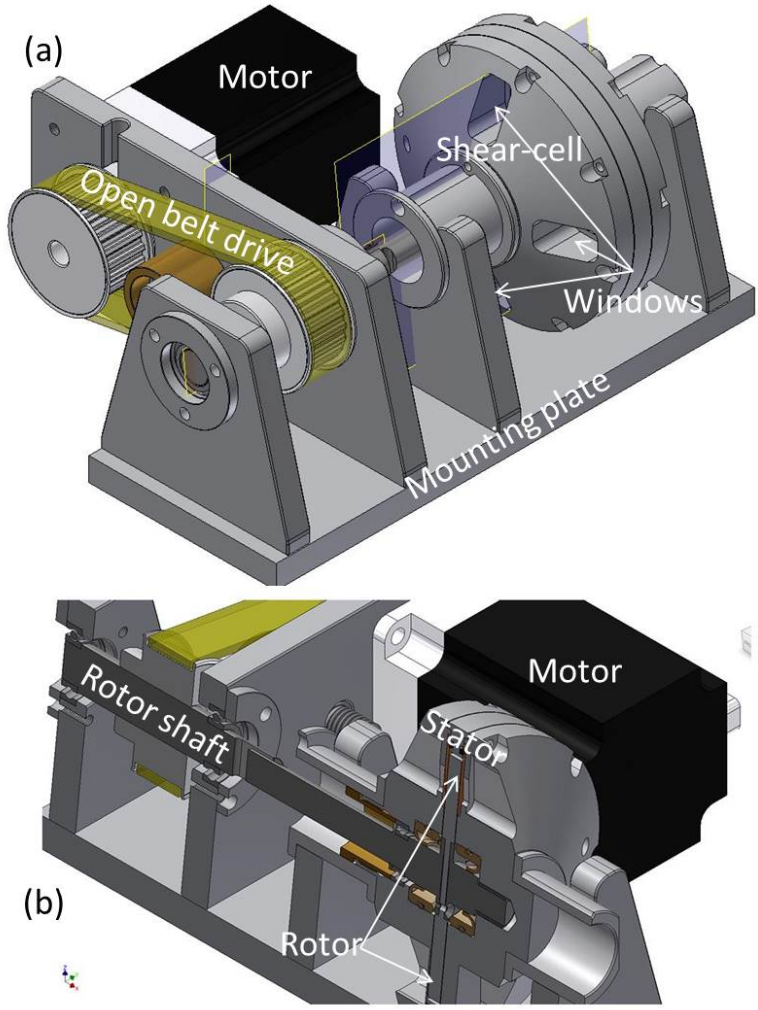

Figure 3.2. A schematic 3D drawing of the developed shear-cell **(A)** and a vertical cross section of it along the rotation axis of the cell **(B)**.

3.2.1. Fit for neutrons and X-rays

In order to make the cell suitable for X-rays and neutrons, special types of windows were necessary for each type of radiation. In case of neutrons 0.4 mm thick aluminum windows with accessible area 10 × 17 mm^2 are integrated in the cell design. Figure 3.3 shows a 2D (A) and 1D (B) SANS patterns from the empty shear cell. For X-rays two circular diamond windows with 0.2 mm thickness and 6 mm diameter were created, which give hardly any background scattering (see Figure 3.3(C) and (D)).

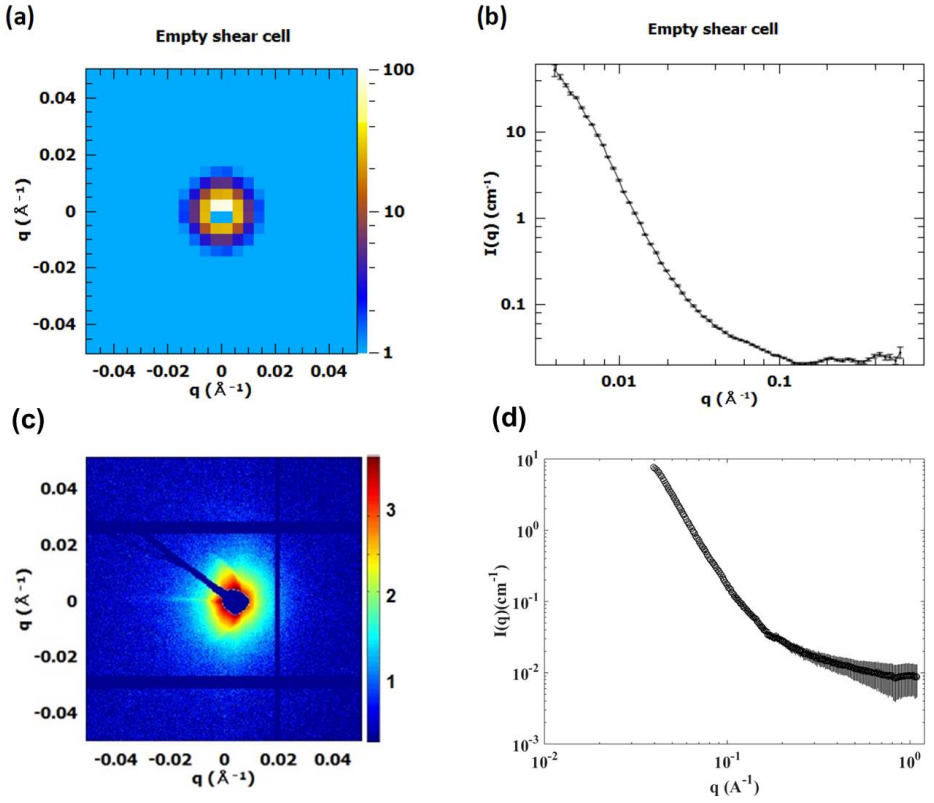

Figure 3.3. 2D **(A)** and 1D **(B)** SANS patterns from the empty shear cell in cone–plate configuration. 2D **(C)** and 1D **(D)** SAXS patterns from the empty shear cell in Taylor–Couette cell geometry. The scattering was collected at LARMOR beamline of ISIS neutron source (**A** and **B**) and at BM26 (DUBBLE) beamline of ESRF (**C** and **D**).

For visual inspection of the sample and potential light scattering applications, 1 mm thick quartz windows with accessible area 8 × 15 mm^2 were added to the cell design. Figure S3.2 (supplementary material) shows the windows positions on the cell. It should be noted, that in order to obtain the most homogeneous sample flow at the measurement position, the cell should be positioned in such a way that required window appears on the side of the cell (in Figure S3.2(A) (supplementary material) quartz and diamond windows are in the right position).

As the cell is also intended to be used for SESANS measurement, we had to minimize magnetic fields appearing due to motor driving the cell. At the current distance between the aluminum window of the cell and the motor (20 cm) we did not observe any effects of the motor magnetic field on the neutron beam polarization.

3.2.2. Shear-SAS cell geometries

The cell is mainly intended to probe the so-called 1–2 scattering plane of the complex fluids. The Taylor–Couette cell geometry for this application is similar to one described in (Gurnon et al., 2014) with the additional possibility for the SAXS experiments. This geometry in combination with intensive neutron or X-ray beam allows for spatially-resolved SAXS/SANS measurements across the gap. Moreover, since the cell is made of aluminum, which is relatively transparent for neutrons, we decided to use this advantage and extend the cell design to two more geometries, namely cone–plate and plate–plate. All three geometries are shown in Figure 3.4.

In the Taylor–Couette geometry, the shear-SAS cell allows access to so-called 1–2 scattering plane, which in combination with intensive beams allows for spatially-resolved SAXS/SANS measurements across the gap. Therefore, it is possible to locally probe structure of the material under investigation. By varying thicknesses of the rotor and outer ring, it is possible to achieve different sample thicknesses along the beam L. However, the minimal value of L is 4 mm due to mechanical limitations. The gap size between the rotor and the ring also can be varied by varying the rotor diameter d. In our experiments we were using a gap size of 1 mm. It can be increased up to 6 mm for X-ray experiments and up to 15 mm for experiments with neutrons.

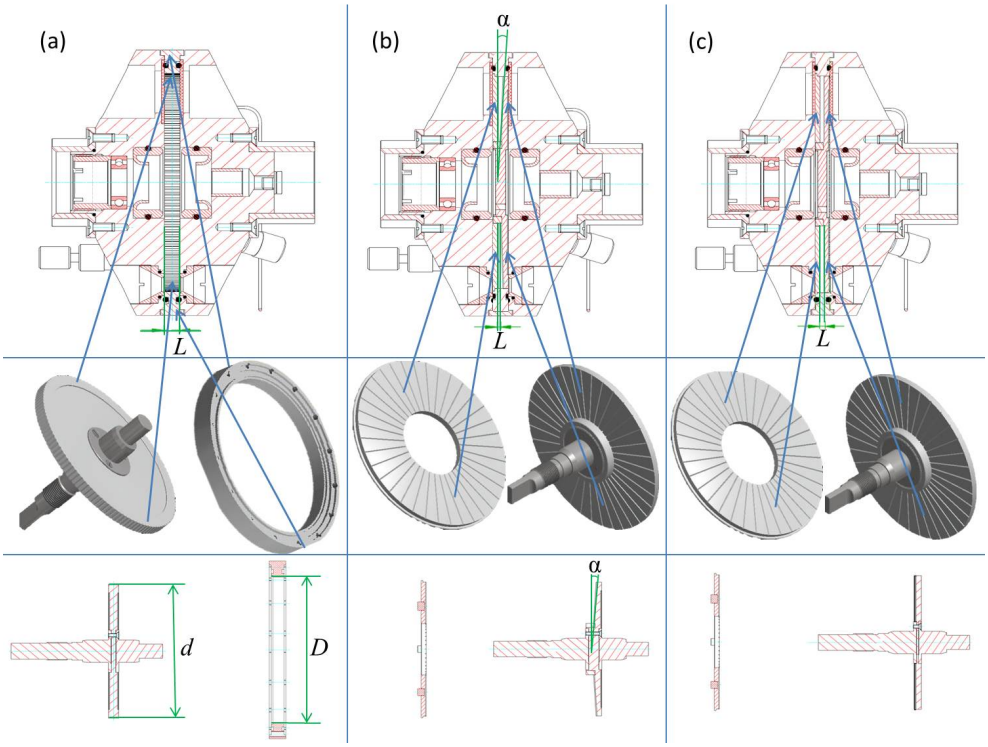

Figure 3.4. Geometries of the cell: **(A)** Taylor–Couette geometry, **(B)** cone–plate geometry, and **(C)** plate–plate geometry. The top row shows a cross section of the entire cell, the stators and rotors for respective geometries are shown in the middle row with their respective cross sections in the bottom row. Blue arrows show where the stators and rotors appear on the drawings of the cross sections. L is a sample thickness on the beam, d is a diameter of the rotor, D is an inner diameter of the housing ring, and α is the cone angle.

In plate–plate or cone–plate geometry the scattering pattern appears in 1–3 scattering plane. In this case the beam is going through the sample along the shear-gradient direction and the scattering pattern is integrated over all shear rates present in the system. In this case the sample thickness along the beam can be varied either by changing the thickness of the rotor or by changing the cone angle α. The cone angle can be varied between 1° and 10°. In our experiments we were using $\alpha = 3°$.

In all three geometries, the surfaces of the rotor and the stator can be made smooth, sand-blasted, or serrated, depending on roughness desired for the planned experiment.

3.2.3. Temperature control

Since rheology and structure of food is highly dependent on temperature and temperature history of the material, we included a special housing for temperature control of the cell in our design. A thermostatic shell was designed for this purpose. The shell is made of 1 mm thick nylon 12 with copper insertions for better temperature exchange. The nylon parts of the cell were 3D-printed and the copper insertions were glued to them with a temperature-resistant glue. The internal surface of the shell follows the shape of the shear cell and has maximal available contact surface area with the cell. The shell is hollow, which allows for the flow of a cooling or heating liquid with desired temperature through it. For temperature measurements a K-type thermocouple is used. Figure S3.3 (supplementary material) shows a cross section of the cell in the thermostatic shell as well as the internal surface of the shell with copper insertions.

3.3. Experimental results and discussion

A couple of in-situ experiments were conducted so far: one at the DUBBLE beamline at ESRF (Borsboom et al., 1998; Bras et al., 2003) and one at the LARMOR instrument at ISIS. In the first case the Taylor–Couette geometry was used in combination with X-ray scattering for investigation of cellulose dispersions and fat crystal dispersions. In the second experiment protein dispersions were studied in plate–plate and cone–plate geometry with aid of neutron scattering.

3.3.1. X-rays: microfibrillated cellulose dispersions

So-called non-local flow behaviour of microfibrillated cellulose was observed by Rheo-MRI (de Kort et al., 2016): the viscosity of the sample was dependent on the position across the cell gap. This can be explained by a formation of flocks of microfibrills, or a formation of an aligned liquid crystal phase.

In order to check these two models, we have performed a shear-SAXS experiment at the BM-26 (DUBBLE) beamline at ESRF. Figure 3.5 shows typical scattering patterns for a sample of microfibrillated bacterial cellulose stabilized by carboxymethylcellulose (BC-CMC) at high and low shear rates. The scattering patterns appear to be isotropic at both shear rates.

This result indicates absence of aligned liquid crystal phase, and sustains the flocculation model as the explanation for the position dependent viscosity.

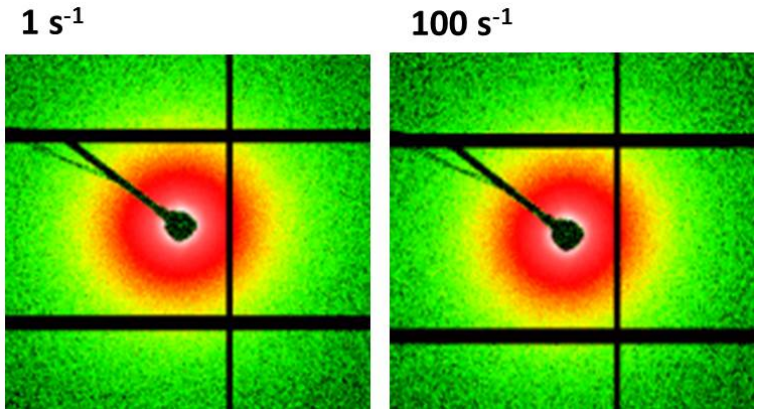

Figure 3.5. 2D SAXS patterns for a sample of microfibrillated bacterial cellulose (BC) with carboxymethylcellulose (CMC) with a concentration of BC 0.2 wt%. and ratio BC:CMC = 4:1 at 1 (left) and 100 (right) s^{-1}. The patterns are shown for a point in the middle of the cell gap.

3.3.2. X-rays: in situ view on fat crystal network formation

Stability and sensorial quality of fat-based products, such as butter and margarine, are defined by the underlying multiscale structure of fat crystal networks (Ramel, Peyronel, & Marangoni, 2016b). A novel route to design the fat crystal structure is based on dispersing micronized fat crystal (MFC) nanoplatelets in oil(Münüklü & Jansens, 2007; Nikolaeva et al., 2018). In this way, the crystallisation of the fat crystal nanoplatelets can be decoupled from the aggregation of fat crystals into larger structures, which could radically simplify manufacturing of food manufacturing routes. However, rational design of these routes is challenging, since kinetics of multiscale network formation is strongly determined by temperature and shear (Maleky & Mazzanti, 2018). The developed shear cell was employed to assess kinetics of fat crystal mesoscale networks in well-controlled shear stress fields at different temperatures (Nikolaeva et al., 2018, 2019).

Figure 3.6(A) shows the 2D SAXS pattern and an radial integration of the first order diffraction peak obtained under imposed shear 0.1 s^{-1} at the BM-26 (DUBBLE) beamline at

ESRF. The rheo-SAXS experiment revealed the alignment of the dispersed MFC nanoplatelets under shear. As most of the information about individual MFC nanoplatelets lies in the first diffraction peak at scattering vectors q = 1.6 nm^{-1}, it was also possible to perform experiments at a lab-scale X-ray diffractometer Bruker D8-Discover (A.12). Even though the obtained 2D pattern (Figure 3.6(B)) had a different signal to noise ratio, the effect of shear on the alignment of MFC nanoplatelets could clearly be observed.

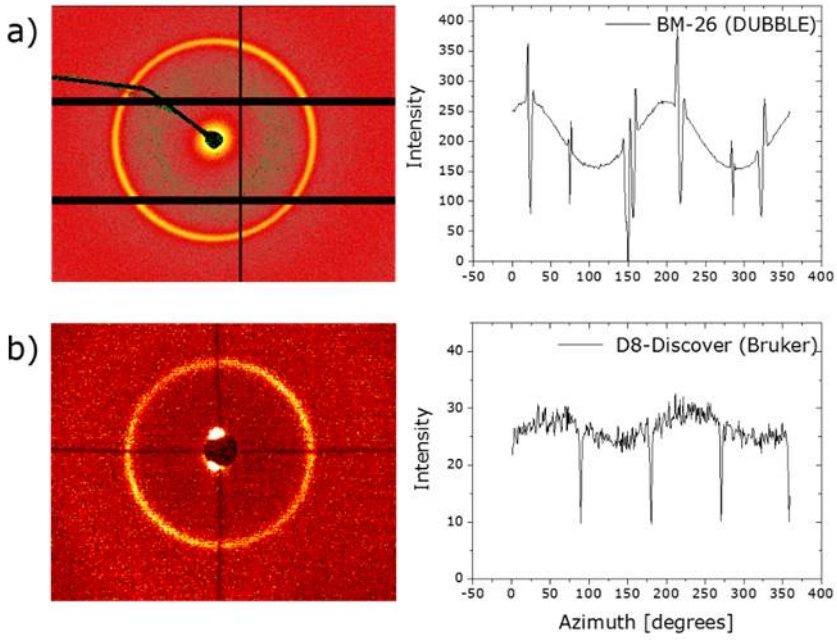

Figure 3.6. 2D SAXS patterns and their radial averages presented in the intensity vs Azimuth angle plots for MFC nanoplatelets dispersed in sunflower oil obtained at the BM-26 (DUBBLE) beamline at ESRF **(A)** and at the lab-scale Bruker D8-Discover X-ray diffractometer **(B)**. Both experiments were performed in the developed Couette geometry with serrated walls at an imposed shear rate of 0.1 s^{-1} and ambient temperatures.

The presence of a well resolved first order diffraction peak allowed real-time assessment of the increase in average crystal thickness (ACT) of the dispersed MFC nanoplatelets under shear. The ACT was estimated based on the Scherrer line shape analysis (den Adel, van Malssen, van Duynhoven, Mykhaylyk, & Voda, 2018; Nikolaeva et al., 2018). Figure 3.7(A)

shows the ACT as a function of time under imposed constant shear of 0.1 s^{-1} at ambient temperature. The scattering patterns were obtained at the BM- 26 (DUBBLE) beamline at ESRF. The increase in ACT during 8–13 h of shear points toward shear induced recrystallisation of the MFC nanoplatelets. This recrystallisation effect was also observed in a shear-SAXS experiment at D8-Discover diffractometer, albeit with lower signal to noise ratio (see Figure 3.7(A)).

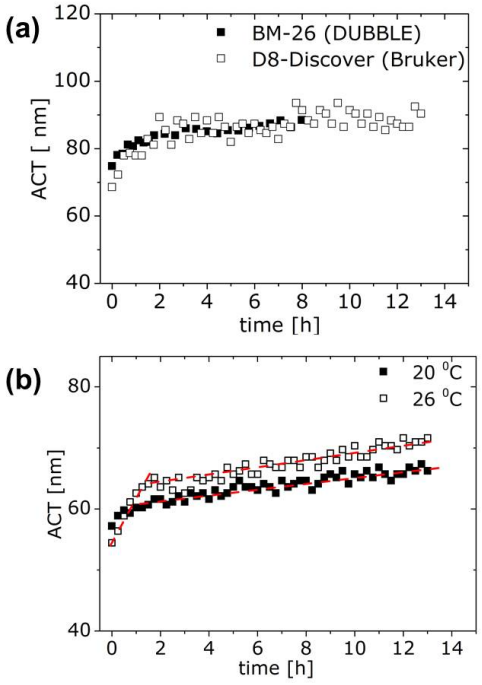

Figure 3.7. (A) A comparison of the ACT data as a function of time obtained at the BM-26 (DUBBLE) beamline at ESRF (solid symbols) and at the lab-scale X-ray diffractometer Bruker D8-Discover (empty symbols). Both experiments were done for MFC nanoplatelets dispersed in sunflower oil in the developed Couette geometry with serrated walls at an imposed shear rate of 0.1 s^{-1} and ambient temperatures. **(B)** ACT as a function of time for MFC nanoplatelets dispersed in bean oil at an imposed shear rate of 1 s^{-1} and temperatures of 20 °C (solid symbols) and 26 °C (empty symbols). The measurements were performed in a rheo-SAXS Couette cell geometry (1 mm gap) at the D8-Discover.

The performance of the variable temperature capability of the shear cell is illustrated by Figure 3.7(B). MFC dispersions were measured at 20 and 26 °C with the shear cell mounted in a lab scale Discover D8 diffractometer for 13 h under constant shear of 1 s^{-1}. Even with this lab scale instrument kinetic curves could be obtained that allow observation of two recrystallisation stages of which one is clearly temperature dependent (see Figure 3.7(B)) (Nikolaeva et al., 2018, 2019). The availability of the rheo-SAXS cell with variable temperature capability which can versatile be mounted in both synchrotron beamlines and labscale instruments has been an important enabler of studies investigated fat crystal network formation (Nikolaeva et al., 2018, 2019). In future work we expect that the cell will also be deployed in combination with ultra small angle X-rays scattering (USAXS) to provide unprecedented views on network formation in the micronscale domain.

3.3.3. Neutrons: protein dispersions

Manski et al. (Manski, van der Goot, & Boom, 2007) found a way to produce fibrous structure from calcium caseinate dispersion by applying simple shear, heat and enzyme transglutaminase. In order to investigate the structuring of calcium caseinate dispersions under shear, we have designed and performed a small-angle neutron scattering experiment. The experiment was conducted at the LARMOR instrument at ISIS.

Figure 3.8(A) shows the typical scattering patterns of the sample. All data were reduced with their corresponding background, for the shear-cell, the background is the cell filled with H_2O. A nearly perfect overlap between the sample measured ex-situ and at 0 s^{-1} inside the shear-cell confirmed the shear-cell did not interfere with the sample. Surprisingly, the scattering pattern obtained at a shear rate as high as 100 s^{-1} also overlapped perfectly with the others, indicating shear had no influence on the sample structure at the length scale studied. Moreover, the scattering is isotropic at all shear rates, as the radially averaged scattering intensity in Figure 3.8(B) shows.

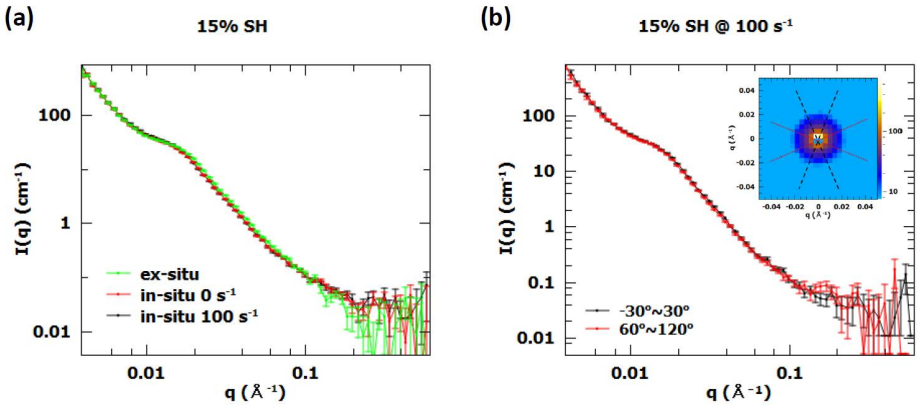

Figure 3.8. Scattering patterns of 15% (w/w) calcium caseinate dissolved in H_2O (SH). **(A)** 1D scattering patterns of the sample sheared at 0, 100 s^{-1} and ex-situ; **(B)** intensities of sector-cut from the 2D patterns of the sample sheared at 100 s^{-1} (inset).

Conclusions

We have designed and built a versatile compact shear cell to perform SAXS, SANS and SESANS measurements with temperature control. The experimental section of the article has shown applications of the designed shear cell in studies of food materials. Each of the obtained results provides a valuable insight into structuring of the soft matter under shear, relevant to both fundamental and applied sciences.

Acknowledgements

We thank Gerrit W.M. Peters (Department of Mechanical Engineering Materials Technology Institute, Eindhoven University of Technology) and Wim Bras (DUBBLE CRG BM26@ESRF, Netherlands Organization for Scientific Research (NWO), European Synchrotron Radiation Facility) for their contribution in the design of the shear cell, Ruud den Adel and Adrian Voda (Unilever R&D Vlaardingen) for their help and technical assistance with the testing of the shear cell and temperature shell with the Bruker D8-Discover diffractometer, Daniel Hermida Merino (DUBBLE CRG BM26@ESRF,

Netherlands Organization for Scientific Research (NWO), European Synchrotron Radiation Facility), Robert Dalgliesh and Adam Washington (LARMOR beamline, ISIS neutron and muon source) for their help and technical assistance during SAXS and SANS experiments, respectively, Netherlands Organization for Scientific Research (NWO) and NWO Domain Applied and Engineering Sciences (AES) for giving us opportunity to perform SAXS experiments at DUBBLE beamline, and Ernst van der Waals (DEMO, TU Delft) for his help and technical assistance with the development of the shear cell and temperature shell. This work is part of the research program Open Technology with project number 13386 which is financed by the Netherlands Organization for Scientific Research (NWO).

References

Augustin, M. A., Riley, M., Stockmann, R., Bennett, L., Kahl, A., Lockett, T., … Cobiac, L. (2016). Role of food processing in food and nutrition security. *Trends in Food Science and Technology*, *56*, 115–125. https://doi.org/10.1016/j.tifs.2016.08.005

Baker, S., Smith, G., Pynn, R., Butler, P., Hayter, J., Hamilton, W., & Magid, L. (1994). *Shear cell for the study of liquid-solid interfaces by neutron scattering*. *Review of Scientific Instruments* (Vol. 65). https://doi.org/10.1063/1.1145148

Borsboom, M., Bras, W., Cerjak, I., Detollenaere, D., Glastra van Loon, D., Goedtkindt, P., … Vlieg, E. (1998). The Dutch–Belgian beamline at the ESRF. *Journal of Synchrotron Radiation*, *5*(3), 518–520. https://doi.org/10.1107/S0909049597013484

Bras, W., Dolbnya, I. P., Detollenaere, D., van Tol, R., Malfois, M., Greaves, G. N., … Heeley, E. (2003). Recent experiments on a small-angle/wide-angle X-ray scattering beam line at the ESRF. *Journal of Applied Crystallography*, *36*(3), 791–794. https://doi.org/10.1107/S002188980300400X

C. Straty, G., J. M. Hanley, H., & J. Glinka, C. (1991). *Shearing apparatus for neutron scattering studies on fluids: Preliminary results for colloidal suspensions*. *Journal of Statistical Physics* (Vol. 62). https://doi.org/10.1007/BF01128174

Cummins, P. G., Staples, E., Millen, B., & Penfold, J. (1990). *A Couette Shear Flow Cell for Small-Angle Neutron Scattering Studies*. *Measurement Science and Technology* (Vol. 1). https://doi.org/10.1088/0957-0233/1/2/013

de Kort, D. W., Veen, S. J., Van As, H., Bonn, D., Velikov, K. P., & van Duynhoven, J. P. M. (2016). Yielding and flow of cellulose microfibril dispersions in the presence of a charged polymer. *Soft Matter*, *12*(21), 4739–4744. https://doi.org/10.1039/C5SM02869H

den Adel, R., van Malssen, K., van Duynhoven, J., Mykhaylyk, O. O., & Voda, A. (2018). Fat crystallite thickness distribution based on SAXD peak shape analysis. *European Journal of Lipid Science and Technology*, *1800222*, 1–6. https://doi.org/10.1002/ejlt.201800222

Doutch, J., & Gilbert, E. P. (2013). Characterisation of large scale structures in starch granules via small-angle neutron and X-ray scattering. *Carbohydrate Polymers*, *91*(1), 444–451. https://doi.org/10.1016/j.carbpol.2012.08.002

Dux, C., Musa, S., Reus, V., Versmold, H., Schwahn, D., & Lindner, P. (1998). *Small Angle Neutron Scattering Experiments From Colloidal Dispersions at Rest and under Shear Conditions*. *The Journal of Chemical Physics* (Vol. 109). https://doi.org/10.1063/1.476828

E. Caputo, F., & R. Burghardt, W. (2001). *Real-Time 1-2 Plane SAXS Measurements of Molecular Orientation in Sheared Liquid Crystalline Polymers*. *Macromolecules* (Vol. 34). https://doi.org/10.1021/ma0107556

Eberle, A. P. R., & Porcar, L. (2012). Flow-SANS and Rheo-SANS applied to soft matter. *Current Opinion in Colloid and Interface Science*, *17*(1), 33–43. https://doi.org/10.1016/j.cocis.2011.12.001

Gurnon, A. K., Godfrin, P., Wagner, N., P R Eberle, A., Butler, P., & Porcar, L. (2014). *Measuring Material Microstructure Under Flow Using 1-2 Plane Flow-Small Angle*

Neutron Scattering. *Journal of visualized experiments : JoVE*. https://doi.org/10.3791/51068

Helgeson, M., D. Reichert, M., Hu, Y., & Wagner, N. (2009). *Relating shear banding, structure, and phase behavior in wormlike micellar solutions*. *Soft Matter* (Vol. 5). https://doi.org/10.1039/b900948e

Helgeson, M., Porcar, L., López-Barrón, C., & Wagner, N. (2010). *Direct Observation of Flow-Concentration Coupling in a Shear-Banding Fluid*. *Physical review letters* (Vol. 105). https://doi.org/10.1103/PhysRevLett.105.084501

Helgeson, M., Vasquez, P., Wagner, N., Cook, L., & Hu, Y. (2009). *Microstructure and shear rheology of entangled wormlike micelles in solution*. *Journal of Rheology* (Vol. 53). https://doi.org/10.1122/1.3072077

J. Richards, J., Wagner, N., & D. Butler, P. (2017). *A strain-controlled RheoSANS instrument for the measurement of the microstructural, electrical, and mechanical properties of soft materials*. *Review of Scientific Instruments* (Vol. 88). https://doi.org/10.1063/1.4986770

Lindner, P., & Oberthür, R. C. (1984). *Apparatus for the investigation of liquid systems in a shear gradient by small angle neutron scattering (SANS)*. *http://dx.doi.org/10.1051/rphysap:01984001909075900* (Vol. 19). https://doi.org/10.1051/rphysap:01984001909075900

López-Rubio, A., Flanagan, B., Shrestha, A., Gidley, M., & Gilbert, E. (2008). *Molecular Rearrangement Of Starch During In Vitro Digestion: Toward A Better Understanding Of Enzyme Resistant Starch Formation In Processed Starches*. *Biomacromolecules* (Vol. 9). https://doi.org/10.1021/bm800213h

Lopez-Rubio, A., & Gilbert, E. P. (2009). Neutron scattering: a natural tool for food science and technology research. *Trends in Food Science & Technology*, *20*(11–12), 576–586. https://doi.org/10.1016/j.tifs.2009.07.008

M. Weigandt, K., Porcar, L., & Pozzo, L. (2011). *In situ Neutron Scattering Study of Structural Transitions in Fibrin Networks Under Shear Deformation*. *Soft Matter* (Vol. 7). https://doi.org/10.1039/C1SM06176C

Maleky, F., & Mazzanti, G. (2018). Lipid Crystal Networks Structured under Shear Flow. In K. Sato (Ed.), *Crystallization of Lipids: Fundamentals and Applications in Food, Cosmetics, and Pharmaceuticals* (First, pp. 211–239). John Wiley & Sons Ltd. https://doi.org/10.1002/9781118593882

Manski, J. M., van der Goot, A. J., & Boom, R. M. (2007). Advances in structure formation of anisotropic protein-rich foods through novel processing concepts. *Trends in Food Science and Technology*, *18*(11), 546–557. https://doi.org/10.1016/j.tifs.2007.05.002

Mezzenga, R., Schurtenberger, P., Burbidge, A., & Michel, M. (2005). *Understanding foods as soft materials*. *Nature materials* (Vol. 4). https://doi.org/10.1038/nmat1496

Molino, F. R., Berret, J.-F., Porte, G., Diat, O., & Lindner, P. (1998). *Identification of flow mechanisms for a soft crystal*. *Physics of Condensed Matter* (Vol. 3). https://doi.org/10.1007/s100510050284

Münüklü, P., & Jansens, P. J. (2007). Particle formation of an edible fat (rapeseed 70) using the supercritical melt micronization (ScMM) process. *Journal of Supercritical Fluids*, *40*(3), 433–442. https://doi.org/10.1016/j.supflu.2006.07.015

Nieuwland, M., Bouwman, W., Bennink, M., Silletti, E., & Jongh, H. (2015). *Characterizing Length Scales that Determine the Mechanical Behavior of gels from Crosslinked Casein Micelles*. *Food Biophysics* (Vol. 10). https://doi.org/10.1007/s11483-015-9399-y

Nikolaeva, T., Adel, R. den, Velichko, E., Bouwman, W. G., Hermida-Merino, D., Van As, H., … van Duynhoven, J. (2018). Networks of micronized fat crystals grown under static conditions. *Food & Function*, *9*, 2102–2111. https://doi.org/10.1039/C8FO00148K

Nikolaeva, T., den Adel, R., van der Sman, R., Martens, K. J. A., Voda, A., Van As, H., & van Duynhoven, J. (2019). Manipulation of Recrystallization and Network Formation of Oil-Dispersed Micronized Fat Crystals. *Langmuir*. https://doi.org/10.1021/acs.langmuir.8b03349

Noirez, L., & Lapp, A. (1997). *Shear Flow Induced Transition from Liquid-Crystalline to Polymer Behavior in Side-Chain Liquid Crystal Polymers*. *Physical Review Letters - PHYS REV LETT* (Vol. 78). https://doi.org/10.1103/PhysRevLett.78.70

Okamoto, S., Saijo, K., & Hashimoto, T. (1994). *Dynamic SAXS Studies of Sphere-Forming Block Copolymers under Large Oscillatory Shear Deformation*. *Macromolecules* (Vol. 27). https://doi.org/10.1021/ma00092a012

Panine, P., Gradzielski, M., & Narayanan, T. (2003). *Combined rheometry and small-angle x-ray scattering*. *Review of Scientific Instruments* (Vol. 74). https://doi.org/10.1063/1.1556943

Peyronel, F., Quinn, B., Marangoni, A. G., & Pink, D. a. (2014). Ultra small angle x-ray scattering in complex mixtures of triacylglycerols. *Journal of Physics. Condensed Matter : An Institute of Physics Journal*, *26*(46), 464110. https://doi.org/10.1088/0953-8984/26/46/464110

Pfleiderer, P., Jae Baik, S., Zhang, Z., Vleminckx, G., Paul Lettinga, M., Grelet, E., … Clasen, C. (2014). *X-ray scattering in the vorticity direction and rheometry from confined fluids*. *Review of Scientific Instruments* (Vol. 85). https://doi.org/10.1063/1.4881796

Porcar, L., Hamilton, W., D. Butler, P., & Warr, G. (2002). *A vapor barrier Couette shear cell for small angle neutron scattering measurements*. *Review of Scientific Instruments - REV SCI INSTR* (Vol. 73). https://doi.org/10.1063/1.1475351

Porcar, L., Pozzo, L., Langenbucher, G., Moyer, J., & D Butler, P. (2011). *Rheo-Small-Angle Neutron Scattering at the National Institute of Standards and Technology Center for Neutron Research*. *The Review of scientific instruments* (Vol. 82). https://doi.org/10.1063/1.3609863

Ramel, P. R. R., Peyronel, F., & Marangoni, A. G. (2016a). Characterization of the nanoscale structure of milk fat. *Food Chemistry*, *203*, 224–230. https://doi.org/10.1016/j.foodchem.2016.02.064

Ramel, P. R. R., Peyronel, F., & Marangoni, A. G. (2016b). Characterization of the nanoscale structure of milk fat. *Food Chemistry*, *203*, 224–230. https://doi.org/10.1016/j.foodchem.2016.02.064

Rekveldt, M., Plomp, J., Bouwman, W., Kraan, W. H., Grigoriev, S. ., & Blaauw, M. (2005). *Spin-echo small angle neutron scattering in Delft*. *REVIEW OF SCIENTIFIC INSTRUMENTS* (Vol. 76). https://doi.org/10.1063/1.1858579

Stellbrink, J., Lonetti, B., Rother, G., Willner, L., & Richter, D. (2008). *Shear induced structures of soft colloids: Rheo-SANS experiments on kinetically frozen PEP–PEO diblock copolymer micelles*. *Journal of Physics: Condensed Matter* (Vol. 20). https://doi.org/10.1088/0953-8984/20/40/404206

Straty, G. C. (1989). *Apparatus for Neutron Scattering Measurements on Sheared Fluids*. *Journal of Research of the National Institute of Standards and Technology* (Vol. 94). https://doi.org/10.6028/jres.094.024

Struth, B., Hyun, K., Kats, E., Meins, T., Walther, M., Wilhelm, M., & Grübel, G. (2011). *Observation of New States of Liquid Crystal 8CB under Nonlinear Shear Conditions as Observed via a Novel and Unique Rheology/Small-Angle X-ray Scattering Combination*. *Langmuir : the ACS journal of surfaces and colloids* (Vol. 27). https://doi.org/10.1021/la103786w

Ubbink, J. (2012). *Soft matter approaches to structured foods: From "cook-and-look" to rational food design? Faraday discussions* (Vol. 158). https://doi.org/10.1039/C2FD20125A

Van Der Goot, A. J., Pelgrom, P. J. M., Berghout, J. A. M., Geerts, M. E. J., Jankowiak, L., Hardt, N. A., … Boom, R. M. (2016). Concepts for further sustainable production of foods. *Journal of Food Engineering*, *168*, 42–51. https://doi.org/10.1016/j.jfoodeng.2015.07.010

Vermant, J., & J Solomon, M. (2005). *Flow-Induced Structure in Colloidal Suspensions*. *Journal of Physics: Condensed Matter* (Vol. 17). https://doi.org/10.1088/0953-8984/17/4/R02

W Liberatore, M., Nettesheim, F., Wagner, N., & Porcar, L. (2006). *Spatially resolved small-angle neutron scattering in the 1-2 plane: A study of shear-induced phase-separating wormlike micelles*. *Physical review. E, Statistical, nonlinear, and soft matter physics* (Vol. 73). https://doi.org/10.1103/PhysRevE.73.020504

Supplementary material

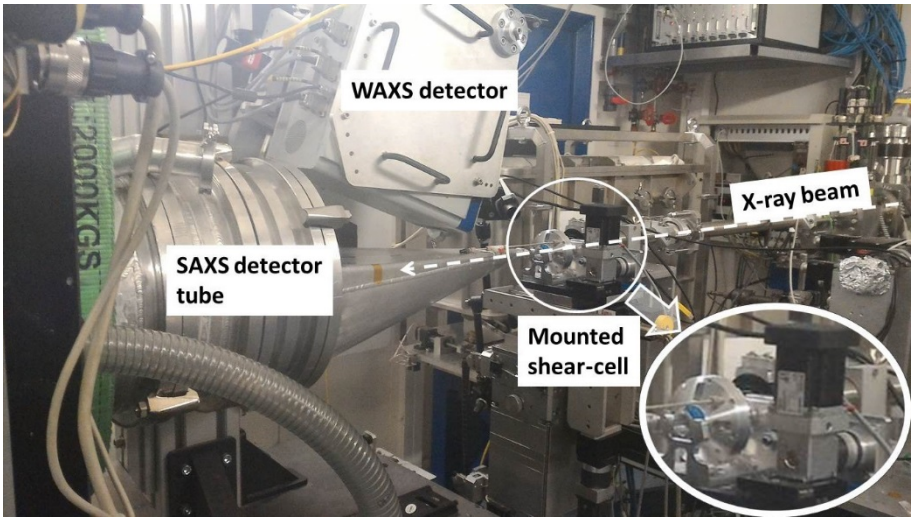

Figure S3.1. An image of the developed shear cell mounted at the SAXS DUBBLE (BM-26) beamline at ESRF.

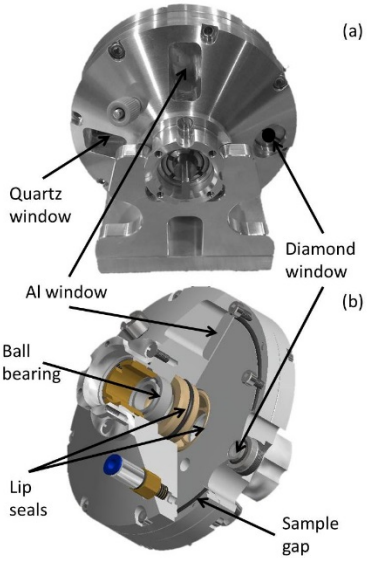

Figure S3.2. A foto **(A)** and a schematic drawing **(B)** of the shear-cell, outlining windows and some other construction elements of the cell

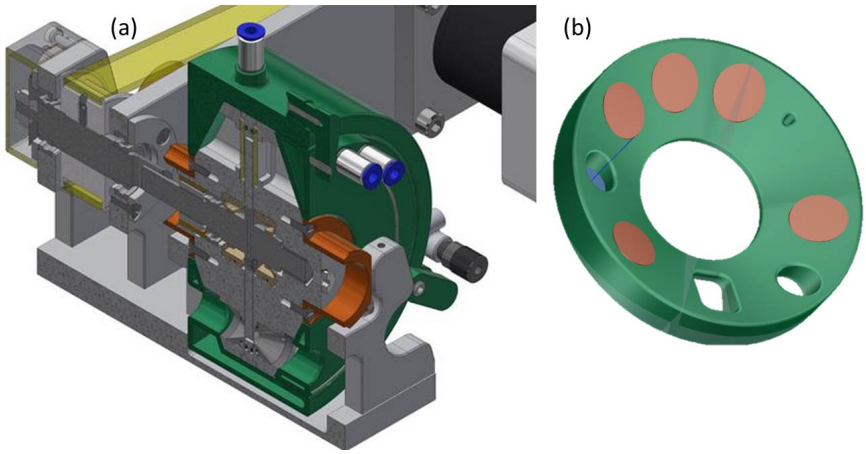

Figure S3.3. A cross section of the cell in thermostatic shell **(A)** and an internal surface of the shell with copper insertions in it **(B)**

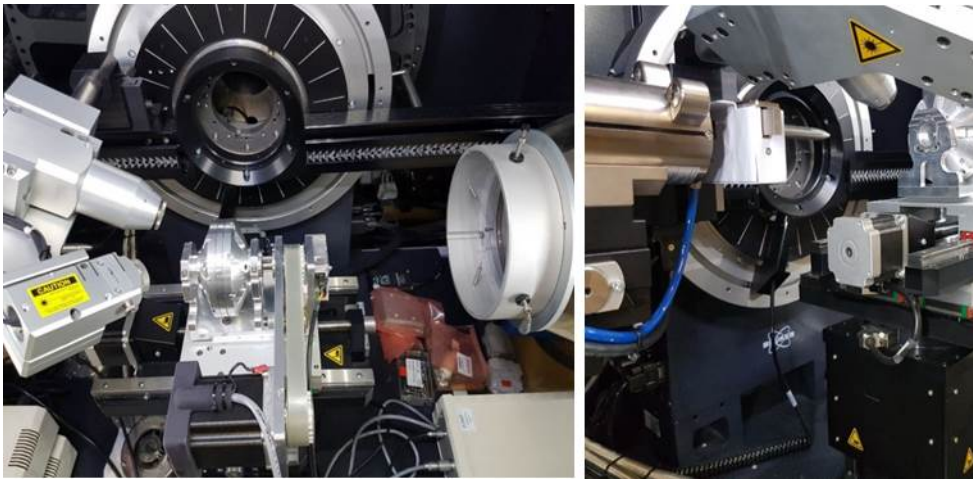

Figure S3.4. An image of the developed Couette shear cell mounted at the lab-scale X-ray diffractometer Bruker D8-Discover

CHAPTER 4

Networks of micronized fat crystals grown under static conditions

This chapter has been published as T. Nikolaeva, R. den Adel, E. Velichko, W. G. Bouwman, D. Hermida-Merino, H. Van As, A. Voda and J. van Duynhoven (2018). Networks of micronized fat crystals grown under static conditions. Food & Function, 2018, 9, 2102-2111. https://doi.org/10.1039/C8FO00148K

Abstract

Dispersing micronized fat crystals (MFCs) in oil is a novel route to largely decouple fat crystallisation and network formation and thus to simplify the manufacture of fat-continuous food products. MFCs dispersed in oil form a weak-interaction network organized by crystal aggregates in a continuous net of crystalline nanoplatelets. The rough surface of MFC nanoplatelets hampers stacking into one-dimensional aggregates, which explains the high mass fractal dimensions of the networks formed in MFC dispersions. Applying shear does not have a significant effect on the fractal dimensions of MFC networks, and MFC aggregates in the range of 5–10 μm remain intact. However, shear leads to a significant loss of storage modulus and yield stress over a time frame of an hour. This can be attributed to irreversible disruption of the continuous net of nanoplatelets. Rheo-SAXS revealed that shear releases nanoplatelets from the continuous net, which subsequently align in the shear field and undergo rapid recrystallisation. The release of thin and metastable nanoplatelets from the weak-link network bears relevance for simplified and more effective manufacturing of emulsified food products by effectively decoupling crystallisation, network formation and emulsification.

4.1. Introduction

The shelf-life stability and sensorial quality of fat-based products are for a major part determined by the structure of fat crystal networks (Campos, Ollivon, & Marangoni, 2010; P. R. R. Ramel, Peyronel, & Marangoni, 2016). These typically adopt a multi-length scale hierarchical organization, which can be manipulated by chemical composition (Bell, Gordon, Jirasubkunakorn, & Smith, 2007; Hartel, 2013; Zárubová, Filip, Kšandová, Šmidrkal, & Piska, 2010) and processing routes based on melting and cooling steps (Macias-Rodriguez & Marangoni, 2017; Piska, Zárubová, Loužecký, Karami, & Filip, 2006). During the cooling of a fat melt, lamellar stacks of triacylglycerol (TAG) bilayers grow into crystalline nanoplatelets(Acevedo & Marangoni, 2010). They can aggregate to larger structures that are plate-like, needle-like or spherulitic (Acevedo & Marangoni, 2014; P. R. Ramel, Co, Acevedo, & Marangoni, 2016). These aggregates form a fractal network, with weak-link interactions between them (Marangoni, 2004). The viscoelastic and yield stress properties (Gonzalez-Gutierrez & Scanlon, 2012; Macias-Rodriguez & Marangoni, 2017; S. Narine & Marangoni, 1999) of networks formed from the melt strongly depend on the processing conditions during cooling, like temperature and shear (Dhonsi & Stapley, 2006; Maleky, 2015; Tran & Rousseau, 2016). These determine an intricate interplay between formation of fat crystals and their aggregation into larger structures (David A Pink, Peyronel, Quinn, Singh, & Marangoni, 2015; Sato & Ueno, 2011). The strong coupling of these two structure formation steps is adding significant complexity to the industrial manufacturing of fat-based food products. This is particularly the case for the industrial manufacturing of fat-continuous food emulsions, where fat crystallisation and network formation occur concomitantly with emulsification (Marangoni & Wesdorp, 2013; Rousseau, 2000). For the manufacturing of products with low levels of saturated (solid) fat, current industrial processing routes have reached their processing and formulation limits (Bot & Floter, 2013).

A novel route to largely decouple fat crystallisation and network formation is to disperse pre-crystallized fat nanoplatelets in oil (Münüklü & Jansens, 2007). Such pre-crystallized fat nanoplatelets can be produced by supercritical melt micronisation (ScMM): saturating a molten fat blend with supercritical CO_2, which is subsequently expanded through a nozzle. The resulting fine powder of rapidly micronized fat crystal (MFC) nanoplatelets can be readily dispersed in oil. By this process, fat crystallisation and network formation can be

largely decoupled, which offers opportunities for simplified and flexible manufacturing of fat-continuous food products (Münüklü & Jansens, 2007). However, no detailed investigation on the obtained MFC networks has appeared so far.

In this study we investigated dispersions of micronized fat crystals (MFCs) in oil that were allowed two weeks of network formation. We hypothesized that within these dispersions diffusion- or reaction-limited aggregation of MFCs would form fractal MFC aggregates which interact *via* weak links. A suite of measurement techniques was used to investigate the multiscale structure of these networks and their viscoelastic and yield stress properties. At the nanoscale, Wide and Small Angle X-ray Scattering (WAXS, SAXS) were used for the assessment of fat crystal polymorphs and the thickness of the nanoplatelets. Their possible arrangement in stacked aggregates (TAGwoods) (D. A. Pink, Townsend, Peyronel, Co, & Marangoni, 2017; David A. Pink, Quinn, Peyronel, & Marangoni, 2013) was studied by means of Ultra Small Angle X-ray Scattering (USAXS). Confocal Raman imaging was deployed to obtain a micron scale view of the fat crystal networks. We used bulk rheology and Magnetic Resonance Imaging (rheo-MRI) to assess viscoelastic and yield stress properties. The macroscopic mechanical properties were modelled using the fractal theory of weak-link networks (Macias-Rodriguez & Marangoni, 2017; Marangoni, 2004). The fractal nature of the network was assessed by USAXS, confocal Raman imaging and bulk rheology. *In situ* rheo-SAXS experiments were conducted to assess shear-induced sub-micron mesoscale structural rearrangements of MFC dispersions.

4.2. Materials and methods

4.2.1. Materials

Micronized fat crystals (MFCs) were obtained by spraying fat blends dissolved in supercritical CO_2 (Münüklü & Jansens, 2007). The TAG composition of the studied MFCs is presented in Tables S4.1 and S4.2 in the supplementary material. The MFCs were dispersed in sunflower oil (SF) by intense mixing under vacuum at a temperature of about 20 °C. The concentration of MFC varied from 5% to 25% (weight). Melt- cool (MC) dispersions were prepared by melting MFC dispersions at 80 °C to erase crystal memory and subsequent

cooling to 20 °C at a rate of 0.1 deg min^{-1} to induce fat crystallization. The MFC and MC dispersions were stored at 20 °C for two weeks to form a stable network.

4.2.2. Bulk rheology

Rheological measurements were performed with an Anton Paar (MCR302 SN81236695) rheometer using a cone-plate (CP) geometry (cone angle of 3.992°, cone diameter of 49.971 mm). An oscillatory strain program was used to determine the boundaries of the linear viscoelastic region (LVR) from which apparent values of storage modulus G' were obtained. The rheometer was run through an oscillatory strain program with applied strain ranging from 0.0001 to 100% at a frequency of 1 Hz and at 20 °C. The weak-link theory (Shih, Shih, Kim, Liu, & Aksay, 1990) provides the relationship between the storage modulus G' of a volume-filling network and the volume fraction of particles (Macias-Rodriguez & Marangoni, 2017; S. S. Narine & Marangoni, 1999; Shih et al., 1990):

$$G' = \lambda \Phi^{\frac{1}{3-D}}$$

where G' is the shear storage modulus, λ is a constant, Φ is the volume fraction and D is the fractal dimension. The volume fraction of fat crystalline nanoplatelets in the dispersions was assumed to be proportional to the mass concentration, c. Fractal dimension values of fat crystal dispersions were obtained from the slopes of log G' *versus* log c (Marangoni & Wesdorp, 2013; Shih et al., 1990).

Two rheological approaches were used to measure yield stress properties of the material. In the first approach the yield stress was defined as the stress value at the limit of linearity of a small deformation mechanical test (Marangoni & Rogers, 2003). In the second one, we determined yield stress values *via* bifurcation measurements (P. Coussot, Nguyen, Huynh, & Bonn, 2002; de Kort et al., 2016), a fixed stress was applied and the rate of strain was then measured as a function of time. In each experiment a fresh sample was used. To every sample, we applied a required constant shear rate for 60 s before the oscillatory strain and bifurcation programs. Shear rates varied from 0.1 to 140 s^{-1}. The same procedure of applying shear as a pre-shear step was used for the characterization of MFC and MC dispersions by Raman-imaging, WAXS, SAXS and USAXS methods.

4.2.3. Rheo-MRI

Rheo-MRI velocity profiles were obtained using a Bruker Avance III spectrometer at 7.0 T magnetic field strength (resonance frequency 300 MHz for ^{1}H) in combination with a Bruker rheo-MRI accessory. As a shear cell, the Couette geometry was chosen with serrated walls, and inner and outer cylinder diameters of 17 and 22 mm, respectively, and hence a gap size of 2.5 mm. The inner cylinder rotation speed ranged from 0.25 to 62.38 s^{-1}. We measured 1D velocity profiles in 1 mm slice thickness by the Spin Echo (SE) sequence (Callaghan, 2011) (repetition time T_R = 1.5 s, echo time T_E = 17 ms, Δ = 13.1 ms, δ = 1 ms). Local velocities were measured with a field of view of 25 mm and a spatial resolution of 48.8 µm. The time needed to obtain a single velocity profile within the gap was of the order of 3 s. The number of scans (NS) = 64 was chosen to improve the signal-to-noise ratio. The temperature in the Couette geometry was controlled at 20 °C. The stability of the NMR signal indicates that no significant temperature variation occurred during the experiments.

We constructed constitutive relations $\sigma(\dot{\gamma})$ by combining local stress $\sigma(r,\omega)$ and local shear rate $\dot{\gamma}$ (r,ω) (Philippe. Coussot, 2005; Guillaume Ovarlez, Bertrand, & Rodts, 2006), which were collected at various positions r within the gap and various angular velocities ω. Rheo-MRI velocity data v gave the magnitude of the local shear rate $\dot{\gamma}(r,\omega)$ (Bird, 1987):

$$\dot{\gamma}(r) = r\frac{\partial(v/r)}{\partial r}$$

The local stress $\sigma(r,\omega)$ was obtained by performing applied torque T measurements for each angular velocity. We used a copy of the rheo-MRI Couette cell and a conventional rheometer Modular Compact Rheometer 301 (MCR301 SN80480600, Anton Paar). From torque data the shear stress was estimated(Bird, 1987) as

$$\sigma(r) = \frac{T}{2\pi R^2 H}$$

($\sigma(r)$ is the local stress as a function of the position, T is a torque, r is the position within the gap and H is the fluid height in the gap), which is valid for a homogeneously distributed material along the vertical direction within the Couette geometry. The local flow curve was constructed by plotting both $\sigma(r,\omega)$ and $\dot{\gamma}(r,\omega)$ in a single $\sigma(\dot{\gamma})$ plot.

4.2.4. Raman imaging

Full details of the experimental procedures can be found elsewhere (Martens et al., 2018; van Dalen et al., 2017). In short, experiments were performed on a WITec confocal Raman (Alpha 300R+) microscope equipped with a Zeiss upright microscope with a 532 nm laser at 25.0 mW. The sample was placed on a 19 °C water-cooled plate. The laser was used with a 100×/1.4 NA oil objective. The Raman spectrometer was coupled to a cooled (−60 °C) EMCCD detector. The obtained Raman spectra were in the range of 100–3800 cm^{-1}.

An integration time of 0.01 s was used for imaging a 200×200 or 50×50 µm×µm area with a resolution of 0.23 µm. The raw data were subjected to corrections and multivariate curve resolution (MCR) performed in MATLAB (The MathWorks Inc.) in order to obtain maps of solid fat content.

Fractal dimensions *D* were determined by the box-counting method, which assessed fractality with better precision compared to other approaches (Martens et al., 2018). An image is overlaid with boxes of decreasing size, determining for each box size how many boxes contain (part of) a self-similar object. The relationship between the number of filled boxes (N_b) and the length of the boxes (l_b) provides the fractal dimension *D*:

$$D = \frac{\Delta \log N_b}{\Delta \log l_b} - 1$$

Fractal dimensions were calculated using MATLAB (The MathWorks Inc.) (Martens et al., 2018).

4.2.5. WAXS and SAXS

Wide and Small Angle X-ray diffraction (WAXS and SAXS) analyses were performed on a Bruker D8-Discover diffractometer in a θ/θ configuration. The sample-to-detector distance was 32.5 cm. For both SAXS and WAXS measurements a modified Linkam stage was used to adjust temperature. In the WAXS configuration, the type of crystal polymorph of the fat blend was identified. The angle of the incident X-ray beam and the angle between the detector and the sample were 10°, allowing collection of WAXS data in the range of $7° < 2\theta < 55°$. In the SAXS mode, the long spacings (thickness of the repeating TAG bi-layers) of the fat

crystallites were measured. The average crystal thickness (ACT) was determined by the Scherrer line shape analysis of the first order diffraction peak (P. R. Ramel et al., 2016):

$$D = \frac{K\lambda}{FWHM \cos\theta}$$

where θ and λ are the Bragg angle and the X-ray wavelength, respectively. FWHM is the line width at half of the maximum peak height in radians corrected for instrumental broadening and was calculated using the EVA software from Bruker AXS. The instrumental line broadening is 2θ = 0.08°, which was determined using the FWHM of the 111 Si reflection of NIST standard reference material 640. *K* and λ are 0.9 and 0.15418 nm, respectively. The Scherrer equation indicates an inverse relationship between crystallite thickness and peak width: the broader the peak, the smaller the crystallites. The crystal thickness distribution (CTD) was determined using the Bertaut–Warren–Averbach (BWA) (Drits, Eberl, & Srodoi, 1998) analysis of the same, first order, diffraction peak.

4.2.6. Rheo-SAXS

The Rheo-SAXS measurements were carried out at the BM26 beamline at the European Synchrotron Radiation Source, Grenoble, France (Borsboom et al., 1998; Bras et al., 2003; Nikitenko et al., 2008; Portale et al., 2013). A home-built horizontal Couette shear- cell (Figure 4.1) allowed the X-ray beam to be directed along the vorticity direction of the flow at different positions across the gap between the inner and outer cylinders. A gap of 1 mm with 38 mm outer radius was used. A rotation speed was applied to the inner cylinder of the Rheo-SAXS cell. MFC dispersions were measured under constant shear for 10 minutes, after which another shear rate was imposed to the same sample. Shear rates applied to the same sample were 0, 1, 5, 35, 70, 100, 140, 1, and 0 s^{-1}. The beam cross-section at the sample position was about 120 μm, which allowed us to measure five different positions across the gap without overlap. We used the Pilatus detector with a resolution of 981×1043 pixels and a pixel size of 172×172 microns square positioned at a distance of 1400 mm away from sample for the SAXS measurements with a wavelength of λ = 1.033 Å. The experimental setup allowed us to probe length scales of the order of 4–210 nm. Standard corrections for sample absorption and background subtraction were applied. The data were normalized to the intensity of the incident beam to correct for primary beam intensity fluctuations and were

corrected for absorption and background scattering. AgBe has been used as a calibration standard.

To investigate the orientation of fat crystalline nanoplatelets, which have a platelet morphology, two-dimensional (2D) SAXS patterns were collected (Mazzanti, Guthrie, Sirota, Marangoni, & Idziak, 2003) (Mazzanti, Marangoni, & Idziak, 2009; Sato, Bayés-García, Calvet, Cuevas-Diarte, & Ueno, 2013). The orientation distribution was quantified using the integration of the low q region as a function of the azimuthal angle (χ). The data were fitted using a Gaussian function and the full width at half maximum, $\Delta\chi$, of the oriented portion and the preferential orientated azimuthal angle, χ_o, were estimated. A smaller $\Delta\chi$ indicates a higher degree of orientation of the lamellar planes.

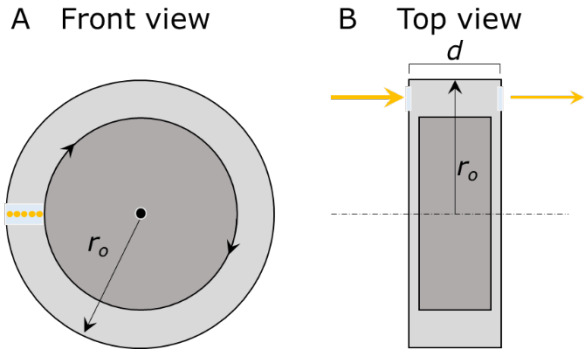

Figure 4.1 A schematic depiction (front **(A)** and top **(B)** views) of the homebuilt horizontal Couette shear-cell used to perform the Rheo-SAXS experiments. The outer radius of the Couette r_o was 38 mm and a gap size of 1 mm was used. The inner and outer surfaces were serrated. The rotation axis is shown by dot and dash-dot lines on the front and top views, respectively. The beam cross-section was about 120 µm at the sample position. The thickness of the sample d was 4 mm. The beam and cell windows are indicated by yellow dots and light blue rectangles, respectively.

4.2.7. USAXS

The USAXS measurements were performed at the ID02 beamline (Sztucki et al., 2008; Sztucki & Narayanan, 2007) at the European Synchrotron Radiation Facility (ESRF),

Grenoble, France. This USAXS configuration allows for a 30 m distance, which translates into the possibility to access scatterer sizes up to ~2.5 µm. The fractal dimensions were determined from USAXS data by means of the Unified Fit (UF) model (Peyronel, Ilavsky, Mazzanti, Marangoni, & Pink, 2013). Data processing was conducted in Igor Pro 6.37 using the Irena SAS 2.57 package. The USAXS signal of an oil sample was subtracted from the data before data modelling. The Unified Fit model provided two parameters for each structural level *i*: the Porod slope, P_i, and the radius of gyration, R_{gi}.

$$I_i(q) = \frac{B_i}{q^{P_i}} e^{\left(\frac{-q^2 {R_{gi-1}}^2}{3}\right)} \left[\mathrm{erf}\left(\frac{-qR_{gi}}{\sqrt{6}}\right)\right]^{3P_i}$$

where B_i is the Porod scale factor that contains specific surface area information (Peyronel et al., 2013; Peyronel, Quinn, Marangoni, & Pink, 2014). The Porod slope, P, provides information about the crystal surface and morphology and equals the fractal dimension if the system is known to be fractal (Peyronel, Ilavsky, Pink, & Marangoni, 2014; Peyronel, Pink, & Marangoni, 2014; David A Pink et al., 2015). For P smaller than 3 the fractal dimension equals P and relates to a mass fractal. Otherwise, the fractal dimension can be calculated as 6 − P and it indicates a surface fractal. The Guinier– Porod (GP) model based on known P and R_g was used to estimate the shape of scatterers from the parameter s (Peyronel et al., 2013; Peyronel, Pink, et al., 2014; Peyronel, Quinn, et al., 2014): s = 0 indicates a spherically symmetric structure, s = 1 a long cylinder indicating the presence of TAGwoods, and s = 2 a thin 2D structure:

$$I(q) = \frac{G}{q^s} \exp\left(\frac{-q^2 {R_g}^2}{3 - S}\right)$$

where G is the Guinier factor.

4.3. Results and discussion

4.3.1. Nanoscale and mesoscale characterization

WAXS diffractograms showed that fat nanoplatelets in MFC dispersions occur in the β polymorph (Figure S4.1, supplementary material). This is in line with the β polymorph observed in dispersions prepared by melting-cooling, hereafter referred to as MC dispersions. We note that in the MFC powder the fat nanoplatelets were in the β′ polymorph, but upon dispersion in sun flower oil and storage under ambient conditions (~20 °C) rapid (hours) conversion to the β form occurred. The predominance of the β polymorph in aged MC and MFC dispersions relates to high levels of saturated triglycerides that have a preference to crystallize in this stable form. The average fat crystal thickness (ACT) in MFC and MC dispersions was obtained by modelling the first order diffraction line recorded in SAXS by means of the Scherrer equation 9 (Table 4.1). On increasing the MFC concentration, the ACT decreases from 66 to 52 nm. Comparison of the ACT in MC *vs.* MFC dispersions revealed thinner crystalline nanoplatelets in the latter, which can be attributed to more rapid crystallisation during micronisation.

We used the Guinier–Porod (GP) and the Unified Fit (UF) models to retrieve mesoscale structural information (Peyronel, Ilavsky, et al., 2014; Peyronel, Pink, et al., 2014; Peyronel, Quinn, et al., 2014; David A. Pink et al., 2013) from the USAXS curves (Figure S4.2, supplementary material). In the q range $0.02 < q < 0.1$ nm^{-1}, which was representative for the nano- and mesoscale of fat crystal networks (Peyronel, Ilavsky, et al., 2014; Peyronel, Pink, et al., 2014), we observed a Porod slope $P_1 = 3.2$ for 20% MFC dispersions. This indicated the presence of nanoplatelets with a rough surface (surface fractal dimension $D_s = 2.8 \pm 0.1$, $R_{g1} = 62 \pm 3$ nm). For the 20% MC dispersions the Porod slope was $P_1 = 3.6$ (surface fractal dimension $D_s = 2.4 \pm 0.1$, $R_{g1} = 114 \pm 4$ nm), which indicated the presence of nanoplatelets with a less rough surface.

The next structural level observed by USAXS was in the range of $0.002 < q < 0.02$ nm^{-1}, which covers crystal aggregates up to 2 μm. At this structural level the GP model was used to estimate the shape of scatterers from the parameter *s* (Peyronel et al., 2013; Peyronel, Pink, et al., 2014).

Table 4.1 Overview of structural parameters derived from 20% MFC and MC dispersions by means of WAXS, SAXS and USAXS using the Scherrer equation (SE) to the first order diffraction line, the Unified Fit (UF) and Guinier–Porod (GP) models. The UF model covered two structural levels and provided the Porod slope, P, and the radius of gyration, R_g for each of them. For fractal systems the Porod slope, P, equals a mass fractal dimension (D_m) if P is smaller than 3 (Peyronel, Ilavsky, et al., 2014; Peyronel, Pink, et al., 2014; David A Pink et al., 2015). Otherwise, the fractal dimension can be calculated as 6 − P indicating a surface fractal (D_s)

		***q* range [nm^{-1}]**		**MFC**	**MC**
WAXS			Polymorph	*β*	*β*
SAXS	SE*		ACT [nm]	52±0.3	82±0.3
USAXS	UF*	0.02< q < 0.1	P_1	3.2±0.1	3.6±0.1
		(level 1, i=1)	D_s	2.8±0.1	2.4±0.1
			R_{g1} [nm]	62 ±3	114±4
		0.002 < q < 0.02	P_2 (D_m)	2.4±0.1	1.8±0.1
		(level 2, i=2)			
	GP*	0.002 < q < 0.02	s	2.4±0.1	1.8±0.1

Here s = 0 indicates a spherically symmetric structure, s = 1 a long cylinder or a fibrillar structure indicating the presence of well-stacked nanoplatelets, and s = 2 a thin 2D structure. We obtained values of s = 2.4 ± 0.1 and s = 1.8 ± 0.1 for MFC and MC dispersions, respectively. The low value of s for MC dispersions indicated the presence of TAGwoods, which were likely to form due to the significant amount of tripalmitin (PPP) (Table S4.1, supplementary material). Under slow crystallization conditions PPP can form pure and

smooth crystals, which are prone to stack into TAGwoods (Peyronel, Ilavsky, et al., 2014; Peyronel, Pink, et al., 2014; D. A. Pink et al., 2017; P. R. Ramel et al., 2016). The higher *s* values for MFC dispersions can be explained by rapid crystallisation during supercritical melt micronisation (ScMM). This process induces growth of mixed MFC nanoplatelets with rough surfaces, which are less prone to stacking interactions and formation of TAGwoods.

4.3.2. Micron-scale characterisation

We investigated the microstructure of MCF and MC dispersions by non-invasive confocal Raman imaging. Micron-scale compositional maps of solid fat (Martens et al., 2018; van Dalen et al., 2017) are shown in Figure 4.2. The MC dispersions were made up of aggregates of 15–20 micrometres, while in MFC dispersions, nanoplatelets were clustered into aggregates with sizes in the range of 5–10 micrometres. These MFC aggregates appear to be randomly distributed in space. The compositional maps (Martens et al., 2018; van Dalen et al., 2017) showed that the solid fat content (SFC) of the aggregates was of the order of 30–33%, indicating a highly porous structure. The continuous oil phase showed the presence of 13–18% SFC, although no aggregates could be discerned there. The presence of solid fat in the continuous phase suggested the existence of a weak-link network between the randomly distributed aggregates in the MFC dispersion.

4.3.3. Fractal network characterisation

Mass fractal dimensions (D_m) were determined by USAXS and small deformation rheology. From USAXS measurements we estimated D_m based on the Porod slope in the $0.002 < q < 0.02$ nm^{-1} range using the UF model (Table 4.1). For MFC dispersions a value of $D_m = 2.4 \pm 0.1$ was obtained, which was independent of the MFC concentration (data not shown). The mass fractal dimension of MFC networks is significantly higher than that observed for MC dispersions where we obtained $D_m = 1.8 \pm 0.1$ (Table 4.1), which is in line with values reported in the literature for dispersions prepared from the melt (Peyronel, Ilavsky, et al., 2014; Peyronel, Quinn, et al., 2014). We also obtained mass fractal dimensions by modelling the dependency of the storage modulus on MFC level by means of the weak-link formalism (S. S. Narine & Marangoni, 1999; Shih et al., 1990). Thus, for MFC dispersions $D_m = 2.7 \pm 0.14$ was determined. Differences between the mass fractal dimensions D_m obtained by USAXS and rheology have been observed previously (David A Pink et al., 2015). These

differences have been attributed to differences in modelling approaches and underlying assumptions considered to determine the fractal dimension based on different experimental techniques. These pertain to different length scales observed by USAXS and rheology and the assumption of self-similarity of fat crystal networks and the weak-link scaling theory (Shih et al., 1990) to describe small deformations in rheology.

The lower fractal dimension for MC dispersions indicates that cluster–cluster aggregation mechanisms such as Reaction or Diffusion-Limited Cluster–Cluster Aggregation (RLCCA or DLCCA) are at play (Meakin, 1999; Meakin & Family, 1988; Peyronel, Pink, et al., 2014; David A Pink et al., 2015; P. R. Ramel et al., 2016). Such mechanisms are in line with the previously observed stacking of nanoplatelets in TAGwoods (D. A. Pink et al., 2017). The aggregation of TAGwoods will then form networks with a low fractal dimension ($D_m < 2$) (Peyronel, Ilavsky, et al., 2014; Peyronel, Pink, et al., 2014). The nanoplatelets that are dispersed in MFC dispersions have rough surfaces, which will impede stacking interactions between them. In this case, Reaction-Limited particle–cluster and Cluster–Cluster Aggregation (RLA and RLCCA) are likely aggregation mechanisms because many collisions between particles or pairs of fat clusters are required before forming a larger aggregate. This will lead to mass fractals of the order of 2.5–3, which is close to the observed values by USAXS ($D_m = 2.4 \pm 0.1$) and rheology ($D_m = 2.7 \pm 0.14$).

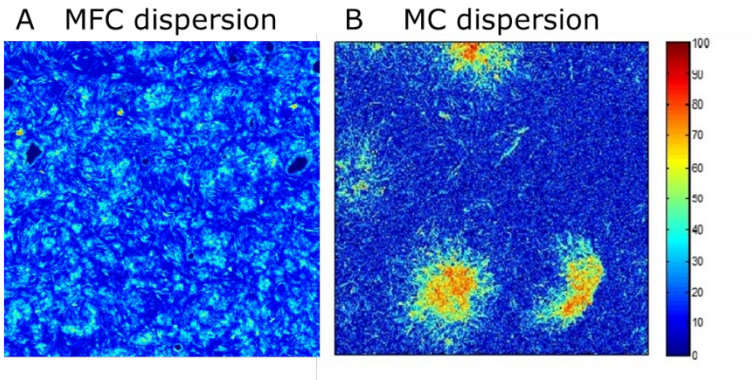

Figure 4.2 The spatial distribution of solid fat of 20% dispersions of (A) MCF and (B) MC in oil as obtained by MCR on confocal Raman images (200 × 200 μm, 843 × 843 spectra). The bar on the right-side indicates the amount of solid fat in percentage.

4.3.4. Impact of shear on storage modulus and yield stress

To understand the effect of shear on the MFC network structure we assessed its impact on elastic and yield stress properties. Rheology measurements by oscillation sweep experiments were conducted on aged MCF dispersions in a cone-plate configuration. These dispersions were subjected to preshear treatment, with shear rates ranging from 0.1 to 140 s^{-1}. The storage modulus G' was obtained in the linear viscoelastic region (LVR) as a function of the pre-shear rate (Figure 4.3(A)).

We observed that the pre-shear treatment leads to a significant decrease of the storage modulus G' for all the studied MFC concentrations (5, 10, 15 and 20 wt%). We also measured the yield stress as a stress value at the limit of linearity of shear storage modulus G' (Marangoni & Rogers, 2003) (Figure 4.3(B)). The yield stress of the MFC dispersions significantly decreased after pre-shear. We also performed velocity bifurcation measurements to investigate the yield stress properties of MFC dispersions after applying different shear rates (P Coussot, Nguyen, Huynh, & Bonn, 2002; de Kort et al., 2016) (Figure S4.3, supplementary material) and a similar result was obtained.

We used rheo-MRI velocimetry to provide a non-invasive view of the shear strength and time-dependence of the loss of yield stress properties in MFC dispersions. For this purpose, we monitored 10% MFC dispersions in a Couette geometry with a 1 mm gap for an hour at fixed shear rates, which were varied from 0.25 to 62.38 s^{-1}. Velocity profiles were collected as a function of position in a 1 mm thick slice of the material. MRI-velocity profiles as a function of shear rate can be found in the ESI (Figure S4.4, supplementary material). Figure 4.4(A) shows the changes of velocity over the gap at an applied shear rate of 6.24 s^{-1} as a function of time. Over time, all the obtained velocity profiles showed a flowing and a static region. We attributed this shear banding behaviour to a combination of heterogeneity of stress over the gap and the presence of a yield stress fluid. The yield stress can be estimated from the constitutive relation $\sigma(\dot{\gamma})$, also known as the local flow curve (G. Ovarlez et al., 2008; Guillaume Ovarlez et al., 2015). Figure 4.4(B) shows how local flow curves changed over 1 hour under a constant shear of 6.24 s^{-1}. We used the Herschel–Bulkley model (P. Coussot, Tocquer, Lanos, & Ovarlez, 2009; Hollingsworth & Johns, 2004) to fit the local flow curves and to estimate the apparent yield stress of the MFC dispersion. Structure degradation was apparent as a shift of the local flow curves towards lower stress values.

(A)

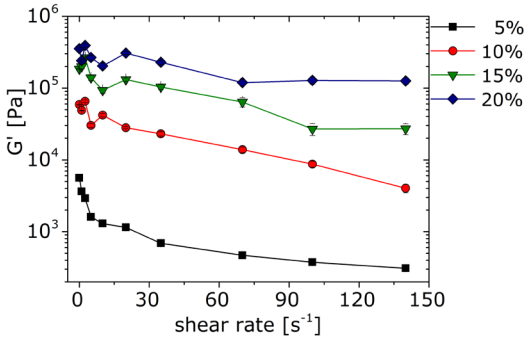

(B)

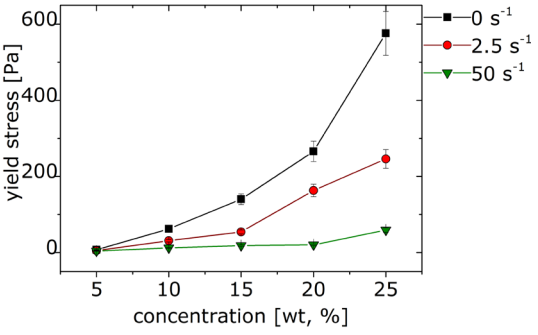

Figure 4.3 (A) Shear storage modulus G' as function of the pre-shear rate (0.1–140 s^{-1}) for MFC dispersions with solid fat concentrations of 5 (□), 10 (○), 15 (∇) and 20 (◊) %. **(B)** Effect of pre-shear (0, 2.5, and 50 s^{-1}) on yield stress as a function of MFC concentration (solids fraction). A constant shear rate was applied to the sample for 60 seconds before the measurement of shear storage modulus G' and yield stress. The lines connecting the data points are given for eye guidance

The fits of the Herschel– Bulkley model indicated that this was largely due to a decrease of the yield stress in the flowing band. Note that in the local flow curve only the flowing part of the velocity profile is represented; throughout the measurements the static band slowly

decreased in width. A continuous disruption of the crystal network at the applied shear rate of 6.24 s^{-1} occurred over a time frame of an hour. This continuous disruption was also observed at higher shear rates (data not shown).

(A)

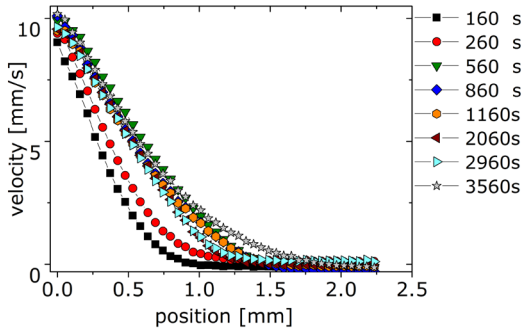

(B)

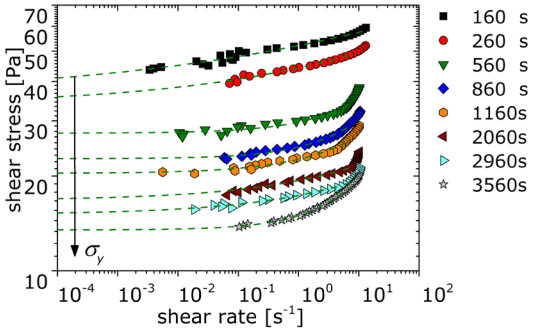

Figure 4.4 MRI-velocity profiles **(A)** and local flow curves **(B)** for a dispersion of 10% MFC in oil under a shear rate of 6.24 s^{-1} as a function of time. For every experiment, a new sample was taken and monitored for 1 hour at a fixed applied shear rate. Rheo-MRI velocity profiles (coexistence of a flowing and a static region) and local flow curves demonstrate yield stress behaviour of MFC dispersions over 1 hour. Dotted green lines in (B) are fits of the Herschel–Bulkley model to the local flow curves. The arrow schematically indicates the loss of yield stress of the MFC network.

The rheology and rheo-MRI experiments demonstrated that shear leads to a significant and continuous disruption of MFC networks at a time scale of an hour. In the next section the underlying microstructural changes are investigated.

4.3.5. Impact of shear on network fractal dimension

To further understand the effect of shear on the MFC network structure we assessed the impact on fractal dimensions. Monitored by rheology, Raman imaging and USAXS, the changes of the fractal dimensions upon shear are small and within standard experimental error for every applied technique (Figure 4.5). The data indicated a weak trend towards an increased fractal dimension upon the application of low shear, suggesting that the distribution of the structural elements became more random. Overall, the data showed that the fractal dimensions D of the MFC network were not sensitive to mild shear (<140 s^{-1}) and stayed invariant. Average fractal dimensions obtained by the confocal Raman imaging, rheology or USAXS were statistically different, in line with previous observations that these techniques probe fractality at different length scales (David A Pink et al., 2015).

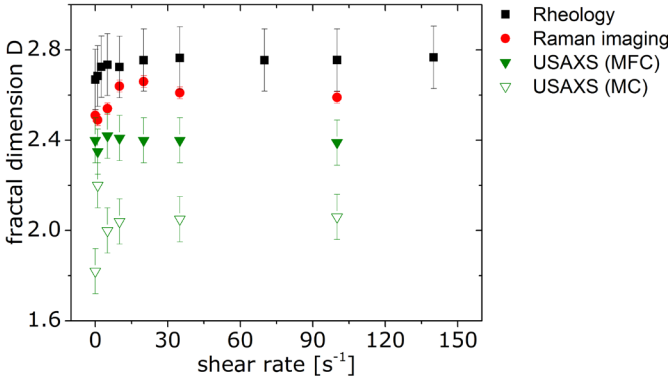

Figure 4.5 Fractal dimensions (D) of aged MFC dispersions as a function of pre-shear rates. Black squares represent the D values obtained by rheology using the colloidal gel fractal theory; red circles and green triangles, respectively, describe D values obtained by Raman imaging and USAXS for a 10% MFC dispersion. Empty green triangles show the D values obtained by USAXS for a 10% MC fat crystal dispersion.

Next, we assessed whether the sizes of MFC aggregates were affected by shear. Raman imaging showed that these MFC aggregates were between 5 and 10 μm, which were invariant to shear. USAXS showed no changes in scattering (Figure S4.5, supplementary material) in a wide length scale (0.005–2.5 μm). No fat crystal stacks or aggregates with radius of gyration R_g below 2.5 μm could be identified. This is either the effect of ageing, in which case the clusters have grown larger, or due to heterogeneous size distribution, such that statistically the scattering function is smeared by a multitude of scatters of different sizes. However, Raman imaging and USAXS data demonstrated that applying shear does not lead to significant destruction of structure in the range of 1–10 micrometres.

4.3.6. Impact of shear on the sub-micron fat crystal network

In order to investigate whether shear has an impact on submicron structures we pursued our investigations by Rheo-SAXS. 2D SAXS patterns were collected in the initial unperturbed state and under the application of shear. We did not notice effects of applied shear on the transmission coefficient *s* (Figure S4.7, supplementary material), indicating that the effects of melting or dissolution were negligible. The selected 2D patterns shown in Figure 4.6 were taken from an oil dispersion containing 20% of MFC under the starting conditions (A) and at shear rates of 5 s^{-1} (B) and 70 s^{-1}(C). For further discussions we focused on the first order diffraction peak at q = 1.5994 nm^{-1}, which is indicated in Figure 4.6. q-Dependencies of the scattered intensity can be founded in the ESI (Figure S4.6, supplementary material). The first SAXS pattern for MFC dispersions under the starting static conditions (Figure 4.6(A)) clearly showed an isotropic diffraction peak characteristic of randomly, non-oriented material. Under imposed shear we obtained 2D SAXS patterns that revealed structural anisotropy (Figure 4.6(B) and (C)), indicating that scattering structures were oriented along a preferred direction during the application of shear. The observed alignment under the shear rate was in line with Peclet number estimates (Maleky, 2015; Mazzanti et al., 2003) of Pe > 10 for MFC nanoplatelets with length/widths of 200–400 nm at shear rates in the $1–10^2$ s^{-1} range. Considering that MFC aggregates up to 2.5 μm were not affected by shear, the scattering structures that align must be MFC platelets that were not part of an aggregate.

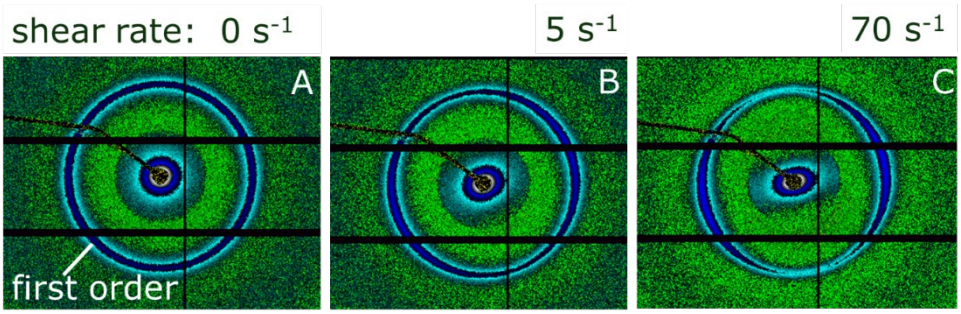

Figure 4.6 Selected 2D SAXS patterns for a 20% MFC dispersion in oil at shear rates of 0 **(A)**, 5 **(B)** and 70 **(C)** s^{-1}, respectively. The black spot in the center of the image is the beam stop to protect the detector from direct X-ray exposure and the black stripes correspond to the physical gaps of the detector.

We took the radial integral of the 2D patterns at q = 1.5994 nm^{-1} to estimate the amount of oriented crystal nanoplatelets. Figure 4.7(A) shows the integration of 2D SAXS patterns of a 20% MFC dispersion obtained under shear rates in the range between 1 and 140 s^{-1}. Here we monitored the number of oriented MFC nanoplatelets as a function of azimuthal angle χ extension. Two peaks with a separation of 180° (Figure 4.7(A)) represented the oriented nanoparticles along the flow direction. Under the starting static conditions (0 s^{-1}) already some alignment can be observed, likely due to manipulation of the sample into the shear cell. On increasing the shear rate the intensity of anisotropic peaks on χ extension increased, which was reflected in a decrease of Δχ (Figure 4.7(B)). This can be explained by shear induced disruption of the weak MFC network in the continuous phase and subsequent orientation of the released platelets along the shear field. The degree of orientation (alignment) of the MFC nanoplatelets slightly changed at different shear rates (Figure 4.7(A)). Fits of the χ extension patterns by a Gaussian function provided estimates of the preferential orientated azimuthal angle χ_o (Figure S4.8, supplementary material). The degree of alignment of MFC nanoplatelets depended on the strength of applied shear and showed the same trend for all the studied concentrations of MFC dispersions. On the variation of shear rate from 1–140 s^{-1} the degree of alignment changed to approximately 150°. We attribute this small deviation from full alignment of platelets with the flow direction at low shear rates to a small degree

of platelet stacking (Brown & Rennie, 2000). On increasing the shear rate the MFC nanoplatelets fully aligned to the flow direction, indicating loss of the residual stacking interactions.

(A)

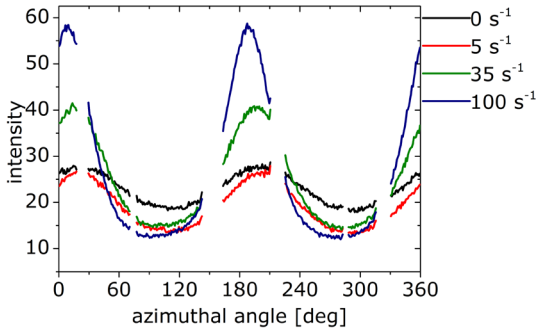

(B)

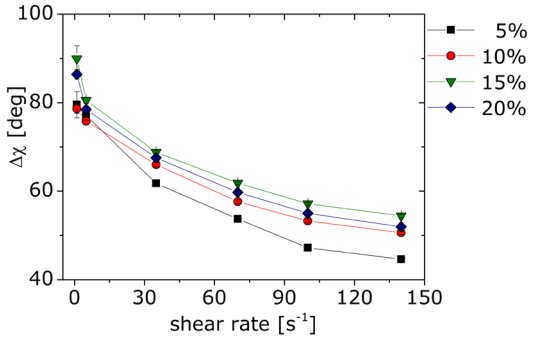

Figure 4.7 (A) Azimuthal angle χ extension patterns from radial intensity averaging of 2D SAXS patterns at q = 1.5994 nm^{-1}. The χ extension patterns show intensity changes for a 20% MFC dispersion at shear rates of 0, 1, 5, 35, 70, 100, 140, 1, and 0 s^{-1}, which were applied for 10 min one after the other. The variation of shear rates was indicated by different colors. The missing points correspond to the physical gaps of the detector. In **(B)** the full width at half maximum Δχ is shown as a function of shear rate (0–140 s^{-1}) for MFC dispersions with solid fat contents of 5 (□), 10 (○), 15 (∇) and 20% (◊).

4.3.7. Shear-induced recrystallisation in MFC networks

Figure 4.8(A) shows that the ACTs increased for all the studied dispersions when shear was applied (1–140 s^{-1}). At the minute time scale of the rheo-SAXS experiment the increase of ACTs occurred immediately.

(A)

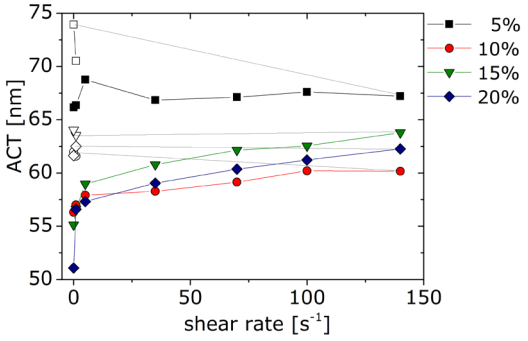

(B)

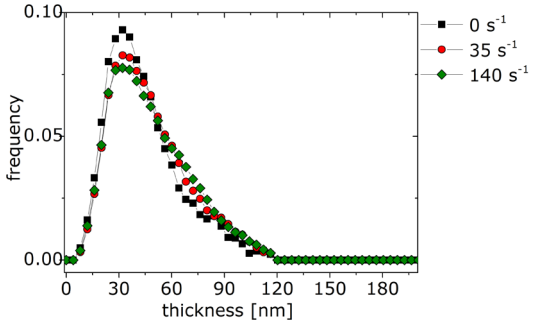

Figure 4.8 (A) Average Crystal Thickness (ACT) as a function of shear rates 0, 1, 5, 35, 70, 100, 140, 1, and 0 s^{-1}, which were applied to 5 (□), 10 (○), 15 (∇) and 20% (◊) MFC dispersions for 10 minutes one after the other. Empty symbols show the ACT values for the last two steps 1 and 0 s^{-1} of the shear protocol. **(B)** Crystal Thickness Distribution (CTD) of fat nanoplatelets obtained after preshear (0, 35 and 140 s^{-1}) of a 20% MFC dispersion for 1 minute.

After the application of shear and returning to the static conditions, the ACTs remained the same. To verify whether the ACT values originated from a unimodal distribution, we assessed the impact of shear on the crystal thickness distribution (CTD). Figure 4.8(B) shows CTDs for a 15% MFC dispersion under static conditions and at shear rates of 35 and 140 s^{-1}. In all cases we observed unimodal distributions and a tendency of the CTD to shift towards larger crystal thicknesses with increasing shear. This is in line with rapid Ostwald ripening, where the thinner MFC nanoplatelets dissolve and recrystallize on the existing nanoplatelets from the weak-link net preferably and likely also on top of the outer nanoplatelets of MFC aggregates (Figure 4.9).

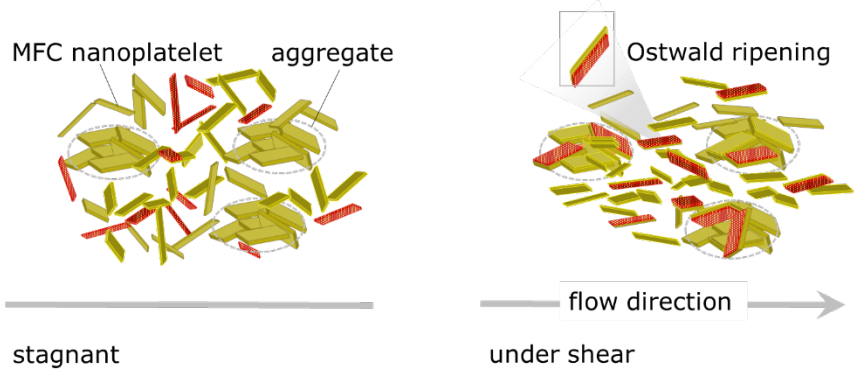

Figure 4.9 Schematic drawing of MFC networks under static and shear conditions. The networks consist of aggregates and a continuous weak-link net of crystalline nanoplatelets. Thin nanoplatelets are indicated in red. Applying shear leads to Ostwald ripening and an alignment of nanoplatelets from the weak-link net along the flow direction. Ostwald ripening is depicted as recrystallisation of thin (red) nanoplatelets onto thicker ones.

In the networks grown under static conditions, the thin platelets are kinetically trapped in a metastable state, until their release by mild shear. This offers opportunities for stabilizing water-droplet interfaces during the manufacturing of fat-continuous food emulsions, and thus more effective use of solid fat crystals. Hence, besides process simplification by decoupling fat crystallization, network formation and emulsification, also lower fat levels may be achieved.

4.4. Conclusions

Under static conditions, MFC dispersions form a weak-link network organized by aggregates connected by a continuous net of dispersed nanoplatelets. During network formation the rough MFC surfaces impede stacking interactions and the formation of TAGwoods. The MFC network fractal dimension (D = 2.4, USAXS) is higher than that for networks formed from the melt (D = 1.8–2.2, USAXS), indicating that the particle– cluster mechanism of aggregation is dominant. Rheo-MRI measurements show that under shear yield stress is slowly lost. The application of shear does not affect the size of the MFC aggregates, but does induce the release of nanoplatelets from the weak-link continuous net and subsequent alignment along the flow direction. The network grown under static conditions is metastable; under shear, rapid recrystallisation of the thinner nanoplatelets occurs. The presence of thin platelets in a metastable network grown under static conditions offers opportunities for simplified formulation and processing routes for the manufacturing of low-fat food products.

Acknowledgements

The authors thank Daan de Kort for advice on the rheo-MRI experiments and Karlijn Theunissen for skilfully performing the rheology measurements. Koen Martens and Patricia Heussen are gratefully acknowledged for measuring the confocal Raman images. The authors thank Kees van Malssen, Jan Wieringa, Jo Janssen, Michiel Meeuse and Peter de Groot from Unilever Discover Vlaardingen for fruitful discussions. The authors thank Wim Bras (NWO) and Gerrit Peters (TUE) for advice on the design of the rheo-SAXS cell. The authors thank the Delft workshop at Delft University of Technology for designing the rheo-SAXS shear cell. The USAXS and Rheo-SAXS experiments were, respectively, performed on beamlines ID02 and BM26 at the European Synchrotron Radiation Facility (ESRF), Grenoble, France. The authors thank T. Narayanan and M. Sztucki for support during experiments on the ID02 beamline at ESRF. This work is part of the research programme SSCANFOODS (project number 13386), which is financed by the Netherlands Organisation for Scientific Research (NWO).

References

Acevedo, N. C., & Marangoni, A. G. (2010). Toward nanoscale engineering of triacylglycerol crystal networks. *Crystal Growth and Design*, *10*(8), 3334–3339. https://doi.org/10.1021/cg100469x

Acevedo, N. C., & Marangoni, A. G. (2014). Nanostructured Fat Crystal Systems. *Annual Review of Food Science and Technology*, *6*, 1–26. https://doi.org/10.1146/annurev-food-030713-092400

Bell, A., Gordon, M. H., Jirasubkunakorn, W., & Smith, K. W. (2007). Effects of composition on fat rheology and crystallisation. *Food Chemistry*, *101*(2), 799–805. https://doi.org/10.1016/j.foodchem.2006.02.033

Bird, R. B. (1987). *Dynamics of polymeric liquids. Vol. 2, Vol. 2,*. New York; Chichester: Wiley.

Borsboom, M., Bras, W., Cerjak, I., Detollenaere, D., Glastra van Loon, D., Goedtkindt, P., … Vlieg, E. (1998). The Dutch–Belgian beamline at the ESRF. *Journal of Synchrotron Radiation*, *5*(3), 518–520. https://doi.org/10.1107/S0909049597013484

Bot, A., & Floter, E. (2013). *Application of Edible Oils*. (W. Hamm, R. J. Hamilton, & G. Calliauw, Eds.) (second edi). Chichester, UK: John Wiley & Sons. https://doi.org/10.1002/9781118535202.ch8

Bras, W., Dolbnya, I. P., Detollenaere, D., van Tol, R., Malfois, M., Greaves, G. N., … Heeley, E. (2003). Recent experiments on a small-angle/wide-angle X-ray scattering beam line at the ESRF. *Journal of Applied Crystallography*, *36*(3), 791–794. https://doi.org/10.1107/S002188980300400X

Brown, A. B. D., & Rennie, A. R. (2000). Monodisperse colloidal plates under shear. *Physical Review E - Statistical Physics, Plasmas, Fluids, and Related Interdisciplinary Topics*, *62*(1 B), 851–862. https://doi.org/10.1103/PhysRevE.62.851

Callaghan, P. T. (2011). *Translational Dynamics and Magnetic Resonance: Principles of Pulsed Gradient Spin Echo NMR*. Oxford: Oxford University Press. https://doi.org/10.1093/acprof:oso/9780199556984.001.0001

Campos, R., Ollivon, M., & Marangoni, A. G. (2010). Molecular Composition Dynamics and Structure of Cocoa Butter. *Crystal Growth & Design*, *10*(1), 205–217. https://doi.org/10.1021/cg900853e

Coussot, P., Nguyen, Q. D., Huynh, H. T., & Bonn, D. (2002). Viscosity bifurcation in thixotropic, yielding fluids. *Journal of Rheology*, *46*(3), 573. https://doi.org/10.1122/1.1459447

Coussot, P., Tocquer, L., Lanos, C., & Ovarlez, G. (2009). Macroscopic vs. local rheology of yield stress fluids. *Journal of Non-Newtonian Fluid Mechanics*, *158*(1–3), 85–90. https://doi.org/10.1016/j.jnnfm.2008.08.003

Coussot, P, Nguyen, Q. D., Huynh, H. T., & Bonn, D. (2002). Avalanche behavior in yield stress fluids. *Physical Review Letters*, *88*(17). https://doi.org/10.1103/PhysRevLett.88.175501

Coussot, Philippe. (2005). *Rheometry of pastes, suspensions, and granular materials : applications in industry and environment*. Hoboken, N.J.: Wiley.

de Kort, D. W., Veen, S. J., Van As, H., Bonn, D., Velikov, K. P., & van Duynhoven, J. P. M. (2016). Yielding and flow of cellulose microfibril dispersions in the presence of a charged polymer. *Soft Matter*, *12*(21), 4739–4744. https://doi.org/10.1039/C5SM02869H

Dhonsi, D., & Stapley, A. G. F. (2006). The effect of shear rate, temperature, sugar and emulsifier on the tempering of cocoa butter. *Journal of Food Engineering*, *77*(4), 936–942. https://doi.org/10.1016/j.jfoodeng.2005.08.022

Drits, V. A., Eberl, D. D., & Srodoi, J. I. (1998). XRD Measurement of Mean Thickness, Thickness Distribution and Strain for Illite and Illite-Smectite Crystallites by the Bertaut-Warren-Averbach Technique. *Clays and Clay Minerals*, *46*(1), 38–50. https://doi.org/10.1346/CCMN.1998.0460105

Gonzalez-Gutierrez, J., & Scanlon, M. G. (2012). Rheology and mechanical properties of fats. In A. G. Marangoni (Ed.), *Structure-function analysis of edible fats* (pp. 127–172). AOCS Press. Retrieved from http://www.researchgate.net/publication/245542288_Rheology_and_Mechanical_Properties_of_Fats/file/5046351d80462bdd29.pdf

Hartel, R. W. (2013). Advances in Food Crystallization. *Annu. Rev. Food Sci. Technol*, *4*, 277–292. https://doi.org/10.1146/annurev-food-030212-182530

Hollingsworth, K. G., & Johns, M. L. (2004). Rheo-nuclear magnetic resonance of emulsion systems. *Journal of Rheology*, *48*(4), 787. https://doi.org/10.1122/1.1753277

Macias-Rodriguez, B. A., & Marangoni, A. A. (2017). Linear and nonlinear rheological behavior of fat crystal networks. *Critical Reviews in Food Science and Nutrition*, 1–18. https://doi.org/10.1080/10408398.2017.1325835

Maleky, F. (2015). Nanostructuring triacylglycerol crystalline networks under external shear fields: A review. *Current Opinion in Food Science*, *4*, 56–63. https://doi.org/10.1016/j.cofs.2015.05.005

Marangoni, A. G. (2004). *Fat Crystal Networks*. CRC Press. https://doi.org/10.1201/9781420030549

Marangoni, A. G., & Rogers, M. A. (2003). Structural basis for the yield stress in plastic disperse systems. *Applied Physics Letters*, *82*(19), 3239–3241. https://doi.org/10.1063/1.1576502

Marangoni, A. G., & Wesdorp, L. (2013). *Structure and Properties of Fat Crystal*.

Martens, K. J. A., van Dalen, G., Heussen, P. C. M., Voda, M. A., Nikolaeva, T., & van Duynhoven, J. P. M. (2018). Quantitative Structural Analysis of Fat Crystal Networks by Means of Raman Confocal Imaging. *Journal of the American Oil Chemists' Society*. https://doi.org/10.1002/aocs.12035

Mazzanti, G., Guthrie, S. E., Sirota, E. B., Marangoni, A. G., & Idziak, S. H. J. (2003). Orientation and phase transitions of fat crystals under shear. *Crystal Growth and Design*, *3*(5), 721–725. https://doi.org/10.1021/cg034048a

Mazzanti, G., Marangoni, A. G., & Idziak, S. H. J. (2009). Synchrotron study on crystallization kinetics of milk fat under shear flow. *Food Research International*, *42*(5–6), 682–694. https://doi.org/10.1016/j.foodres.2009.02.009

Meakin, P. (1999). Historical introduction to computer models for fractal aggregates.

Journal of Sol-Gel Science and Technology, *15*(2), 97–117. https://doi.org/10.1023/A:1008731904082

Meakin, P., & Family, F. (1988). Structure and kinetics of reaction-limited aggregation. *Physical Review A*, *38*(4), 2110–2123. https://doi.org/10.1103/PhysRevA.38.2110

Münüklü, P., & Jansens, P. J. (2007). Particle formation of an edible fat (rapeseed 70) using the supercritical melt micronization (ScMM) process. *Journal of Supercritical Fluids*, *40*(3), 433–442. https://doi.org/10.1016/j.supflu.2006.07.015

Narine, S., & Marangoni, A. G. (1999). Fractal nature of fat crystal networks. *Physical Review E*, *59*(2), 1908–1920. https://doi.org/10.1103/PhysRevE.59.1908

Narine, S. S., & Marangoni, A. G. (1999). Microscopic and rheological studies of fat crystal networks. *Journal of Crystal Growth*, *198–199*(pt 2), 1315–1319. https://doi.org/10.1016/S0022-0248(98)01016-1

Nikitenko, S., Beale, A. M., Van Der Eerden, A. M. J., Jacques, S. D. M., Leynaud, O., O'Brien, M. G., … Bras, W. (2008). Implementation of a combined SAXS/WAXS/QEXAFS set-up for time-resolved in situ experiments. *Journal of Synchrotron Radiation*, *15*(6), 632–640. https://doi.org/10.1107/S0909049508023327

Ovarlez, G., Rodts, S., Ragouilliaux, A., Coussot, P., Goyon, J., & Colin, A. (2008). Wide-gap Couette flows of dense emulsions: Local concentration measurements, and comparison between macroscopic and local constitutive law measurements through magnetic resonance imaging. *Physical Review E - Statistical, Nonlinear, and Soft Matter Physics*, *78*(3), 1–13. https://doi.org/10.1103/PhysRevE.78.036307

Ovarlez, Guillaume, Bertrand, F., & Rodts, S. (2006). Local determination of the constitutive law of a dense suspension of noncolloidal particles through magnetic resonance imaging. *Journal of Rheology*, *50*(3), 259–292. https://doi.org/10.1122/1.2188528

Ovarlez, Guillaume, Mahaut, F., Deboeuf, S., Lenoir, N., Hormozi, S., & Chateau, X. (2015). Flows of suspensions of particles in yield stress fluids. *Journal of Rheology*, *59*(6), 1449–1486. https://doi.org/10.1122/1.4934363

Peyronel, F., Ilavsky, J., Mazzanti, G., Marangoni, A. G., & Pink, D. A. (2013). Edible oil structures at low and intermediate concentrations. II. Ultra-small angle X-ray scattering of in situ tristearin solids in triolein. *Journal of Applied Physics*, *114*(23). https://doi.org/10.1063/1.4847997

Peyronel, F., Ilavsky, J., Pink, D. A., & Marangoni, A. G. (2014). Quantification of the physical structure of fats in 20 minutes: Implications for formulation. *Lipid Technology*, *26*(10), 223–226. https://doi.org/10.1002/lite.201400051

Peyronel, F., Pink, D. A., & Marangoni, A. G. (2014). Triglyceride nanocrystal aggregation into polycrystalline colloidal networks: Ultra-small angle X-ray scattering, models and computer simulation. *Current Opinion in Colloid and Interface Science*, *19*(5), 459–470. https://doi.org/10.1016/j.cocis.2014.07.001

Peyronel, F., Quinn, B., Marangoni, A. G., & Pink, D. a. (2014). Ultra small angle x-ray scattering in complex mixtures of triacylglycerols. *Journal of Physics. Condensed Matter : An Institute of Physics Journal*, *26*(46), 464110. https://doi.org/10.1088/0953-8984/26/46/464110

Pink, D. A., Townsend, B., Peyronel, F., Co, E. D., & Marangoni, A. G. (2017). Sheared

edible oils studied using dissipative particle dynamics and ultra small angle X-ray scattering: TAGwood orientation aggregation and disaggregation. *Food Funct.* https://doi.org/10.1039/C7FO00514H

Pink, David A., Quinn, B., Peyronel, F., & Marangoni, A. G. (2013). Edible oil structures at low and intermediate concentrations. I. Modeling, computer simulation, and predictions for X ray scattering. *Journal of Applied Physics*, *114*(23). https://doi.org/10.1063/1.4847996

Pink, David A, Peyronel, F., Quinn, B., Singh, P., & Marangoni, A. G. (2015). Condensation versus diffusion. A spatial-scale-independent theory of aggregate structures in edible oils: applications to model systems and commercial shortenings studied via rheology and USAXS. *Journal of Physics D: Applied Physics*, *48*(38), 384003. https://doi.org/10.1088/0022-3727/48/38/384003

Piska, I., Zárubová, M., Loužecký, T., Karami, H., & Filip, V. (2006). Properties and crystallization of fat blends. *Journal of Food Engineering*, *77*(3), 433–438. https://doi.org/10.1016/j.jfoodeng.2005.07.010

Portale, G., Cavallo, D., Alfonso, G. C., Hermida-Merino, D., Van Drongelen, M., Balzano, L., … Bras, W. (2013). Polymer crystallization studies under processing-relevant conditions at the SAXS/WAXS DUBBLE beamline at the ESRF. *Journal of Applied Crystallography*, *46*(6), 1681–1689. https://doi.org/10.1107/S0021889813027076

Ramel, P. R., Co, E. D., Acevedo, N. C., & Marangoni, A. G. (2016). Structure and functionality of nanostructured triacylglycerol crystal networks. *Progress in Lipid Research*, *64*, 231–242. https://doi.org/10.1016/j.plipres.2016.09.004

Ramel, P. R. R., Peyronel, F., & Marangoni, A. G. (2016). Characterization of the nanoscale structure of milk fat. *Food Chemistry*, *203*, 224–230. https://doi.org/10.1016/j.foodchem.2016.02.064

Rousseau, D. (2000). Fat crystals and emulsion stability - A review. *Food Research International*, *33*(1), 3–14. https://doi.org/10.1016/S0963-9969(00)00017-X

Sato, K., Bayés-García, L., Calvet, T., Cuevas-Diarte, M. À., & Ueno, S. (2013). External factors affecting polymorphic crystallization of lipids. *European Journal of Lipid Science and Technology*, *115*(11), 1224–1238. https://doi.org/10.1002/ejlt.201300049

Sato, K., & Ueno, S. (2011). Crystallization, transformation and microstructures of polymorphic fats in colloidal dispersion states. *Current Opinion in Colloid and Interface Science*, *16*(5), 384–390. https://doi.org/10.1016/j.cocis.2011.06.004

Shih, W.-H., Shih, W., Kim, S.-I., Liu, J., & Aksay, I. (1990). Scaling behavior of the elastic properties of colloidal gels. *Physical Review A*, *42*(8), 4772–4779. https://doi.org/10.1103/PhysRevA.42.4772

Sztucki, M., Gorini, J., Vassalli, J. P., Goirand, L., Van Vaerenbergh, P., & Narayanan, T. (2008). Optimization of a Bonse-Hart instrument by suppressing surface parasitic scattering. *Journal of Synchrotron Radiation*, *15*(4), 341–349. https://doi.org/10.1107/S0909049508008960

Sztucki, M., & Narayanan, T. (2007). Development of an ultra-small-angle X-ray scattering instrument for probing the microstructure and the dynamics of soft matter. *Journal of Applied Crystallography*, *40*(SUPPL. 1), 459–462. https://doi.org/10.1107/S0021889806045833

Tran, T., & Rousseau, D. (2016). Influence of shear on fat crystallization. *Food Research International*, *81*, 157–162. https://doi.org/10.1016/j.foodres.2015.12.022

van Dalen, G., van Velzen, E. J. J., Heussen, P. C. M., Sovago, M., van Malssen, K. F., & van Duynhoven, J. P. M. (2017). Raman hyperspectral imaging and analysis of fat spreads. *Journal of Raman Spectroscopy*, (February), 1075–1084. https://doi.org/10.1002/jrs.5171

Zárubová, M., Filip, V., Kšandová, L., Šmidrkal, J., & Piska, I. (2010). Rheological and crystalline properties of trans-free model fat blends as affected by the length of fatty acid chains. *Journal of Food Engineering*, *99*(4), 459–464. https://doi.org/10.1016/j.jfoodeng.2008.08.030

Supplementary material

Table S4.1 The TAG composition of MFC.

TAG	%
PPP	16.82
LaLaLa	1.33
LaPP	9.73
LaLaMy	0.73
LaLaP	4.28
PLaP	5.60
POP	5.10
PPO	4.82
CyLaLa	0.33
LaMyLa	0.38
CiLaLa	0.49
MyPP	3.45
LaLaS	0.29
LaOP	2.96
PPS	2.32
PMyP	2.06

Table S4.2. FA composition of MFC and SF.

Fatty acid		**MFC**
Saturated, S (Cx:0):		82%
	Stearic acid; St (C18:0)	5%
	Palmitic acid; P (C16:0)	50%
	Myristic acid; M (C14:0)	7%
	Lauric acid; L (C12:0)	20%
Unsaturated; U (C18:x)		12%
Others		6%

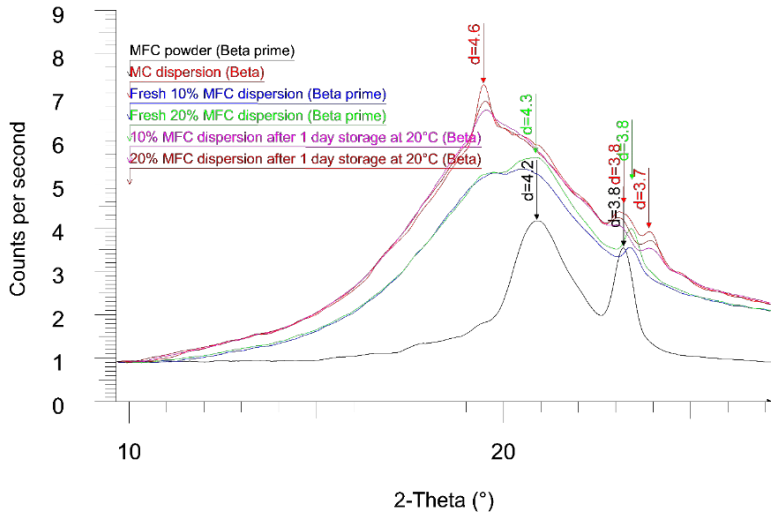

Figure S4.1. WAXS diffractograms of MFC powder, 10 and 20% MFC dispersions freshly dispersed and after 1 day of ageing and a MC dispersion obtained by heat-cooling the aforementioned 20% MC dispersions.

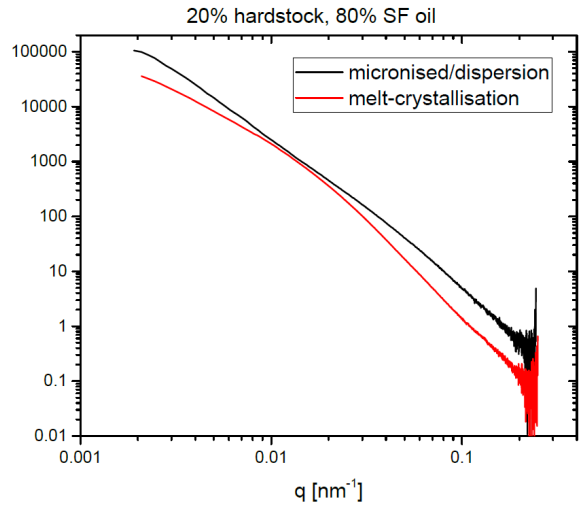

Figure S4.2. USAXS intensity as a function of scattering vector for 20% of MFC dispersions (black line) and MC dispersions (red line). Values of P and Rg obtained by the Unified Fit model are shown in Table 4.1.

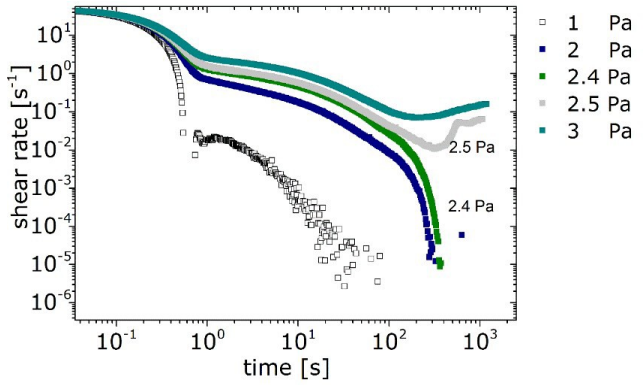

Figure S4.3. Viscosity bifurcation measurements on 5 % MFC dispersion in sandblasted 2° CP geometry. Before imposing constant stress, the dispersions were pre-sheared at 50 s^{-1} for 60s.

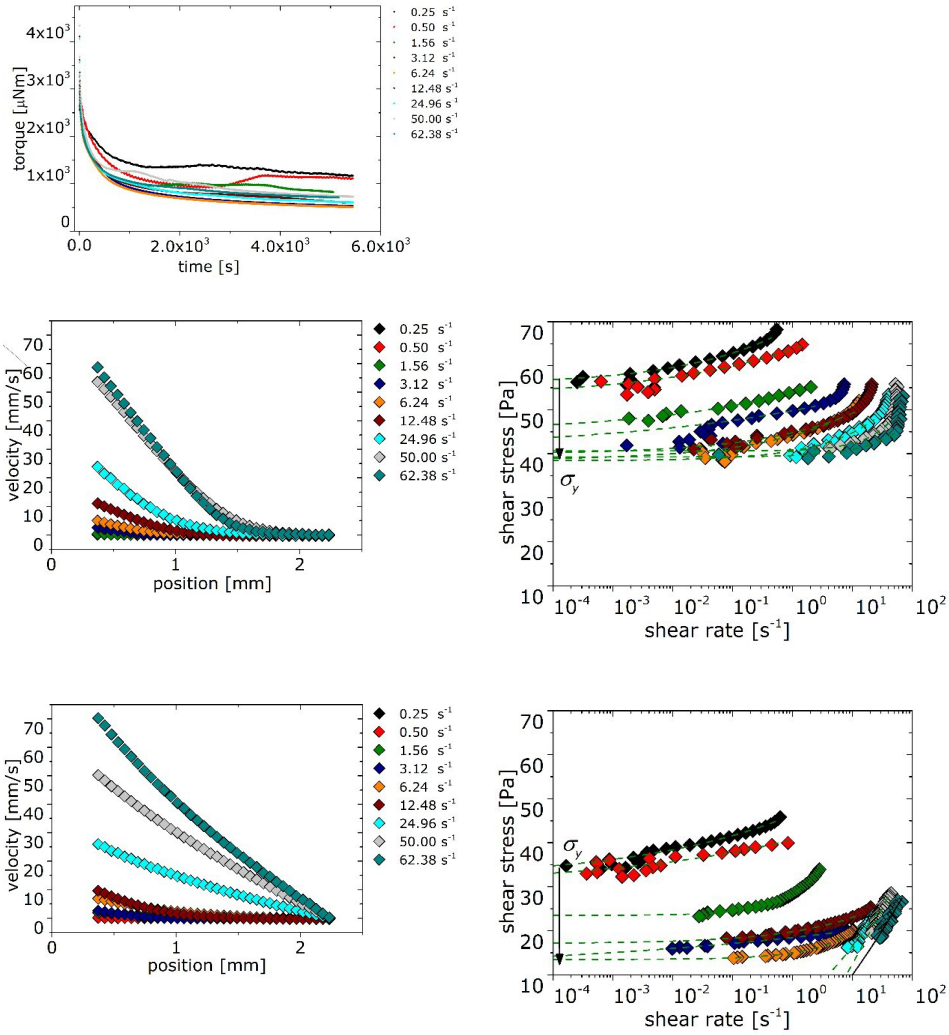

Figure S4.4. (A) Torque measurements over time for 10 % MFC dispersion at applied constant shear rate. Shear rates were varied in a range of 0.25 – 62.38 s^{-1}. (**B**) and (**C**) show the velocity profiles and local flow curves obtained at 260 s after a required shear rate was imposed. Thus, the banding of velocity curves, indicated a critical stress, decreased significantly with increasing shear rates (**B**). It showed the loss of strength of the fat crystal network, which can be observed on local flow curve plot (**C**). (**D**) and (**E**) present velocity profiles and flow curves of the same sample, which were collected at 3600 s after the applied shear. After 1 hour of continuous shear the banding of velocity curves is less pronounced or disappeared completely (**D**). the yield stress also decreased significantly with time (**E**).

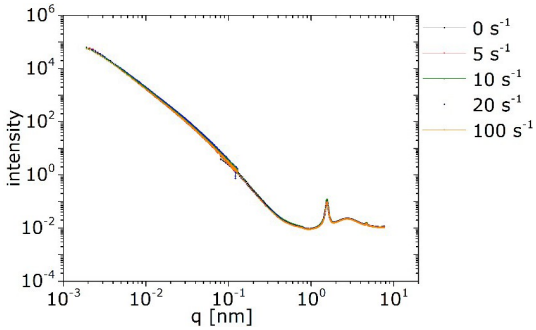

Figure S4.5. USAXS intensity as a function of scattering vector for 10% of MFC dispersions. The samples were pre-sheared at 0; 5; 10; 20; 100 s^{-1}, which were applied for 10 min after each other. The USAXS showed no changes in scattering.

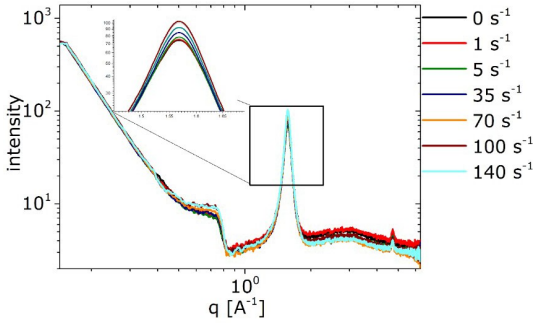

Figure S4.6. q-dependencies of the scattered intensity for fat crystal dispersion in oil at shear rate range 0-140 s^{-1} for 15% fat crystal dispersion. The shear rates 0; 1; 5; 35; 70; 100; 140; 1; 0 s^{-1} were applied for 10 min after each other.

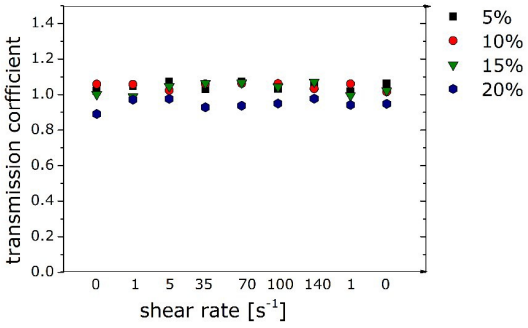

Figure S4.7. Transmission coefficient as a function of shear rates during Rheo-SAXS experiments. MFC dispersions with solid fat contents of 5 (□), 10 (o), 15 (∇) and 20 (◊) %

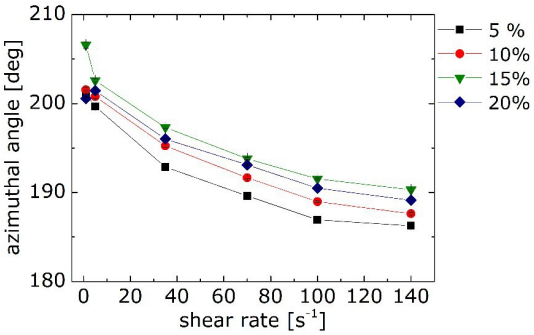

Figure S4.8. Azimuthal angle χ extension patterns from radial intensity averaging of 2D SAXS patterns at q=1.5994 nm^{-1}. The χ extension patterns show intensity changes for 20% MFC dispersion at shear rates 0; 1; 5; 35; 70; 100; 140; 1; 0 s^{-1}, which were applied for 10 min after each other. Fit of χ extension patterns by a Gaussian function gave an estimate of the preferential orientated azimuthal angle χ_o and the full width at half maximum $\Delta\chi$ (Figure 4.7 B) as a function of shear rate (0-140 s^{-1}) for MFC dispersions with solid fat contents of 5 (□), 10 (o), 15 (∇) and 20 (◊) %. Lines have been drawn through the points to aid the eye.

CHAPTER 5

Manipulation of recrystallization and network formation of oil-dispersed micronized fat crystals

This chapter has been published as T. Nikolaeva, R. den Adel, R. van der Sman, K. J. A. Martens, H. Van As, A. M. Voda and J. van Duynhoven (2019). Manipulation of Recrystallization and Network Formation of Oil-Dispersed Micronized Fat Crystals. Langmuir, 2019, 35, 6, 2221-2229. https://doi.org/10.1021/acs.langmuir.8b03349

Abstract

A detailed investigation was carried out on the modulation of the coupling between network formation and the recrystallization of oil-dispersed micronized fat crystal (MFC) nanoplatelets by varying oil composition, shear, and temperature. Sunflower (SF) and bean (BO) oils were used as dispersing media for MFC nanoplatelets. During MFC dispersion production at high shear, a significant increase in the average crystal thickness (ACT) could be observed, pointing to recrystallization of the MFC nanoplatelets. More rapid recrystallization of MFC occurred in the SF dispersion than in the BO dispersion, which is attributed to higher solubility of MFC in the SF oil. When the dispersions were maintained under low shear in narrow gap Couette geometry, we witnessed two stages of recrystallization (measured via rheo-SAXD) and the development of a local yield stress (measured via rheo-MRI). In the first stage, shear-enabled mass transfer induces rapid recrystallization of randomly distributed MFC nanoplatelets, which is reflected in a rapid increase in ACT (rheo-SAXD). The formation of a space-filling weak-link MFC network explains the increase in yield stress (assessed in real time by rheo-MRI). In this second stage, recrystallization slows down and yield stress decreases as a result of the formation of MFC aggregates in the weak link network, as observed by confocal Raman imaging. The high fractal dimension of the weak-link network indicates that aggregation takes place via a particle-cluster mechanism. The effects of oil type and shear on the recrystallization rate and network strength could be reproduced in a stirred bowl with a heterogeneous shear stress field, which opens perspectives for the rational manipulation of MFC thickness and network strength under industrial processing conditions.

5.1. Introduction

Current design rules for the processing and formulation of fat-based food with appropriate sensorial properties are based on insights into the underlying organization of fat crystal nanoplatelets in a multiscale network (Macias-Rodriguez & Marangoni, 2017; Farnaz Maleky & Mazzanti, 2018; Ramel, Co, Acevedo, & Marangoni, 2016; Sato, Bayés-García, Calvet, Cuevas-Diarte, & Ueno, 2013). Over the last decades, manufacturing routes have been optimized by the careful matching of fat blend compositions with intricate temperature and shear trajectories (Acevedo & Marangoni, 2014a; Dhonsi & Stapley, 2006; Peyronel, Ilavsky, Pink, & Marangoni, 2014; Tran & Rousseau, 2016). Here a major complication is that the events in the cascade of nucleation, primary crystal growth, polymorphic transitions, and the recrystallization and aggregation of crystals are strongly coupled (Hartel, 2013; Peyronel & Marangoni, 2014; Tran & Rousseau, 2016). Hence, achieving fat crystal networks with desired properties by the manipulation of fat blend composition, temperature, and shear trajectories stands as a considerable challenge (Acevedo & Marangoni, 2014a; Campos, Ollivon, & Marangoni, 2010; Dhonsi & Stapley, 2006; David A Pink, Peyronel, Quinn, Singh, & Marangoni, 2015; Ramel et al., 2016).

Recently it was shown that a major simplification of manufacturing routes for fat crystal networks can be achieved by introducing precrystallized fat crystals (Münüklü & Jansens, 2007). By dispersing a powder of micronized fat crystal (MFC) nanoplatelets in oil, crystallization can be decoupled from crystal aggregation, which offers the opportunity to turn the design of fat crystal networks into a colloidal aggregation game. In recent work, we could largely confirm the decoupling principle, but we also observed that MFC networks grown under static conditions are metastable: rapid recrystallization occurs when shear is applied(Nikolaeva et al., 2018). This suggests a coupling between MFC recrystallization and network formation. In the current study, we present a detailed investigation of factors that can modulate the coupling between these two events. We hypothesize that shear, temperature, and oil composition act as the main modulating factors. We investigated MFC recrystallization during dispersion under high shear in oil and subsequently under low-shear conditions that allow for network formation (Figure 5.1).

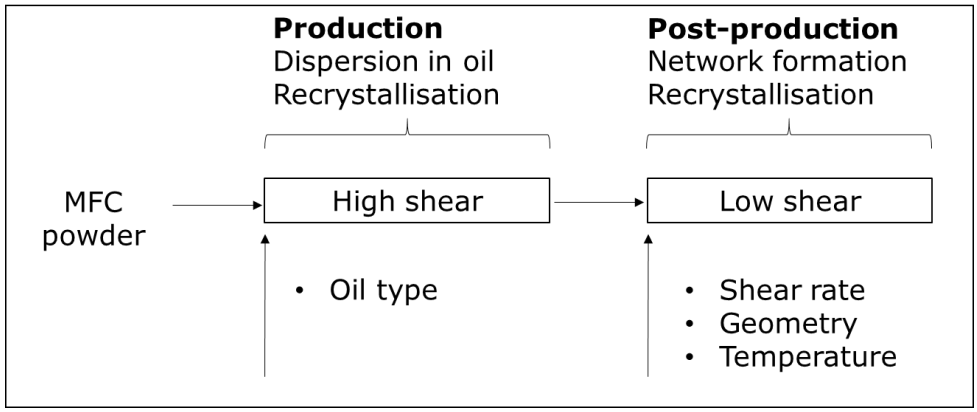

Figure 5.1. Schematic representation of MFC dispersion and network formation stages under high- and low-shear conditions, respectively. Recrystallization and network formation were manipulated by variations of the oil type, shear rate, geometry, and temperature. Postproduction network formation was monitored by using two types of geometry: Couette cells and a stirred bowl

As dispersing media, we selected sunflower (SF) and bean (BO) oils because we expected that they would provide a realistic experimental variation in the solubility of MFC nanoplatelets. Real-time measurements of recrystallization and network formation in these dispersions under low-shear conditions were achieved by rheo-small angle X-ray diffraction (rheo-SAXD) and rheo-MRI, respectively, in Couette geometries with small variations in shear stress over the gap (Nikolaeva et al., 2018). In the rheo-SAXD cell, two shear rates were applied to the SF and BO dispersions, one where recrystallization is expected to be diffusion-limited and one where shear-enhanced mechanisms kick in. Furthermore, the impact of temperature on the MFC recrystallization rate in SF and BO dispersions was studied. The recrystallization kinetics of these dispersions was compared to the time-dependent local flow curves obtained by rheo-MRI (de Kort, Nikolaeva, & Dijksman, 2017), which gave a real-time view of network formation. We also studied recrystallization and network formation under relatively low shear conditions in a stirred bowl, which is representative of industrial processing conditions where typically a heterogeneous shear stress field exists with a wide range of shear rates. The open geometry of the bowl allowed

for the ex situ assessment of recrystallization (SAXD), micrometer-scale network structure (Raman confocal imaging), and the storage modulus (bulk rheology).

5.2. Experimental procedures

5.2.1. Materials

Micronized fat crystal (MFC) nanoplatelets were obtained by spraying a fat blend dissolved in supercritical CO_2 through a narrow nozzle (Münüklü & Jansens, 2007). The triacylglyceride (TAG) and fatty acid (FA) compositions of the fat blend used are presented in Tables S5.1 and S5.2 (supplementary material). The MFC powder was dispersed at a concentration of 10 w/w% in sunflower (SF) and bean (BO) oils. FA compositions of these oils are presented in Table S5.3 (supplementary material). Initially, the MFC nanoplatelets were dispersed in oil by intense mixing under vacuum (0.1 bar) at a temperature of 15 °C for 1 h at constant speed of 500 rpm. The obtained MFC dispersions were kept under static conditions at 15 °C and measured within a few hours or stored at −20 °C for later measurements. In the latter case, stored MFC dispersions were warmed to the measurement temperature just before experimental procedures. For the assessment of dissolution of hardstock in oil, freshly prepared dispersions were centrifuged for 45 min at 15 °C and the supernatant was separated immediately thereafter. The FA compositions of the oils used for preparing the dispersions and of the supernatants obtained by centrifugation of dispersions were determined by transesterification to fatty acid methyl esters (FAME), followed by quantification by gas chromatography−mass spectrometry (GC−MS). The FA compositional analysis was conducted on duplicate samples.

5.2.2. Solid Fat Content

A Minispec MQ NMR spectrometer operating at a magnetic field strength of 0.4 T, corresponding to a resonance frequency of 20 MHz for ^1H, was used to acquire FID-CPMG decay curves. The measurements were performed with a variable-temperature probehead, maintained at 20 °C, with a 90° pulse of 2 μs and 180−180° pulse spacing in the CPMG sequence of 0.2 ms. Typically, 16 decay curves were accumulated. Constrained fitting of the decay curves with a sum of Abraghamiam, Gaussian, and exponential functions provided the

amount of solid fat (Trezza, Haiduc, Goudappel, & van Duynhoven, 2006). Measurements were conducted on duplicate samples.

5.2.3. Ex Situ Monitoring of Network Formation in a Stirred Bowl

MFC dispersions were mixed in a temperature-controlled bowl that was 30 cm in diameter. An impeller was used for mixing at a rotational speed of 28 rpm. The energy input exerted on the vane varied between 0.1 and 1 W, indicating an average shear rate on the order of $1-10\ s^{-1}$ (Peyronel & Marangoni, 2014). Every half an hour, samples were collected and measured by bulk rheology, small angle X-ray diffraction (SAXD), and confocal Raman imaging. (The experimental details are discussed below.) For all techniques, measurements were conducted on three replicates.

5.2.4. Bulk Rheology

Measurements of the storage modulus G' were made on an TA (AR 2000) rheometer set up with a cone−plate (CP) configuration (cone angle of 2°, cone diameter of 40 mm). The rheometer was run through an oscillatory strain program with applied strain ranging from 0.003 to 150% at a frequency of 1 Hz and a temperature of 20 °C. The apparent values of storage modulus G' were estimated from the linear viscoelastic region (LVR) (Acevedo & Marangoni, 2014a).

5.2.5. Confocal Raman Imaging

Full details of the experimental procedures for obtaining hyperspectral confocal Raman images can be found elsewhere (Martens et al., 2018; van Dalen et al., 2017). In short, experiments were performed on a WITec confocal Raman (alpha 300R+) imaging system equipped with a Zeiss upright microscope fitted with a 100×/1.4 NA oil objective with a 532 nm laser at 25.0 mW. The sample was placed on a 19 °C water-cooled plate. The Raman spectrometer was coupled to a cooled (−60 °C) EMCCD detector. An integration time of 0.01 s was used to image a $50 \times 50\ \mu m^2$ area with a resolution of 0.23 μm with Raman spectra in the range of 100−3800 cm^{-1}. The raw data was corrected via cosmic spike removal and background correction in MATLAB (The MathWorks inc.). Multivariate curve resolution with alternating least squares (MCR-ALS) was used in the range of 500−2000 cm^{-1} to fit spectra of known components to the hyperspectral information acquired from the sample

(Martens et al., 2018; van Dalen et al., 2017), thus providing compositional maps of solid fat (SFC, 0−100 w/w %). These compositional maps were used to determine two-dimensional fractal dimensions of the MFC networks by the box-counting method (Martens et al., 2018). Because it is known that MFC networks are self-similar, their three-dimensional fractal dimension is one unit larger than the one determined by the two-dimensional box-counting method.

5.2.6. WAXD and SAXD

A Bruker D8-Discover diffractometer in a θ/θ configuration was used for wide- and small-angle X-ray diffraction (WAXD and SAXD) measurements. The beam cross section at the sample position was about 1 mm. The distance and angle between a detector and a sample were 32.5 cm and 10°, respectively. The collection of WAXD data was in the range of 7° < 2θ < 55°. In SAXD mode, a distribution of thicknesses of the repeating crystalline TAG bilayers was measured, and the average crystal thickness (ACT) was determined by the Scherrer line shape analysis of the first-order diffraction peak (Nikolaeva et al., 2018; Ramel et al., 2016)

$$d = \frac{K\lambda}{\text{fwhm}\cos\theta}$$

where K is the shape factor, θ is the Bragg angle, fwhm is the line width at half of the maximum peak height corrected for instrumental broadening, and λ is the X-ray wavelength. Further details can be found elsewhere (den Adel, van Malssen, van Duynhoven, Mykhaylyk, & Voda, 2018; Nikolaeva et al., 2018).

5.2.7. Rheo-SAXD

Design details of the home-built horizontal Couette shear cell can be found elsewhere (Nikolaeva et al., 2018). In short, the geometry of the cell allowed the X-ray beam to be directed along the vorticity direction of the flow at different positions across the gap between the inner and outer cylinders. A gap of 1 mm with a 38 mm outer radius was used, and rotation was applied to the inner cylinder of the shear cell. The shear cell was mounted in a Bruker D8-Discover diffractometer in a θ/θ configuration with a cell-to-detector distance of 32.5 cm. Data acquisition and processing were carried out according to procedures outlined for static SAXD measurements. MFC dispersions were measured under constant shear during 12 h.

Shear rates applied to the same sample were 0.025 and 0.25 rpm, corresponding to shear rates of 0.1 and 1 s^{-1}, respectively. The rheo-SAXD measurements were performed at a controlled temperature of either 20 or 26 °C. To investigate the orientation of fat crystal nanoplatelets, two-dimensional (2D) SAXD patterns were collected (Mazzanti, Guthrie, Sirota, Marangoni, & Idziak, 2003; Mazzanti, Marangoni, & Idziak, 2009; Sato et al., 2013). The orientational distribution was presented as the integration of the low-*q* region as a function of the azimuthal angle (χ).

5.2.8. Rheo-MRI

A Couette geometry was used with serrated walls, an outer cylinder diameter of 22 mm, and a gap size of 1 mm. The inner cylinder was 20 mm in diameter and 58 mm in length and rotated at 0.96 or 3 rpm, respectively, with a corresponding shear rate of 1.16 or 3.62 s^{-1}. The temperature in the Couette cell was controlled at 20 °C.

The stability of the NMR signal indicated that no significant temperature variation occurred during the experiments. Rheo-MRI measurements of space-resolved velocity (Callaghan, 2011) were performed with a Bruker Avance III spectrometer at 7.0 T magnetic field strength (resonance frequency 300 MHz for ^{1}H) in combination with a Bruker rheo-MRI accessory. Velocity profiles over the position *r* in the gap ν(*r*) were measured by a PFG spin echo (PFG SE) sequence (repetition time T_R = 1.5 s, echo time T_E = 17 ms, Δ = 13.1 ms, δ = 1 ms). The 1 D velocity profiles ν(*r*) had a field of view of 25 mm and a spatial resolution of 48.8 μm. A slice thickness of 2 mm and 32 scans gave good signal-to-noise ratio velocity profiles within 1 min 36 s.

For every position *r* within the gap, at angular velocity ω, rheo-MRI velocity data ν(*r*) provided the magnitude of the local shear rate $\dot{\gamma}(r,\omega)$: $\dot{\gamma}(\mathrm{r}) = \mathrm{r}\frac{\partial(v/r)}{\partial r}$. The local stress σ(*r*, ω) was estimated from torque *T* measurements for each angular velocity as $\sigma(r) = \frac{T}{2\pi r^2 H}$ (*H* is the fluid height in the gap) (Bird, 1987). To measure torque as a function of time, we used a replicate of the rheo-MRI Couette cell in a conventional Modular Compact Rheometer 301 (MCR301 SN80480600, Anton Paar).[14] The apparent local yield stress was obtained from fits of the Herschel-Bulkey model to local flow curves (i.e., local stress σ(*r*, ω) vs local shear rate $\dot{\gamma}(r,\omega)$ (Philippe. Coussot, 2005; Ovarlez, Bertrand, & Rodts, 2006). The local viscosity

data were deduced by using the equation $\eta = \frac{\sigma(r)}{\dot{\gamma}(r,\omega)}$. Both the apparent yield stress and the local viscosity data reflect the MFC network strength (Nikolaeva et al., 2018; Ovarlez et al., 2015).

5.3. Results and discussion

5.3.1. Dispersion Production: High-Shear Dispersion of MFC Nanoplatelets in Oil

WAXD and SAXD measurements were performed on the micronized fat crystal (MFC) nanoplatelets in their powder form (Münüklü & Jansens, 2007) and during their dispersion in oil. In MFC powder, the fat crystal nanoplatelets existed in the β′ polymorph and had an average crystal thickness (ACT) of 39.4 nm (Figure 5.2). Upon vigorously mixing the MFC powder with either sunflower (SF) or bean (BO) oil, MFC nanoplatelets remained in the β′ polymorph, while the ACT showed an increasing trend, pointing to shear-induced Ostwald ripening (Johansson & Bergenståhl, 1995; Nikolaeva et al., 2018). Figure 5.2 shows that the ACT values increased more rapidly for MFC nanoplatelets dispersed in SF compared to BO. Because dissolution is a mediating factor in shear-induced mass transfer, we verified that the solubility of micronized fat in BO and SF is different. For this purpose, the MFC dispersions were subjected to centrifugation in order to obtain the oil phase. The oil and MFC phases could not be fully separated, so a collapsed MFC network comprising oil and an oil fraction (supernatant) were obtained. The FA analysis of the oil supernatant revealed differences in the content of palmitic acid P (C16:0) (Table S5.3, supplementary material). Because P (C16:0) was the most abundant fatty acid in MFC (Table S5.2, supplementary material), we considered its increase in the content as a measure of the amount of dissolved fat. We observed 70 and 17% increases in the content of P (C16:0) in the SF and BO dispersions, respectively, indicating a larger solubility of micronized fat crystals in SF. This explained the shear-enhanced recrystallization of MFC nanoplatelets and the more rapid ACT growth in SF dispersions. When the dispersions were kept at 15 °C for a few hours, no changes in ACT were observed. WAXD measurement, however, indicated that the MFC nanoplatelets converted from the β′ to β polymorph during this period. In the next few sections, we present the results of the in situ study of recrystallization and network formation in MFC dispersions under postproduction conditions where only low shear is applied (Figure 5.1).

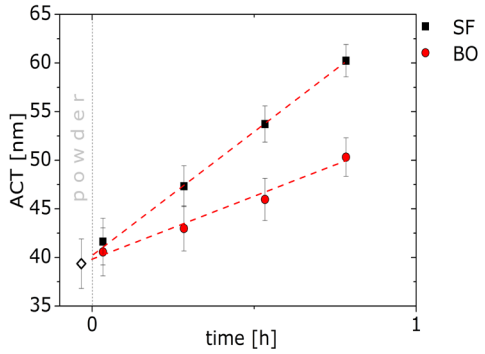

Figure 5.2. Average crystal thicknesses (ACT) for MFC in powder form (◊) and upon dispersion in SF (■) and BO (red ●) at 15 °C. The dispersion of MFC was monitored for an hour. Error bars are based on duplicate measurements. The dashed lines are intended to guide the eye.

acid in MFC (Table S5.2, supplementary material), we considered its increase in the content as a measure of the amount of dissolved fat. We observed 70 and 17% increases in the content of P (C16:0) in the SF and BO dispersions, respectively, indicating a larger solubility of micronized fat crystals in SF. This explained the shear-enhanced recrystallization of MFC nanoplatelets and the more rapid ACT growth in SF dispersions. When the dispersions were kept at 15 °C for a few hours, no changes in ACT were observed. WAXD measurement, however, indicated that the MFC nanoplatelets converted from the β′ to β polymorph during this period. In the next few sections, we present the results of the in situ study of recrystallization and network formation in MFC dispersions under postproduction conditions where only low shear is applied (Figure 5.1).

5.3.2. Postproduction Structure Evolution in Narrow Gap Couette Geometry: Recrystallization

Effect of Oil. Rheo-SAXD experiments were employed to monitor changes in the ACT at shear rates that were low enough to allow for network formation. The measurements were performed in Couette geometry with a gap of 1 mm, over which the shear stress varied by

5% (Nikolaeva et al., 2018). Figure 5.3(A) shows the ACT values of SF and BO MFC dispersions obtained under a constant shear rate of 0.1 s^{-1} and at a temperature of 20 °C. The ACT values of MFC nanoplatelets dispersed in SF were greater than in BO, which is in line with their more rapid recrystallization observed during the dispersion production.

Effect of Shear Rate. Figure 5.3(B) demonstrates the effect of shear on the ACT values of the MFC nanoplatelets dispersed in SF at 20 °C. (The ACT values of BO dispersions can be found in Figure S5.1, supplementary material) Shear rates of 0.1 and 1 s^{-1} were applied, which correspond to Peclet numbers of ~0.1 and 1 (Farnaz Maleky, 2015; Farnaz Maleky & Mazzanti, 2018; Mazzanti et al., 2003). For both shear rates, a rapid and slow stage in the ACT growth can be observed. Imposing a shear rate of 1 s^{-1} resulted in an initially faster ACT increase during the first few hours. The acceleration of the recrystallization can be explained by shear-enhanced mass transport. After a few hours, the recrystallization rate slowed down, indicating that shear-enhanced mass transport became less effective in enhancing the recrystallization of MFC nanoplatelets.

Effect of Temperature. Figure 5.3(C) shows the ACT changes at the higher temperature of 26°C for MFC nanoplatelets dispersed in SF at a constant shear of 1 s^{-1}. (The full data set is shown in Figure S5.2, supplementary material). At this temperature, the rapid and slow recrystallization stages were more pronounced. During the first few hours, the recrystallization rate for MFC nanoplatelets in the SF dispersion was significantly enhanced, before it slowed down to a similar rate as observed at 20 °C. Furthermore, the first stage lasted for a longer time at higher temperature, suggesting that besides the enhancement of mass transport due to shear, a supplementary amount of TAGs was dissolved, which further enhanced recrystallization. For the BO dispersions, a similar enhancement of the recrystallization rate can be observed (supplementary material, Figures S5.1 and S5.2), although it was more modest than observed for SF dispersions.

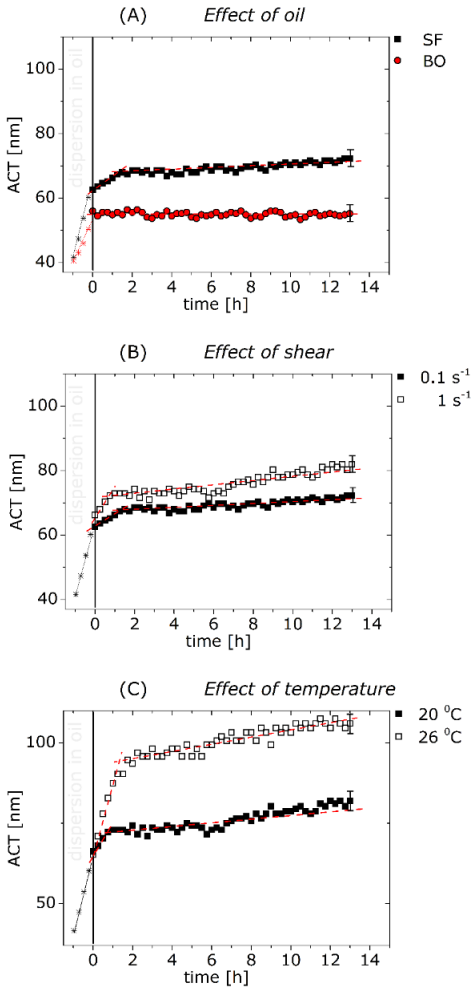

Figure 5.3 (A) Effect of oil. Average crystal thickness (ACT) as a function of time for MFC nanoplatelets dispersed in SF (black) and BO (red) oils at 20 °C at an imposed shear rate of $0.1 s^{-1}$. **(B)** Effect of shear. ACT as a function of time for MFC nanoplatelets dispersed in SF at 20 °C at imposed shear rates of 0.1 s^{-1} (solid symbols) and 1 s^{-1} (empty symbols). **(C)** Effect of temperature. ACT as a function of time for MFC nanoplatelets dispersed in SF at an imposed shear rate of 1 s^{-1} and temperatures of 20 °C (solid symbols) and 26 °C (empty symbols). All experiments were performed in rheo-SAXD Couette cell geometry (1 mm gap). The solid curves with * symbols for times <0 h indicate increases in ACT during MFC dispersion. (See Figure 5.2 for more detail.) Error bars represent the deviation between duplicate rheo-SAXD runs. The dashed curves for times >0 h are intended to guide the eye.

To verify whether the aforementioned effects of shear and temperature were not caused by the crystallization of dissolved fat instead of Ostwald ripening, we determined whether the amount of crystalline material varied with time. During the rheo-SAXD experiments, the intensity of the SAXD signal did not change during the measurement time for any of the prepared MFC dispersions. The MFC dispersions were also monitored in time by NMR in static mode. The solid fat content (SFC) remained constant, indicating the absence of crystallization or the dissolution of fat (Figure S5.3, supplementary material). We also observed that the MFC nanoplatelets remained in the stable β polymorph during all postproduction structure evolution experiments. Hence, polymorphic transitions can also be excluded to explain the effects of temperature and shear on the recrystallization of MFC nanoplatelets. The enhancement of the recrystallization rate by shear is most pronounced in the first 1 to 2 h, in particular at elevated temperature. The observed rapid recrystallization points to shear-enhanced mass transfer (Acevedo & Marangoni, 2014b; Farnaz Maleky & Mazzanti, 2018; Tran & Rousseau, 2016) between the MFC nanoplatelets being initially present in a nonaggregated state and randomly distributed in a continuous weak-link network (Figure 5.4). Once the MFC nanoplatelets start to aggregate (Nikolaeva et al., 2018; Peyronel, Acevedo, Pink, & Marangoni, 2018), shear is less effective in enhancing mass transfer, and as a consequence, recrystallization slows down. The presence of nonaggregated MFC nanoplatelets in the weak-link network was visible through an asymmetry in the rheo-SAXD 2D diffratograms, which indicated the alignment of nanocrystals (Nikolaeva et al., 2018; Peyronel et al., 2018). From the radial integral of the 2D SAXD pattern at q = 1.5994 nm^{-1} as a function of azimuthal angle χ extension (Figure S5.4, supplementary material), we estimated the Herman orientation factors (Bhattacharyya et al., 2003). These were approximately 0.07, which indicates that the nanocrystals are weakly aligned (0 and 1 indicate random and full parallel orientation, respectively). The weak alignment of the nanoplatelets is in line with the low estimated Peclet numbers of 0.1 and 1 (Farnaz Maleky, 2015; Mazzanti et al., 2003) and indicates that the weak-link network is predominantly isotropic.

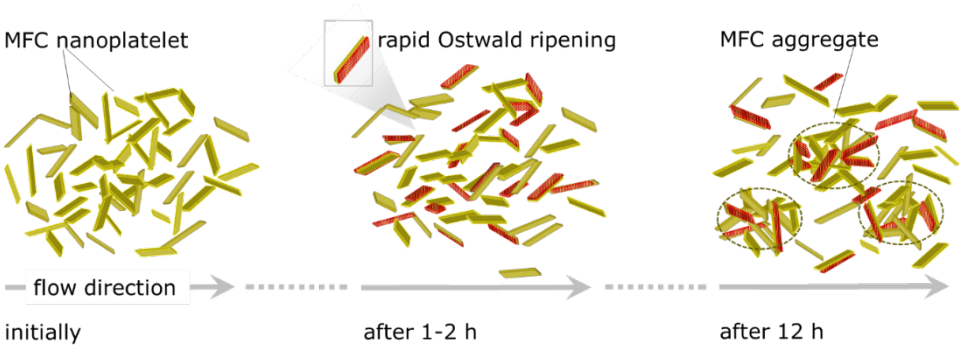

Figure 5.4. Schematic drawing of recrystallization and network formation of MFC nanoplatelets under low shear. The ACT of the MFC nanoplatelets is in the range of 40−120 nm, and their aspect ratio (>10) is not drawn to scale. Initially, the MFC nanoplatelets are randomly distributed in a continuous weak-link net. During the first few hours of shear rapid, Ostwald ripening occurs, with recrystallized nanoplatelets indicated in red. Subsequently, Ostwald ripening slows down because of the formation of MFC aggregates. Ostwald ripening is depicted as the recrystallization of thin (red) nanoplatelets onto thicker ones.

5.3.3. Postproduction Structure Evolution in a Narrow Gap Couette Geometry. Local Flow Behavior and Network Formation

Real-time local flow curves were obtained by combining the stress distribution over the gap of the Couette geometry with the shear rates determined from rheo-MRI velocity profiles (P. Coussot, Tocquer, Lanos, & Ovarlez, 2009; de Kort et al., 2017; Nikolaeva et al., 2018). The stress distribution was obtained by measuring the torque on the inner cylinder of the Couette geometry with a 1 mm gap size at 20 °C and a shear stress variation of 17%. From the evolution of the local flow curves (Figure S5.5, supplementary material), the time-dependent apparent yield stress could be obtained, which can be regarded as a measure of the MFC network strength (Nikolaeva et al., 2018; Ovarlez et al., 2015). Figure 5.5 shows the behavior of the time-dependent yield stress of MFC dispersions in SF and BO at 20 °C under a constant shear rate of 1.16 s^{-1}. A rapid increase in the apparent yield stress values during the first hour can be observed, indicating the formation of the MFC nanoplatelet network. In this stage, we

also witness a rapid increase in ACT, pointing to rapid shear-enhanced recrystallization. Subsequently, we observed the slow loss of yield stress between 1 and 12 h. This coincides with the second time stage with a slower recrystallization rate, 1−12 h, which we attribute to the aggregation of MFC nanoplatelets.

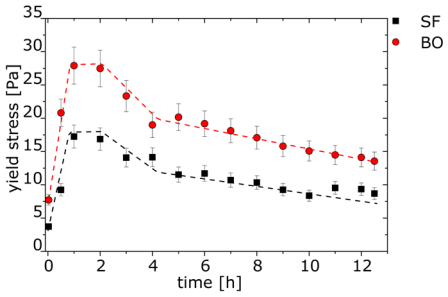

Figure 5.5. Apparent yield stress as a function of time for MFC nanoplatelets dispersed in SF (■) and BO (red ●), determined in 1 mm gap Couette geometries by rheo-MRI. The apparent yield stress was deduced from local flow curves (Figure S5.5, supplementary material) obtained at 1.16 s^{-1} and 20 °C. Error bars are based on fits of the Herschel−Bulkley model to local flow curves obtained by rheo-MRI. The dashed curves are intended to guide the eye.

The effect of oil composition could also be recognized in the behavior of the apparent yield stress. The MFC nanoplatelets dispersed in BO form a stronger network than in SF. This can be directly related to the ACT value, which is smaller in BO dispersion. The coarser MFC nanoplatelets as present in SF dispersions cannot form the dense and firm space-filling networks as the thinner MFC nanoplatelets dispersed in BO do. In both cases, we observed a decrease in yield stress in the subsequent 1−12 h stage. This can be explained by the formation of micrometer-scale aggregates interacting via a weak-link nanoplatelet network within the interstitial space (Nikolaeva et al., 2018).

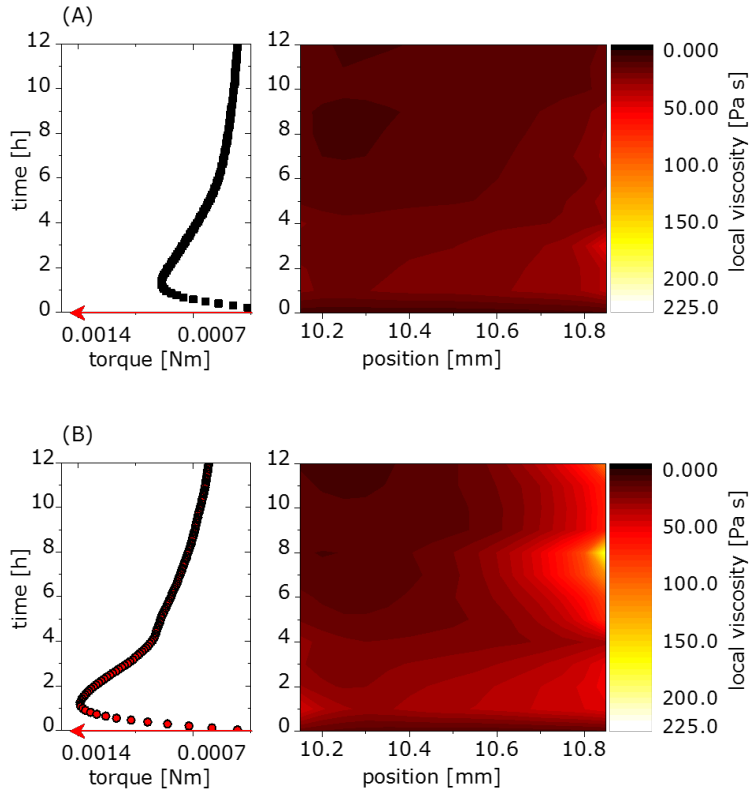

Figure 5.6. Two-dimensional viscosity maps as a function of time and position within the gap of Couette geometry for MFC nanoplatelets dispersed in SF **(A)** and BO **(B)** at 1.16 s^{-1}. The color gradient has an increment of 5 Pa s. On the left side of the 2D viscosity maps, the graphs of torque over time are shown. The red arrows schematically demonstrate the increase in the torque values.

The rheo-SAXD experiment showed that in this weak-link network the nanoplatelets are weakly aligned, indicating that shear is effective at inducing mass transfer. As a consequence, the weak-link interacting nanoplatelets recrystallize more rapidly than the MFC nanoplatelets involved in micrometer-scale aggregates. Although there is not a clear-cut relationship between the thickness of nanoplatelets and their length and width (Acevedo & Marangoni, 2010, 2014a, 2014b; Farnaz Maleky & Mazzanti, 2018; Tran & Rousseau, 2016), we deem the increase in ACT strong enough to conclude that a coarser and less space-filling network

is formed. This will weaken the overall network strength, resulting in the (further) loss of yield stress. The anisotropy within the weak-link network is too weak to contribute to the loss of yield stress (Nikolaeva et al., 2018; Tran & Rousseau, 2016).

To determine the consequences of the development of a weak-link network in a heterogeneous shear field, we determined the spatially resolved apparent viscosity values using the local flow curves obtained in real time by rheo-MRI. Figure 5.6 shows the 2D plots of viscosity as a function of position in the gap and in time. On the left side of the plots, the torque values are presented as a function of time to show the changes in strength during MFC network formation. In the first hour, uniform viscosity over the gap can be observed for SF and BO dispersions at the given shear rate. During the next 11 h, viscosity gradients were observed and were most pronounced for the BO dispersion. After 5 h, the local viscosity at the outer wall of the Couette cell achieved a value of more than 150 Pa s, indicating a nonmoving MFC dispersion (i.e., shear banding).

5.3.4. Postproduction Structure Evolution in a Stirred Bowl: Recrystallization and Network Formation

To determine whether the effects of shear and oil type used for dispersing the MFC nanoplatelets would also exist under industrially relevant processing conditions (Farnaz Maleky & Mazzanti, 2018)(Fatemeh Maleky & Marangoni, 2008), we also studied network formation under stirring conditions in a bowl where the shear stress field is highly heterogeneous. The used geometry resembles industrial mixing vessels where only average shear rates can be derived. From the energy input exerted on the mixer, we estimated an average shear rate on the order of 1−10 s^{-1} (Farnaz Maleky & Mazzanti, 2018).

Samples were taken at relevant time intervals, and rheological and structural parameters were determined. All experiments were conducted at a controlled temperature of 20 °C. The time evolution of ACT for dispersions of MFC in SF and BO oils, under stirring conditions, is presented in Figure 5.7(A). The observed trends were in line with the in situ rheo-SAXD experiments in Couette geometry. Also for the stirred bowl experiment, the increase in ACT values was more rapid for MFC nanoplatelets dispersed in SF than for those dispersed in BO. The development of storage modulus G' in time is presented in Figure 5.7(B). The storage

modulus values were generally higher for the dispersions in BO compared to those in SF. This is in line with thinner crystals building a stronger space-filling network in the BO dispersions than in the SF dispersions (Acevedo & Marangoni, 2014a; Ramel et al., 2016). However, under stirring conditions we observed that for the BO dispersions the ACT of MFC nanoplatelets increased with two recrystallization rates being close to each other (Figure 5.7(A)). At the same time, the storage modulus after the initial increase in the first 1−3 h was accompanied by a continuous slow increase during the next 6 h of observation time. For the SF dispersions, we observed the behavior of the recrystallization and network formation of MFC nanoplatelets to be similar to what we observed in the narrow gap Couette geometry: two well-separated rescrystallization rates with a rapid increase, followed by a steady decrease in the storage modulus.

The open geometry of the bowl allowed for ex situ monitoring of MFC aggregation by means of confocal Raman imaging (Martens et al., 2018; van Dalen et al., 2017). The imaging time was on the order of 11 min, which allowed the observation of network formation with adequate time resolution. The hyperspectral Raman images were converted to quantitative maps of solid fat content (SFC), which allowed direct visualization of micrometer-scale aggregates and indirectly the interstitial weak-link network (Martens et al., 2018). A selection of compositional maps of SFC for MFC dispersed in BO over the network formation time is shown in Figure 5.8. These quantitative SFC maps (Martens et al., 2018; Nikolaeva et al., 2018) showed that the interstitial phase between the aggregates contained a significant amount of saturated fat of 12% on average, indicating the presence of a weak-link network. By means of the box-counting method (Martens et al., 2018; van Dalen et al., 2017), fractal dimensions of 2.6−2.8 were obtained, which did not vary during network formation under stirring conditions in the first 12 h (data are not shown).

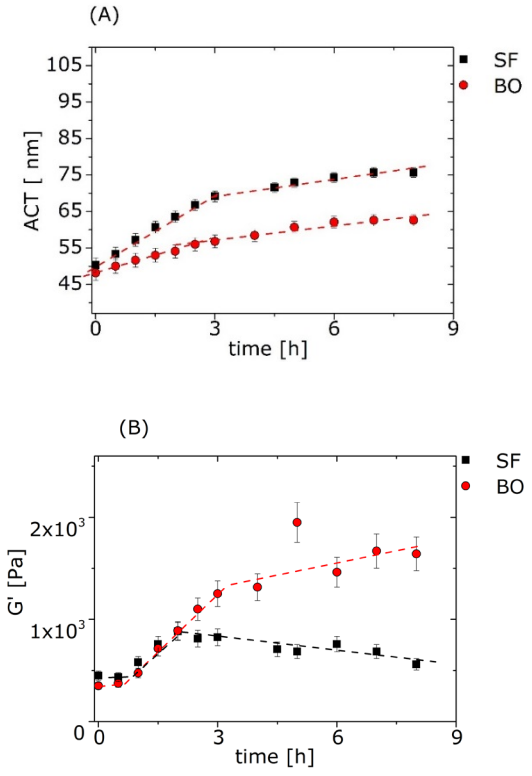

Figure 5.7. (A) Average crystal thickness (ACT) and **(B)** shear storage modulus G' as a function of time for MFC nanoplatelets dispersed in SF (■) and BO (red ●) during shearing in a bowl. Error bars are based on triplicate measurements. The dashed curves are intended to guide the eye.

This was in line with observations made for the MFC network formed under static conditions, demonstrating that the aggregation of MFC nanoplatelets was via a particle-cluster mechanism and that the involvement of TAGwood aggregate clustering (D. A. Pink, Townsend, Peyronel, Co, & Marangoni, 2017) could be excluded. MFC nanoplatelet aggregates were clearly observed after 4 h, which is in line with the slowing down of recrystallization and network formation (Figure 5.7(A) and (B)). In the images obtained at 4 and 6 h, the MFC aggregates can be clearly distinguished from the interstitial weak-link phase. The growth of micrometer-scale aggregates is at the expense of crystalline material present in the interstitial phase, which explains the loss of yield stress. Similar results

obtained for the MFC nanoplatelets dispersed in SF are shown in Figure S5.6 (supplementary material).

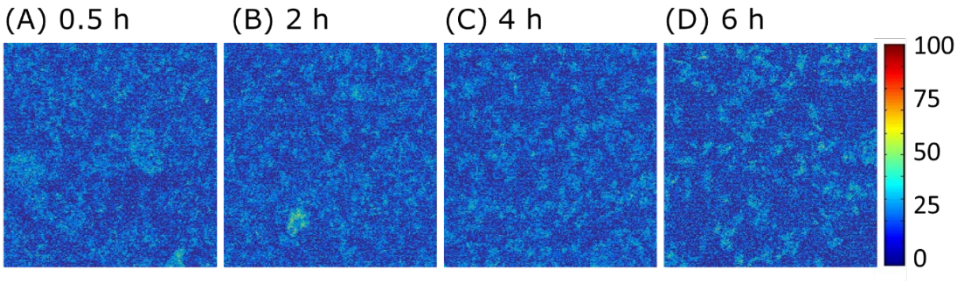

Figure 5.8. Compositional maps (50 × 50 μm^2) obtained from 216 × 216 hyperspectral Raman cubes recorded for MFC nanoplatelets dispersed in BO during network formation under shear in a stirred bowl. The scale bar represents the solid fat content (SFC) on a scale of 0 to 100% (weight percentage). The compositional maps represent the MFC network at **(A)** 0.5, **(B)** 2, **(C)** 4, and **(D)** 6 h. In half an hour **(A)**, a random spatial distribution of solid fat was observed, while after 6 h of shear **(D)**, the MFC aggregates became more apparent.

The results for the stirred bowl experiments with their heterogeneous shear stress field reproduce the findings in the defined Couette geometries by means of rheo-SAXD and rheo-MRI. The reproducibility of the results indicates that the variations in oil type, average shear rate, time, and temperature also determine the MFC network formation in heterogeneous shear fields. This opens perspectives for the rational manipulation of MFC network formation on the industrial scale, where the mixing and storage of fat crystal dispersions typically occur in large stirred vessels. The time behavior of MFC recrystallization and yield stress during and after dispersion production clearly suggests that formulation and processing parameters can be adjusted to tune the strength of the fat crystal network and define a sweet spot for desirable product firmness. The observation of shear banding by rheo-MRI indicates that under such conditions local shear stresses should be maintained above a critical stress to avoid network heterogeneity on the macroscopic scale. Our results also show that the ACT of fat crystal nanoplatelets can be controlled under industrial conditions. This offers opportunities for the Pickering stabilization of water droplet interfaces with the thin fat-

crystal nanoplatelets that can easily be released from the weak-link continuous phase (Rousseau, 2013) when water is emulsified in MFC dispersions.

5.4. Conclusions

During the dispersion of MFC powder in vegetable oil, thin MFC nanoplatelets (40 nm on average) undergo rapid recrystallization enabled by mass transfer under high shear. The recrystallization rates for MFC nanoplatelets dispersed in sunflower (SF) and bean (BO) oils are different and dependent on the solubility of the MFC nanoplatelets in these oils. During MFC network formation in Couette geometry at low shear ($Pe = 0.1-1$), recrystallization and network formation proceed via two stages. In the initial stage (0−1 h), recrystallization is shear enhanced due to efficient mass transfer between the MFC nanoplatelets (Figure 5.4). Concomitantly, weak-link interactions of the individual MFC nanoplatelets enable the formation of a space-filling network and a rapid increase in the yield stress. BO dispersions exhibit faster growth of the yield stress than the SF dispersions as a result of their thinner nanoplatelets (smaller ACT), which allow for a denser space-filling network. In the next stage (1−h), a major part of the MFC nanoplatelets participate in micrometer-scale aggregates, where recrystallization cannot be enhanced by shear and as a consequence slows down. The strength of the weak-link network decreases because of the predominant involvement of nanoplatelets in strong-link interactions within MFC aggregates. Within the weak-link network, shear-enhanced recrystallization is still active, leading to further coarsening of MFC nanoplatelets and a concomitant loss of yield stress. The effects of oil type and shear on the recrystallization rate and network strength can be reproduced in a stirred bowl with a highly heterogeneous shear stress field. This bears relevance to manipulating the MFC thickness and network strength by variations of the oil type, shear rate, and temperature under industrial-scale mixing and storage conditions.

Acknowledgments

Patricia Heussen is gratefully acknowledged for recording the confocal Raman images. The authors thank Kees van Malssen, Jan Wieringa, Jo Janssen, Michiel Meeuse, and Peter de Groot from Unilever Discover Vlaardingen for fruitful discussions. The authors thank the Delft workshop at Delft University of Technology for designing and manufacturing the rheo-SAXD shear cell. The authors thank T. Narayanan and M. Sztucki from the European Synchrotron Radiation Facility (ESRF), Grenoble, France, for their intellectual contributions to this work. The authors thank Frank Vergeldt and John Philippi for advice on the rheo-MRI experiments.

References

Acevedo, N. C., & Marangoni, A. G. (2010). Toward nanoscale engineering of triacylglycerol crystal networks. *Crystal Growth and Design*, *10*(8), 3334–3339. https://doi.org/10.1021/cg100469x

Acevedo, N. C., & Marangoni, A. G. (2014a). Functionalization of Non-interesterified Mixtures of Fully Hydrogenated Fats Using Shear Processing. *Food and Bioprocess Technology*, *7*(2), 575–587. https://doi.org/10.1007/s11947-013-1110-z

Acevedo, N. C., & Marangoni, A. G. (2014b). Nanostructured Fat Crystal Systems. *Annual Review of Food Science and Technology*, *6*, 1–26. https://doi.org/10.1146/annurev-food-030713-092400

Bhattacharyya, A. R., Sreekumar, T. V., Liu, T., Kumar, S., Ericson, L. M., Hauge, R. H., & Smalley, R. E. (2003). Crystallization and orientation studies in polypropylene/single wall carbon nanotube composite. *Polymer*, *44*(8), 2373–2377. https://doi.org/10.1016/S0032-3861(03)00073-9

Bird, R. B. (1987). *Dynamics of polymeric liquids. Vol. 2, Vol. 2,*. New York; Chichester: Wiley.

Callaghan, P. T. (2011). *Translational Dynamics and Magnetic Resonance: Principles of Pulsed Gradient Spin Echo NMR*. Oxford: Oxford University Press. https://doi.org/10.1093/acprof:oso/9780199556984.001.0001

Campos, R., Ollivon, M., & Marangoni, A. G. (2010). Molecular Composition Dynamics and Structure of Cocoa Butter. *Crystal Growth & Design*, *10*(1), 205–217. https://doi.org/10.1021/cg900853e

Coussot, P., Tocquer, L., Lanos, C., & Ovarlez, G. (2009). Macroscopic vs. local rheology of yield stress fluids. *Journal of Non-Newtonian Fluid Mechanics*, *158*(1–3), 85–90. https://doi.org/10.1016/j.jnnfm.2008.08.003

Coussot, Philippe. (2005). *Rheometry of pastes, suspensions, and granular materials : applications in industry and environment*. Hoboken, N.J.: Wiley.

de Kort, D. W., Nikolaeva, T., & Dijksman, J. A. (2017). Rheo-NMR: Applications to Food. In G. A. Webb (Ed.), *Modern Magnetic Resonance.* (pp. 1–21). Springer, Cham. https://doi.org/10.1007/978-3-319-28275-6_19-1

den Adel, R., van Malssen, K., van Duynhoven, J., Mykhaylyk, O. O., & Voda, A. (2018). Fat crystallite thickness distribution based on SAXD peak shape analysis. *European Journal of Lipid Science and Technology*, *1800222*, 1–6. https://doi.org/10.1002/ejlt.201800222

Dhonsi, D., & Stapley, A. G. F. (2006). The effect of shear rate, temperature, sugar and emulsifier on the tempering of cocoa butter. *Journal of Food Engineering*, *77*(4), 936–942. https://doi.org/10.1016/j.jfoodeng.2005.08.022

Hartel, R. W. (2013). Advances in Food Crystallization. *Annu. Rev. Food Sci. Technol*, *4*, 277–292. https://doi.org/10.1146/annurev-food-030212-182530

Johansson, D., & Bergenståhl, B. (1995). Sintering of fat crystal networks in oil during post-crystallization processes. *Journal of the American Oil Chemists' Society*, *72*(8), 911–920. https://doi.org/10.1007/BF02542069

Macias-Rodriguez, B. A., & Marangoni, A. A. (2017). Linear and nonlinear rheological behavior of fat crystal networks. *Critical Reviews in Food Science and Nutrition*, 1–18. https://doi.org/10.1080/10408398.2017.1325835

Maleky, Farnaz. (2015). Nanostructuring triacylglycerol crystalline networks under external shear fields: A review. *Current Opinion in Food Science*, *4*, 56–63. https://doi.org/10.1016/j.cofs.2015.05.005

Maleky, Farnaz, & Mazzanti, G. (2018). Lipid Crystal Networks Structured under Shear Flow. In K. Sato (Ed.), *Crystallization of Lipids: Fundamentals and Applications in Food, Cosmetics, and Pharmaceuticals* (First, pp. 211–239). John Wiley & Sons Ltd. https://doi.org/10.1002/9781118593882

Maleky, Fatemeh, & Marangoni, A. G. (2008). Process development for continuous crystallization of fat under laminar shear. *Journal of Food Engineering*, *89*(4), 399–407. https://doi.org/10.1016/j.jfoodeng.2008.05.019

Martens, K. J. A., van Dalen, G., Heussen, P. C. M., Voda, M. A., Nikolaeva, T., & van Duynhoven, J. P. M. (2018). Quantitative Structural Analysis of Fat Crystal Networks by Means of Raman Confocal Imaging. *Journal of the American Oil Chemists' Society*. https://doi.org/10.1002/aocs.12035

Mazzanti, G., Guthrie, S. E., Sirota, E. B., Marangoni, A. G., & Idziak, S. H. J. (2003). Orientation and phase transitions of fat crystals under shear. *Crystal Growth and Design*, *3*(5), 721–725. https://doi.org/10.1021/cg034048a

Mazzanti, G., Marangoni, A. G., & Idziak, S. H. J. (2009). Synchrotron study on crystallization kinetics of milk fat under shear flow. *Food Research International*, *42*(5–6), 682–694. https://doi.org/10.1016/j.foodres.2009.02.009

Münüklü, P., & Jansens, P. J. (2007). Particle formation of an edible fat (rapeseed 70) using the supercritical melt micronization (ScMM) process. *Journal of Supercritical Fluids*, *40*(3), 433–442. https://doi.org/10.1016/j.supflu.2006.07.015

Nikolaeva, T., Adel, R. den, Velichko, E., Bouwman, W. G., Hermida-Merino, D., Van As, H., … van Duynhoven, J. (2018). Networks of micronized fat crystals grown under static conditions. *Food & Function*, *9*, 2102–2111. https://doi.org/10.1039/C8FO00148K

Ovarlez, G., Bertrand, F., & Rodts, S. (2006). Local determination of the constitutive law of a dense suspension of noncolloidal particles through magnetic resonance imaging. *Journal of Rheology*, *50*(3), 259–292. https://doi.org/10.1122/1.2188528

Ovarlez, G., Mahaut, F., Deboeuf, S., Lenoir, N., Hormozi, S., & Chateau, X. (2015). Flows of suspensions of particles in yield stress fluids. *Journal of Rheology*, *59*(6), 1449–1486. https://doi.org/10.1122/1.4934363

Peyronel, F., Acevedo, N. C., Pink, D. A., & Marangoni, A. G. (2018). Supramolecular Assembly of Fat Crystal Networks from the Nanoscale to the Mesoscale. In K. Sato (Ed.), *Crystallization of Lipids: Fundamentals and Applications in Food, Cosmetics, and Pharmaceuticals* (First, pp. 143–181). John Wiley & Sons Ltd. https://doi.org/10.1002/9781118593882

Peyronel, F., Ilavsky, J., Pink, D. A., & Marangoni, A. G. (2014). Quantification of the physical structure of fats in 20 minutes: Implications for formulation. *Lipid Technology*, *26*(10), 223–226. https://doi.org/10.1002/lite.201400051

Peyronel, F., & Marangoni, A. G. (2014). In search of confectionary fat blends stable to heat: Hydrogenated palm kernel oil stearin with sorbitan monostearate. *Food Research International*, *55*, 93–102. https://doi.org/10.1016/j.foodres.2013.10.036

Pink, D. A., Townsend, B., Peyronel, F., Co, E. D., & Marangoni, A. G. (2017). Sheared edible oils studied using dissipative particle dynamics and ultra small angle X-ray scattering: TAGwood orientation aggregation and disaggregation. *Food Funct.* https://doi.org/10.1039/C7FO00514H

Pink, David A, Peyronel, F., Quinn, B., Singh, P., & Marangoni, A. G. (2015). Condensation versus diffusion. A spatial-scale-independent theory of aggregate structures in edible oils: applications to model systems and commercial shortenings studied via rheology and USAXS. *Journal of Physics D: Applied Physics*, *48*(38), 384003. https://doi.org/10.1088/0022-3727/48/38/384003

Ramel, P. R., Co, E. D., Acevedo, N. C., & Marangoni, A. G. (2016). Structure and functionality of nanostructured triacylglycerol crystal networks. *Progress in Lipid Research*, *64*, 231–242. https://doi.org/10.1016/j.plipres.2016.09.004

Rousseau, D. (2013). Trends in structuring edible emulsions with Pickering fat crystals. *Current Opinion in Colloid and Interface Science*, *18*(4), 283–291. https://doi.org/10.1016/j.cocis.2013.04.009

Sato, K., Bayés-García, L., Calvet, T., Cuevas-Diarte, M. À., & Ueno, S. (2013). External factors affecting polymorphic crystallization of lipids. *European Journal of Lipid Science and Technology*, *115*(11), 1224–1238. https://doi.org/10.1002/ejlt.201300049

Tran, T., & Rousseau, D. (2016). Influence of shear on fat crystallization. *Food Research International*, *81*, 157–162. https://doi.org/10.1016/j.foodres.2015.12.022

Trezza, E., Haiduc, A. M., Goudappel, G. J. W., & van Duynhoven, J. P. M. (2006). Rapid phase-compositional assessment of lipid-based food products by time domain NMR. *Magnetic Resonance in Chemistry*, *44*, 1023–1030. https://doi.org/10.1002/mrc.1893

van Dalen, G., van Velzen, E. J. J., Heussen, P. C. M., Sovago, M., van Malssen, K. F., & van Duynhoven, J. P. M. (2017). Raman hyperspectral imaging and analysis of fat spreads. *Journal of Raman Spectroscopy*, (February), 1075–1084. https://doi.org/10.1002/jrs.5171

Supplementary material

Table S5.1 Triacylglyceride (TAG) composition of MFC powder obtained by GCMS.

TAG	%
PPP	16.82
LaLaLa	1.33
LaPP	9.73
LaLaMy	0.73
LaLaP	4.28
PLaP	5.60
POP	5.10
PPO	4.82
CyLaLa	0.33
LaMyLa	0.38
CiLaLa	0.49
MyPP	3.45
LaLaS	0.29
LaOP	2.96
PPS	2.32
PMyP.	2.06

Table S5.2. Fatty acid (FA) composition of MFC powder obtained by GCMS.

Fatty acid	**MFC**
Saturated, S (Cx:0):	**82%**
Stearic acid; St (C18:0)	5%
Palmitic acid; P	50%
Myristic acid; M	7%
Lauric acid; L (C12:0)	20%
Unsaturated; U (C18:x)	**12%**
Others	**6%**

Table S5.3. Fatty acid (FA) compositions of sunflower (SF) and bean oils (BO) oils used for MFC dispersions, of supernatants (SF-sup, BO-sup) obtained by centrifugation of these MFC dispersions. Fatty acid compositions were obtained by GCMS.

	Oils		**Supernatants**		**Relative increase**	
Fatty acid	**SF**	**BO**	**SF-sup**	**BO-sup**	**SF-sup**	**BO-sup**
C12:0	0.1	0	1.9	1.5		
C14:0	0.1	0	0.8	0.5		
C16:0	7.1	11.2	12	13.1	70%	16%
C18:0	3.4	3.9	3.4	3.8		
C20:0	0.3	0.4	0.2	0.4		
C22:0	0.7	0.4	0.6	0.4		
C24:0	0.3	0	0.2	0.1		
C18:1	30.4	24.8	27.5	24.2		
C18:2	57	51.4	52.1	47.9		
C18:3	0.1	7	0.2	6.7		

(A) (B)

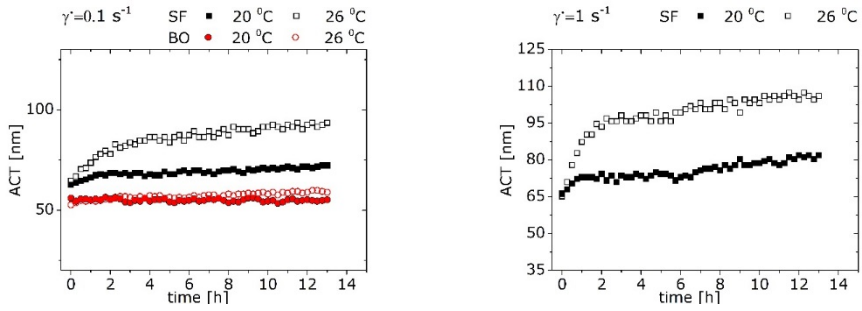

Figure S5.1. *Effect of temperature on the recrystallisation of the MFC nanoplatelets.* Average Crystal Thickness (ACT) as a function of time for MFC nanoplatelets dispersed in sunflower (SF) (black) and bean (BO) (red) oils at 20 ^{0}C and 26 ^{0}C at imposed shear rate 0.1 and 1 s^{-1}*:* ACT were obtained in rheo-SAXS Couette cell geometry (1 mm gap).

(A) (B)

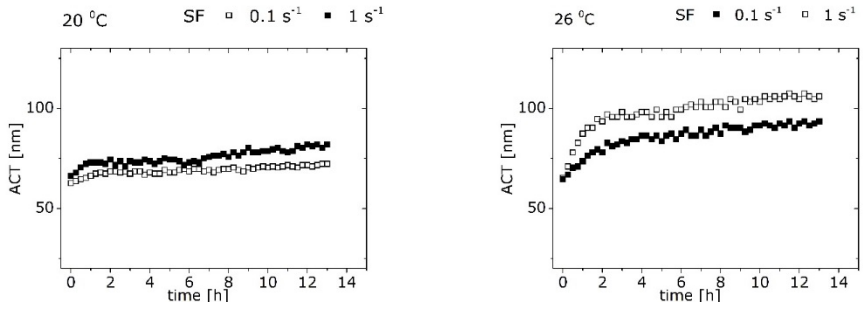

Figure S5.2. *Effect of shear on the recrystallisation of the MFC nanoplatelets.* Average Crystal Thickness (ACT) as a function of time for MFC nanoplatelets dispersed in sunflower (SF) oil at 0.1 s^{-1} and 1 s^{-1} at imposed temperatures of **(A)** 20 ^{0}C and**(B)** 26 ^{0}C*:* ACT were obtained in rheo-SAXS Couette cell geometry (1 mm gap).

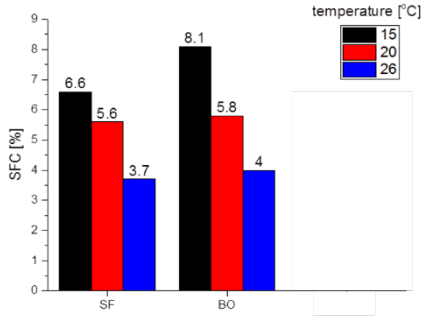

Figure S5.3. Solid Fat Content (SFC) measured for MFC nanoplatelets dispersed in sunflower (SF) and bean oils (BO) oils at 15 ^{0}C, 20 ^{0}C and 26 ^{0}C.

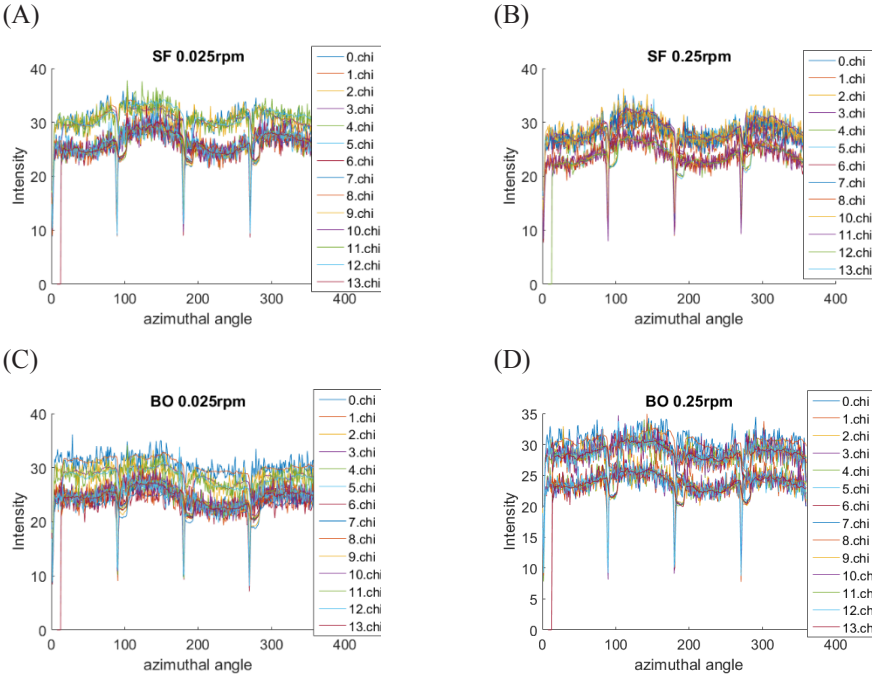

Figure S5.4. Azimuthal angle χ extension patterns from radial intensity averaging of 2D SAXS patterns at q=1.5994 nm^{-1}. The χ extension patterns show intensity changes for 10% MFC nanoplatelets dispersed in **(A)** and **(B)** SF and **(C)** and **(D)** BO at imposed shear rates 0.1 and 1 s^{-1} which were applied for 12 hours. The χ extension patterns were collected at every hour (shown by different colors). The narrow peaks correspond to the physical gaps of the detector

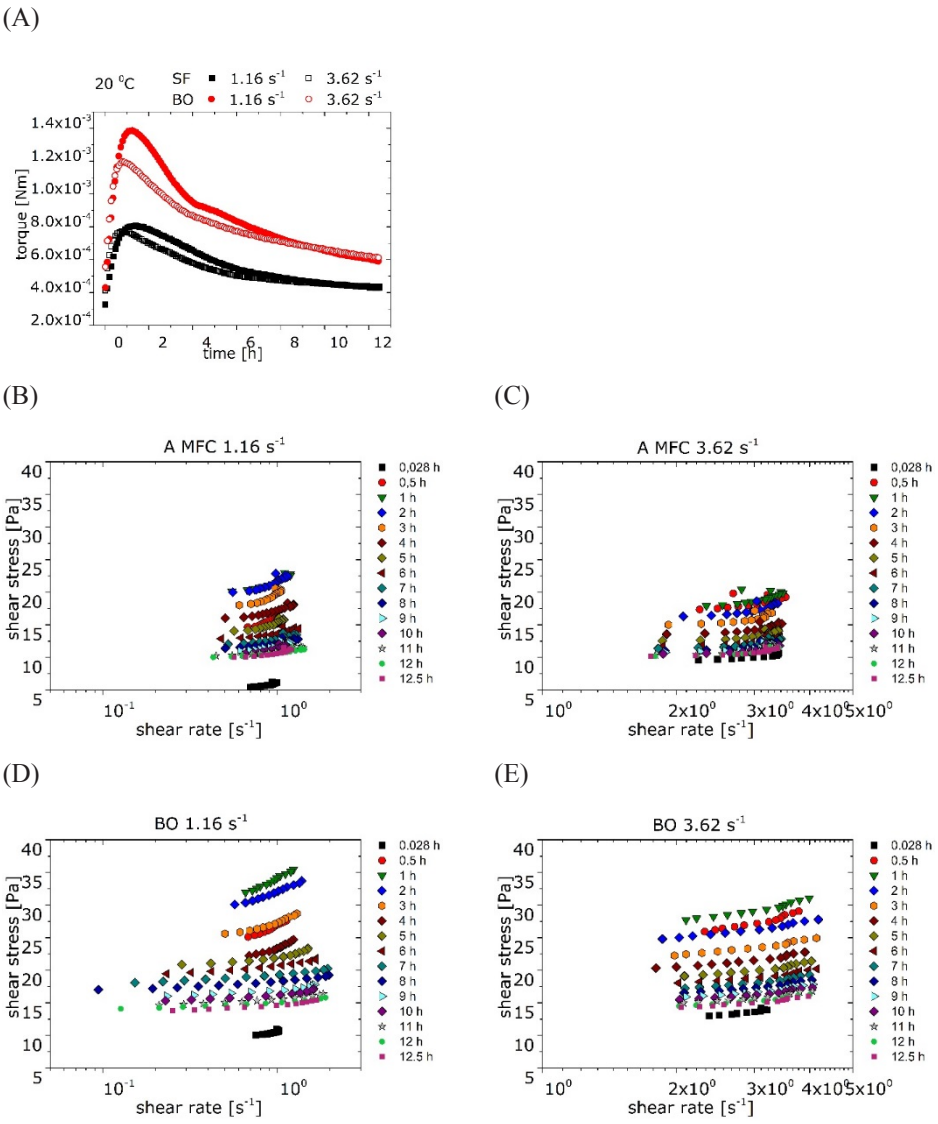

Figure S5.5. (A) Torque measurements over time for 10 % MFC nanoplatelets dispersed in Sunflower (black) and bean (BO) oils at imposed constant shear rates 1.16 (solid symbols) and 3.62 s^{-1}(empty symbols). Corresponded to the torque measurements local flow curves obtained for MFS nanoplatelets dispersed in SF (**B**) and (**C**) and BO (**D**) and (**E**) at imposed constant shear rates 1.16 and 3.62 s^{-1}.

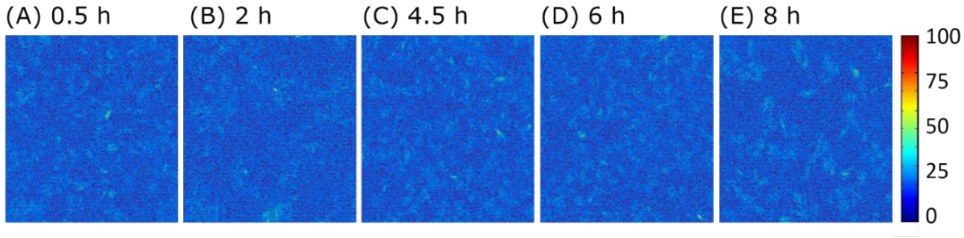

Figure S5.6.

Compositional maps (50x50 μm) obtained from 216x216 hyperspectral Raman cubes recorded for MFC nanoplatelets dispersed in SF during network formation under shear in a stirred bowl. The scale bar represents solid fat content (SFC) on a scale between 0-100% (weight percentage). The compositional maps represent the MFC network at (A) 0.5, (B) 2, (C) 4.5 (D) 6 and (E) 8 hours. In half an hour (A) a random spatial distribution of solid fat was observed, while after 8 hours of shear (E) the MFC aggregates became more apparent.

CHAPTER 6

Impact of water degumming and enzymatic degumming on gum mesostructure formation in crude soybean oil

This chapter has been submitted as T. Nikolaeva, T. Rietkerk, A. Sein, R. Dalgliesh, W. G. Bouwman, E. Velichko, B. Tian, H. Van As and J. van Duynhoven (2019). Impact of water degumming and enzymatic degumming on gum mesostructure formation in crude soybean oil.

Abstract

Phospholipid (PL) mesostructures of gums formed in crude soybean oil after water degumming (WD) and enzymatic degumming (ED) were studied at a range of PL and water concentrations. For ED, phospholipase C (PLC), phospholipase A2 (PLA2) and a mixture of phospholipases Purifine 3G (3G) were used. Both WD and ED resulted in lamellar liquid-crystalline phases, where the dependence of the water layer thickness on the ratio between water and amount of amphiphilic lipids differed for WD and PLA2 ED vs PLC and 3G ED. The distinct difference between these two types of gums was attributed to differences in amphiphilic lipid composition, in particular the partial incorporation of diglycerides (DGs) and free fatty acids (FFAs) into gum bilayers after PLC and 3G ED. In relaxation FID-CPMG NMR decays, the gum is represented by populations with T_2 relaxation times of 15-20 μs ($p(gum_r)$, rigid amphiphilic lipid protons present in bilayers) and 12-45 ms ($p(gum_m)$, protons of water and mobile amphiphilic lipid headgroups). Also, the dependencies of relaxation rate $1/T_2$ on bilayer spacings as measured by SANS and SAXS followed distinct behaviours for WD and PLA2 ED vs PLC and 3G ED. The quantification of the total gum phase (water and amphiphilic lipids) according to the sum of the two T_2 fractions ($p(gum_r)$ and $p(gum_m)$) was in agreement with lipid compositional data, which confirms that the gum phase consists of water, PLs and part of their enzymatic conversion products. The efficiency of WD and ED treatments can be estimated from the resulting amount rigid of amphiphilic lipids (gum_r).

6.1. Introduction

Degumming is a main refining step to remove phospholipids (PLs) as gums from crude oils in order to obtain high qualitative edible oil products (Dijkstra, n.d.; Sagalowicz et al., 2016). Water degumming (WD) is the traditional refining process effectuated by hydration of PLs and their reorganization into a lamellar liquid-crystalline mesophase (Sein, Hitchman, & Dayton, 2019) The WD gums are usually separated from the oil phase by gravitational forces. The separation efficiency of WD is however poor, leading to high loss of neutral oil via the gum. A well-known alternative to WD is enzymatic degumming (ED) performed by phospholipases that hydrolyze phospholipids and, thus, significantly improve separation efficiency (Dayton & Galhardo, 2014; Sein et al., 2019). So far, most investigations into ED focussed on the chemical characterization of the enzymatic conversion of PLs into their post-reaction products (Dijkstra, 2011; Jiang, Chang, Wang, Jin, & Wang, 2014; Sein et al., 2019; Xie & Dunford, 2017; Ye et al., 2016). The implication of the different degumming treatments on gum mesostructures have however been largely neglected. Our current insights in the mesoscale structure of gum-like systems are mainly based on binary models consisting of single PLs and water (Kučerka, Pencer, Sachs, Nagle, & Katsaras, 2007; Nagle & Tristram-Nagle, 2000). In these binary model systems, PLs occur as bilayers separated by water layers, comprising a swollen lamellar phase. In a previous study (Lei, Ma, Kodali, Liang, & Ted Davis, 2003) a partial phase diagram was constructed of the soybean oil/PL/water model system, which can be considered as a model for gums formed in oil after WD. Based on investigations of the swelling capacity of PLs at various PL-to-water ratios, it was concluded that under industrial relevant WD conditions, gums exist as hydrated PLs in a lamellar liquid-crystalline (LC) phase. Several hypotheses on gum mesostructure were proposed, but these were not underpinned by structural characterisations (Lei et al., 2003).

To the best of our knowledge no detailed investigation on the impact of ED on gum mesostructures has been performed to date. The lack of detailed insights in modifications of gum mesostructures impedes optimisation of both WD and ED processes (Dijkstra, 2011; Sen Cupta, 1986; Ye et al., 2016).

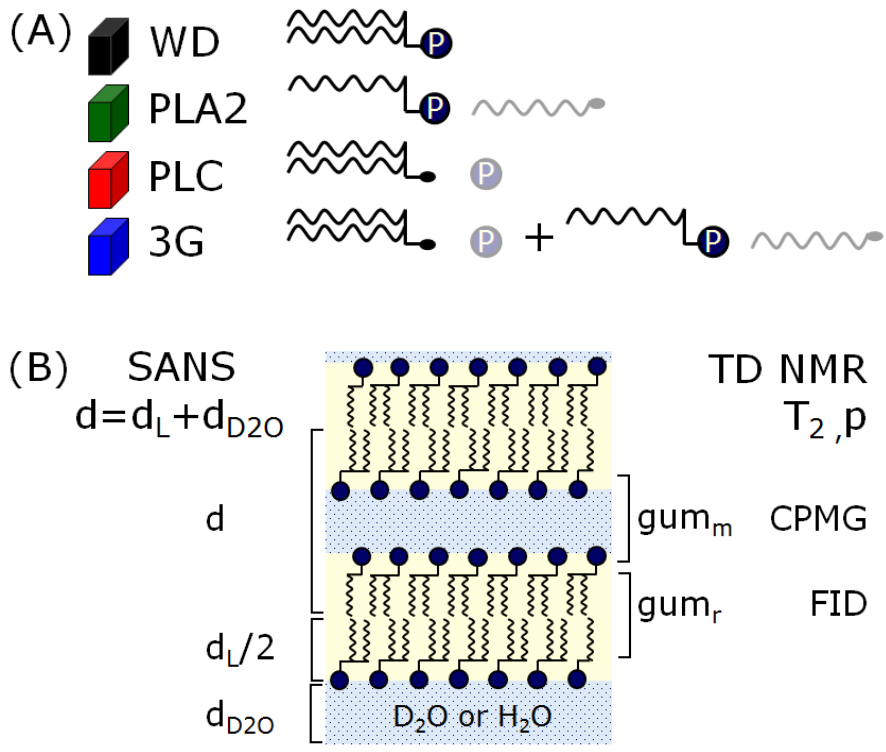

Figure 6.1. (A) Schematic representation of the impact of water degumming (WD -black), phospholipase C (PLC - red), phospholipase A2 (PLA2 - green) and their mixture Purifine 3G (3G - blue) enzymatic degumming (ED) on phospholipids (PLs) in oil. **(B)** A schematic picture of a PL bilayer and its mesostructural characterization by SANS and time-domain (TD) NMR T_2 relaxometry. The spacings (d) obtained from SANS experiments are determined by dimensions of amphiphilic lipids (d_L) and a water layers (d_{D2O}). From FID-CPMG NMR relaxometry T_2 values and proton populations (p) can be obtained for the mobile aqueous layer ($p(gum_m)$, CPMG) and the rigid hydrophobic layer ($p(gum_r)$, FID) consisting of packed alkyl chains.

In this study we will focus on quantitative characterization of gum mesostructures after WD and ED using phospholipase A2 (PLA2), phospholipase C (PLC), or a mixture of phospholipases Purifine 3G (3G), under industrially relevant conditions. The 3G ED process involved a mixture of PLC, phosphatidyl-inositol-specific PLC, PI-PLC, and a minor amount

of PLA2, and it is known for its highly efficient conversion of PLs into predominantly diglycerides (DGs), phosphates, some free fatty acids (FFAs) and lysophospholipids (LPLs) (Sein et al., 2019). An overview of the expected enzymatic conversion products is given in Figure 6.1(A).

WD and ED were performed at initial water concentrations (relative to PLs) between 1.5 and 31 w/w% on native and lecithin-enriched soybean crude oils with a known range of PLs (PC, PE, PI and PA). 31P and 1H quantitative NMR (qNMR) (Van Duynhoven, van Velzen, & Jacobs, 2013; van Rijn, J., Groen, P., Lankhorst, 2019) were used to monitor the impact of WD and ED on lipid compositions. SANS and SAXS were used to estimate thickness of the hydration water layers by quantifying the repeating distance between the bilayers d (spacings). For the SANS experiments, WD and ED was mimicked using D2O instead of H2O, in order to enhance contrast and specifically assess the water layers between the PL bilayers (Figure 6.1(B)). 2H NMR spectroscopy and 1H time-domain (TD) NMR T2 relaxometry were used to obtain information about molecular mobility in the gum mesophase and its overall quantification. We hypothesized that T2 relaxometry would be able to distinguish the molecular mobility of water and hydrated headgroups from the rigid hydrophobic layer consisting of packed alkyl chains (Figure 6.1(B)). Furthermore, we investigated whether TD NMR T2 relaxometry can be used to quantify the amount of gum in gum/oil dispersions upon the various degumming treatments.

6.2. Materials and methods

6.2.1. Materials

Crude soybean oil was obtained as Expander Soybean, DSM. The crude soybean oil contained phosphatidylcholine (PC) 0.83w/w%, phosphatidylethanolamine (PE) 0.57w/w%, phosphatidylinositol (PI) 0.51w/w%, phosphatidic acid (PA) 0.23w/w%, free fatty acids (FFAs) 0.21w/w% and diglycerides (DGs) 0.62w/w%. Lecithin was obtained as Leciplus F NMG # 71CMAS2001 by Cereal Docks Food (Italy), which contained 30-40w/w% phospholipids (PLs) with a similar PL profile as crude soy bean oil, the remaining part being predominantly triglyceride (TG) oil. The total PL concentration in the crude oil was

2.2w/w%, according to compositional analysis by ^{31}P NMR. PL-enriched oil samples were obtained by adding lecithin in weight concentrations of 12.1 and 27.5w/w% in order to end up with estimated total PL concentrations of respectively 6 and 12w/w%. All reported PL concentrations of the enriched-oil samples are based on actual compositional analyses performed by ^{31}P NMR. Phospholipases were provided by DSM Food Specialties (Delft, the Netherlands): phospholipase A2 (PLA2), phospholipase C (PLC) and Purifine® 3G (3G). The PLA2 enzyme was produced by a selected strain of *Aspergillus niger*. The PLC enzyme produced by a selected strain of *Pichia Pastoris*, a PI specific phospholipase C enzyme produced by a selected strain of *Pseudomonas fluorescence*. Purifine® 3G is a combination of three separate phospholipase enzymes [PLC, PI-PLC and PLA2].

6.2.2. Sample preparation

Samples were made to mimic the state of PLs after WD or ED processes before separation of gum from oil. High-shear mixing (using an Ultra Turrax) during 15min at full power was applied at ambient temperature to homogenize the crude oil or crude oil with aliquots of lecithin. The homogenized oil was weighed out as 100 or 50 or 10g aliquots in a 250ml or 20ml screw-top Erlenmeyer flask or glass vial, respectively. The samples were placed on a 10-position digital magnetic hotplate stirrer to heat the samples up to 55 – 60ºC, while mixing at 550RPM. The enzyme solutions were prepared separately by dispersing the phospholipases in H_2O or D_2O. Water was added as either D_2O (99.9 atom%, Cambridge Isotope) or H_2O. Samples prepared with D_2O were used for SANS and ^{2}H NMR experiments. After adding water or the enzyme solutions to crude oil the system was homogenised with the Ultra Turrax during 15s. Subsequently, the samples were put on the magnetic hotplate stirrer for 5 hours in order to achieve near complete conversion. WD was provided at the same conditions by adding D_2O or H_2O at the required concentration. Each type of samples had at least two replicates.

6.2.3. PLM and SEM

Polarized light microscopy (PLM) images of the oil/gum systems were observed by an Olympus BX53 light microscope (Olympus Nederland B.V., Zoeterwoude, the Netherlands), using bright field and crossed polar mode at room temperature. Images were recorded by a digital camera. To obtain electron microscopy images the oil/gum samples were rapidly

frozen in slushed nitrogen and cryo-fractured by a razor blade knife using a QuorumTech PP3000T cryo-prep unit under high vacuum conditions (10-6 mBar) and a temperature of -135°C. Freshly made fractured surfaces were coated with a conductive Ir layer for 60 s at 20mA using the in-line coater. Samples were transferred into a Versa 3D HR FEG-Scanning Electron Microscope (Thermofisher Scientific, formerly FEI) equipped with a cryo-stage while maintaining the cryo conditions. The samples were observed at a beam voltage of 5kV and the images were recorded using an Everhart Thornley Secondary Electron Detector.

6.2.4. Lipid compositional analysis by ^{31}P quantitative NMR

The detailed description of the NMR quantification of lipid compositions has been provided elsewhere(van Rijn, J., Groen, P., Lankhorst, 2019). In short, homogenised oil/gum samples (native crude oil ~300mg, crude oil enriched with lecithin 12.1w/w% ~150mg and 27.5w/w% ~75mg) were mixed with 1ml of deoxycholic acid (DOC) buffer. The DOC buffer was prepared by dissolving 25g of DOC (97+%, Sigma-Aldrich), 5.84g of ethylenediaminetetraacetic acid (EDTA) (99+%, Aldrich), 10.9g of tris(hydroxymethyl)aminomethane (TRIS) (99.9+%, Merck) in 100mL Deuterium oxide (D_2O) (99.9 atom %, Cambridge Isotope) and 800mL MilliQ water. The pH of the DOC buffer was adjusted to pH 9.00 with a 4M potassium hydroxide solution. After 1 hour mixing by vortex the resulted samples were centrifuged and 600µL of the bottom PL/DOC layer was mixed with 50µL of an internal standard solution (triisopropyl phosphate (TIP) (96%, Aldrich) in DOC buffer at a concentration of 10 g/L). The samples were measured in standard 5mm NMR tubes. ^{31}P NMR experiments were performed on a Bruker Avance 400 III HD spectrometer equipped with a CPP BBO 400S1 BB-H&F-d-05 Z ET NMR probe. 1D ^{31}P NMR spectra were measured by at a ^{31}P Larmor frequency of 161.97 MHz and proton decoupling was achieved with the 16 WALTZ sequence. A pulse of 11.45µs, a relaxation delay (RD) of 11.5 seconds and 128 scans (NS) were used to record the spectra. The experiments were performed at temperature 27°C (300K). Concentrations were determined from the ^{31}P NMR signal ratios of phospholipids and TIP, the internal standard. The detection limit of the ^{31}P NMR method was 40µmol/100g oil per individual phospholipid and the repeatability was 3-4%.

6.2.5. Lipid compositional analysis by ^{1}H quantitative NMR

Homogenized gum/oil samples of ~20mg were mixed with 1mL of a solvent which included dimethoxybenzene (DMB) (Sigma Chemical Company) as internal standard (1g/L). The solvent was prepared by mixing chloroform-d ($CDCl_3$) (Cambridge Isotope), methanol-d4 (MeOH) (Cambridge Isotope), pyridine-d6 (PYR) (Cambridge Isotope) in the ratio 1:2:0.02 ($CDCl_3$:MeOH:PYR). The samples were measured in standard 5mm NMR tubes. The 600 MHz ^{1}H NMR experiments were performed on a Bruker Avance 600 III HD spectrometer, equipped with a CP2 TCI 600S3 H-C/N-D05 Z P NMR probe. 1D ^{1}H NMR spectra were measured by applying a pulse of 6μs, using 8 scans and a recycle delay of 25s. Concentrations of diglycerides (DGs) and free fatty acids (FFA) were determined via their ^{1}H NMR signal integrals and the one of an internal standard.

6.2.6. SANS measurements

Small-angle neutron scattering (SANS) measurements were performed at the LARMOR instrument at ISIS neutron and muon source (Didcot, the United Kingdom). The SANS mode of the LARMOR instrument has allowed for a total momentum transfer (q) range of 0.004-0.7Å^{-1}. The samples were loaded in 1 mm path length, 1 cm width, quartz Hellma cells, which were placed in a temperature-controlled sample holder. The temperature of the experiments was kept at 20^{o}C. Data were reduced using the standard routines of Mantid. Data were normalised to sample transmission and corrected for detector efficiencies and the scattering from an empty cell. The scattering of the pure solvents was subtracted accounting for the incoherent contribution to each sample. The output data was absolute scattered intensity, I(q) in cm^{-1}, versus the momentum transfer, q in Å^{-1}. The data were analyzed in SasView (www.sasview.org) in order to describe the Bragg peaks. For that the Lamellae and Lamellar_hg_stack_caille models were used where the scale, the spacing of repeated bilayers (d_spacing) and Caille parameters were varied. The fit was used in the range 0.01-0.2Å^{-1}. An average length of a PL tail and an average length of a PL head were estimated as 12.4Å and 6.8Å, respectively. The hydrophobic scattering length density (SLD) was estimated -3.8 10^{-6}/Å^{2}, hydrophilic SLD was 1.9 10^{-6}/Å^{2}, and the SLD of the solvent was 6.4 10^{-6}/Å^{2}.

6.2.7. SAXS measurements

The small angle X-ray scattering (SAXS) experiments were performed at the European Molecular Biology Laboratory (EMBL, Hamburg) at the beamline P12 (Blanchet et al., 2015). The sample was put in a capillary made of special 'Lindemann' glass (Hilgenberg, Germany) with an outer diameter of 1.5mm, wall thickness of 0.01mm and length of 80mm. Each sample was exposed to the beam for 0.045s with a wavelength of 0.124 nm. The temperature of the experiments was kept at 22ºC. Data were integrated and reduced using a standard and automated SAXS pipeline routine at P12.

6.2.8. ^{2}H NMR

The ^{2}H NMR experiments were performed on a Bruker Avance 400 III HD NMR spectrometer equipped with a CPP BBO 400S1 BB-H&F-d-05 Z ET probe. 1D ^{2}H NMR spectra were recorded by at a Larmor frequency of 61.42MHz, by applying a 90° pulse of 275μs, using 64 scans and a recycle delay of 1.2s. The FWHM of the ^{2}H NMR signal was obtained by fitting with a Lorenzian function in MestReNova (Willcott, 2009).

6.2.9. Time domain NMR relaxometry

Measurements of spin-spin relaxation times (T_2) were performed on a Maran Ultra NMR spectrometer (Resonance Instruments Ltd., Witney, United Kingdom) at 30.7MHz ^{1}H resonance frequency (0.72T magnetic field strength) at a temperature of 2 ºC ± 1ºC. To obtain full T_2 relaxation decay curves that cover both the liquid-crystalline and liquid part of the gum/oil system Carr Purcell Meiboom Gill (CPMG) and FID-CPMG pulse sequences were combined. The CPMG decay consisted of 4096 echoes with dwell time (DW) of 20μs, 5 points per echo, an echo time of 300μs and a repetition time of 3s. Experiments were averaged over 16 scans and repeated five times to define a standard deviation for the fitted T_2 values and populations. The FID-CPMG decay consisted of a FID part measured at DW of 1μs and with number of points varied between 30-70, and a CPMG part with DW of 1μs, 20 points per echo, TE of 300μs and with an echo number of 400. There was a constant difference in intensity between the CPMG and FID-CPMG relaxation decays due to the filters used for the sequences. The scaling factor was found as the ratio between CPMG parts of the respective sequences. At a next step, the FID part was adjusted by the scaling ratio. The final relaxation decay was normalised on the highest intensity of the signal. To obtain the T_2 relaxation time

distribution in oil/gum systems CPMG relaxation decays were analysed as a continuous distribution of exponents by CONTIN and as a discrete sum of exponents by SplMod (Peters et al., 2016) (Figure S6.2, supplementary material). Quantification of the normalised FID-CPMG relaxation decays was done in Origin (OriginLab, Northampton, MA). By multi exponential fitting of the CPMG part of the relaxation decay a T_2 value and a proton population (p) were obtained for every exponent. The fit of CPMG comprised data point acquired between 0.01-1.23s, which excluded the FID, and the earliest time points (2-6ms) since these were sensitive to modulations due to B_1 inhomogeneity. The relaxation decays of the highly lecithin enriched (27.5w/w%) crude oil samples were fitted with the sum of three exponentials, whereas for the lower enriched crude oil samples (12.1w/w% lecithin) and the crude oil required a fit with the sum of four exponentials.The T_2 and p values of the first (shortest T2) CPMG component were attributed to the mobile part of the gum (gum_m), which comprised water and headgroups of PL protons (Figure 6.1). The T_2 values of the rigid part of the gum (gum_r), predominantly consisting of packed alkyl chains ofPLs and other amphiphilic lipids, were obtained from the FID part of the relaxation decay by performing a linear fit. The $p(gum_r)$ was obtained from the normalized FID and CPMG data according to equation:

$$p(gum_r) = 1 - p_r(gum_m) - \sum p(oil)$$

where p(oil) corresponded to the protons of oil. The $p_r(gum_m)$ was recalculated from the proton population of the first CPMG component. Small odd-even echo modulations were present in the first points of the CPMG relaxation decay (2-6ms), these were not corrected for and decays were fitted as is.

6.2.10. Diffusion-relaxation correlation spectroscopy

A pulsed field gradient stimulated echo NMR pulse sequence (PFG-STE) to measure self-diffusion was combined with a CPMG pulse sequence to measure transversal relaxation. Measurements were performed on a Maran Ultra NMR spectrometer (Resonance Instruments Ltd., Witney, United Kingdom) mentioned above at a temperature of 21°C ± 1°C. The PFG-STE sequence was performed with a diffusion encoding time (Δ) of 40ms, and a PFG duration (δ) of 4ms. The experiment was repeated 23 times with PFG gradient strengths increasing from 0.12 to 1.11T/m, using 16 repetitions to improve signal-to-noise, and a

repetition time (TR) of 3s. The CPMG sequence was run as described above. This sequence was analysed using a 2D numerical inverse Laplace transform resulting in a 2D spectrum, showing the correlation between T2 and D (Hürlimann & Venkataramanan, 2002; Song et al., 2002). The 2D datasets were processed in IDL (ITT Visual Information Solution, Boulder, CO USA) and analysed with MATLAB (The MathWorks, Inc., Natick, MA USA) to obtain DRCOSY spectra (Peters et al., 2017s). The 2D experiment was performed with Δ values of 40, 80, 120 and 180ms.

6.2.11. DOSY

The DOSY experiments were done on a Bruker Avance 400 III HD NMR spectrometer equipped with a PH MIC 400S1 DIFF/30 probe with maximum gradient 18 T/m. 1D ^{1}H NMR spectra were recorded by applying a 90° pulse of 13.3μs. The PFG-STE sequence was performed at Δ=40ms and δ=4.16ms. The experiment was repeated 128 times with PFG gradient strengths increasing from 0.02 to 3.6 T/m, using 32 repetitions, and TR=2.31 s. The DOSY experiments were done at a temperature of 20ºC±1ºC. The analysis of the DOSY was performed in Bruker Dynamics Center 2.5.3.

6.3. Results and discussion

6.3.1. Impact of degumming on amphiphilic lipid composition

Quantitative compositional profiles of amphiphilic lipids were obtained by ^{1}H and ^{31}P qNMR. They included (weight) concentrations of phospholipids (PLs), lysophospholipids (LPLs), phosphate compounds, diglycerides (DGs) and free fatty acids (FFAs). Figure 6.2 shows the compositional profiles of lipids after water (WD) and enzymatic degumming (ED) by phospholipase C (PLC - red), phospholipase A2 (PLA2 - green) and a mixture of phospholipases Purifine 3G (3G - blue). The chart represents data obtained after the degumming processes performed in the presence of approximately 13w/w% D_2O. These profiles were similar for gums obtained with other D_2O concentrations (Figure S6.3, supplementary material). Compositional analyses for H_2O based samples (Figure S6.3, supplementary material) were also in line with those shown in Figure 6.2.

As expected, the PL compositional profiles after WD in the native and lecithin-enriched soybean crude oils consisted of phosphatidylcholine (PC), phosphatidylethanolamine (PE), phosphatidylinositol (PI) and phosphatidic acid (PA). The compositional profiles of amphiphilic lipids after ED were in line with known enzymatic conversion of the respective enzymes used (Figure 6.1 (A)). The PLA2 ED was accompanied by a PL conversion into LPLs and FFAs. After PLC ED treatments most of PC and PE were converted to 1,2-DG and phosphate compounds (Figure S6.3, supplementary material). As expected, the 3G most efficiently converted all types of PLs into LPLs, DGs and FFAs (Figure 6.1 (A)) (Sein et al., 2019).

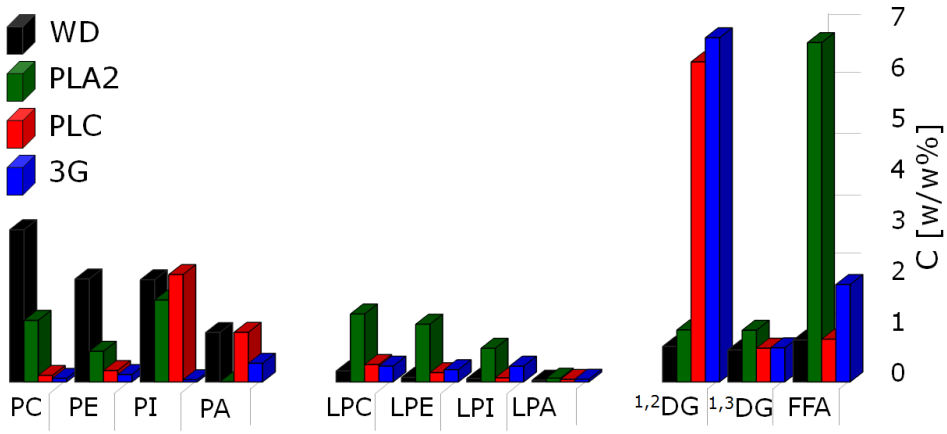

Figure 6.2. Phospholipid (PL: PC, PE, PI, PA), lysophospholipid (LPL: LPC, LPE, LPA, LPI), 1,2- and 1,3-diglyceride (1,2- and 1,3-DG) and free fatty acid (FFA) compositions in w/w% after WD (black) and ED PLC (red), PLA2 (green) and 3G (blue). The samples were prepared based on D_2O. The weighed in D_2O concentration was approximately 13w/w%, and PL concentration was between 10-11w/w%. Compositional data were obtained by ^{31}P and ^{1}H qNMR.

6.3.2. Microscale structure of gums

Figure 6.3 shows polarised light microscopy (PLM) images of gums after WD (A) and PLA2 ED (B) vs PLC (C) and 3G (D) ED processes on crude oil. All of them demonstrate the presence of lamellar liquid-crystalline (LC) phases, schematically represented in Figure 6.1 (B) (further interpretation of the PLM images can be found in Figure S6.4, supplementary material) (Sein et al., 2019). However, the topology of the lamellar phases varies for all studied samples. The WD gum shows a more planar structure on the microscale, whereas the images of the ED gums indicate the presence of spherulites that consist of curved bilayers. These could be formed because the average molecular shape of the polar lipids formed upon PLC and 3G ED treatments become more a truncated-cone like. (Sein et al., 2019; van Nieuwenhuyzen & Tomás, 2008). Figure 6.3 (E, F) shows EM images of gum formed after 3G ED on crude oil. The electron microscopy (EM) images revealed a layered morphology on the submicron scale (Figure 6.3 (E), (F)). The layer thickness is estimated to be in the order of 100-200 Å. From the PLM and EM images obtained for other degumming treatments we concluded that they all resulted in gums with lamellar LC phases, but all with a different lamellar topology. The PLM and EM images only allow for a qualitative view on submicron structures and could not resolve structural features at the nanometer scale. For further characterisation and quantification of the structural features of gums we have therefore used SANS, SAXS and NMR techniques.

6.3.3. Impact of degumming on gum mesostructure

SANS and SAXS were used to characterize and quantify the structural differences at mesoscale between gums obtained after WD and ED. Typical SANS scattering curves of gums after WD and ED are shown in Figure 6.4 (A). D_2O based samples provided a good contrast between amphiphilic lipid and water layers and this allowed for accurate determination of their repeating distances (Figure 6.1). The repeating bilayer structures manifested themselves by first and the second order Bragg peaks (Figure 6.4 (A)). Their positions were reciprocal to spacings d between the bilayers (Nieh, Glinka, Krueger, Prosser, & Katsaras, 2001; Pottage et al., 2014).

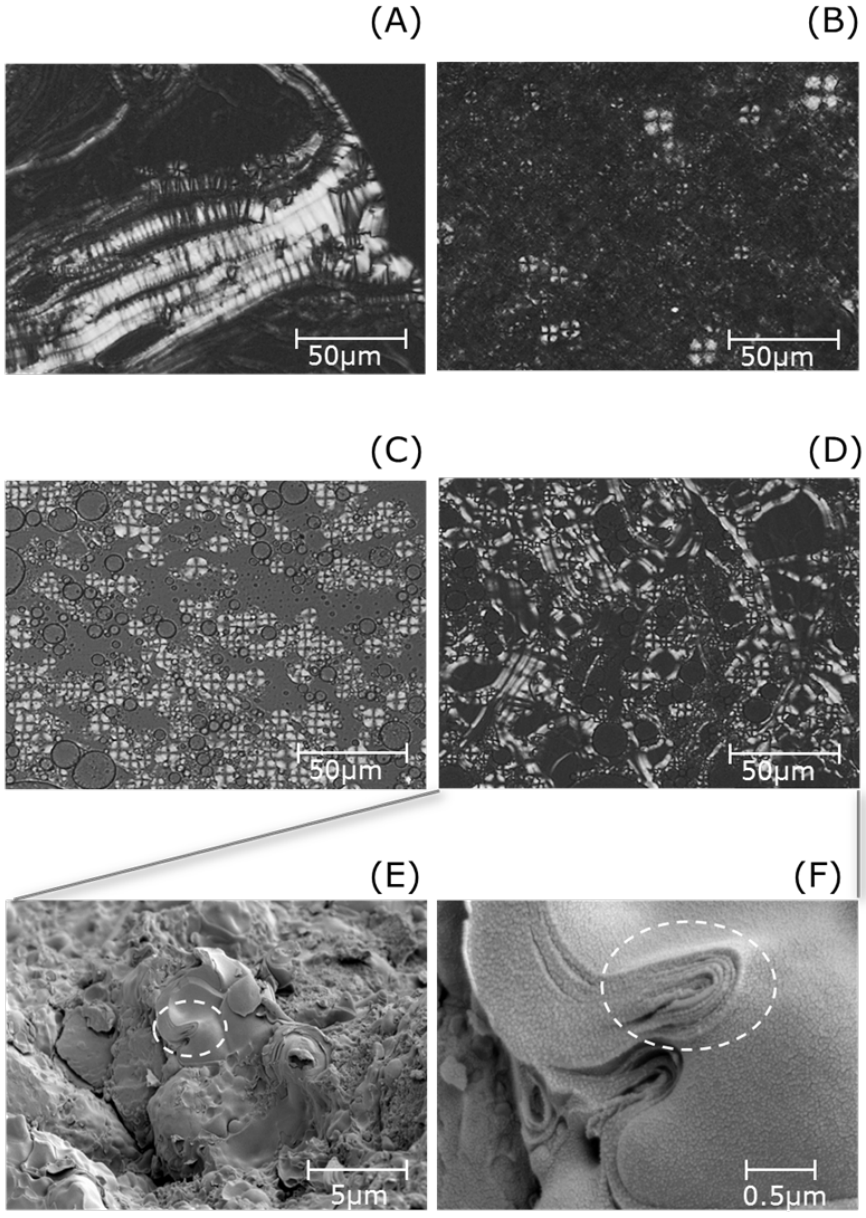

Figure 6.3. Polarized light microscopy (PLM) images obtained for gums after water degumming (WD) (A), PLA2 (B), PLC (C) and 3G (D) enzymatic degumming (ED) treatments. Electron microscopy (EM) images (E) and (F) of gums after 3G ED treatment.

The positions of the first and the second order peaks observed for the WD and PLA2 ED gums differed by a factor of two, which indicated planar lamellar LC structures at the meso scale. A curvature of the lamellar structures, as shown in the Figure 6.3, occurs at a much larger length scale (micron scale) than the repeating distance obtained by SANS. For lamellar LC phases obtained after WD and PLA2 ED conditions, the spacings were in the range from 70Å to 120Å for a low and high D_2O/PL ratios, respectively. For the samples obtained after the PLC and 3G ED treatments, the Bragg peaks were broad, pointing to the less ordered and heterogeneous structures, and/or highly flexible, undulating bilayers. The Bragg peaks were shifted to the lower q range, corresponding to spacings in the range of 100-170Å – depending on the D_2O/PL ratios.

Besides SANS experiments with D_2O based samples we also performed SAXS experiments where we could use samples prepared with H_2O. The spacings deduced from these SAXS experiments were in line with the SANS results and can be found in Figure S6.5 (supplementary material). Given the higher quality of the SANS curves, due to the contrast provided by using D_2O, we continued our analysis using these results. The slopes of the SANS curves differed significantly between samples and their replicates, indicating strong heterogeneity at the (sub)-micron scale. Hence, we refrained from attempts to characterize the gum structure at this length scale.

In order to establish the impact of ED on gum mesostructure, we assessed by ^{1}H and ^{31}P qNMR differences in amphiphilic lipid composition of the separated gum and oil phases. As expected the separated oil phase contained negligible amounts of PLs and LPLs, hence both compound classes almost exclusively ended up in the gum phase. The presence of triglycerides (TG) in the gum phase indicated that part of the oil phase was entrained there. As a consequence, we should also find DGs and FFAs in the gum since these are oil soluble. We did however find different molar ratios between triglycerides (TGs), DGs and FFAs in the separated oil and gum phases. Since the DG and FFA concentrations should be equal in the separated bulk oil and in the oil entrained in the gum, we can estimate their concentrations in the bilayer phase (Figure S6.6, supplementary material). We found that gums were up to 25% enriched by DGs and FFAs, and hypothesized that these were present as structural component in the bilayer parts.

(A)

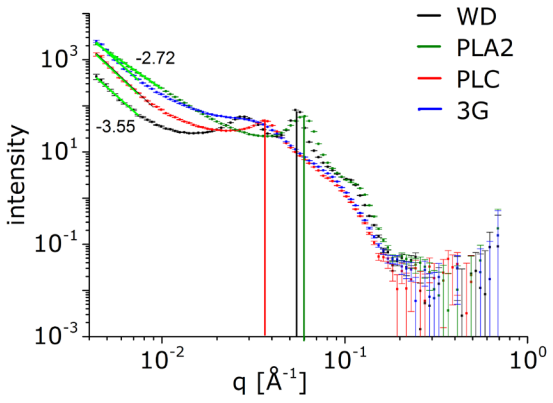

(B)

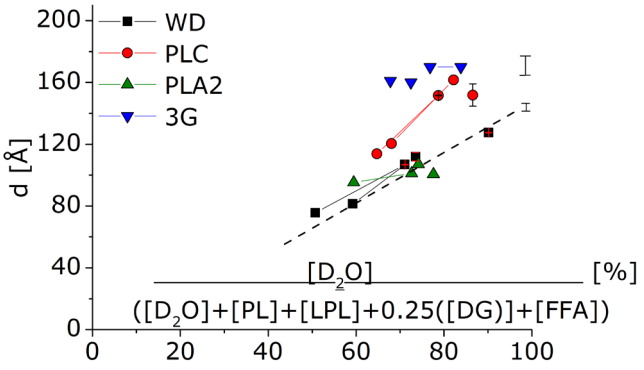

Figure 6.4. (A) SANS scattering curves of crude oil with weighed in water and lecitihin concentrations of order 13 and 27.5w/w%, respectively, after water degumming (WD - black), phospholipase C (PLC - red), phospholipase A2 (PLA2 - green) and their mixture Purifine 3G (3G - blue) enzymatic degumming (ED) treatments. The vertical lines correspond to the Bragg peaks resulting from repeating bilayers d. **(B)** Dependencies of the spacings d on ratios between D_2O and amphiphilic compounds including 25% of DGs and FFAs. The PL, LPL, DG and FFA weighted concentrations were obtained by ^{31}P and ^{1}H qNMR compositional analysis. The dashed line is intended to guide the eye.

Figure 6.4 (B) presents the correlation between spacings d deduced from the well-assigned SANS Bragg peaks and the ratio between water and the amphiphilic lipids present in the WD and ED gums. The amphiphilic lipid compositions were assumed to consist of PLs, LPLs and this excess 25% of DGs and FFAs. Overall, the relations between spacings and water/amphiphilic lipid ratio were different for WD and PLA2 ED vs PLC and 3G ED. In the case of WD and PLA2 ED the ratio between water (D_2O) and amphiphilic components were defined mainly by PLs and LPLs and FFAs (for PLA2) (Figure 6.2), since DGs were absent for these treatments. The observed linear dependence was in line with thicker water layers between PL and LPL headgroups with increasing water concentrations (Lei et al., 2003; Rand, 1989). For the PLC and 3G ED treatments also thicker water layers were found, and the ratio between water and amphiphilic components was impacted by the relative high amount of DGs expected to contribute to the bilayers – see above. We note that for the low PL and LPS levels after PLC and 3G ED treatments also the effect of glycolipids cannot be neglected. The obtained results for PLC and 3G ED showed that upon hydrolysis of the majority of PLs the resulting DGs become partially incorporated into the lamellar LC phase. Figure 6.4 (B) shows that this leads to increased spacings compared to the lamellar structures produced by WD and PLA2 ED, which can be attributed to the enhanced hydration capacity of the bilayer (Rand, 1989). The incorporation of DGs and FFAs in the bilayers may also be a main contributor to the highly flexible and possibly undulating nature of the bilayers of the gum phases after 3G or PLC ED.

6.3.4. Assignment of populations in time domain relaxation NMR decays

Time domain NMR relaxometry experiments were performed in order to quantify mobility and phase composition of the oil-gum systems. The concentration of different phases in the oil-gum systems was quantified via their proton populations and their mobility via the T_2 transverse relaxation times. A multicomponent fit with 4-5 exponentials was performed on the FID and CPMG relaxation decays recorded on native and lecithin-enriched crude soybean oils upon WD and ED in the presence of H_2O. The FID part was described with one fast-relaxation component, where T_2 values were in order of 15-20μs, with proton populations p in the range of 1-13% of the total proton population (Figure S6.2, supplementary material). This component represented the most rigid part of the gum (gum_r) and was assigned to protons from packed alkyl chains within the bilayers (Figure 6.1 (B)).

The first components of the CPMG decay had T_2 values in the range of 12-45ms and populations p between 2-35% of the total proton population, these varied with the water concentrations used for WD and ED (Figure S6.2, supplementary material). The T_2 values of this component correlated with reciprocal values of a full width at half maximum (FWHM) of ^2H NMR spectral lines of gums prepared with D_2O (Figure 6.5). This correlation indicated that this CPMG component for a major part represented protons of water between the bilayers (Figure 6.1 (B)). Their short T_2 values could be explained by surface relaxation at the bilayer interface with its strongly hydrated headgroups. This finding was corroborated by 2D diffusion-relaxation correlation experiments, where T_2 values of water and oil components were distinguished based on self-diffusion coefficients (Figure S6.7, supplementary material). DOSY experiments in addition, showed that the first CPMG component also included protons from the headgroups of the amphiphilic lipids of the gum. The 2D DOSY plots, where ^1H NMR spectra were separated based on self-diffusion coefficients, showed an overlap of water and lipid methylene signals in the range of 4.5-5.5ppm (Figure S6.7, supplementary material). This indicated that the first T_2 CPMG component comprised both water and mobile head groups of PLs, collectively making up the mobile part of the gum (gum_m).

The other CPMG components were believed to correspond to the neutral oil in the WD and ED samples (Figure S6.2, supplementary material). For the crude oil in native form and enriched with 12.1w/w% lecithin, three components with T_2 values of 53, 110 and 270ms were needed to describe the remainder of the CPMG decay. For highly lecithin-enriched (27.5w/w%) crude oil samples, only two components (85 and 260ms) could be resolved for the smaller oil signal. The T_2 values of the neutral oil components were stable and did not depend on type of degumming treatments (Figure S6.2, supplementary material).

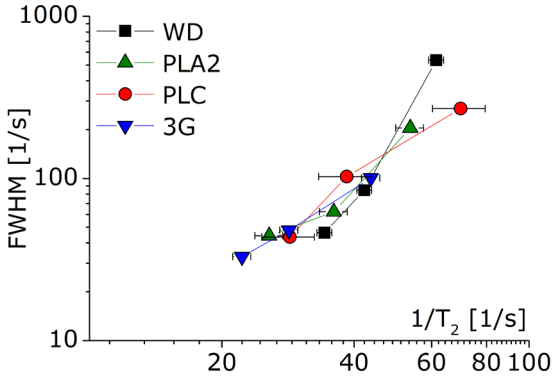

Figure 6.5. Correlation between full width at half maximum (FWHM) of D_2O ^2H NMR lineshapes (gums prepared with D_2O) and the transverse relaxation rate ($1/T_2$) of the first CPMG component (gums prepared with H_2O). Data were obtained for the lecithin-enriched crude oil with 27.5 w/w% PL concentration. The legend shows water degumming (WD - black), phospholipase C (PLC - red), phospholipase A2 (PLA2 - green) and their mixture Purifine 3G (3G - blue) enzymatic degumming (ED) treatments.

The transversal relaxation rates ($1/T_2$) of the gum_m for WD and ED correlated with the reciprocal SANS spacings d (Figure 6.6). This was in line with transversal relaxation of water layers between the bilayers of amphiphilic lipids being determined by surface-to-volume ratio. The relaxation rates were grouped in two different dependencies on the bilayer thickness, one for WD and PLA2 ED and one for PLC and 3G ED. This indicated that the mesophases formed by these two groups of degumming treatments differed with surface relaxation of the hydration water at the interface with the headgroups of the amphiphilic bilayers. This result is in line with the different dependence of the bilayer spacing on water content in the gum for the different treatments (Figure 6.4 (B)).

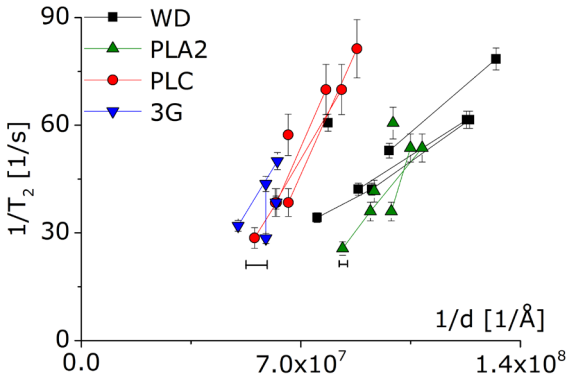

Figure 6.6. Correlation between the transverse relaxation rate ($1/T_2$) of the water layers with partly amphiphilic lipid elements and the reciprocal SANS spacings d. The legend shows water degumming (WD - black), phospholipase C (PLC - red), phospholipase A2 (PLA2 - green) and Purifine 3G (3G - blue) enzymatic degumming (ED) treatments.

6.3.5. Quantification of gums by time domain NMR relaxometry

We compared the sum of the $p(gum_r)$ and $p(gum_m)$ proton populations for the full system consisting of oil and gum by TD NMR relaxometry, with the (weight) concentrations of water and amphiphilic lipid components, as obtained by ^{31}P and ^{1}H qNMR (Figure 6.7 (A)). A well-defined correlation was observed. This confirmed that the gum mesophase consisted of water and PLs, LPLs, DGs and FFAs. We note that the majority of the DGs and the FFAs still partitioned in the bulk oil phase. The correlation also demonstrated that TD NMR T_2 relaxometry could be used as a method for quantitative assessment of the gum phase in gum/oil dispersions.

In order to assess whether TD NMR relaxometry has a potential to predict the efficiency of degumming treatments, we considered the $p(gum_r)$ population (Figure 6.1 (B)) as a measure of amphiphilic lipids present in lamellar structures. The rationale was that since $p(gum_r)$ reflected alkyl chains, present in ordered and relatively structured, rigid bilayers, it could be taken as a measure for the amount of amphiphilic lipids that could be separated by gravitational forces. Figure 6.7 (B) shows $p(gum_r)$ populations of gums after WD and ED treatments on crude oil enriched with 27.5w/w% of PLs at different water concentrations.

(A)

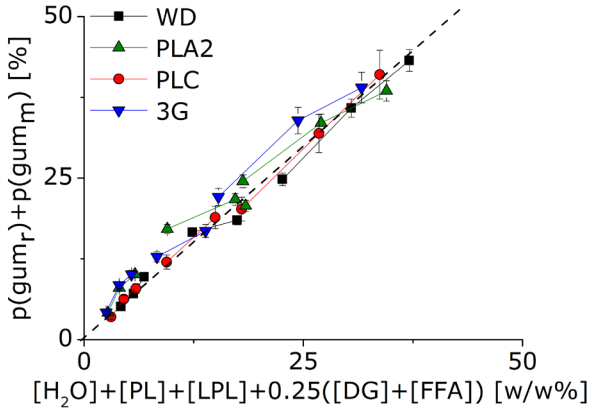

(B)

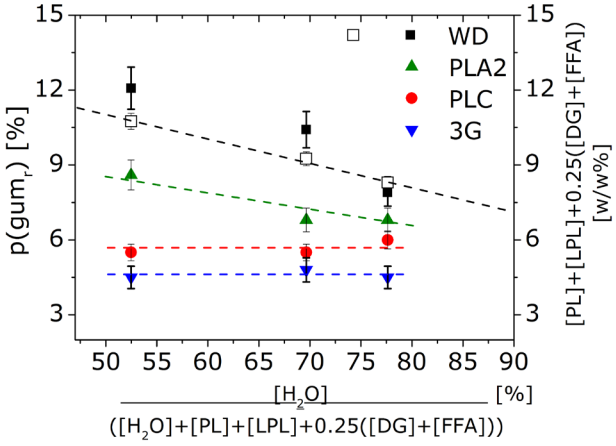

Figure 6.7. (A) Correlation between mesophase mass concentrations as determined by time domain (TD) NMR relaxometry (vertical axis) and compositional analysis by ^{31}P and ^{1}H NMR (horizontal axis). The quantification by TD NMR relaxometry is based on the amplitudes of proton populations p with T_2 relaxation times of 15–20μs (gum_r) and 12-45ms (gum_m). The concentration on the horizontal axis comprises water and amphiphilic lipids (phospholipids (PLs), lysophospholipids (LPLs), diglycerides (DGs), free fatty acids (FFAs)). **(B)** Dependencies of p(gum_r) populations for WD and ED gums (left axis) on ratio between initial concentrations of H_2O and amphiphilic compounds in gums before enzymatic conversions. The data were obtained for the crude oil enriched with 27.5w/w%

PLs. The PL, LPL, DG and FFA weighted concentrations were obtained by ^{31}P and ^{1}H qNMR compositional analysis of the enriched crude oil. The straight line and black empty squares represent the starting concentrations (before degumming) of PL, LPL, DG and FFA compounds (right axis). The legends show water degumming (WD - black), phospholipase C (PLC - red), phospholipase A2 (PLA2 - green) and their mixture Purifine 3G (3G - blue) enzymatic degumming (ED) treatments. The dashed lines are intended to guide the eye.

The $p(gum_r)$ populations were plotted as a function of the ratio between initial concentrations of H_2O and amphiphilic compounds in gums, before WD and ED treatments. The decrease in $p(gum_r)$ population for WD gums followed the decrease in initial weight fraction of amphiphilic lipids due to the increased water concentration (Figure 6.7 (B)). This validated that the amphiphilic lipids predominantly ended up in the bilayers of the gum phase. For the ED we observed that the amount of amphiphilic lipids incorporated in the lamellar LC phase decreased significantly. This was in line with the enzymatic conversion of amphiphilic lipids. The decreased amount of lamellar LC phase as reflected in $p(gum_r)$ populations followed the order WD, PLA2, PLC and 3G, which was in line with the expected efficiency of enzymatic conversions of the initially present PLs (Figure 6.1(A) and 6.2).

For lower initial levels of PLs the observed effects on $p(gum_r)$ were smaller compared to experimental error, but still we could discern similar trends as shown in Figure 6.7 (B). Further investigations are necessary to explore whether the separation efficiency of gums from oil after WD and ED can quantitatively be monitored via TD-NMR assessment of $p(gum_r)$ populations.

6.4. Conclusions

Both WD and ED resulted in gum phases composed of amphiphilic lipids, which form lamellar liquid crystalline phases. After PLC and 3G ED the gum structures were depleted in phospholipids (PLs) and enriched in diglycerides (DGs) and free fatty acids (FFAs). SAXS and SANS showed that gums formed by PLC and 3G ED were more swollen as compared to

those formed by WD and PLA2 ED. Compositional analysis of the separated oil and gum phases indicated that this distinct difference between these two types of gums could be attributed to incorporation of DGs and FFAs in bilayers of gums formed by PLC and 3G ED. Time domain (TD) NMR relaxometry showed that this also introduced more effective surface relaxation for the hydration layers in these gums. Both the total amount of gum as well as the amount of amphiphilic lipids in the gum can be determined by means of TD FID-CPMG relaxation NMR, which opens the opportunity to assess the efficiency of degumming treatments.

Acknowledgements

Adam Washington (LARMOR 247 beamline, ISIS neutron and muon source, UK) is acknowledged for his help and technical assistance during SANS experiments. The synchrotron SAXS data was collected at beamline P12 operated by EMBL Hamburg at the PETRA III storage ring (DESY, Hamburg, Germany). We would like to thank Dmitry "Dima" Molodenskiy for the assistance in using the beamline. Myraise van Stijn, Pierre Noirez (DSM, Geleen) acquired electron microscopy micrographs. Remco Muntendam, Tony van den Burg are acknowledged for help and technical assistance during preparation of gum samples after different types of degumming treatments. This work is part of the SSCANFOODS (project number 13386) research program, which is financed by The Netherlands Organisation for Scientific Research (NWO).

References

Blanchet, C. E., Spilotros, A., Schwemmer, F., Graewert, M. A., Kikhney, A., Jeffries, C. M., … Svergun, D. I. (2015). Versatile sample environments and automation for biological solution X-ray scattering experiments at the P12 beamline (PETRA III, DESY). *Journal of Applied Crystallography*, *48*(2), 431–443. https://doi.org/10.1107/s160057671500254x

Dayton, C. L. G., & Galhardo, F. (2014). Enzymatic Degumming. *Green Vegetable Oil Processing*, 107–145. https://doi.org/10.1016/B978-0-9888565-3-0.50009-1

Dijkstra, A. J. (n.d.). Edible Oil Processing: Introduction to Degumming. Retrieved from http://lipidlibrary.aocs.org/OilsFats/content.cfm?ItemNumber=40325

Dijkstra, A. J. (2011). Enzymatic degumming. *Lipid Technology*, *23*(2), 36–38. https://doi.org/10.1002/lite.201100085

Hürlimann, M. D., & Venkataramanan, L. (2002). Quantitative measurement of two-dimensional distribution functions of diffusion and relaxation in grossly inhomogeneous fields. *Journal of Magnetic Resonance*, *157*(1), 31–42. https://doi.org/10.1006/jmre.2002.2567

Jiang, X., Chang, M., Wang, X., Jin, Q., & Wang, X. (2014). A comparative study of phospholipase A1 and phospholipase C on soybean oil degumming. *JAOCS, Journal of the American Oil Chemists' Society*, *91*(12), 2125–2134. https://doi.org/10.1007/s11746-014-2555-6

Kučerka, N., Pencer, J., Sachs, J. N., Nagle, J. F., & Katsaras, J. (2007). Curvature effect on the structure of phospholipid bilayers. *Langmuir*, *23*(3), 1292–1299. https://doi.org/10.1021/la062455t

Lei, L., Ma, Y., Kodali, D. R., Liang, J., & Ted Davis, H. (2003). Ternary phase diagram of soybean phosphatidylcholine-water-soybean oil and its application to the water degumming process. *JAOCS, Journal of the American Oil Chemists' Society*, *80*(4), 383–388. https://doi.org/10.1007/s11746-003-0708-y

Nagle, J. F., & Tristram-Nagle, S. (2000). Structure of lipid bilayers. *Biochimica et Biophysica Acta - Reviews on Biomembranes*, *1469*(3), 159–195. https://doi.org/10.1016/S0304-4157(00)00016-2

Nieh, M.-P., Glinka, C. J., Krueger, S., Prosser, R. S., & Katsaras, J. (2001). SANS Study of the Structural Phases of Magnetically Alignable Lanthanide-Doped Phospholipid Mixtures. *Langmuir*, *17*(9), 2629–2638. https://doi.org/10.1021/la001567w

Peters, J. P. C. M., Vergeldt, F. J., As, H. Van, Luyten, H., Boom, R. M., Jan, A., & Goot, V. Der. (2016). Food Hydrocolloids Time domain nuclear magnetic resonance as a method to determine and characterize the water-binding capacity of whey protein microparticles. *Food Hydrocolloids*, *54*, 170–178. https://doi.org/10.1016/j.foodhyd.2015.09.031

Peters, J. P. C. M., Vergeldt, F. J., As, H. Van, Luyten, H., Boom, R. M., Jan, A., & Goot, V. Der. (2017). Food Hydrocolloids Unravelling of the water-binding capacity of cold-gelated whey protein microparticles. *Food Hydrocolloids*, *63*, 533–544. https://doi.org/10.1016/j.foodhyd.2016.09.038

Pottage, M. J., Kusuma, T., Grillo, I., Garvey, C. J., Stickland, A. D., & Tabor, R. F.

(2014). SI_Fluorinated lamellar phases: structural characterisation and use as templates for highly ordered silica materials. *Soft Matter*, (May 2014), 1–2. https://doi.org/10.1039/c4sm00666f

Rand, R. (1989). (CUL-ID:1654990) Hydration forces between phospholipid bilayers. *Biochimica et Biophysica Acta (BBA) - Reviews on Biomembranes*, *988*(3), 351–376. https://doi.org/10.1016/0304-4157(89)90010-5

Sagalowicz, L., Moccand, C., Davidek, T., Ghanbari, R., Martiel, I., Negrini, R., … Michel, M. (2016). Lipid self-assembled structures for reactivity control in food. *Philosophical Transactions A*, *374*, 20150136. https://doi.org/10.1098/rsta.2015.0136

Sein, A., Hitchman, T., & Dayton, C. L. G. (2019). Enzymes in Vegetable Oil Degumming Processes. In A. Vogel & O. May (Eds.), *Industrial Enzyme Applications* (pp. 323–350). Wiley-VCH.

Sen Cupta, A. K. (1986). Neuere Entwicklungen auf dem Gebiet der Raffination der Speiseöle. *Fette Seifen Anstrichm.*, *88*, 79–86. https://doi.org/https://doi.org/10.1002/lipi.19860880302

Song, Y. Q., Venkataramanan, L., Hürlimann, M. D., Flaum, M., Frulla, P., & Straley, C. (2002). T1-T2 correlation spectra obtained using a fast two-dimensional Laplace inversion. *Journal of Magnetic Resonance*, *154*(2), 261–268. https://doi.org/10.1006/jmre.2001.2474

Van Duynhoven, J., van Velzen, E., & Jacobs, D. M. (2013). *Quantification of complex mixtures by NMR*. *Annual Reports on NMR Spectroscopy* (1st ed., Vol. 80). Elsevier Ltd. https://doi.org/10.1016/B978-0-12-408097-3.00003-2

van Nieuwenhuyzen, W., & Tomás, M. (2008). *Update on vegetable lecithin and phospholipid technologies*. *European Journal of Lipid Science and Technology* (Vol. 110). https://doi.org/10.1002/ejlt.200800041

van Rijn, J., Groen, P., Lankhorst, P. et al. (2019). Robust and reliable quantification of phospholipids in edible oils using 31P NMR spectroscopy. *Journal of the American Oil Chemists' Society*. https://doi.org/submitted

Willcott, M. R. (2009). MestRe Nova. *The Journal of the American Chemical Society*, 906709–906709. https://doi.org/10.1021/ja906709t

www.sasview.org. (n.d.). Retrieved from http://www.sasview.org/

Xie, M., & Dunford, N. T. (2017). Lipid composition and emulsifying properties of canola lecithin from enzymatic degumming. *Food Chemistry*, *218*, 159–164. https://doi.org/10.1016/j.foodchem.2016.09.074

Ye, Z., Qiao, X., Luo, Z., Hu, C., Liu, L., & He, D. (2016). Optimización y comparación del desgomado con agua y el desgomado con fosfolipasa C de aceite de colza. *CYTA - Journal of Food*, *14*(4), 604–612. https://doi.org/10.1080/19476337.2016.1182218

Supplementary material

The equation for the scattering length density:

$$\rho_b = \frac{1}{V_0}\sum_d b_d$$

b_D = 6.674 fm
b_O = 5.805 fm
b_C = 6.6484 fm
b_H = -3.742 fm
b_N = 9.36 fm
b_P = 5.13 fm

$V_{0,D2O}$ = 30 Å^3
$V_{0,hydrophobic}$ = 808 Å^3
$V_{0,hydrophilic}$ = 319 Å^3

Hydrophobic: 2*$C_{14}H_{29}$
Hydrophilic: $C_8H_{14}NO_8P$

Filling in de equation with the quantities:

$$\rho_{b,D_2O} = \frac{1}{V_{0,D_2O}}(2b_D + b_O) = 6.384 \cdot 10^{10} / cm^2$$

$$\rho_{b,hydrophobic} = \frac{1}{V_{0,hydrophobic}}(2 \cdot 14 \cdot b_C + 2 \cdot 29 \cdot b_H) = -3.822 \cdot 10^{9} / cm^2$$

$$\rho_{b,hydrophilic} = \frac{1}{V_{0,hydrophilic}}(8 \cdot b_C + 14 \cdot b_H + b_N + 8 \cdot b_O + b_P) = 1.935 \cdot 10^{10} / cm^2$$

$$\rho_{b,DMPC} = \frac{1}{V_{0,hydrophobic} + V_{0,hydrophilic}}(36 \cdot b_C + 72 \cdot b_H + b_N + 8 \cdot b_O + b_P) = 2.737 \cdot 10^{9} / cm^2$$

The excess scattering length density:

$$\Delta\rho = \rho_b - \rho_s$$

Taking the values from the previous calculation:

$$\Delta\rho_{hydrophobic} = \rho_{hydrophobic} - \rho_{D_2O} = -6.766 \cdot 10^{10} / cm^2$$

$$\Delta\rho_{hydrophilic} = \rho_{hydrophilic} - \rho_{D_2O} = -4.449 \cdot 10^{10} / cm^2$$

$$\Delta\rho_{average} = \rho_{DMPC} - \rho_{D_2O} = -5.994 \cdot 10^{10} / cm^2$$

Figure S6.1. Scattering length densities used for the analysis of SANS data.

(A)

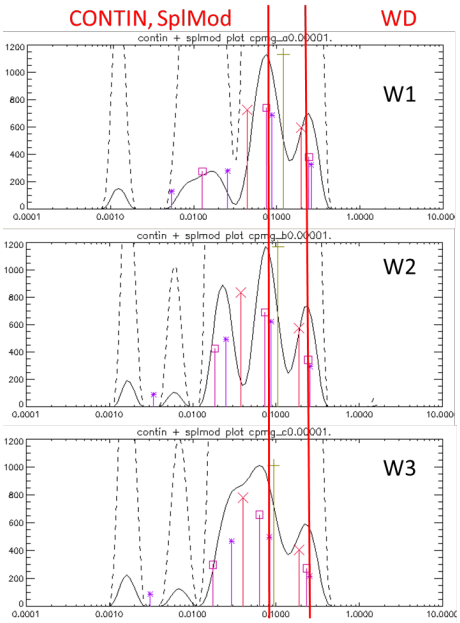
CONTIN, SplMod
WD
W1
W2
W3

(B)

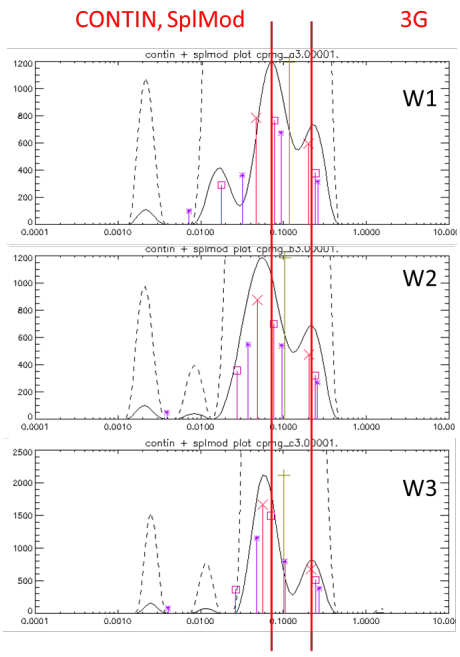
CONTIN, SplMod
3G
W1
W2
W3

(C)

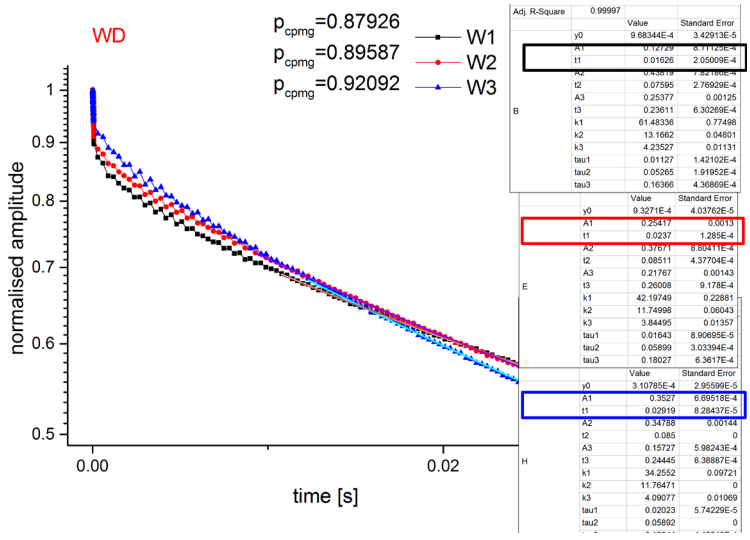
WD
p_{cpmg}=0.87926
p_{cpmg}=0.89587
p_{cpmg}=0.92092
W1
W2
W3
normalised amplitude
time [s]
Adj. R-Square 0.99997
Value Standard Error
y0 9.68344E-4 3.42913E-5
t1 0.01626 2.05009E-4
t2 0.07595 2.76929E-4
A3 0.25377 0.00125
t3 0.23611 6.30269E-4
k1 61.48336 0.77498
k2 13.1662 0.04801
k3 4.23527 0.01131
tau1 0.01127 1.42102E-4
tau2 0.05265 1.91952E-4
tau3 0.16366 4.36869E-4
Value Standard Error
y0 9.3271E-4 4.03762E-5
A1 0.25417 0.0013
t1 0.0237 1.285E-4
A2 0.37671 8.80411E-4
t2 0.08511 4.37704E-4
A3 0.21767 0.00143
t3 0.26008 9.178E-4
k1 42.19749 0.22881
k2 11.74998 0.06043
k3 3.84495 0.01357
tau1 0.01643 8.90695E-5
tau2 0.05899 3.03394E-4
tau3 0.18027 6.3617E-4
Value Standard Error
y0 3.10785E-4 2.95599E-5
A1 0.3527 6.69518E-4
t1 0.02919 8.28437E-5
A2 0.34788 0.00144
t2 0.085 0
A3 0.15727 5.98243E-4
t3 0.24445 6.38887E-4
k1 34.2552 0.09721
k2 11.76471 0
k3 4.09077 0.01069
tau1 0.02023 5.74229E-5
tau2 0.05892 0

(D)

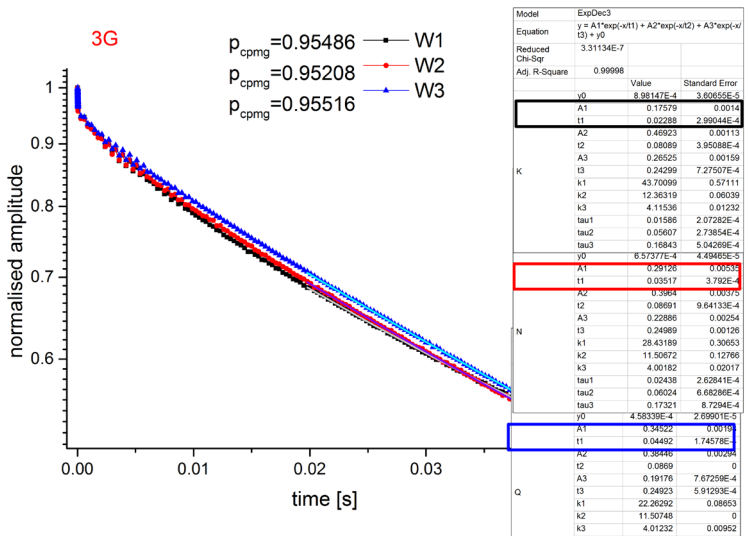

Model	ExpDec3		
Equation	y = A1*exp(-x/t1) + A2*exp(-x/t2) + A3*exp(-x/t3) + y0		
Reduced Chi-Sqr	3.31134E-7		
Adj. R-Square	0.99998		
		Value	Standard Error
K	y0	8.98147E-4	3.60655E-5
	A1	0.17579	0.0014
	t1	0.02288	2.99044E-4
	A2	0.46923	0.00113
	t2	0.08089	3.95088E-4
	A3	0.26525	0.00159
	t3	0.24299	7.27507E-4
	k1	43.70099	0.57111
	k2	12.36319	0.06039
	k3	4.11536	0.01232
	tau1	0.01586	2.07282E-4
	tau2	0.05607	2.73854E-4
	tau3	0.16843	5.04269E-4
N	y0	6.57377E-4	4.49465E-5
	A1	0.29126	0.00535
	t1	0.03517	3.792E-4
	A2	0.3964	0.00375
	t2	0.08691	9.64133E-4
	A3	0.22886	0.00254
	t3	0.24989	0.00126
	k1	28.43189	0.30653
	k2	11.50672	0.12766
	k3	4.00182	0.02017
	tau1	0.02438	2.62841E-4
	tau2	0.06024	6.68286E-4
	tau3	0.17321	8.7294E-4
Q	y0	4.58339E-4	2.69901E-5
	A1	0.34522	0.0019
	t1	0.04492	1.74578E-4
	A2	0.38446	0.00204
	t2	0.0869	0
	A3	0.19176	7.67259E-4
	t3	0.24923	5.91293E-4
	k1	22.26292	0.08653
	k2	11.50748	0
	k3	4.01232	0.00952

Figure S6.2. Analysis of the time domain FID-CPMG NMR relaxation data by CONTIN (A) and (B), SplMod and exponential fitting (C) and (D), respectively. The data are shown for gums after water degumming (A) and (C) and 3G enzymatic degumming (B) and (D) on lecithin-enriched (27.5 w/w% of PLs) soybean crude oil at three different concentration of H_2O (11.9, 21.2 and 28.8 w/w% for WD and 11.7, 21.1 and 28.7 w/w% for 3G ED).

(A) D_2O

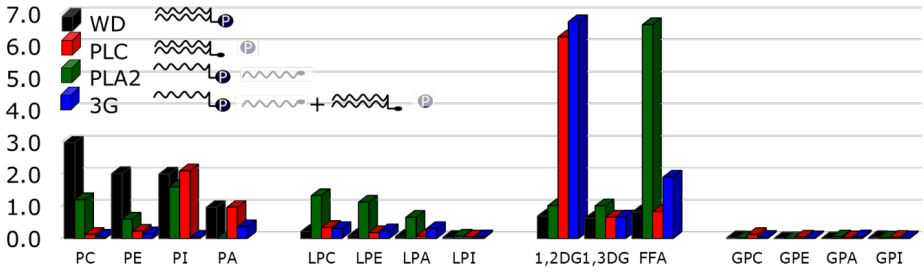

(B) H_2O

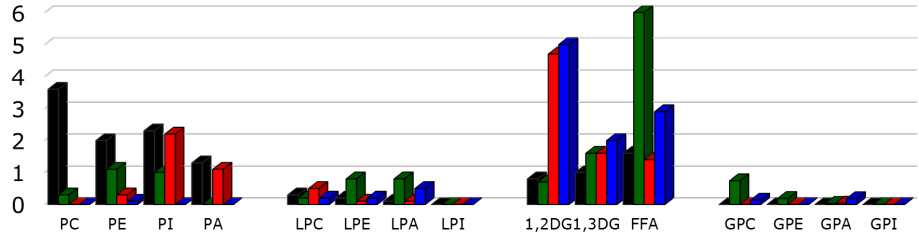

Figure S6.3. Phospholipid (PL: PC, PE, PI, PA), lysophospholipid (LPL: LPC, LPE, LPA, LPI), 1,2- and 1,3-diglyceride (1,2- and 1,3-DG) free fatty acid (FFA) and phosphate compositions in w/w% after WD (black) and ED PLC (red), PLA2 (green) and 3G (blue). The samples were prepared based on D_2O (A) and H_2O (B) and lecithin-enriched (27.5 w/w% of PLs) soybean crude oil.

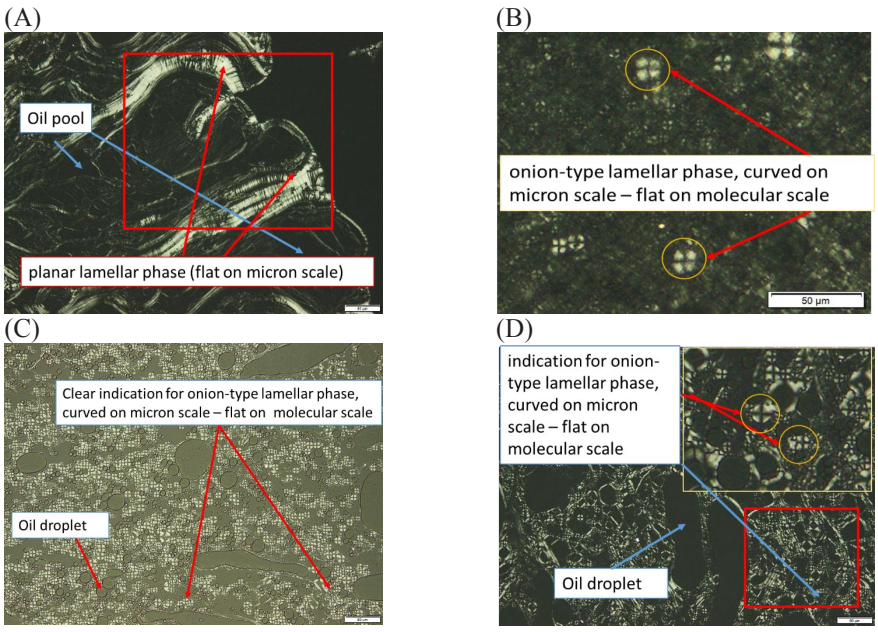

Figure S6.4. Interpretation of the polarized light microscopy (PLM) images obtained for gums after water degumming (WD) (A), PLA2 (B), PLC (C) and 3G (D) enzymatic degumming (ED) treatments.

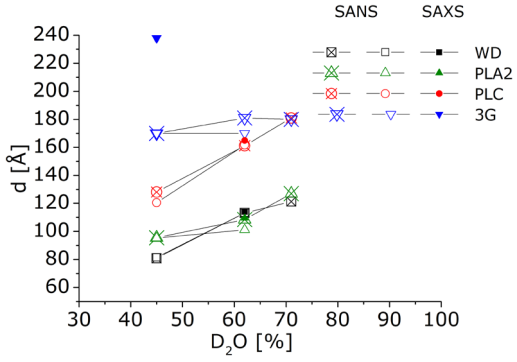

Figure S6.5. Correlation between spacings measured by SAXS and SANS. The legend shows water degumming (WD - black), phospholipase C (PLC - red), phospholipase A2 (PLA2 - green) and their mixture Purifine 3G (3G - blue) enzymatic degumming (ED) treatments.

(A)

$$R_{bulk} = \frac{DG_{bulk}}{TG_{bulk}}$$

$$R_{gum} = \frac{(DG_{droplet}+DG_{bil})}{TG_{gum}} = \frac{DG_{droplet}}{TG_{gum}} + \frac{DG_{bil}}{TG_{gum}}$$

$$\frac{DG_{droplet}}{TG_{gum}} = \frac{DG_{bulk}}{TG_{bulk}} = R_{bulk}$$

$$R_{gum} = R_{bulk} + \frac{DG_{bil}}{TG_{gum}}$$

$$\frac{DG_{bil}}{TG_{gum}} = R_{gum} - R_{bulk}$$

since $[TG]_{gum}$ < [gum] then

estimation of upper limit of DG_{bil} in gum

$$\frac{DG_{bil}}{[gum]} < R_{gum} - R_{bulk}$$

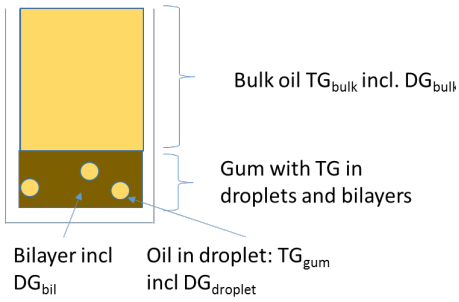

$$TDNMRgum = gumr + gumm = \frac{gum}{TGgum + gum}$$ (TDNMR data for gum phase!)

$$TGgum = gum \frac{1-TDNMRgum}{TDNMRgum}$$

$$\frac{DGbil}{gum} = \{DGNMRgum - DGNMRbulk\}^* \frac{1-TDNMRgum}{TDNMRgum}$$

Figure S6.6. Equations to estimate an upper limit of DGs in bilayers of gum phase and (B) a loss of DGs in bilayers of gum phase via gum.

(A)

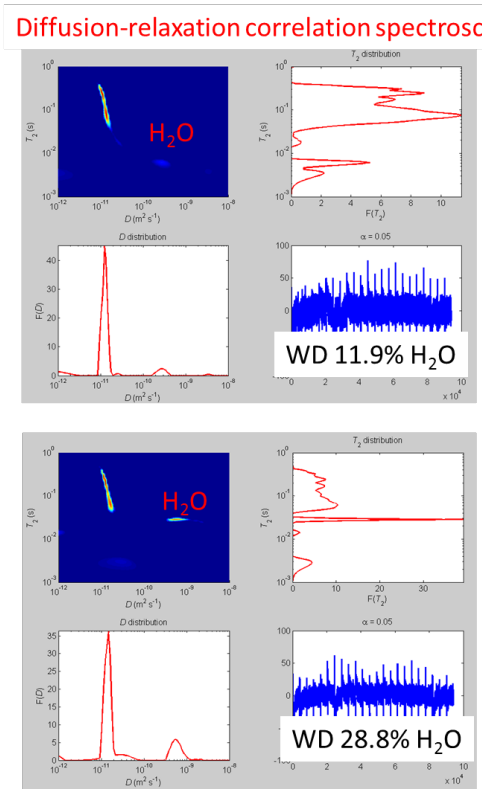
Diffusion-relaxation correlation spectroscopy
H2O
WD 11.9% H2O
H2O
WD 28.8% H2O

(B)

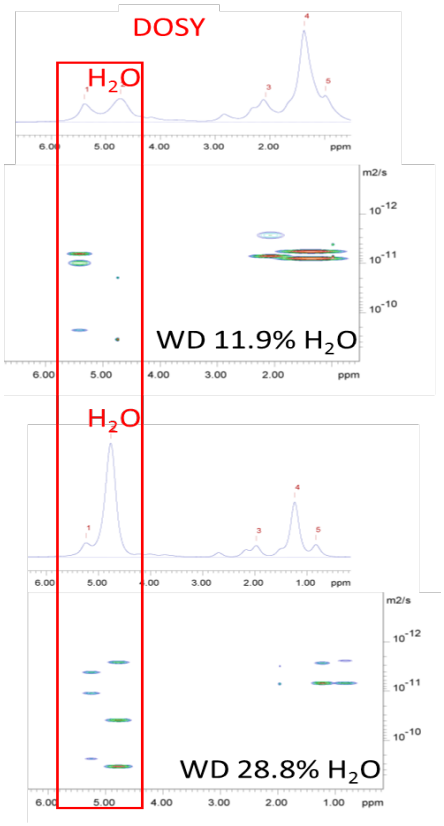
DOSY
H2O
WD 11.9% H2O
H2O
WD 28.8% H2O

(C) (D)

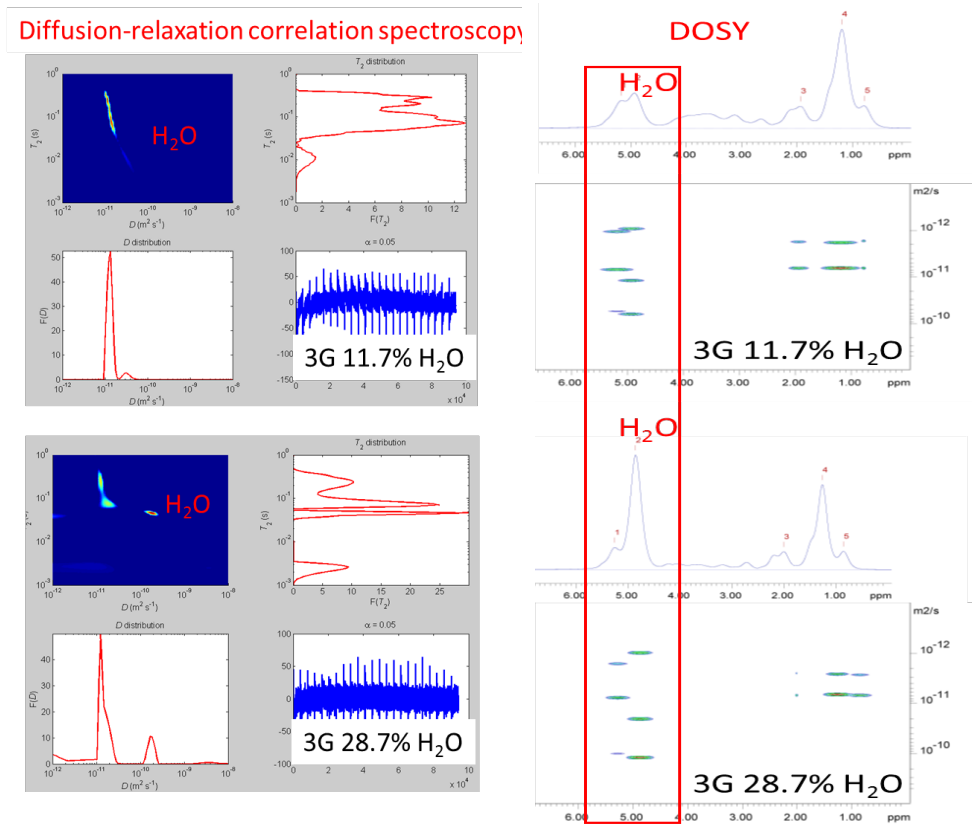

Figure S6.7. 2D diffusion-relaxation correlation (A) and (C) and DOSY (B) and (D) experiments of gums after water degumming and 3G enzymatic degumming on lecithin-enriched (27.5 w/w% of PLs) soybean crude oil at two different concentration of H_2O (11.9 and 28.8 w/w% for WD and 11.7 and 28.7 w/w% for 3G ED)

CHAPTER 7

General discussion

7.1. Main findings and conclusions

This thesis describes implementation and application of complementary methodologies to quantify multiscale crystalline and liquid-crystalline (LC) structures under static and dynamic processing conditions. The multiscale assessment under shear was enabled by rheo-microMRI and rheo-SAS techniques developed for the structural characterization of complex dispersions. **Chapter 2** described the implementation and application range of rheo-microMRI in millimeter gap sized concentric cylinder (CC) geometries at high magnetic field and strong magnetic field gradients which allows temporally and spatially resolved flow measurements with high sensitivity. The necessary precautions were described to perform experiments at low shear on lipid systems with dispersed chemical shifts. Subsequently it was shown that rheo-microMRI measurements were able to provide information about position and time dependent flow behaviour in real time manner which allowed for quantification in terms of local constitutive laws known as local flow curves. **Chapter 3** presented a design of a versatile vertical, temperature controlled rheo-SAS cell. A millimeter gap sized concentric cylinder (CC) rheo-cell was implemented for use with both x-ray sources from a high-end synchrotron facility as well as with lab-based equipment to quantify multiscale fat crystal networks under a wide range of shear rates. Rheo-SAS experiments on complex lipid dispersions provided in a real-time manner information about anisotropy, crystal growth, phase transition and changes in spatial distribution of crystals (network fractality).

Next, rheo-microMRI and -SAS methodologies were applied together with complementary techniques (confocal Raman-imaging, rheology, SFC NMR, rheo-microMRI, X-ray diffraction and scattering techniques) for dynamic assessment of multiscale micronized fat crystal (MFC) network structures (**Chapters 4** and **Chapter 5**). The studies presented in **Chapter 4** revealed that MFCs form a weak-link network of fat aggregates connected by a continuous net of dispersed MFC nanoplatelets. The rough surface of MFC nanoplatelets hampered stacking into large aggregates indicating that particle–cluster aggregation was dominant. Application of shear did not affect the size of the MFC aggregates but released them from the weak-link continuous network, they then subsequently aligned along the flow direction. Moreover, it was shown that shear contributed to a rapid recrystallisation of the thinner MFC nanoplatelets. **Chapter 5** describes the detailed investigation of the coupling

between the recrystallization and network formation of oil-dispersed MFC nanoplatelets by rheo-microMRI, rheo-SAXD and confocal Raman-imaging. Variation of oil composition, temperature and shear provided a means to manipulate MFC recrystallization rate and thus network strength, both under laboratory and industry relevant conditions.

Chapter 6 presented results of multiscale assessment of oil gums obtained under industrial relevant conditions by water degumming (WD) and enzymatic degumming (ED) processes applied on a crude vegetable oil. Mesostructural (SANS, SAXS) and compositional (NMR) assessment of these multicomponent lipid systems (gums) allowed recognition and quantification of lamellar LC phases obtained by WD and ED treatments of crude soybean oils. Thicknesses of the hydration water layers deduced from SANS and SAXS experiments were investigated as a function of water concentration for four WD and ED treatments. Partial incorporation of non-polar lipids (diglycerides (DGs) and free fatty acids (FFAs)) into gum bilayers occurred, which affected the dynamics of the LC bilayers. We were able to establish a link between these effects and molecular mobility as probed by ^{1}H time-domain (TD) NMR T_2 relaxometry measurements. Both the total amount of gum as well as the amount of amphiphilic lipids in the gum could be determined by means of FID-CPMG measurements, which opens the opportunity to assess the efficiency of degumming treatments. This last chapter will provide an outlook how the findings in this thesis can be exploited for improvement of industrial processing routes. Next suggestions will be made how the methodologies presented in this thesis can be built upon for more detailed multiscale assessment of the MFC networks and lamellar LC structures.

7.2. Perspectives for industrial processing

7.2.1. TAG crystalline structures: MFC networks

The insight that formation of pre-crystallised MFC nanoplatelets networks can be modulated by oil type, temperature, shear can turn the design of lipid-based food products into a colloidal game. The rules of this game can be established by rheo-SAXD and rheo-MRI techniques, which can directly assess the impact of shear and temperature on recrystallisation of MFC nanoplatelets. This allows tuning of processing conditions to obtain MFC networks with desired textural properties. Our results (**Chapter 4** and **5**) show that the thickness of

MFC nanoplatelets can be controlled by varying oil type, temperature and shear strength. MFC nanoplatelets with preset thicknesses released from the weak-link continuous phase of the crystal network allow for an efficient Pickering stabilization of water droplet interfaces which can provide a route for simplified manufacturing of emulsified food products.

7.2.1. Liquid-crystalline structures: phospholipid gums

Application of phospholipases in the ED process allows for considerable yield improvements and cleaner processes with reduced use of chemicals in an environment-friendly manner. Our investigation revealed that ED can be efficient at lower water concentrations than used in current protocols. Further investigations of ED LC mesostructures at different temperature and shear conditions can contribute to optimization of upstream processes of the ED treatments. To be able to improve conditions of crude oil extraction and their storage, structural characterisations of WD and ED gums of different types of crude oils might also be useful, since lipid composition of crude oils strongly depends on the seed or bean of origin and upstream processing conditions. Gums are used to obtain lecithins which are commercially added into various food products as emulsifiers (Sein, Hitchman, & Dayton, 2019). The lecithins produced from ED gums have a high value being enriched with lysophospholipids, diglycerides and free fatty acids. The structural features of the ED lecithin-enriched food products are poorly explored which impedes a successful application of ED lecithin in food industry. Further investigation of emulsifying properties of LC lecithin structures after ED (Xie & Dunford, 2017) can offer new opportunities for improving emulsion stability by preventing creaming, droplet coalescence and sedimentation during shelf life of food products (Van Nieuwenhuyzen & Tomás, 2008).

7.3. Perspectives for multiscale structural assessment of TAG crystalline and liquid-crystalline structures

7.3.1. Assessment of MFC nanoplatelets thickness by ^{1}H Spin diffusion NMR

^{1}H spin-diffusion NMR (Figure 7.1) (Cherry, Fujimoto, Cornelius, & Alam, 2005; Clauss, Schmidt-Rohr, & Spiess, 1993; Hou, Chen, & Schmidt-Rohr, 2004; Mokeev & Zuev, 2015; Schlagnitweit et al., 2015; Wang, 1996) is an alternative technique to quantify nano-domain

sizes materials where SAXD and microscopic techniques have struggles due to overlapping with background signals, limitations in imaging contrast (optical or electron), scattering density, or periodicity. A particular advantage of spin-diffusion NMR over SAXD is that it can sense very thin fat crystal nanoplatelets which cannot be detected by SAXD. The potential of ^{1}H spin-diffusion NMR as a tool to measure crystal domain sizes in fat based food dispersions has recently been demonstrated (Voda, Den Adel, van Malssen, & van Duynhoven, 2017). In this study the magnetization of the crystalline nanoplatelets was selected using a double quantum (DQ) filter.

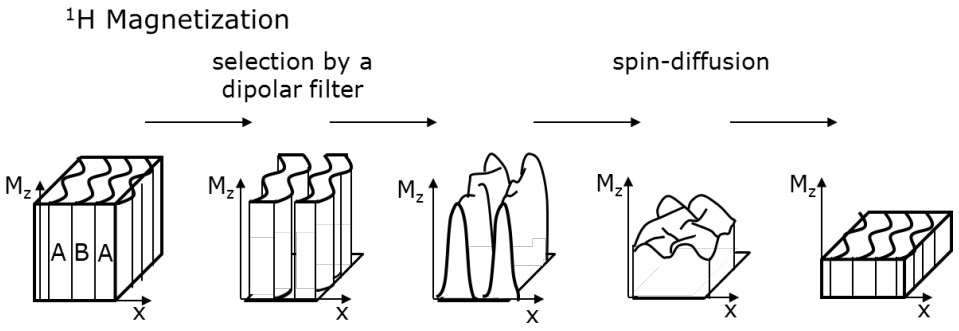

Figure 7.1. Schematic representation of the ^{1}H spin-diffusion process in a dispersion of crystalline nanoplatelets (A) in oil (B). The magnetisation (M_z) of the nanoplatelets (A) can be selected by a double quantum (DQ) filter, subsequently the magnetization will diffuse from the A to B domains. The spin-diffusion kinetics can provide accurate information on the size of domains. Conversely the magnetisation of the liquid oil (B) can be selected with a MAPE filter. Also in this case the subsequent spin-diffusion kinetics (from B to A) can provide quantitative information on domain sizes. The picture is adapted from (Clauss et al., 1993).

As an alternative for the DQ filter the MAPE (Magic and Polarization Echo) magnetization filter (Mauri, Thomann, Schneider, & Saalwächter, 2008; Saalwächter, 2007; Schäler et al., 2015) can be used (Figure 7.2). This filter has the advantage that it can also be applied to diluted systems where selection of the magnetization of the crystalline phase would not be

successful. In first instance modelling of the spin-diffusion kinetics with a mobile (oil) and rigid (crystalline) components only (Figure 7.1) did not provide satisfactory results. Preliminary results obtained by heteronuclear $^{1}H-^{13}C$ WISE experiments clearly showed that also a third intermediate (semirigid) phase is present in TAG crystalline structures. By including this intermediate phase in the model describing spin-diffusion kinetics better description of the spin-diffusion processes in the fat crystal dispersions could be achieved (Figure 7.2). These preliminary results show the potential of using spin-diffusion NMR for assessment of fat crystal domain sizes in dilute fat crystal dispersions. As a next step also heterogeneity in domain sizes should be accounted for, by introducing sophisticated longitudinal/transversal relaxation filters and sophisticated modelling approaches, for example.

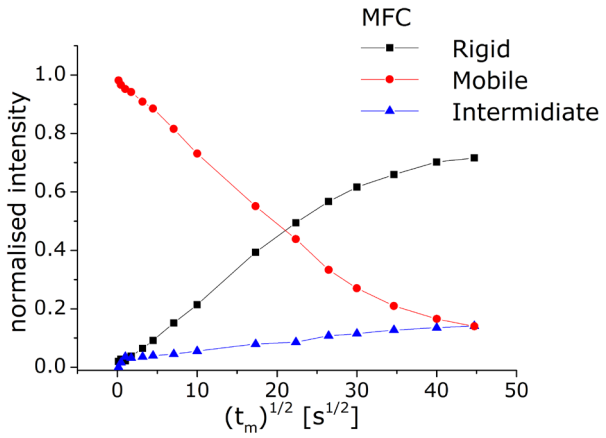

Figure 7.2. ^{1}H spin-diffusion curves obtained with MAPE dipolar filter for a micronized fat crystal (MFC) dispersion. The rigid (crystalline), mobile (non-crystalline) and intermediate phases were observed via multicomponent line shape deconvolution which discriminated the three phase fractions on the basis of ^{1}H molecular mobility. The rigid fraction is attributed to the crystalline entities defining the repeating bilayers of TAGs, the mobile fraction to the TAGs with high chain mobility, the intermediate fraction to an interface between the crystalline and the mobile domains.

7.3.2. Assessment of multiscale structures by rheo-microMRI

Rheo-microMRI can be developed further to investigate local flow behaviour in narrow gaps (less than 1 mm), where non-local material properties are in play. Non-local effects have been observed in cases where the width of the channel or gap is only one or two decades larger than the size of the dispersed particles (de Kort et al., 2016; Ovarlez, Cohen-Addad, Krishan, Goyon, & Coussot, 2013). Narrow gaps force complex materials to behave in a very specific, non-local flow manner. Mechanisms of the non-locality have been observed also for fat crystal dispersions and can be attribute to persistent micron-scale structural heterogeneity or to a migration or a dilatation of such micron-size particles under shear, leading to density differences and consequently viscosity differences across the narrow gaps (de Kort et al., 2016; Ovarlez et al., 2013). The visualisation and characterisation of non-local flow properties may bring understanding of the flow behaviour of fat crystal dispersions being sheared in confined geometries, for example during manufacturing and consumer use (spreading).

Further technical development of rheo-microMRI is required to be able to investigate multicomponent food related structures with time-dependent, heterogeneous flow behaviour. Recently, the use of chemically selective velocity profiles for assessment of migration of oil in water/oil emulsions was demonstrated (Serial, Nikolaeva, Vergeldt, van Duynhoven, & Van As, 2019). Further optimisations of experimental protocols for chemically resolved flow measurements are required to assess the effect of particle migration on complex flow behaviour.

Rheo-MRI setup should also be tailored to mimick dynamic processing conditions. An first step would be to implement temperature control. Possible designs of temperature controlled rheo-microMRI cells with cone-plate and concentric cylinder (CC or Couette) geometries are shown on Figure 7.3. The suggested design includes water channels in close contact with the cone-plate and outer cylinder in the CC geometry. These water channels are isolated from the measured system with 0.5mm PEEK wall. This design should allow for relatively fast and stable temperature control and can be fabricated in a straightforward manner with PEEK or even by means of 3D printing techniques.

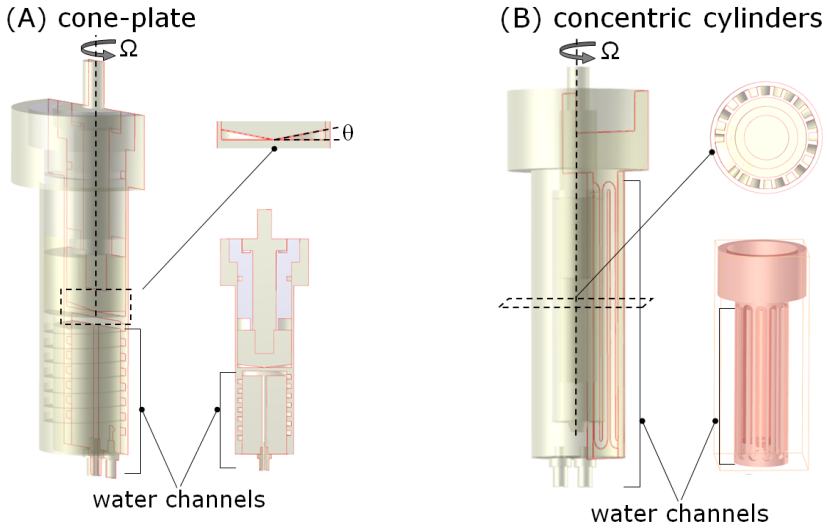

Figure 7.3. Proposed designs of temperature-controlled rheo-microMRI cone-plate (A) and concentric cylinder (CC) or Couette (B) cells where temperature regulation is done by circulating water through channels.

7.3.3. Perspectives in structural assessment of phospholipid gums

The structural assessment of the gum structures can be pursued in several directions. The ^{1}H time-domain (TD) NMR T_2 relaxometry approach can be developed further to be able to quantify the efficiency of the degumming treatments in industrial relevant conditions during degumming treatments on crude oils. The small amount of phospholipids in crude oils will make it necessary to increase sensitivity of the TD NMR measurements, this can be achieved by modifying sample handling procedure to increase amount of gum in NMR tubes. *In situ* centrifugation of NMR samples would concentrate the gum phase in the sensitive region of the NMR tube. This should result in more accurate gum phase quantification. It would also allow to use the proton population of gum phase as an accurate and precise measure of degumming efficiency in crude oils with low amounts of phospholipids.

Other investigations can be devoted to more detailed assessment of the mesoscale gum structure. We showed that the WD and ED gums contain lamellar LC phases with different topology. However, due to lipid compositional heterogeneity of the systems we could not

provide more detailed information on phase type. Use of scattering techniques at different water concentrations and at variable temperatures can provide additional information of phase compositions and transitions. Another way to investigate phase composition is by using the recently developed 2D solid-state (^{31}P MAS) NMR approach (Warschawski, Arnold, & Marcotte, 2018). By this technique, the phase of LC structures can be probed via chemical shift anisotropy of the ^{31}P NMR nucleus of the phospholipids. This is a promising approach for providing structural information in heterogeneous LC food systems.

References

Cherry, B., Fujimoto, C., Cornelius, C., & Alam, T. (2005). Investigation of domain size in polymer membranes using double-quantum-filtered spin diffusion magic angle spinning NMR. *Macromolecules*, *38*(4), 1201–1206. https://doi.org/10.1021/ma047885

Clauss, J., Schmidt-Rohr, K., & Spiess, H. W. (1993). Determination of domain sizes in heterogeneous polymers by solid-state NMR. *Acta Polymerica*, *44*(1), 1–17. https://doi.org/10.1002/actp.1993.010440101

de Kort, D. W., Veen, S. J., Van As, H., Bonn, D., Velikov, K. P., & van Duynhoven, J. P. M. (2016). Yielding and flow of cellulose microfibril dispersions in the presence of a charged polymer. *Soft Matter*, *12*(21), 4739–4744. https://doi.org/10.1039/C5SM02869H

Hou, S. S., Chen, Q., & Schmidt-Rohr, K. (2004). Two-dimensional 13C NMR with 1H spin diffusion for characterizing domain sizes in unlabeled polymers. *Macromolecules*, *37*(6), 1999–2001. https://doi.org/10.1021/ma034659b

Mauri, M., Thomann, Y., Schneider, H., & Saalwächter, K. (2008). Spin-diffusion NMR at low field for the study of multiphase solids. *Solid State Nuclear Magnetic Resonance*, *34*(1–2), 125–141. https://doi.org/10.1016/j.ssnmr.2008.07.001

Mokeev, M. V., & Zuev, V. V. (2015). Rigid phase domain sizes determination for poly(urethane–urea)s by solid-state NMR spectroscopy. Correlation with mechanical properties. *European Polymer Journal*, *71*, 372–379. https://doi.org/10.1016/j.eurpolymj.2015.08.003

Ovarlez, G., Cohen-Addad, S., Krishan, K., Goyon, J., & Coussot, P. (2013). On the existence of a simple yield stress fluid behavior. *Journal of Non-Newtonian Fluid Mechanics*, *193*, 68–79. https://doi.org/10.1016/j.jnnfm.2012.06.009

Saalwächter, K. (2007). Proton multiple-quantum NMR for the study of chain dynamics and structural constraints in polymeric soft materials. *Progress in Nuclear Magnetic Resonance Spectroscopy*, *51*(1), 1–35. https://doi.org/10.1016/j.pnmrs.2007.01.001

Schäler, K., Roos, M., Micke, P., Golitsyn, Y., Seidlitz, A., Thurn-Albrecht, T., … Saalwächter, K. (2015). Basic principles of static proton low-resolution spin diffusion NMR in nanophase-separated materials with mobility contrast. *Solid State Nuclear Magnetic Resonance*, *72*, 50–63. https://doi.org/10.1016/j.ssnmr.2015.09.001

Schlagnitweit, J., Tang, M., Baias, M., Richardson, S., Schantz, S., & Emsley, L. (2015). A solid-state NMR method to determine domain sizes in multi-component polymer formulations. *Journal of Magnetic Resonance*, *261*, 43–48. https://doi.org/10.1016/j.jmr.2015.09.014

Sein, A., Hitchman, T., & Dayton, C. L. G. (2019). Enzymes in Vegetable Oil Degumming Processes. In A. Vogel & O. May (Eds.), *Industrial Enzyme Applications* (pp. 323–350). Wiley-VCH.

Serial, M. R., Nikolaeva, T., Vergeldt, F. J., van Duynhoven, J., & Van As, H. (2019). Selective oil-phase rheo-MRI velocity profiles to monitor heterogeneous flow behavior of oil/water food emulsions. *Magnetic Resonance in Chemistry*, 1–5. https://doi.org/10.1002/mrc.4811

Van Nieuwenhuyzen, W., & Tomás, M. C. (2008). Update on vegetable lecithin and phospholipid technologies. *European Journal of Lipid Science and Technology*, *110*(5), 472–486. https://doi.org/10.1002/ejlt.200800041

Voda, A., Den Adel, R., van Malssen, K., & van Duynhoven, J. (2017). Quantitative Assessment of Triacylglycerol Crystallite Thickness by 1H Spin-Diffusion NMR. *Crystal Growth and Design*, *17*(4), 1484–1492. https://doi.org/10.1021/acs.cgd.6b00501

Wang, J. (1996). On the determination of domain sizes in polymers by spin diffusion. *The Journal of Chemical Physics*, *104*(12), 4850–4858. https://doi.org/10.1063/1.471179

Warschawski, D. E., Arnold, A. A., & Marcotte, I. (2018). A New Method of Assessing Lipid Mixtures by 31 P Magic-Angle Spinning NMR. *Biophysical Journal*, *114*(6), 1368–1376. https://doi.org/10.1016/j.bpj.2018.01.025

Xie, M., & Dunford, N. T. (2017). Lipid composition and emulsifying properties of canola lecithin from enzymatic degumming. *Food Chemistry*, *218*, 159–164. https://doi.org/10.1016/j.foodchem.2016.09.074

SUMMARY

Establishing structure-function relationships is a key step in the development of novel sustainable food formulations and processing technologies. In the manufacturing of lipid-based foods, critical functionalities (shelf life stability, texture and mouth feel) are governed by underlying multiscale lipid structures. Understanding the dynamics of multiscale structural changes in lipid systems under processing conditions will allow for production of food products with desired functionalities. The aim of this thesis was to develop and apply novel complementary methodologies to characterize and quantify multiscale structures of food lipids under static and dynamic processing conditions. The focus is on investigation of micronized fat crystal (MFC) networks and phospholipid liquid crystalline (LC) structures formed after degumming.

Non-invasive multiscale assessment under shear was enabled by rheo-microMRI and rheo-SAS techniques specifically developed for the structural characterization of complex lipid dispersions. **Chapter 2** describes the implementation and application range of rheo-microMRI in millimeter gap sized concentric cylinder (CC) geometries at high magnetic field and strong magnetic field gradients which allows for temporal and spatially resolved flow measurements with high sensitivity. Precautions needed to be taken to perform experiments at low shear on lipid systems which have dispersed chemical shifts. Subsequently it was shown that rheo-microMRI measurements can provide information about position- and time-dependent flow behaviour. This allowed for quantitative assessment of local constitutive laws. **Chapter 3** presents the design of a versatile temperature controlled rheo-SAS cell. It was shown that this concentric cylinder (CC) rheo-cell can be used with both X-ray sources from a high-end synchrotron facility as well as with lab-based equipment. The application of the designed CC rheo-SAS cell for quantitative assessment of multiscale fat crystal networks under a wide range of shear rates was demonstrated. Structural anisotropy, crystal growth, phase transition and changes in spatial distribution of crystals could be monitored in a real-time manner.

These rheo-microMRI and -SAS methodologies together with complementary techniques (confocal Raman-imaging, rheology, SFC NMR X-ray diffraction and scattering techniques) were subsequently used for dynamic assessment of multiscale micronized fat crystal (MFC) structures. **Chapter 4** reveals that MFCs form a weak-link network of aggregates connected by a continuous net of dispersed nanoplatelets. The rough surface of MFC nanoplatelets hampers stacking into large aggregates indicating that particle–cluster aggregation was dominant. Application of shear released

nanoplatelets from the weak-link continuous net, which subsequently aligned along the flow direction. Moreover, shear induced rapid recrystallisation of the thinner MFC nanoplatelets. **In Chapter 5** the investigation of the coupling between the recrystallization and network formation MFC nanoplatelets is pursued by rheo-microMRI, rheo-SAXD and confocal Raman-imaging. Variation of oil composition, temperature and shear provided a means to manipulate MFC recrystallization rate and thus network strength.

Chapter 6 presents results of multiscale assessment of crude oil gums obtained under industrial relevant conditions by water degumming (WD) and enzymatic degumming (ED). Mesostructural (SANS, SAXS) and compositional (NMR) assessment of these compositional heterogeneous lipid systems allowed structural quantification of lamellar LC phases in these gums. Partial incorporation of non-polar lipids (diglycerides (DGs) and free fatty acids (FFAs)) into gum bilayers occurred. This affected the dynamics at molecular scale as seen by ^{1}H time-domain (TD) NMR T_2 relaxometry. The results showed that both the total amount of gum as well as the amount of amphiphilic lipids in the gum can be determined by means of FID-CPMG measurements, which opens the opportunity to assess the efficiency of degumming treatments.

ACKNOWLEDGEMENTS

This PhD has been an incredible journey. I have thoroughly enjoyed it. I had so many rooms to explore, so many things to learn and so many amazing people to meet! I would like to thank and acknowledge everyone who accompanied me during my PhD.

First and foremost, I would like to thank my supervisors John van Duynhoven and Henk Van As for allowing me the opportunity to work at the Laboratory of Biophysics. You made the past four years a pleasant and memorable period. Your interest and curiosity to results during our weekly Friday's meetings sustained my motivation throughout my PhD. You were always able to put things into perspective. Thanks for all your support, for helping me deal with all the uncertainties, disappointments and discoveries. Thanks for scientific guidance, discussions and time. I enjoyed so much to work together.

Adrian Voda, thank you for all your help. You were like a provider for me, especially in the fat crystal and spin-diffusion fields. Thanks for your dedication, enthusiasm, and originality. I appreciate your help and really enjoyed our informal discussions which would usually start with the very inviting "tell me".

My gratitude goes to all members of the SSCANFoods project for active collaboration and fruitful discussions. I would like to thank Maaike Nieuwland, Kirsten Ampt, Arjen Bot, Hans Tromp, Atze Jan van der Goot, Paul Venema. I would like to thank Wim Bouwman, Chris Duif, Evgenii Velichko and Bei Tian for their help with variable SAS experiments. It has been an incredible experience to work with you on synchrotron and nuclear facilities.

I would like to thank my collaborators from DSM Arjen Sein, Tim Rietkerk, Margo Schooneveld, Adriana Carvalho de Souza and Tony van den Burg. It has been so exciting to dive into the degumming story, to explore it and to see the evolution of our understanding of this story. Especially many thanks to Arjen and Tim! I also would like to thank Remco and Tony for explanation and help while running the enzymatic degumming processes.

Ruud den Adel, Patricia Heussen, Gerard van Dalen, Peter de Groot, Gert-Jan Goudappel, Niels de Roo, Ewoud van Velzen, Kees van Malssen thank you all for your help with scattering and diffraction

experiments, with obtaining Raman images and with rheological measurements. Thank you for interesting discussions. I must say that I always enjoyed a friendly atmosphere at your offices at Unilever.

My gratitude goes to all people who helped with work on the rheo-MRI project. John Philippi and Frank Vergeldt, thank you for all your help, technical support, a lot of right and tricky questions, for your openness to *detailed* discussions and creative thinking and for your interest in my projects. I would like to thank the WUR workshop, Johan Belgraver and Hans de Rooij for great realization of our designs of rheo-MRI cells. My gratitude goes to Joshua Dijksman and Paul Venema for help with rheological measurements and fruitful discussions of all related problems and results that brought us to finding of links between rheology and rheo-MRI. Daan de Kort, Steven van Kesteren, Julia Krug, Raquel Serial and Camilla Terenzi, thank you all for great collaborations.

Thank you all other Biophysics colleagues and friends! There are so many names that I would like to acknowledge, because so many of you helped me out with many different issues and contributed to the wonderful atmosphere at work: Herbert van Amerongen, Emilie Wientjes, Arjen Bader, Cor Wolfs, Rob Koehorst, Elena Golovina, Folkert Hoekstra, Edo Gerkema, Pieter de Waard, Alena Prusova, Evgenia Iermark, Carel Feijen, Yashar Ranjbar, Shazia Farouq, Shanthi Pagadala, Karlijn Theunissen, Ahmad Bhatti, Abbas Jabermoradi, Suyeon Yang. Netty Hoefakker, I greatly appreciate your administrative support, and the reserve of sweets in your office. Johannes Hohlbein, I enjoyed a lot to be your teaching assistant. It was a lot of fun to work together with WUR students. A special thanks to Koen Martens and Mattia Fontana for being useful colleagues, my friends, my paranymphs, and for balancing me between "light and dark" sides in our office.

My acknowledgements would not be incomplete without thanking all my friends and family. My dear people from the InMotion dance traces and the ELAP project, thank you all for your spirit, I enjoyed to explore and to improvise with you in the studio and in life. I would like to thank my Pandora's friends for a great time in Wageningen! My warm thanks go to Alisa and Dzhamilia, thanks for all the talks, all your support and great moments! I would like to thank a lot of people in Russia, my big Russian family, thank you. And last but not least, I would like to sincerely thank my dear parents. Thank you for all your support in my ideas and initiatives, for all your unlimited trust /*Мои дорогие родители, огромное спасибо вам за поддержку моих идей и начинаний, за ваше неограниченное доверие*/.

ABOUT THE AUTHOR

Tatiana Nikolaeva was born March 6th 1989 in Naberezhnye Chelny, Russia, and grew up in Zelenodolsk. In 2006, she completed her secondary education with honors and afterwards she moved to Kazan to study Physics at Kazan Federal University. During her second year she became interested in research and joined the group of Physics of Molecular Systems to learn about NMR methods and their applications to soft matter systems. Showing a high interest to the multidisciplinary fields, Tatiana continued the education specializing in medical physics and the exploration of NMR techniques. In 2011, she completed her higher education with honors. Her diploma project was in titled *Spin lattice relaxation time as NMR sign of cancer* and was done under supervision of Prof. Dr Vladimir Skirda. Based on the obtained results Tatiana received an individual grand of Russian Federation program «Participant of the youth scientific and innovation contest» («U.M.N.I.K.») (2011-2013).

In 2015 Tatiana moved to the Netherlands and started to work as a PhD candidate in the Laboratory of Biophysics at Wageningen University & Research on the project *Multiscale assessment of food lipid structures* under supervision of Prof. Dr John van Duynhoven and Dr Henk Van As. The project was done in close collaboration with Radiation Science and Technology group of TU Delft and the Research & Development groups of Unilever and DSM, which allowed her to investigate crystalline and liquid-crystalline food lipid structures using advanced microscopic, scattering and NMR techniques.

LIST OF PUBLICATIONS

This thesis:

T. Nikolaeva, F. J. Vergeldt, R. Serial, J. A. Dijksman, P. Venema, A. Voda, J. van Duynhoven, H. Van As (2019). High field microMRI velocimetric measurement of quantitative local flow curves. (Submitted for publication)

E. Velichko, B. Tian[1], **T. Nikolaeva[1]**, J. Koning, J. van Duynhoven, W. G. Bouwman (2019). A versatile shear cell for investigation of structure of food materials under shear. Colloids and Surfaces A: Physicochemical and Engineering Aspects, 566, 21-28. https://doi.org/10.1016/j.colsurfa.2018.12.046

T. Nikolaeva, R. den Adel, E. Velichko, W. G. Bouwman, D. Hermida-Merino, H. Van As, A. Voda, J. van Duynhoven (2018). Networks of micronized fat crystals grown under static conditions. Food & Function, 9, 2102-2111. https://doi.org/10.1039/C8FO00148K

T. Nikolaeva, R. den Adel, R. van der Sman, K. J. A. Martens, H. Van As, A. M. Voda, J. van Duynhoven (2019). Manipulation of Recrystallization and Network Formation of Oil-Dispersed Micronized Fat Crystals. Langmuir, 35, 6, 2221-2229. https://doi.org/10.1021/acs.langmuir.8b03349

T. Nikolaeva, T. Rietkerk, A. Sein, R. Dalgliesh, W. G. Bouwman, E. Velichko, B. Tian, H. Van As, J. van Duynhoven (2019). Impact of water degumming and enzymatic degumming on gum mesostructure formation in crude soybean oil. (Submitted for publication)

[1] Equal contribution

Other publications:

D. W. de Kort, **T. Nikolaeva**, J.A. Dijksman (2017). Rheo-NMR: Applications to Food. In G. A. Webb (Ed.), Modern Magnetic Resonance. (pp. 1–21). Springer, Cham. https://doi.org/10.1007/978-3-319-28275-6_19-1

K. J. A. Martens, G. van Dalen, P.C.M. Heussen, A. M. Voda, **T. Nikolaeva**, J. P. M. van Duynhoven (2018). Quantitative Structural Analysis of Fat Crystal Networks by Means of Raman Confocal Imaging. Journal of the American Oil Chemists' Society. https://doi.org/10.1002/aocs.12035

M. R. Serial, **T. Nikolaeva**, F .J. Vergeldt, J. P. M. van Duynhoven, H. van As (2019). Selective oil-phase rheo-MRI velocity profiles to monitor heterogeneous flow behavior of oil/water food emulsions. Magnetic Resonance in Chemistry, 1–5. https://doi.org/10.1002/mrc.4811

S. van Kesteren, **T. Nikolaeva**, H. Van As, J. A. Dijksman (2019) Direct evidence of stress-induced hydrogen-bond thickening in macromolecular complexes. (Submitted for publication)

OVERVIEW OF COMPLETED TRAINING ACTIVITIES

Discipline specific activities

Courses

Small Angle Scattering Mini-School (Utrecht, The Netherlands)	2015
NWI-SM023D-2015-KW2-V: 1516 Magnetic Resonance II (Nijmegen, The Netherlands)	2015-2016
Advanced food analysis (Wageningen, The Netherlands) [1]	2017
Internship at DSM (Delft, The Netherlands)	2017
WUR Rheology workshop (Wageningen, The Netherlands)	2017 [2],2018

Conferences

Food Valley Expo (Wageningen, The Netherlands) [2]	2015
16th International Food Colloids Conference (Wageningen, The Netherlands) [1]	2016
Mini-symposium "Mesostructures under shear" (Wageningen, The Netherlands) [2]	2016
Presentation of project results at Unilever (Vlaardingen, The Netherlands) [2]	2016
13th International conference on the Applications of Magnetic Resonance in Food Science (Karlsruhe, Germany) [2]	2017
14th International Conference on Magnetic Resonance Microscopy (ICMRM) (Halifax, Canada) [1]	2017
Rheo-NMR workshop (ICMRM) (Halifax, Canada) [2]	2017
Forum for Analytical Science and Technology (FAST) (Veldhoven, The Netherlands) [2]	2018
14th International Conference on the Applications of Magnetic Resonance in Food Science (Rennes, France) [2]	2018

Neutrons and Food 5 (Sydney, Australia) [2]	2018

General courses

VLAG PhD week	2015
Training in Rheo-NMR and spin-diffusion NMR	2015
Interpersonal Communication for PhD Students	2016
Scientific Writing	2017
Scientific Publishing	2017
Mobilising your Scientific Network	2017

Optional courses and activities

Preparing PhD research proposal		
BIP group meetings and colloquia		2015-2019
Project meetings, and meetings with STW SSCANFOODS utilisation committee		2015-2019
Weekly group meetings		
Dutch NMR Discussion Group (NMRDG):		
	Utrecht	2015
	Wageningen	2016
	Geleen	2017
	Nijmegen	2018
WUR NMR discussion group		2016-2019

[1] Poster presentation

[2] Oral presentation

Research presented in this thesis was performed at the Laboratory of Biophysics, Wageningen University, the Netherlands.

This work is part of the research programme SSCANFoods with project number 13386, which is (partly) financed by the Netherlands Organisation for Scientific Research (NWO).

Printed by GVO drukkers & vormgevers, Ede